Design and Development of Compact Two Mode Interference and Multimode Interference Couplers for Photonic Integrated Devices

A thesis submitted in part fulfillment of the requirements for award of the degree of Doctor of Philosophy

BIDYUT DEKA
Regn. No: 012/2009

School of Engineering
Department of Electronics & Communication Engineering
Tezpur University

This thesis is dedicated to Beloved Parents,
Family and Teachers

&

In the memory of Nuruddin Ahmed sir

ABSTRACT

In recent years, optical network has grown tremendously to fulfill the enormous demand of bandwidth requirements due to remarkable increase of network users and services in nationwide network backbone consisting of nodes. The key devices of network nodes are photonics matrix switch, wavelength division multiplexer/demultiplexer, adaptive equalizer, add/drop multiplexer etc. Traditionally, these devices consisted of bulky and heavy components that require careful alignments, protection against vibrations, moisture and temperature drift. In order to make them compatible with the modern technology, *Photonic Integrated Circuits (PIC)* based on planar waveguide was first coined by S. E. Miller in 1969 for implementation of these devices. The introduction of Photonic Integrated Devices (PID) for applications in high speed optical networks providing multiple services to more number of users is indispensable as this requires large scale integration (LSI) and the miniaturization of PID device components remains a very challenging task.

The basic components of PID are planar waveguide technology based directional coupler (DC), Two-Mode Interference (TMI) coupler and Multimode Interference (MMI) coupler. For PID, it is required to select the components on the basis of issues such as compactness, higher fabrication tolerance, polarization independence and lower power loss. In this thesis, study is carried out on these device components with their new proposed structures considering the above issues.

The introduction of DC, Multimode Interference (MMI) principle and Two Mode Interference (TMI) principle in PID are made in 1969, 1973 and 1977 respectively. Optical Directional Coupler (DC) consists of two dielectric waveguides placed in close proximity to each other for coupling of guided power based on phase difference of two guided modes– even mode and odd mode. On the other hand, the MMI couplers are based on self-imaging principle which is a property by which an input field profile is reproduced in single or multiple images at periodic intervals along the propagation direction of the guide. It consists of a multimode central waveguide section (excitation of more than two modes) with input and output single mode access waveguides. TMI coupler consists of central waveguide (TMI section) with zero waveguide separation gap connected to two input and output single mode access waveguides and power transferred to the output waveguides depends on the phase difference between two excited modes – fundamental and first order. In optical networks, DC, MMI coupler and TMI coupler based integrated optic devices, such as Waveguide Division Multiplexer (WDM), add/drop multiplexer, optical switches have been used.

Extensive studies have been made for implementation of such device components using a variety of materials such as Lithium Niobate, polymers, III-V semiconductors and silicon based materials. Out of these materials Silicon (Si) based materials have the potential to allow strong confinement of light with moderately low propagation losses, high index contrast, low material cost and its compatibility with well known conventional silicon based IC technology. The Si based waveguide materials are Silicon-On-Insulator (SOI) (silicon core), SiO_2/SiO_2-GeO_2 (Core) and SiO_2/Silicon Oxynitride (SiON) core. Among these materials Silicon Oxynitride (SiON) as core and SiO_2 as cladding is considered as a promising material for PID as it offers the wide range of refractive index in between 1.45 (SiO_2) to 2.0 (Si_3N_4) providing the auxiliary advantage for high index contrast designs and due to the property of optical transparence from 210 nm to beyond 2000 nm. This optical property has permitted to develop low loss waveguides for long range applications such as nationwide networks, optical waveguide sensor and integrated quantum optical circuits etc.

Apart from the materials, previous authors have reported on studies of different geometries such as tapered geometry (parabolic tapered, linearly tapered at middle, parabolic tapered at middle) and periodic grating structure with different shape for DC, TMI couplers and MMI couplers for more compactness, higher fabrication tolerances etc. Recently, T. Sai *et al.* have shown tooth shaped grating assisted TMI coupler for wavelength division multiplexing.

Within this frame it is seen that very few studies are made for comparative study of DC, TMI coupler and MMI coupler. M. Rajarajan *et al.* in 1999, reported a simulation study for performance comparison between DC and MMI coupler using vector finite element and least square boundary residual numerical tools. Further, S. Y. Lee *et al.* in 2004 has presented a comparison of ridge-type DC and MMI coupler in terms of transformation relationship and coupling characteristics. From the best of our knowledge, no existing literature has been found stating comparative study on conventional couplers such as DC with TMI coupler and DC with TMI as well as MMI couplers.

As discussed earlier, development of passive optical compact components (such as DC, TMI coupler and MMI coupler etc.) for large scale integration (LSI) with low insertion loss, low polarization dependent structures so as to reduce polarization dependent loss and higher fabrication tolerance with low crosstalk is very much required. In this Ph. D. work, all these aspects of DC, TMI and MMI based devices have been studied and the prime objectives of this thesis are considered as follows:

I. To develop a mathematical model using Simple Effective Index Method (SEIM) based on sinusoidal modes for accurate estimation of coupling power in directional coupler (DC), Two Mode Interference (TMI) coupler, Multimode Interference (MMI) coupler and find a transformation relationship of DC with TMI coupler and MMI coupler with silica waveguides using silicon oxynitride as a core material.

II. To design a compact TMI coupler using tooth shaped grating assisted geometry for Photonic Integrated Devices. Also design and propose tooth shaped grating assisted Directional Coupler and MMI coupler for compactness.

III. To design double S-bend structures for compact TMI coupler and proposed MMI coupler for PID.

IV. To fabricate the designed DC, TMI coupler and MMI coupler using silica waveguides with silicon oxynitride as a core and characterize it for performance analysis.

In this research effort, a mathematical model using simple effective index method (SEIM), based on sinusoidal mode has been developed for accurate estimation of coupling power in the DC, TMI and MMI couplers. The results obtained using SEIM are found to be accurate and comparable with the other reported results and commercially available simulation tool such as optiBPM. A transformation relationship has been established among these couplers and in addition, the conventional structures of these couplers were fabricated and their experimental results were compared in order to verify with the theoretical predictions. Further, tooth shaped grating assisted (GA) geometry have been incorporated in the coupling region of these couplers for reduction of coupling length.

Although it is found that GA-TMI coupler has the shorter beat length than the other two types of optical couplers (GA-DC and GA-MMI), the total device length of GA-MMI coupler is most compact. The beat length of grating assisted couplers are ~50% compact than that of the conventional couplers. In the proceeding chapter of the thesis, double S-bend (DS) structure of TMI and MMI couplers has been studied. The coupling characteristics of DS-TMI coupler and DS-MMI coupler are compared theoretically and experimentally with their conventional geometries. Finally, at the end of thesis work, future scopes and possible application of the current study have been discussed.

AUTHOR'S DECLARATION

I, Bidyut Deka, hereby declare that the work incorporated in this thesis entitled "*Design and Development of Compact Two Mode Interference and Multimode Interference Couplers for Photonic Integrated Devices*" submitted by me for the award of degree of Doctor of Philosophy (Ph.D.) to the Tezpur University has been carried out by me under the guidance of Dr. Partha Pratim Sahu, Professor, Tezpur University, Assam. Neither the thesis nor any part of it has been submitted for the award of any degree elsewhere and that it has not been submitted in any previous application for a higher degree. I further declare that:

- wherever contributions of others are involved, every effort is made to indicate this clearly, with due reference to the literature and acknowledgement of discussions, this is always clearly attributed;

- where I have quoted from the work of others, the source is always given. With the exception of such quotations, this thesis is entirely my own work;

Place: Tezpur University
Date: 25th Feb'2013

Signed: Bidyut Deka

TEZPUR UNIVERSITY

Certificate

This is to certify that the thesis entitled ***Design and Development of Compact Two Mode Interference and Multimode Interference Couplers for Photonic Integrated Devices*** submitted to the School of ***Engineering***, Tezpur University in part fulfillment for the award of the degree of Doctor of Philosophy in **Electronics & Communication Engineering** is a record of research work carried out by **Mr. Bidyut Deka** under my supervision and guidance.

All help received by him/her from various sources have been duly acknowledged.

No part of this thesis has been submitted elsewhere for award of any other degree.

(Dr. Partha Pratim Sahu)
Ph. D. Supervisor

Professor,
Department of Electronics & Communication Engineering
School of Engineering
Tezpur University

TEZPUR UNIVERSITY

Ph.D. THESIS EXAMINER'S REPORT

1. Name of the candidate: ______________________________

2. School. ______________________________

3. Department______________________________

4. Title of the thesis ______________________________

____

5. Name, designation and complete address of the Examiner:

____

____

The thesis has been examined by me and I recommend that: (please delete all except any one relevant)

(a) The thesis is found suitable for oral defence evaluation without further examination or amendment.

(b) The thesis is found suitable y for oral defence evaluation, subject to inserting the corrections and/or additions/modifications suggested by me in the thesis. This should subsequently be found to be satisfactory by ODEC without further reference to me.

(c) The thesis is not suitable for oral defence evaluation, but the candidate be asked to re-submit the thesis in a revised form for re-examination. Areas requiring major modifications are detailed in my attached report.

(d) The thesis is rejected.

6. If the thesis is recommended for acceptance whether:

    a.) It is fit for publication by the candidate in its original form or in any modified form.

    b) The thesis is of such outstanding merit that the university would be justified in publishing it at its own cost.

Date: ________ **Signature of the External Examiner**

Acknowledgments

I am enthusiastically waiting for years to write this page but as the day arrived, I realize the difficulty to squeeze everyone into one single page.

In the name of God to whom I am beset with gratefulness for his persistent assist throughout the pathway of knowledge.

My research work is made possible by many blessing I accept in my personal life.

First and foremost, it gives me immense pleasure to offer my sincerest gratitude and thanks to my principal supervisor, Dr. Partha Pratim Sahu, who has supported me at all times, throughout my thesis with his patience and knowledge whilst allowing me the room to work in my own way. It has been an honor to be his first Ph.D. student. I am very appreciative of his generosity and it would not have been possible to write this doctoral thesis without him.

I am deeply and forever indebted to my loving parents (Mr. Barun Chandra Deka and Mrs. Makani Deka), elder brother Pranjal Deka, my sister Archana Deka, sister-in-law Daijee Deka and all the family members for their unambiguous support throughout my work, for which my mere expression of thanks likewise does not suffice.

I would like to thank all the faculty members, Department of Electronics & Communication Engineering, Tezpur University who have helped me the past few years.

I am truly beholden to Mr. Anukul Baishya Sir for the valuable technical discussions and support throughout my stay at Tezpur University on both an academic as well as on personal level.

I would like to express deep love and gratitude to my friends Mohendra Roy, Ankur Gogoi, Ratan Baruah, Vijay Chatterjee, Hemanga Kr. Das, Mahipal Singh, Anup Kr.

Bordoloi, Madhurjya Pratim Das, Nimisha Dutta, Pranjal Borah, Nilima Gogoi and Shashikala Kalita.

My sincere thanks to Aradhana Dutta for her noble support, encouragement and helpful discussions in everything and being with me in all ups and downs during the course of this thesis work.

Thanks to all of the technicians who helped to make my work possible. My special thanks to Montu Mali and Mitharam Handique from Tezpur University for their help and support in preparation of hardware set-up.

Special thanks to department of Physics, Tezpur University for their support in experimental measurements.

Thanks to the office staff, Department of Electronics & Communication Engineering, Tezpur University, who are enthusiastically waiting for I am finish writing this Ph. D. thesis and proceed forward for a brilliant career.

I take the opportunity to express the profound gratitude from my deep heart to my relatives, dear brother and sisters: Ajoy Rajkhowa, Jyotiprakash, Manashi, Kamal, Bikram, Nidhashana, Debashis, Oliv, Ankita, Nipam, Raja, Tiku, Deep, Babu, Niku, Biku, Babli and Tanke for their love, generosity and encouragement while writing this thesis.

I would finally like to acknowledge the help and supports for the fabrication part that was carried out at the CENSE, IISc under INUP at IISc which have been sponsored by DIT, MCIT, Government of India. My sincere gratitude to Dr. Gopal Hegde, Prof. K. N. Bhatt, Prof. Sivsankar, Dr. Vijayraghaban, Dr. Vinoy and Dr. Srivastav sir for their valuable suggestion and discussion held during the fabrication work. Thanks to Dr. Sabhitha, Smita, Srinivas, Satya, Pavandeep, Vamsi for their help and support.

I would like to thank the Council of Scientific & Industrial Research (CSIR), HRDG, New Delhi for providing financial support under the scheme of Senior Research Fellowship (SRF) for the thesis work.

At the last but not the least, I would like to offer my sincere gratitude to my home institute Tezpur University.

Bidyut Deka

Table of contents

List of Tables

List of Figures

Fig.-2.11: Coupling length (mm) versus grating depth (μm) [72] for different index profiles, +++: sawtooth, XXX: symmetric triangular, 000: sinusoidal. GADC parameters: n_o=3.18, n_l=3.282, n_g=3.18, n_r=n_{fr}=3.282, n_s=3.18, t_l=0.2 μm, t_2=0.4238 μm, t_g=1.5-t_r /2 μm, t_{fr} = 0.5-t_r /2 μm, t ranging from 0.01 to 0.15 μm.

Fig-2.12: Coupling efficiency (%) versus grating depth (μm) for different index profiles, ***: squared (50%), +++: sawtooth, boxes: optimized rectangular (42%). GADC [72] parameters: n_0 = 3.18, n_l=3.282, n_g=3.18, n_r=n_{fr}=3.282, n_s=3.18, t_l=0.2 μm, t_2=0.4238 μm, t_g =1.5–t_r/2 μm, t_{fr}=0.5– t_r/2 μm, t_r ranging from 0.01 to 0.15 μm.

Fig-2.13: Schematic design of an ultra compact TMI wavelength division multiplexer using a tooth shaped grating structure.

Fig- 2.14: Mode-dependent E-field spectra of the toothed-grating TMI multiplexer. (a) The bold line was detected at the observation point O_1(x=0, z=0) and the thin one at O_2(x=W_m/4, z=0). (b) The bold line was detected at O_3 and the thin one at O_4.

Fig-2.15(a): Mode independent patterns of 1538 nm and 1572 nm in GA-TMI coupler.

Fig-2.15(b): Intensity contrasts of 1538 nm and 1572 nm in GA-TMI coupler.

Fig-2.16: Insertion loss of 1538 nm and 1572 nm wavelengths in GA-TMI coupler.

Fig-2.17(a): Amplitude distribution, wave fronts, time averaged poynting vector of fundamental mode on a straight and a bent waveguide section.

Fig-2.17(b): T_B versus R for Δn=0.0025 at λ=1.3 μm and 1.55 μm.

Fig-2.18(a): Transition region TOMZ switch-(a) Transition region (b) Single S-bend.

Fig-2.18(b): T_B (90) vs R for Δn=0.0025, 0.0045, 0.0075 and 0.015 at λ=1.55μm.

Fig-2.18(c): C_1 and C_2 versus index contrast (Δn) for V ~2.4.

Fig-2.18(d): Loss coefficient versus R for Δn =0.0025, 0.0045, 0.0075 and 0.015.

Fig-2.19 (a): Nation wide optical backbone: NSFNET T1 [67]-[68].

Fig-2.19 (b): Nation wide optical back bone: Indian network [67]-[68].

Fig-2.19(c): Schematic block diagram of reconfigurable node consisting of 3x3 TOSW, W-MUX and W-DMUX.

Fig-2.20: (a) Lay out of 8x8 optical matrix switch demonstrated by Kasahara et. al [10] using SiO_2/SiO_2-GeO_2 waveguide.(b) Arrangement of eight switching units in each stage giving 64 units for eight stages (c) single TOMZ unit.

CHAPTER-3

CHAPTER-4

Fig-4.11: Schematic 3D diagram of GA-TMI coupler.

CHAPTER-5

CHAPTER-6

CHAPTER-7

Fig-7.3: Beam propagation results of DB-MMI coupler with W_{mmi}=7 μm, a=b=1.5 μm, λ=1.55 μm, n_2=1.45 and Δn=5 % for (a) conventional (A=0^0), (b) A=22^0, (c) A=26^0 and (d) A=30^0 respectively.

Fig.-7.4: Double S-Bend loss versus H of the proposed DB-MMI structure with bending angle A=26^0 for h=4 μm, a=b=1.5 μm, cladding index~1.45 and Δn~5%.

Fig.-7.5: Power imbalance characteristics versus MMI width tolerance (δw) for conventional (solid line), proposed structure and parabolic tapered (at the middle) 3dB MMI coupler with cladding index~1.45, h~4 μm, Δn~5%, a=b=1.5 μm and wavelength~1.55 μm. (•)- experimental point of 3dB conventional MMI structure, (+)- experimental point of the proposed 3dB DS-MMI coupler with A=26^0.

Fig-7.6: Power Imbalance characteristics versus wavelength variation for double band assisted MMI coupler (dotted line), tooth shaped grating assisted MMI coupler (dashed line) and conventional MMI coupler (solid line) with a=1.5 μm, b=1.5 μm, h~4.0 μm, A=26^0, index contrast ~5 % and cladding index~1.45.

Fig-7.7: Normalized coupling power distribution of DB-MMI coupler for both TE-mode (solid line) and TM-mode (dashed line) with h=4.0 μm, A=26^0, a=b=1.5 μm, cladding index~1.45, Δn=5% and λ~1.55 μm respectively.

Fig.-7.8: Dependence of h on longitudinal beat length and access transition length (L_T) of the proposed DB-MMI structure with bending angle A=26^0 for h=4 μm, a=b=1.5 μm, wavelength~1.55 μm, cladding index~ 1.45 and Δn~5 %. The cross sign represents L_T and longitudinal beat length of fabricated DB-MMI coupler.

Fig-7.9: Power loss measurement set-up.

Fig.-7.10: Flow chart of fabrication process steps.

Fig-7.11: SEM images and corresponding beam spot measurements of (a), (c) conventional MMI coupler of longitudinal coupling length ~79.9 μm, A=0^0 and (b), (d) proposed DB-MMI coupler of longitudinal coupling length ~67.2 μm and A=26^0.

List of Abbreviations

B

BPM	Beam Propagation Method

C

CCD	Closed Circuit Camera
CMT	Coupled Mode Theory
CAE	Computer-Aided-Engineering
CeNSE	Center of Excellence for Nano Science and Engineering
CIF	Catalogue Information Format

D

DC	Directional Coupler
DI	De-Ionised
DOS	Digital Optical Switch
DS	Double S-bend
DB-TMI	Double S-Bend Two-Mode Interference
DB-MMI	Double S-Bend Multimode Interference
DS-TMI	Double S-bend Two-Mode Interference
DS-MMI	Double S-bend Multimode Interference
DXF	Drawing eXchange Format

E

EIM	Effective Index Method
EDFA	Erbium Doped Fiber Amplifiers

F

FDTD	Finite Difference Time Domain
FTIR	Fourier Transform Infrared
FFT-BPM	Fast Fourier Transform Beam Propagation Method
FD-BPM	Finite Difference Beam Propagation Method
FDVBPM	Finite Difference Vector Beam Propagation
FD-SVBPM	Finite Difference Semi Vector Beam Propagation
FWHM	Full Width Half Maximum

G

GA	Grating Assisted
GA-DC	Grating Assisted Directional Coupler
GATS	Grating Assisted Tooth Shaped
GA-TMI	Grating Assisted Two-Mode Interference
GA-MMI	Grating Assisted Multimode Interference
GDSII	Graphic Database System

I	
IISc.	Indian Institute of Sciences
IO	Integrated Optics
L	
LDF	Laser Draw Format
M	
MMI	Multimode Interference
MZ	Mach Zehnder
MZI	Mach Zehnder Interferometer
N	
NSFNET -T1	National Science Foundation Network
P	
PECVD	Plasma Enhanced Chemical Vapour Deposition
PID	Photonic Integrated Devices
PR	Photoresist
R	
RF	Radio Frequency
RCA	Radio Corporation of America
RIE	Reactive Ion Etching
S	
SAIF	Sophisticated Analytical Instrument Facility
SEIM	Simple Effective Index Method
SMSEIM	Sinusoidal mode Simple Effective Index Method
SEM	Scan Electron Microscope
T	
TE	Transverse Electric
TM	Transverse Magnetic
TMI	Two-Mode Interference
TOSW	Thermo-Optic switch
U	
UV	Ultraviolet
USA	United States of America
W	
W-MUX	Wavelength Multiplexer
W-DMUX	Wavelength De-multiplexer
WDM	Wavelength Division Multiplexer

1D	One dimensional
2D	Two Dimensional
3D	Three Dimensional

List of Publications

Referred Journal papers

1. **B. Deka**, P. P. Sahu, "Tooth Shaped Grating Assisted Structure for Compact Multimode Interference (MMI) Coupler", *Applied Optics*, Vol. 50, Issue 25, pp.E193-E199, 2011.
2. **B. Deka**, P. P. Sahu, "Tooth Shaped Grating Assisted Geometry for Two Mode Interference (TMI) Coupler", *J. of Optics (Springer)*, http://dx.doi.org/10.1007/s12596-011-0049-6, 2011.
3. **B. Deka**, P. P. Sahu, "Transformation relationship of directional coupler with multimode interference (MMI) coupler and two mode interference (TMI) coupler", *J. of Optics (Springer)*, vol.-38, Issue-2, pp.75-87, 2009.

Submitted paper

(i) **B. Deka** and P. P. Sahu, "Compact Multimode Interference Coupler Based on Double S-Bend Geometry", *IEEE J. Lightwave Technology, 2013. (under review)*

Conference/Workshop contributions

1. **B. Deka**, A. Dutta and P. P. Sahu, "Study on compactness of planar waveguide based integrated optic couplers using tooth shaped grating assisted geometry", *8th Ibero American Optics Meeting/11th Latin American Meeting on Optics, Lasers, and Applications (RIAO-OPTILAS 2013)*, ORAL presentation, held at University of Porto, Portugal, July 22-26, 2013 (*To be published in the Proceeding of SPIE*).
2. **B. Deka**, A. Dutta and P. P. Sahu, "Comparative study on compact planar waveguide based photonic integrated couplers using simple effective index method", *8th Ibero American Optics Meeting/11th Latin American Meeting on Optics, Lasers, and Applications (RIAO-OPTILAS 2013)*, Poster presentation, held at at University of Porto, Portugal, July 22-26, 2013 (*To be published in Proceeding of SPIE*).
3. **B. Deka**, A. Dutta and P. P. Sahu, "Design and Fabrication of Compact Integrated Optic Waveguide Coupler using SiON/SiO_2 Material", *AIP International conference on Recent Trends in Applied Physics & Material Science (RAM 2013)*, Feb 01-02, 2013, Bikaner, India(*To be published in AIP Conference Proceeding*).
4. **B. Deka**, A. Dutta, G. Hegde, P. Sahu, "Fabrication and comprehensive study of silicon oxynitride based compact directional coupler and multimode interference coupler", International Conference on Communication and Electronics System Design (ICCESD), *Proc. of SPIE*, vol. 8760, pp. 876024-5, January 28–30, 2013, Jaipur, India.
5. **B. Deka** and P. P. Sahu, "Photonic Integrated Devices Based on Two-mode Interference (TMI) Coupler and Multimode Interference (MMI) Coupler", ***2012***

***Winter College on Optics: Advances in Nano-Optics and Plasmonics and its Preparatory School* (SMR2328 & SMR2397) held at The Abdus Salam International Centre for Theoretical Physics (ICTP), Trieste, Italy** during January 30th to February 17th, 2012.

6. **B. Deka**, P. P. Sahu, "Comparative Study of Tooth Shaped Grating Assisted Compact Directional Coupler, Two-Mode Interference Coupler and Multimode Interference Coupler", Trends in Optics and Photonics II, *Proc. of International Conference on Trends in Optics and Photonics*, pp. 470-475, University of Calcutta, Kolkata, December 7-9, 2011.
7. **B. Deka**, A. Dutta, N. Gogoi, P. P. Sahu, "Comparative Study of Directional Coupler and Two-Mode Interference Coupler Based on Tooth Shaped Grating Assisted Structure", *Proc. of Frontier in Optics and Photonics 2011 XXXVI OSI Symposium*, pp. 149-152, Indian Institute of Technology (IIT), NewDelhi, December 3-5, 2011.
8. N. Gogoi, **B. Deka**, P. P. Sahu, "A Comparative Study of Directional Coupler (DC), Two-mode Interference (TMI) Coupler and Multimode Interference (MMI) Coupler", *Proc. of National Conference on Electronics, Communication and Signal Processing (NCECS-2011)*, September, 2011.
9. **B. Deka**, P. P. Sahu, "Compact two mode interference (TMI) couplers based on tooth shaped grating assisted structure", *Proc. of 10th International Conference on Fibre Optics and Photonics: PHOTONICS-2010*", December, 2010.
10. **B. Deka**, P. P. Sahu, "Transition of waveguide directional coupler to multimode interference coupler (MMI) and two mode interference coupler (TMI)", *Proc. of XXXIII OSI Symposium on Optics and Optoelectronics*, pp. 39-41, 2007.

Chapter-1:

General Introduction

Overview of the Problem
Present State-of-Art
Objectives of the research
Motivation of the research
Aims and Objectives
Methodology adopted
Research achievement
Thesis organization

For the last few years, optical network has grown tremendously to fulfill the enormous demand of bandwidth requirements due to remarkable increase of network users and services in nationwide optical backbone [1]. The flexible operation of optical networks are performed by the nodes in which main devices are photonics matrix switch [2]-[3], wavelength division multiplexer/demultiplexer [4]-[6], add/drop multiplexer [7]-[8] etc. Traditionally, the basic designs of optical device consisted of bulky and heavy components that require careful alignments, protection against vibrations, moisture and temperature drift. In an effort to resume the problem *Photonic Integrated Circuits (PIC)* based on planar waveguide was first coined by S. E. Miller [9] in 1969 for implementation of these devices for optical networks.

The basic components of Photonic Integrated Devices (PID) are directional coupler (DC) [10-11], Two-Mode Interference (TMI) coupler [12-14] and Multimode Interference (MMI) coupler [15-16]. The large scale integration of PID for optical networks accommodating more numbers of users requires compactness and higher fabrication tolerances. In this thesis, the study has been made for these components delivering these issues. For PID, it is required to select the components on the basis of issues such as compactness, higher fabrication tolerance, polarization independence and lower power loss. In this thesis, study is carried out on these device components with improved performance considering the above issues.

The introduction of DC, Multimode Interference (MMI) principle and Two Mode Interference (TMI) principle in PID are made in 1969 [17], 1973 [18] and 1977 [19] respectively. The Directional Coupler (DC) consists of two dielectric waveguides placed in close proximity to each other for coupling of guided power based on phase difference of two guided modes– even mode and odd mode. On the other hand, the MMI couplers are based on self-imaging principle which is a property by which an input field profile is reproduced in single or multiple images at periodic intervals along the propagation direction of the guide. It consists of a multimode central waveguide section (with excitation of more than two modes) with input and output access waveguides. TMI coupler consists of central waveguide

(TMI section) with zero waveguide separation gap connected to two input and output access waveguides and power transferred to the output waveguides depends on the phase difference between two excited modes-fundamental and first order. In this thesis, effort has been made to study the compact structure for their device components.

1.1. Present State-of-Art

Extensive studies have been made for implementation of such device components using a variety of materials such as Lithium Niobate [20]-[22], polymers [23]-[25], III-V semiconductors [26]-[27] and silicon based materials [28]-[31]. Out of these materials, Silicon (Si) based materials provides strong confinement of light with moderately low propagation losses, low material cost and compatibility with well known conventional silicon based IC technology. These Si based materials are Silicon-On-Insulator (SOI) (silicon core), SiO_2/SiO_2-GeO_2 (Core) and SiO_2/Silicon Oxynitride (SiON) core. Among these materials SiO_2/SiON is considered as a promising material for PID as it offers the wide range of refractive index in between 1.45 (SiO_2) to 2.0 (Si_3N_4) providing the auxiliary advantage for high index contrast designs and due to the property of optical transparence from 210 nm to beyond 2000 nm [32]-[33]. This optical property has permitted to develop low loss waveguides for long range applications such as nationwide networks, optical waveguide sensor and integrated quantum optical circuits etc.

Apart from the materials, previous authors [16],[33] have reported on studies of different geometries such as tapered geometry (parabolic tapered [16], linearly tapered at middle [34], parabolic tapered at middle [35]) and periodic grating structure with different shape [36]-[37], tooth shaped grating assisted geometry for TMI [5],[38] and MMI couplers.

It is seen that till now no study has been made to establish transformational relationship between conventional directional coupler, TMI coupler and MMI coupler. From the transformational relationship, coupling power transferred to the access waveguides can be determined by using simple effective index method. From the existing work in the relevant literature it is found that no such report is available to develop an accurate model for determination of coupling power distribution for tooth shaped grating assisted structures of directional coupler, TMI coupler and MMI coupler. In this direction therefore, an effort has been made for a comparative study on conventional couplers such as DC with TMI coupler and DC with TMI as well as MMI couplers.

1.2. Motivation

Owing to the high demand of large scale integration of PID for optical networks, small device dimensions along with better fabrication tolerances are mandatory in order to reduce process costs with better performances, and contribute to PID production as the market demand. In the recent years, it is seen that photonic integrated devices based on TMI and MMI effects fulfils the above requirements giving low loss, compactness and good performances [2]-[3],[31]. The excellent properties such as coupling compatibility with optical transmission fiber and easy fabrication have led to their brisk incorporation in more complex PID's. It is also required to find compact geometry for DC, TMI, and MMI coupler which should be suitable for large scale integrated photonic devices with mass production.

1.3. Aims and Objectives

As discussed earlier, the development of passive optical compact components (such as DC, TMI coupler and MMI coupler etc.) for large scale integration (LSI) with low insertion loss, low polarization dependent structures so as to reduce polarization dependent loss and higher fabrication tolerance with low crosstalk is very much required. In this Ph. D. work, all these aspects of DC, TMI and MMI based devices have been studied and the prime objectives of this thesis are considered as follows:

I. To develop a mathematical model using Simple Effective Index Method (SEIM) based on sinusoidal modes for accurate estimation of coupling power in directional coupler (DC), Two Mode Interference (TMI) coupler, Multimode Interference (MMI) coupler and find a transformation relationship of DC with TMI coupler and MMI coupler with silica waveguides using silicon oxynitride as a core material.

II. To design a compact TMI coupler using tooth shaped grating assisted geometry for Photonic Integrated Devices. Also design and propose tooth shaped grating assisted geometry for Directional Coupler and MMI coupler in order to get compactness.

III. To design double S-bend structures for compact TMI coupler and proposed MMI coupler for PID.

IV. To fabricate the designed DC, TMI coupler and MMI coupler using silica waveguides with silicon oxynitride as a core and characterize it for performance analysis.

1.4. Methodology adopted

The most accepted argument in favour of this research work is based on small device dimension and better fabrication tolerance for TMI and MMI based waveguide coupler for reduction of process costs and contribution of large-scale PID components production. The scope of the present research work has focused specifically on:

1. Proper selection of materials for fabrication of waveguide core, cladding and the substrate.

2. Analytical modeling, simulation and fabrication of low loss waveguides structure based on Simple Effective Index Method (SEIM) with compact device dimensions and better fabrication tolerance in an endeavor to achieve process costs reduction.

3. Determination of the coupling length and study of coupling characterisitics/ behaviour of the design structures as a function of the designed waveguide dimension, waveguide gap and effective index difference.

6. Development of compact photonic components using silicon oxynitride material with low crosstalk, polarization independent and low insertion loss.

7. Measurement and characterization of the realized device for the performance evaluation.

1.5. Research achievement

In this research effort, a mathematical model using Simple Effective Index Method (SEIM) [41]-[43], based on sinusoidal modes has been developed for accurate estimation of coupling power in the DC, TMI coupler and MMI coupler. The results obtained by using SEIM are found to be accurate (which has been shown in our work), as these results are more close to the experimental results.

The prime contributions are as given below:

1. Design and realization of conventional DC, TMI coupler and MMI coupler using SiO_2/SiON material and derivation of a transformation relationship between DC, TMI coupler and MMI coupler for accurate analysis of coupling characterization. It has been found that TMI coupler (having higher fabrication tolerance) is more compact compared to the other two couplers.
2. Tooth shaped grating assisted TMI (GA-TMI) coupler has been studied and compared with tooth shaped grating assisted DC. It has been found that

GA-TMI coupler is two times compact in comparison to conventional TMI coupler and 4.5 times compact in comparison to conventional DC.

3. Tooth shaped grating assisted geometry for MMI (GA-MMI) coupler has been proposed and studied. It is found that the overall device length (including waveguide length and coupling length) of GA-MMI is less than that of GA-TMI coupler.
4. Double S-bend structures for multimode interference couplers have been studied using the same material platform and compared with double S-bend assisted two mode interference. It is observed that the overall length of DB-MMI coupler is 9 % less than that of conventional MMI coupler, but compactness is less than that of GA-TMI coupler and GA-MMI coupler.

1.6. Thesis organization

The overall thesis is outlined into eight chapters and the summary of each chapters are as follows:

In ***Chapter-1*** an overview of general introduction on the thesis work including the idea, problem definition, prime objectives and adopted methodologies are presented highlighting the motivation behind the development of compact PID components.

Since in this thesis, basic PID components such as DC, TMI coupler and MMI coupler have been studied, ***Chapter-2*** provides a review study on PID components based on different material platform. The chapter starts with planar wave equation and reviews on different numerical tools such as SEIM, Marcuse's method, FEM, FDTD and BPM briefly for the analysis of planar waveguide. The basic coupling behaviors of conventional DC, TMI coupler, MMI coupler and its related previous works have been mentioned. Since tooth shaped grating assisted geometry for MMI coupler have been proposed in the third objective, the grating assisted geometry and its related previous works has also been discussed. As the bent access waveguides of TMI and MMI coupler have been designed for reduction of total device length, the basic theory of single bending and S-bending and it's related previous works have been discussed. Since, the fourth and final objective covers the fabrication of these components using SiO_2/SiON waveguide material; it is indispensable to present a comparative study with other waveguide materials such as SOI, SiO_2/SiO_2-GeO_2, Ti: LiNbO3, GaAsInP/InP and polymeric materials. Finally, in this chapter, the motivation for the use of SiO_2/SiON material over other mentioned materials in PID have been discussed.

For high speed optical networks having large number of nodes, LSI is required in PID where the uses of compact, high fabrication tolerance and polarization insensitive device are key components. In ***Chapter-3***, the basic components (as mentioned earlier) in terms of compactness, fabrication tolerances and polarization independent characteristics have been compared before its use in PID. In order to study the above, a simple effective index model based on sinusoidal modes has been developed for accurate estimation of coupling power. A transformation relationship between DC, TMI and MMI couplers has been established for formulation of coupling behavior of TMI and MMI coupler. It has been seen that the beat length (defined as coupling length for full cross coupling/to achieve π phase between guided modes) of conventional DC, TMI coupler and MMI coupler with index contrast (Δn) = 5% and cladding index~1.45 and wavelength~ 1.55 μm are 91 μm, 45 μm and 80 μm respectively. The beat length of TMI coupler has been found to be two times shorter than DC and 1.5 times shorter than MMI coupler. The fabrication tolerance of TMI coupler has been found to be higher than that of MMI coupler and DC due to having less number of designed parameters. It has also been observed that the polarization insensitiveness of TMI coupler is almost close to that of MMI coupler but found to be less than that of DC. Finally, the results obtained using SEIM have been compared with that using Beam Propagation Method (BPM) results (obtained with optiBPM software (V 9.0)).

Further as the basic requirement of PID components is compactness, our study in ***Chapter-4*** concentrates on the inclusion of compact structure for these components. In this direction, tooth shaped grating assisted geometry for Directional Coupler (DC) and Two Mode Interference (TMI) coupler has been used. At first, the coupling behavior of these structures has been formulated using Simple Effective Index Method (SEIM), based on sinusoidal modes for its accurate analysis. The coupling characteristics, beat length and fabrication tolerances of Grating Assisted Two Mode Interference (GA-TMI) coupler with Grating Assisted Directional Coupler (GA-DC), conventional TMI coupler and conventional DC have been compared. It has been found that the beat length of GA-TMI coupler is 22.3 μm which is ~more than two times less that of GA-DC and ~4.5 times less than conventional DC. Although the fabrication tolerance of GA-TMI is less than that of conventional TMI, it is more than that of conventional DC.

As discussed in Chapter-4, reduction of the total device length (sum of beat length and access waveguide length having S-bend) has not been studied. For the reduction of total device length it is required to study the longitudinal access waveguide length (known as transition length) for TMI coupler and MMI coupler. In ***Chapter-5***, tooth shaped Grating Assisted Geometry of MMI coupler for reduction of total device length has been proposed. Initially, the coupling behavior of Grating Assisted MMI (GA-MMI) coupler, using Simple Effective Index Method (SEIM) based on sinusoidal modes have been analyzed theoretically and the coupling characteristics, beat length and fabrication tolerances for GA-MMI coupler with GA-DC and GA-TMI coupler have been compared. It has been found that, although beat length of GA-TMI coupler with grating width (ΔW) = 0.25 μm is ~ 1.6 times less than that of GA-MMI coupler with grating width (ΔW) = 0.25 μm, but the total device length of GA-MMI coupler by inclusion of access waveguide length with permissible bending loss of 0.01 dB is ~ 7.5 % less than GA-TMI coupler. A transformation relationship of GA-DC, GA-TMI coupler and GA-MMI coupler has also been established to formulate coupling behavior of these devices. These results have also been verified with Beam Propagation Method (BPM) results obtained by using optiBPM software (V 9.0).

Subsequent to the design of two mode interference (TMI) coupler, multimode interference (MMI) coupler and directional coupler (DC), the fabrication of these device components using SiO_2/SiON materials with Δn=5 % and cladding index ~ 1.45 have been discussed in ***Chapter-6***. The TMI waveguide width (2a) ~3 μm, access waveguide width (a) ~1.5 μm and transition length (L_T) ~130 μm have been kept and in case of MMI coupler, MMI waveguide width (2a+h)~7 μm, access waveguide width (a)~1.5 μm and transition length (L_T) ~117 μm respectively. The lower cladding of SiO_2 layer of 3 μm thickness on Si substrate has been deposited using Plasma Enhanced Chemical Vapour Deposition (PECVD) technique. Then after, Silicon Oxynitride (SiON) layer of thickness ~1.5 μm and refractive index ~1.5 on the top of SiO_2 layer have been deposited using PECVD by controlling the flow rate of N_2O, NH_3, and Silane precursor gases. SiON waveguide core has been made using photolithography with chrome MASK written with the help of laser writer and Reactive Ion Etching (RIE) by controlling flow of SF_4 and Ar^{++} gases respectively. Finally the top cladding SiO_2 layer of thickness 3 μm has been deposited using PECVD technique. It has been found that the beat length obtained experimentally for TMI coupler, MMI coupler and Directional Coupler are ~ 45.1 μm, 79.9 μm and 91.2 μm respectively, which are almost close to that obtained theoretically using SEIM based on sinusoidal modes. Although the tooth shaped grating assisted DC, TMI coupler and MMI coupler have been designed, the fabrication of tooth shaped grating assisted structures of grating width (ΔW)~0.25 μm with permissible propagation loss ~0.15 dB/cm is challenging using standard photolithography technique and fabrication process steps.

As discussed in Chapter-6, instead of fabricating grating assisted structures, it has been shown theoretically that the tooth shaped grating assisted geometry certainly reduces the device length as mentioned in chapter-4 and chapter-5. In the ***Chapter-7,*** double S-bend MMI (DB-MMI) coupler has been studied both theoretically and experimentally using the same waveguide materials (as discussed earlier) and Simple Effective Index Method (SEIM) based on sinusoidal modes for compactness of photonic integrated devices. The DBMMI coupler has been fabricated using the same fabrication process steps as mentioned in chapter-6. It is found that the device length of DB-MMI coupler is 193 μm which is almost close to that obtained theoretically (~209 μm). The device length is 10 % less than that of conventional MMI coupler, but it is less compact in comparison to GA-MMI coupler.

Finally, in ***Chapter-8,*** a general conclusion of the research is summarized with key contributions of this research work. The contributions are as given below:

1. Design and realization of conventional DC, TMI coupler and MMI coupler using SiO_2/SiON material and a transformation relationship between DC, TMI coupler and MMI coupler has been derived. It has been found that TMI coupler (having higher fabrication tolerance) is more compact compared to the other two couplers.
2. Tooth shaped grating assisted TMI (GA-TMI) coupler has been studied and compared with tooth shaped grating assisted DC. It has been found that GA-TMI coupler is two times compact in comparison to conventional TMI coupler and 4.5 times compact in comparison to conventional DC.
3. Tooth shaped grating assisted geometry for MMI (GA-MMI) coupler has been proposed and studied. It is found that the total device length of GA-MMI is less than that of GA-TMI coupler.
4. Double S-bend structures for two mode interference and multimode interference couplers have been studied using the same material platform. It is observed that the device length of DB-MMI coupler is 10 % less than that of conventional MMI coupler, but compactness is less than that of GA-TMI coupler and GA-MMI coupler.

As future prospects an attempt can be made to fabricate these GA-TMI coupler and GA-MMI coupler with ΔW~0.25 μm, higher index contrast (i.e. Δn>5%) and permissible propagation loss of ~0.15 dB/cm in order to use these components in large scale integrated optic devices such as wavelength division multiplexer [8] [42]-[43], add/drop multiplexer [20]-[21] and photonic matrix switches [10] [46] for high speed optical networks. Although the reduction of total device length of the designed devices is studied with increase of index contrast (Δn) but SiO_2/SiON material has been used with Δn maximum up to 5% only for time limitations and other constraints in fabrication of these compact device components. Moreover, insertion loss increases with increase of Δn, due to having more fiber to device coupling losses.

Reference:

1. Izhaki, N., & Horin, N. B. Planar lightwave circuit (PLC) switches answer the call for next-generation all-optical switching. http://www.lynxpn.com/data/uploads/WhitePapers/Planar%20Lightwave%20Circuit%20%28PLC%29%20Switches%20Answer%20the.pdf ,2005.
2. Zhou, J., et al. Operation principle for optical switches based on two multimode interference couplers, *J. of Lightwave Tech.* **30**, 15-21, 2012.
3. Chatterjee, R. et al. Nanomechanical Proximity Perturbation for Switching in Silicon-Based Directional Couplers for High-Density Photonic Integrated Circuits, *J. of Microelectromechanical Syst.*, 19 (3), 657-662, 2010.
4. Runde, D, et al. Mode-selective coupler for wavelength multiplexing using $LiNbO_3$:Ti optical waveguides, *Cent. Eur. J. Phys.* **6**, 588-592, 2008
5. Tsai, T. Y., et al., A novel ultra compact two-mode-interference wavelength division multiplexer for 1.5 μm operation, *IEEE J. Quantum Electron.* **41**, 741-746, 2005.
6. Chin, M. K., et al., High-index-contrast waveguides and devices, *Appl. Opt.* **44**, 3077-3086, 2005.
7. Castro, J. M., et al., Optical add-drop multiplexers based on the antisymmetric waveguide Bragg grating, *Appl. Opt.* **45**, 1236-1243, 2006.
8. Tran, A.V., et al. Optical add-drop multiplexers with low crosstalk, *IEEE*

Photonic Tech. Lett. **13**, 582-584, 2001.

9. Miller, S. E. Integrated optics: an introduction, *J. Bell Syst. Tech.* **48**, 2059-2068, 1969.
10. Marcatili, E.A. J. Dielectric rectangular waveguide and directional coupler for integrated optics, *J. Bell. Syst. Tech.* **48**, 2071-2102, 1969.
11. Marcuse, D. Directional couplers made of nonidentical asymmetric slabs. Part I: synchronous coupler, *J. of Lightwave Tech.* **LT-5**, 113-118, 1987.
12. Yiling, S., et al. Integrated optical isolators based on two-mode interference couplers, *J. Opt. (IOP)* **12**, 1-5, 2010.
13. Chen, K., et al., Silicon oxynitride optical waveguide ring resonator utilizing a two-mode interference structure, *Int. J. Photoenergy* **Dec**, 1-5, 2012
14. Sahu, P. P. A compact optical multiplexer using silicon nano waveguides, *IEEE J. Sel. Topics Quantum Electron.* **15**, 1537-1541, 2009.
15. Yao, C., et al. An ultracompact multimode interference wavelength splitter employing asymmetrical multi-section structures, *Opt. Exp.* **20**, 18248-18253, 2012.
16. Sahu, P. P., Parabolic tapered structure for an ultracompact multimode interference coupler, *Appl. Opt.* **48**, 206-211, 2009
17. Marcatili, E.A. J. Dielectric rectangular waveguide and directional coupler for integrated optics, *J. Bell. Syst. Tech.* **48**, 2071-2102, 1969.
18. Bryngdahi, O. Image formation using self-imaging techniques, *J. Opt. Soc. Amer.* **63**, 416-418, 1973.
19. Papuchon, M., et al. Electrically active optical bifurcation: BOA, *J. of Appl. Phy. Lett.* **31**, 266-267, 1977.
20. Runde, D, et al. Mode-selective coupler for wavelength multiplexing using $LiNbO_3$:Ti optical waveguides, *Cent. Eur. J. Phys.* **6**, 588-592, 2008
21. Rottmann, F., et al. Integrated-optic wavelength multiplerxers on lithium niobate based on two-mode interference, *J. of Lightwave Tech.* **6**, 946-952, 1988.
22. Lin, J.P., et al. Four-channel wavelength division multiplexer on Ti: $LiNbO_3$

Electronics Lett. **25**, 1608-1609, 1989.

23. Mule, A.V., et al. Photopolymer-based diffractive and MMI waveguide couplers, *IEEE Photonic Tech. Lett.* **16**, 2490-2492, 2004.
24. Ibrahim, M. H., et al. A novel 1x2 multimode interference optical wavelength filter based on photodefinable benzocyclobuene polymer, *J. of Microwave and Optical Tech. Lett.* **49**, 1024-1028, 2007.
25. Chan, H.P., et al. A wide angle X-junction polymeric thermo optic digital switch with low crosstalk, *IEEE Photonic Tech. Lett.* **15**, 1210-1212, 2003.
26. Chin, M. K., et al., High-index-contrast waveguides and devices, *Appl. Opt.* **44**, 3077-3086, 2005.
27. Nishihara, H., Haruna, M., & Suhara, T. *Optical Integrated Circuits*, McGraw-Hill, New York, 1989.
28. Miya, T. Silica-based planar lightwave circuits: passive and thermally active devices, *IEEE J. Sel. Topics Quantum Electron.* **6**, 38-45, 2000.
29. Yamada, H., et al. Si photonic wire waveguide devices, *J. of IEICE Trans. Electron.* **E90-C**, 59-64, 2007.
30. Kashahara, R, et al., New structures of silica-based planar light wave circuits for low power thermooptic switch and its application to 8x8 optical matrix switch, *J. Lightwave Tech.* **20**, 993-1000, 2002.
31. Worhoff, K., et al., Design, toleramce analysis and fabrication of silicon oxynitride based planar optical waveguides for communication devices, *J. of Lightwave Tech.* **17**, 1401-1407, 1999.
32. Bona, G. L., et al. SiON high refractive-index waveguide and planar lightwave circuit, *IBM J. Res. & Dev.* **47**, 239-249, 2003.
33. Chen, K., et al., Silicon oxynitride optical waveguide ring resonator utilizing a two-mode interference structure, *Int. J. Photoenergy* **Dec**, 1-5, 2012
34. Base, P.A., et al. New 2x2 and 1x3 multimode interference couplers with free selection power splitting ratios, *J. of Lightwave Tech.* **14**, 2286-2292, 1996.

35. Levy, D. S., et al. Fabrication of ultracompact 3 dB 2x2 MMI power splitters, *IEEE Photonic Tech. Lett.* **11**, 1009-1011, 1999.
36. Passaro, V. M. N. Optimal design of grating-assisted directional couplers, *J. of Lightwave Tech.* **18**, 973-984, 2000.
37. Hardy, A. Exact Derivation of the Coupling Coefficient in Corrugated Waveguides with Rectangular Tooth Shape, *IEEE J. Quantum Electron.* **20**, 1132-1139, 1984.
38. Tsai, T. Y., et al., A novel wavelength-division-multiplexer using grating assisted two-mode interference, *IEEE Photonic Tech. Lett.* **16**, 2251-2253,2004
39. Rajarajan, M., et al. A rigorous comparison of the performance of directional couplers with multimode interference devices, *J. of Lightwave Tech.* **17**, 243-248, 1999.
40. Lee, S. Y., et al. Transformation between directional couplers and multimode interferometers based on ridge waveguides, *Opt. Exp.* **12**, 3079-3085, 2004.
41. Chiang, K.S. Effective index method for the analysis of optical waveguide couplers and arrays: an asymptotic theory, *J. of Lightwave Tech.* **9**, 62-72, 1991.
42. Wang, Q., et al. Effective index method for planar lightwave circuits containing directional couplers, *J. of Optics Communications* **259**, 133-136, 2006.

****

Chapter-2:

Theoretical Foundation and Review Study on Waveguide Devices

Introduction

Waveguide Theory and Numerical Tools

Materials for Optical Waveguides

A Review

Conclusion

2.1. Introduction

Photonic integrated devices with SiO_2/SiON waveguides is one of the promising devices because of its substantial advantages including high performances levels, high productivity and long term stability for optical networks. The basic components of these devices are Directional Coupler (DC), Two Mode Interference (TMI) coupler, Multimode Interference (MMI) coupler and Mach-Zender structures for optical switches. In this chapter, these basic components are reviewed using SiO_2/SiON [1]-[7], [28] and these components have also been considered using SiO_2/SiO_2-GeO_2 [8]-[12], [29], InP/GaAsInP [13]-[17], $LiNbO_3$ [18]-[25] and polymer materials [26]-[27] for comparison. At the first, rectangular waveguide with its field distribution for TE mode and TM mode are discussed and then different numerical techniques are used for their analysis. In section 2.3, theoretical analysis of coupling characteristics of DC is discussed and the coupling coefficients derived by Digonnet et al. [31] and Marcuse [30] are compared. The results as demonstrated by other authors for directional coupler are shown in Table-2.1. In section-2.4, theoretical analysis for coupling characteristics of MMI coupler is mentioned and the results of MMI coupler as reported by different authors are reviewed. Section-2.5 describes TMI couplers and the results as demonstrated by other authors. It is found that the TMI coupler provides the lower coupling length than the other two couplers. In section-2.6, we have discussed different grating assisted geometries and its comparison for DC and tooth shaped grating assisted geometry for TMI coupler. It is seen from the studies of grating assisted geometry by previous authors that DC and TMI coupler has not been studied considering compactness, polarization independence and fabrication tolerances. As the bending of waveguide in photonic integrated devices (PID) is an important part which changes the direction of signals inside PID, we have reviewed bending losses of the waveguide determined by different authors in section-2.8. In section-2.9, motivation and advantages of waveguide material SiO_2/SiON over other materials such as SOI, SiO_2/SiO_2-GeO_2, InP/GaAsInP, Ti:LiNbO3 and polymeric materials have been discussed. A brief review of key devices such as wavelength division multiplexer/de-multiplexer, optical matrix switch and add/drop multiplexer for optical networks have been mentioned in section-2.10. For these devices it is seen that the basic components are DC, TMI and MMI coupler. It is required to make these basic components more compact and polarization independent to accommodate more number of users in optical networks for large scale integration of PID.

2.2. Planar Waveguide

Fig-2.1(a) shows a rectangular waveguide of core width w and thickness t. The refractive index of core and surrounding cladding are n_2 and n_1 respectively. In the figure, the width and thickness of the waveguide are considered along x-axis and y-axis respectively, whereas the wave is propagating along the z-direction. From Maxwell's equations, the various components of electric field and magnetic fields (H_x, E_x, H_y and E_y) of the wave are expressed in terms of z-component of electric field E_z and magnetic field H_z in the waveguide core and are written as [18],

$$\left.\begin{aligned} H_x &= \frac{jw\varepsilon}{k^2} - \frac{j\beta}{k^2}\frac{\partial H_z}{\partial x}, \qquad & E_x &= -\frac{j\beta}{k^2}\frac{\partial E_z}{\partial x} + \frac{j\omega\mu}{k^2}\frac{\partial H_z}{\partial y}, \\ H_y &= \frac{j\beta}{k^2}\frac{\partial H_z}{\partial y} - \frac{j\omega\varepsilon}{k^2}\frac{\partial E_z}{\partial x}, \qquad & E_y &= \frac{j\omega\mu}{k^2}\frac{\partial H_z}{\partial x} - \frac{j\beta}{k^2}\frac{\partial E_z}{\partial y}, \end{aligned}\right\} \tag{2.1}$$

where ω=angular frequency, β=propagation constant, $k^2 = -\beta^2 + \omega^2\varepsilon\mu$, ε=permittivity and μ=permeability. For easy analysis of propagation characteristics for three dimensional (3D) structures, normally planar 2D waveguide structure is used for which the equation (2.1) reduces to

$$\left.\begin{aligned} H_x &= -\frac{j\beta}{k^2}\frac{\partial H_z}{\partial x}, \quad & E_x &= -\frac{j\beta}{k^2}\frac{\partial E_z}{\partial x} \\ H_y &= -\frac{j\omega\varepsilon}{k^2}\frac{\partial E_z}{\partial x}, \quad & E_y &= \frac{j\omega\mu}{k^2}\frac{\partial H_z}{\partial x} \end{aligned}\right\} \quad (2.2)$$

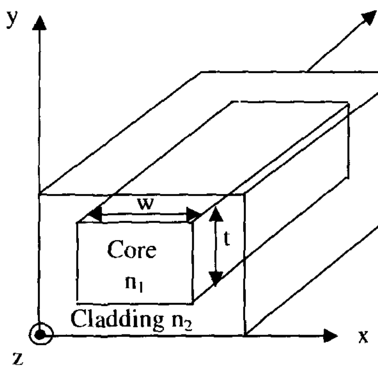

Fig-2.1(a): A rectangular waveguide of core width w and thickness t

Fig-2.1(b) shows planar waveguide (2D) structure of core width, w and core index, n_2. From the above equations, it is observed that there must be existence of one z-component field either E_z or H_z, otherwise all the components of the fields would be zero and as a result, there would be no fields at all in the region considered. So we may consider a transverse electric field (TE) wave for which E_z=0 and a transverse magnetic (TM) wave for which H_z=0. For TE wave, the electric fields and magnetic fields following Maxwell's equations can be written as [18]

$$\left.\begin{aligned} & H_z = -\frac{1}{j\omega\mu}\frac{\partial E_y}{\partial x}, \quad H_x = -\frac{\beta}{\omega\mu}E_y, \\ & \frac{\partial^2 E_y}{\partial x^2} + (k_0^2 n^2 - \beta^2)E_y = 0 \end{aligned}\right\} \quad (2.3)$$

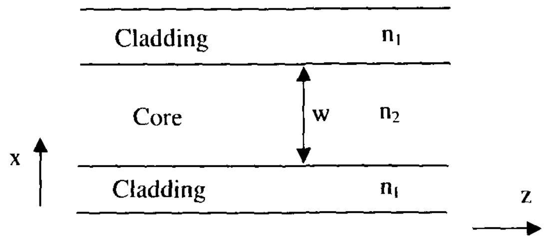

Fig-2.1(b): Planar waveguide of core width w and index n_2 and cladding index n_1

For TM wave, we get [18]

$$\left.\begin{aligned} E_z &= \frac{1}{j\omega\epsilon n^2}\frac{\partial H_y}{\partial x}, \\ E_x &= \frac{\beta}{\omega\epsilon n^2}H_y, \\ &\frac{\partial^2 H_y}{\partial x^2} + (k_0^2 n^2 - \beta^2)H_y = 0, \end{aligned}\right\} \tag{2.4}$$

The field solutions and boundary conditions at the interface of the rectangular waveguide of core width, w leads to the following dispersion equations that determine the propagation constant β for TE wave and TM wave [18].

For TE wave, the dispersion equation is written as [18],

$$V\sqrt{1-b_E} = (q+1)\pi - 2\tan^{-1}\sqrt{\frac{1-b_E}{b_E}} \tag{2.5}$$

where, q is an integer, b_E=normalized guide index=$(n_{eff}^2 - n_1^2)/(n_2^2 - n_1^2)$ and V= normalized frequency $= k_0 w\sqrt{(n_2^1 - n_1^2)}$, $k_0 = 2\pi/\lambda$ and $n_{eff} = \beta/k_0$.

For TM mode, the dispersion equation can be written as [18],

$$V\sqrt{q_s}(n_2/n_1)\sqrt{1-b_M} = (q+1)\pi - 2\tan^{-1}\sqrt{\frac{1-b_M}{b_M}} \tag{2.6a}$$

where $q_s = \frac{n_{eff}^2}{n_1^2} + \frac{n_{eff}^2}{n_2^2} - 1$ and $b_M = \frac{(n_{eff}^2 - n_1^2)}{(n_2^2 - n_1^2)}\left(\frac{n_2}{q_s n_1}\right)^2$ (2.6b)

The two dimensional (2D) structure is converted into 3D structure using the same dispersion equations by well known Effective Index method [18]. For propagation of single mode (i.e. only fundamental mode) in the waveguide, the normalized frequency is chosen V≤ 2.4. The six electric field components for TE_{10} mode i.e. fundamental mode are written as

$$E_Z = 0, \quad \text{TE requirement} \tag{2.7a}$$

$$E_y = A\sin\frac{\pi x}{w}e^{-j\beta z}, \tag{2.7b}$$

$$E_x = 0, \tag{2.7c}$$

$$H_z = B\cos\frac{\pi x}{w}e^{-j\beta z}, \tag{2.7d}$$

$$H_y = 0, \tag{2.7e}$$

$$H_x = C\sin\frac{\pi x}{w}e^{-j\beta z} \tag{2.7f}$$

where A, B and C are constants which are determined from the boundary conditions at the interface of the waveguide cores. The variations of these field components of TE_{10} as a function of z are portrayed in figures-2.2(a), (b) and (c) respectively. Fig-2.2(a) shows the variations of electric field component E_y, along z direction, following the equation (2.7b). In the figure, intensity of electric field E_y is maxima at z=0 and its maximum and minimum values changes alternatively along z direction. Fig-2.2(b) shows the variation of magnetic field component H_z as a function of z, following the equation (2.7d). In the figure, the magnetic field H_z is maximum at edges and minimum at center of the waveguide. Fig-2.2(c) shows the field distribution of all the components of electric and magnetic field propagated along z-direction inside rectangular waveguide core. The width and thickness of the waveguide is considered along x-axis and y-axis respectively, whereas the wave is propagated along the z-direction. The electric field component E_y (indicated by solid line) and magnetic field component H_x (indicated by dashed line) are maximum at x=w/2 and minimum at x=0 and w whereas magnetic field component H_z (represented by dashed line) is maximum at x=0 and w and minimum at x=w/2. So the intensity of both electric field and magnetic field is maximum at x=w/2 i.e. at the center of the waveguide.

The six electric field components for TM_{10} mode i.e. fundamental mode are written as

$$H_Z = 0, \quad \text{TM requirement} \tag{2.8a}$$

$$H_y = D \sin \frac{\pi x}{w} e^{-j\beta z}, \tag{2.8b}$$

$$H_x = 0, \tag{2.8c}$$

$$E_z = E \cos \frac{\pi x}{w} e^{-j\beta z}, \tag{2.8d}$$

$$E_y = 0, \tag{2.8e}$$

$$E_x = F \sin \frac{\pi x}{w} e^{-j\beta z} \tag{2.8f}$$

where D, E and F are constants which are determined from the boundary conditions at the interface of the waveguide cores.

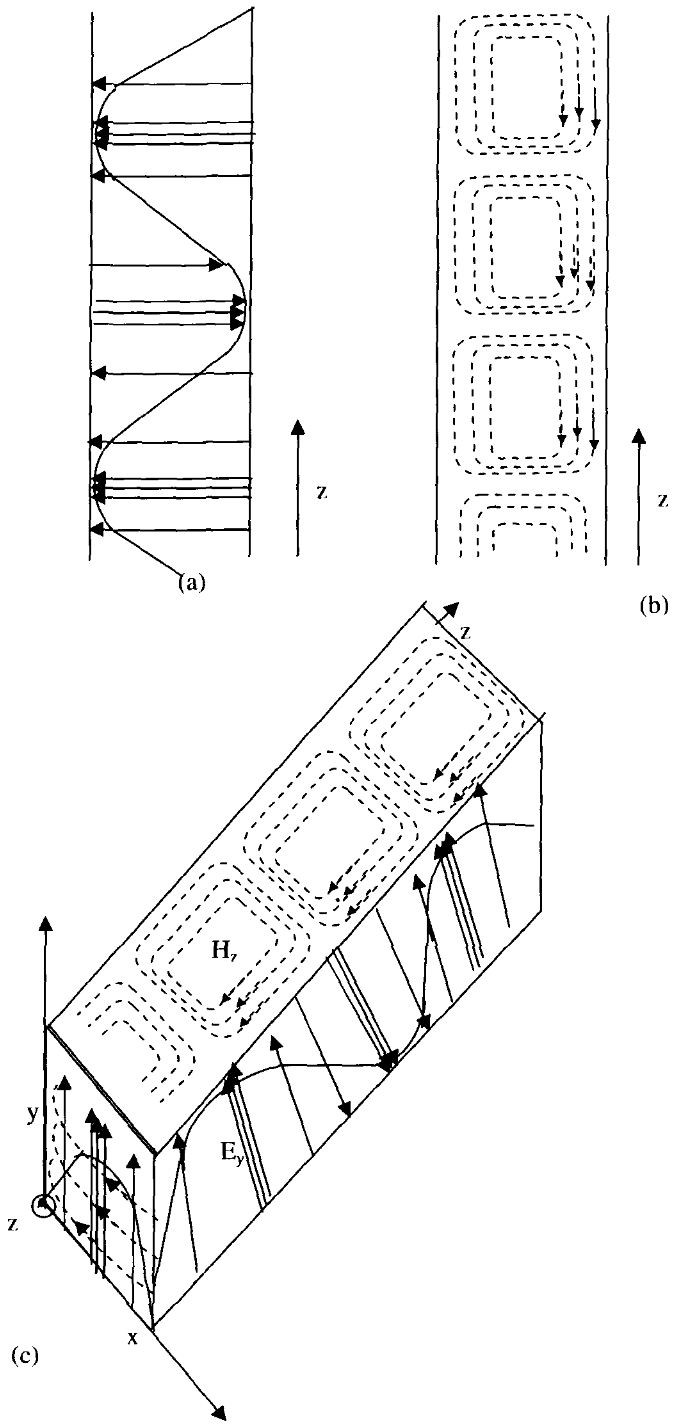

Fig-2.2: Variation of all field components of TE_{10} mode as a function of z
(a) Electric field component E_y along z (b) Magnetic field Component along z (c) field distribution of all components along z

The variations of these field components of TM_{10} mode as a function of z are portrayed in Fig.-2.3(a). In the figure, electric field component H_y (indicated by the dashed line) and magnetic field component E_z (indicated by the solid line) are maximum at x=w/2 and minimum at edges along x-axis whereas magnetic field component H_z (indicated by dashed line) is maximum at x=0 and w and minimum at x=w/2. Like TE mode, here, the intensity at the center of waveguide core is maximum and minimum at the edges of the waveguide.

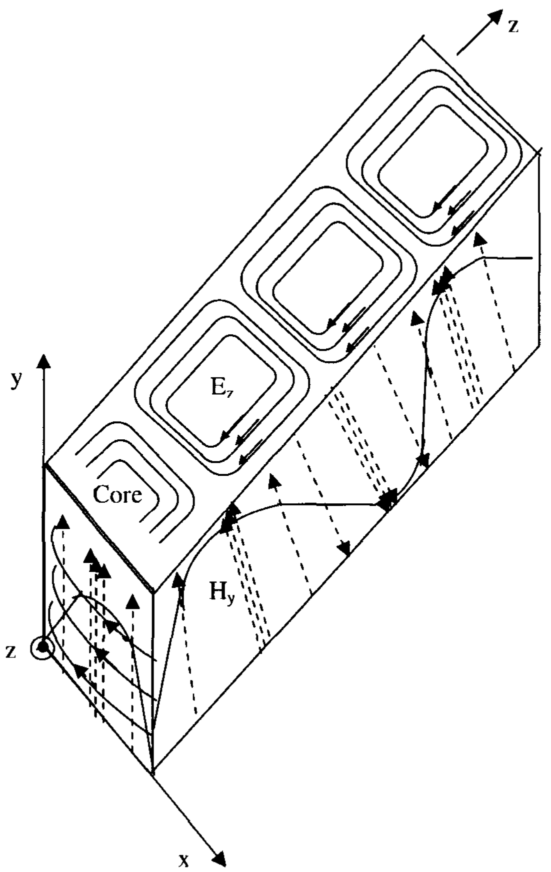

Fig-2.3(a): Field distribution of electric and magnetic field components of TM_{10} mode along z-direction of rectangular waveguide

2.2.1 Effective Index Method

Marcatili's method (Marcatili, 1969) [89] was extended by Knox and Toulios (1970) [90] who proposed the effective index (EI) method, which soon after became one of the most popular methods for the analysis of optical waveguides. Unlike numerical methods, this EI method is considered as semi-analytical methods, which make certain approximation to the structure under consideration and then solve the resulting simplified problem analytically. The popularity of the EI method is due to its simplicity, which comes from the fact that it reduces the three dimensional wave guiding structures to an equivalent two-dimensional structure.

This method is one of the simplest approximate methods for obtaining the modal fields and the propagation constant analysis for calculating the propagation modes of channel waveguides. It applies the tools developed for planar waveguides to solve the problem of two-dimensional structures in channel waveguides having arbitrary geometry and index profiles. It consists of solving the problem in one dimension, described by the x coordinate, in such a way that the other coordinate (the y-coordinate) acts as a parameter. In this way, one obtains a y-dependent effective index profile; this generated index profile is treated once again as a one-dimensional problem from which the effective index of the propagating mode is finally obtained. The propagation constants supported by a 2D channel waveguide having a refractive index profile which depends on two coordinates n=n(x, y) are then calculated by solving the propagation modes for two 1D planar waveguides. The EIM treats the channel waveguide as the superimposition of two 1D waveguides: planar waveguide-I confines light in the x-direction, while planar waveguide-II traps light in the y-direction [as shown in Fig.-2.3(b)]. For propagating modes polarized mainly along the x-direction $\left(E_x^{pq}\right)$, where that the major field components are E_x, H_y and E_z. The propagation of these polarized modes is similar to the TM modes in a 1D planar waveguide, and their solutions will correspond to the effective indices N_I. Further, the second planar waveguide (waveguide-II) is considered to be built from a guiding film of refractive index N_I, which has previously been calculated. The modes for the second planar waveguide are TE polarized, with E_x, H_y and H_z as non-vanishing components, because the light is mainly polarized along the x-direction.

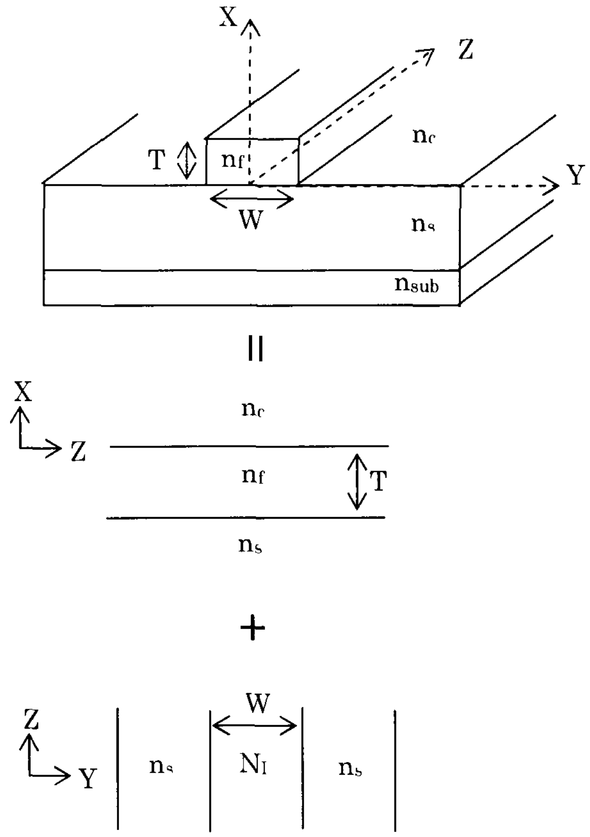

(a) 3D Waveguide-I

(b) 2D Waveguide-I

(c) 2D Waveguide-II

Fig-2.3(b): Analytical model of effective index method for 3D waveguide geometry [56]

In the Fig-2.3(b), an analytical model of simple effective index method (SEIM) for three dimensional (3D) waveguide geometry has been shown, where

N_I = Effective refractive index of 2D waveguide-I

$n_s = n_c$ =Refractive index of upper cladding and lower cladding

n_{sub} =Refractive index of substrate

T = Thickness of 2D waveguide-I and

W =Width of 2D waveguide-II

The Effective Index calculation procedure for three dimensional (3D) waveguide geometry can be summed up as follows [56]:

(i) The two dimensional optical waveguide is replaced with a combination of two one dimensional optical waveguides.
(ii) For each one dimensional waveguide, the effective is calculated index along y-axis.
(iii) The waveguide is modeled by using the effective index calculated in step (2) along x-axis.
(iv) The effective index is to be obtained by solving the model in step-3 along x-axis.

In the analysis of practical optical waveguides, analytical methods such as effective index method (EIM), Marcatili's methods etc. are slightly less accurate than Finite Difference Time Domain (FDTD) and Beam Propagation Method (BPM) [79]. In spite of the lower accuracy, inability to put in fabricated index profile, these methods have become popular waveguide design tools because of their simplicity, easier to use, requires lesser numerical calculations since SEIM solves the reduced vector wave equation instead of the full vector wave equation that governs the modes. The ability to convert a two dimensional problem into a one dimensional one is the main feature and advantage of this method [56]. Based on the above feature and advantage of simple effective index method, we have tried to implement for detail study of mode propagation and a comparison of beat length for the basic photonic integrated devices (PID) components such as directional coupler, two mode interference coupler and multimode interference coupler in the proceeding chapters of the thesis.

2.2.2 Marcuse Method

In 1987, Dietrich Marcuse [30] has illustrated the directional couplers made of non-identical asymmetric slab waveguides for the TE and TM mode. An approximate expressions are provided for the coupling coefficients of synchronous (no grating) couplers and their accuracy is checked by comparison with exact solutions that are based on solving the guided mode problem of the total structure consisting of the two slabs considered to be a single waveguide.

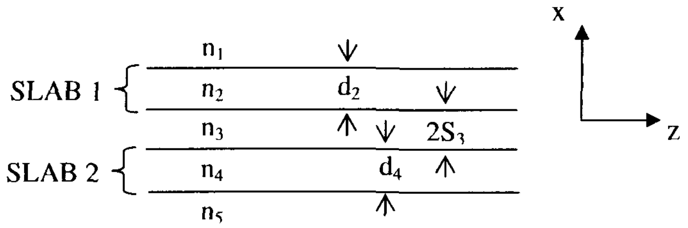

Fig.-2.4(a): Schematic of slab directional coupler

The directional coupler consisting of two asymmetric slab waveguides placed in close proximity to each other is schematically shown in Fig-2.4(a). The two slabs have dielectric core regions of thickness d_2 and d_4 with refractive index n_2 and n_4. It is assumed that $n_2 > n_1$, n_3 and $n_4 > n_3$, n_5 where the spacing between the slab cores is $2S_3$. Marcuse described TE and TM modes of the compound structure consisting of the five dielectric media by introducing a field function F which represents the E_y component of the electric field for TE modes and the H_y component of the magnetic field for TM modes. In the five regions of space, F is defined as follows,

$$\begin{aligned}
F &= A_1 \exp\left[-\gamma_1 (x - S_3 - d_2)\right] \qquad , for\ x \geq S_3 + d_2 \\
&= A_2 \cos\left[K_2\left(x - S_3 - \frac{d_2}{2}\right)\right] + A_3 \sin\left[K_2\left(x - S_3 - \frac{d_2}{2}\right)\right], \\
&\qquad\qquad for\ S_3 + d_2 \geq x \geq S_3 \\
&= A_4 \exp(-\gamma_3 x) + A_5 \exp(\gamma_3 x) \qquad , for\ -S_3 \leq x \leq S_3 \\
&= A_6 \cos\left[K_4\left(x + S_3 + \frac{d_4}{2}\right)\right] + A_7 \sin\left[K_4\left(x + S_3 + \frac{d_4}{2}\right)\right], \\
&\qquad\qquad for\ -S_3 \leq x \leq -S_3 - d_4 \\
&= A_8 \exp\left[\gamma_5 (x + S_3 + d_4)\right], \qquad , for\ x \leq -(S_3 + d_4)
\end{aligned} \tag{2.9}$$

2.2.3 Finite Element Method (FEM)

The finite-element method uses a variational formulation for solution of waveguide problems. For dielectric waveguides, the usual approach is to use all three components of the H or the E vector. The advantage of using the three components of the field is that no boundary conditions need to be set except at the exterior boundary. From Maxwell's equations,

$$\nabla\times\varepsilon_r^{-1}(\nabla\times H)=k_0^2H \tag{2.10}$$

Taking the inner product of this equation with H^* leads to a functional of the form

$$F=\int_S\left[(\nabla\times H)^*.\varepsilon_r^{-1}(\nabla\times H)-k_0^2H..H^*\right]dxdy \tag{2.11}$$

If the trial function coefficients are a_i, then requiring $\partial F/\partial a_i=0$ provides the equations for the matrix eigen value problem. The trial functions must span the whole domain and satisfy the exterior boundary conditions, and this becomes difficult for arbitrary shapes. Thus, the finite-element method discretizes the domain into a set of adjoining triangles, and the trial functions are defined within each triangle with unknown coefficients. In the nodal element scheme, the trial functions are expressed in the non-orthogonal area coordinates ζ_I, and linear and higher order trial functions in terms of the ζ_I can be used. Further, the integrations of the functional can be performed for each triangle before the matrix equation is assembled. The problem with the functional in (2.11) is that, spurious eigen value modal solutions occur. Furthermore, the formulation requires that β be specified, and the corresponding frequency ω in k_0 is obtained. Since the divergence equation has not been specifically set in this functional, inclusion of this equation in the functional with a summation parameter α mitigates this. While this approach does not eliminate the spurious modes, it pushes them to the higher order modes depending on the choice of α. Some check needs to be made to ensure that the spurious modes are eliminated from the solutions by running the code with different values of α. Using this technique, Rahman and Davies [81] have obtained results on a ridge guide that remain the benchmark against which all other methods are compared. This method has also been used by other groups [82] for modal solutions. An improvement on the three component field method was suggested by Cendes [83], in which the transverse fields are defined by edge elements and the longitudinal field is defined by the usual nodal elements. An edge element between the triangle vertices is defined by,

$$W_{ij} = \left(\zeta_i \nabla \zeta_j - \zeta_j \nabla \zeta_i\right) l_{ij} \tag{2.11a}$$

where ζ_I is the area coordinate defined above and l_{ij} is the length of the edge between these vertices.

The result of this definition is that the edge element is a trial function that is along the edge ij. The functional used here is given in (2.11), and the preferred field set is the components of E. With this choice of trial functions, the spurious modes are eliminated. Use of second-order edge elements has given excellent results. Recent work in the finite-element area has focused on the use of edge elements.

2.2.4 Finite Difference Time Domain (FDTD) method

The FDTD technique represents a widely used propagation solution technique in integrated optics, especially in photonic band gap device computations where the beam propagation solutions are inadequate, or cannot cope with the geometry. The major limitation is that the three-dimensional version requires large storage and extremely long computation times. The basic technique has been outlined in several papers and books devoted to the technique, for example, [84] and [85]. The solution of the wave propagation is by direct integration in the time domain of the Maxwell curl equations in discretized form. For example, the component of the curl equation is given by,

$$\frac{\partial H_y}{\partial x} - \frac{\partial H_x}{\partial y} = \frac{\partial D_z}{\partial t} \tag{2.11b}$$

Discretizing via central differences in time and space gives,

$$\varepsilon\left[\frac{E_z^{t+\Delta t}(x,y,z)-E_z^{t}(x,y,z)}{\Delta t}\right]$$
$$=\left[\frac{H_y^{t+\Delta t/2}(x+\Delta x/2,y,z)-H_y^{t+\Delta t/2}(x-\Delta x/2,y,z)}{\Delta x}\right]$$
$$-\left[\frac{H_x^{t+\Delta t/2}(x,y+\Delta y/2,z)-H_x^{t+\Delta t/2}(x,y-\Delta y/2,z)}{\Delta y}\right] \quad (2.12)$$

The grid is staggered in time and space (the so-called Yee mesh following [3]), and the equations for the other field components follow this form. With a given excitation at the input either in CW or pulsed form, the excitation may be propagated through the structure by time stepping through the entire grid repeatedly. This first-order difference formulation is second-order accurate. In the interest of time and computational speed, most of the computations in the integrated optics area are in two dimensions. Higher order formulations are also available but the overhead that is carried slows down the marching algorithm, while improving accuracy for a specific grid size. The integrated form of the curl equations leads to a finite volume formulation. Again, a marching algorithm is developed on a split grid, as above. A recent two-dimensional alternative to the above first-order formulation, as applied to optical guides, is the higher order compact algorithm based on the split operator technique of Strang [86] and Shang [87]. In this approach, two fields, for example, E_z and B_x, are combined to define a Riemann time invariant variable, and the propagation of this variable uses the piecewise parabolic approximation suggested by Woodward and Colella [88]. Since the algorithm is two-dimensional the run times are smaller, and because of the parabolic approximation, higher order accuracy is obtained without the overhead of the higher order formulation.

2.2.5 Beam Propagation Method

One of the fundamental aspects in integrated optics is the analysis and simulation of electromagnetic wave propagation in photonics devices based on waveguide geometries, including optical waveguides. The problem is to be solved such as for a given arbitrary distribution of refractive index n(x,y,z), and for a given wave field distribution at the input plane at z=0, E(x, y, z = 0), the spatial distribution of light E(x, y, z) at a generic point *z* must to be found. In this case, the distribution of the refractive index is known, which defines the optical circuit. When a light beam is injected at *z*=0, the problem is to determine the light intensity distribution at the exit, and in particular, what will be the output light intensity in each of the output branches.

The "Beam Propagation Method" (BPM) is useful to the study of light propagation in integrated photonics devices based on optical waveguides with the help of a paraxial form of the Helmholtz relation, known as the Fresnel equation. This relation is valid for paraxial propagation in slowly varying optical structures, which is the starting point to develop BPM algorithms.

The solution to the Helmholtz equation or the Fresnel equation applied to optical propagation in waveguides is known as the Beam Propagation Method (BPM) [79]. Two numerical schemes have been used to solve the Fresnel equation. In one numerical scheme, optical propagation is modeled as a plane wave spectrum in the spatial frequency domain, and the effect of the medium in homogeneity is interpreted as a correction of the phase in the spatial domain at each propagation step. The use of the fast Fourier techniques connects the spatial and spectral domains, and this method is therefore called Fast Fourier transform BPM (FFT-BPM). The propagation of EM waves in inhomogeneous media can also be described directly in the spatial domain by a finite difference (FD) scheme [79]. This technique allows the simulation of strong guiding structures, and also of structures that vary in the propagation direction. The beam propagation method which solves the paraxial form of the scalar wave equation in an inhomogeneous medium using the finite difference method is called FD-BPM. Also methods based on finite differences which solve the vector wave equation, called FDVBPM, have been developed. There is an intermediate approximation, which starts from the wave equation but ignores coupling terms between the transversal components of the fields, and for that reason this method is usually referred to as semi-vector (FD-SVBPM)

The BPM is one of the commonly used numerical tools for modelling structures that are non uniform in propagation direction for time harmonic optical signals Since the optical carrier frequency is usually very large compared to the signal bandwidth modelling with a monochromatic wave is sufficiently accurate for many devices Commercialized computer aided design software (e.g OptiWave, RSoft, BBV) based on this technique is available and their capabilities concerning wide angle problems, bidirectional propagation and anisotropy are steadily improved

Since the BPM algorithm based on finite differences in general has superior performance than that of the BPM based on the fast Fourier transform method, it has been used with the help of optiBPM software (V 9 0) (commercialized by OptiWave) for the simulation study and verifications of our theoretical and experimental results for the light wave propagation in designed integrated optical elements

2.3 Directional Coupler

Fig-2 4(b) shows 3D view of a typical asymmetric directional waveguide coupler consisting of two rectangular waveguides: waveguide-1 of width, w_1 and thickness t_1 and waveguide-2 of width w_2 and thickness t_2 β_1 and β_2 are the propagation constants in wave guides 1 and 2 without coupling, respectively The refractive indices of spacing in coupling region, core-1, core-2 and their surroundings are n_3, n_2, n_4 and n_1 respectively The gap between two waveguides in coupling region is h The input power P_1 and P_2 are incident in waveguide-1 and waveguide-2, respectively when the output powers P_3 and P_4 are obtained in waveguide-1 and waveguide-2, respectively after coupling. The coupling takes place in the $0 < z < L$ region in which the even and odd modes can propagate with propagation constants β_e and β_o

The phase shift between the even and odd modes becomes π, when the propagation distance L_π is given by [18],

$$L_\pi = \pi/(\beta_e - \beta_o) \tag{2.13}$$

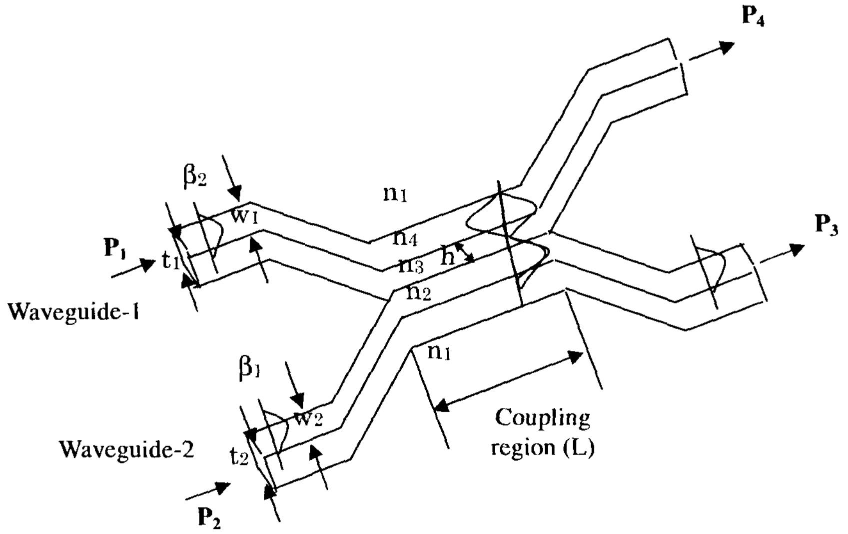

Fig-2.4(b): 3D view of asymmetric directional coupler of coupling length L consisting of waveguide-1 and waveguide-2.

In a symmetrical directional coupler where $t_1=t_2$, $n_2=n_4$ and $w_1=w_2$ i.e. $\beta_1=\beta_2$, considerable coupling occurs in the h<8 μm range [18]. On the other hand, in an asymmetrical directional coupler where $t_1 \neq t_2$, $n_2 \neq n_4$ and $w_1 \neq w_2$ and, hence, $\beta_1 \neq \beta_2$, the coupling is not noticeable unless h is less than 5 μm [18]. The power transfer due to mode coupling is generally characterized by a phase mismatch ($\beta_1 - \beta_2$) between the two waveguides and the coupling coefficient is determined by [18]

$$k = \tfrac{1}{2}(\beta_e - \beta_o) \tag{2.14}$$

To study the mathematical analysis of directional coupler, coupled mode theory is required which is discussed in the next section.

2.3.1 Coupled Mode Theory

Coupled mode theory is a powerful tool for studying optical waveguide coupling behavior. The concept of coupled mode theory is based on two-mode coupling theory. It is seen that when the energy is incident on one of the waveguide, then there is a periodic exchange between two waveguides– 1 and 2. To explain the coupling behavior, we should know the coupled mode equations, which describe the variation of amplitude of the modes propagating in each individual waveguide of the coupler.

The coupled mode equations may be written as [23]

$$\frac{da}{dz} = -j\beta_1 a(z) - jk_{12} b(z) \tag{2.15}$$

$$\frac{db}{dz} = -j\beta_2 b(z) - jk_{21} a(z) \tag{2.16}$$

where k_{12} and k_{21} represent strength of coupling between two modes and are also called as coupling coefficient. In absence of coupling, k_{12}=k_{21}=0. The coupling coefficients depend on the waveguide parameters, separation between the waveguides in coupling region h and wavelength.

2.3.2. Power transferred between two waveguides due to coupling

In order to solve the coupled mode equations we have considered the trial solutions of the equations (2.15) and (2.16) as follows [14],

$$\left.\begin{aligned} a(z) &= a_0 e^{-j\beta_1 z} \\ b(z) &= b_0 e^{-j\beta_2 z} \end{aligned}\right\} \tag{2.17}$$

Substituting a(z) and b(z) in the equations (2.15) and (2.16), we get,

$$a_0(\beta - \beta_1) - k_{12} b_0 = 0 \tag{2.18}$$

$$b_0(\beta - \beta_2) - k_{21} a_0 = 0 \tag{2.19}$$

So, we can write from the equations (2.18) and (2.19),

$$\beta^2 - \beta(\beta_1 + \beta_2) + (\beta_1\beta_2 - k^2) = 0 \tag{2.20}$$

Thus, $$\beta_{e,o} = \frac{1}{2}(\beta_1 + \beta_2) \pm [\frac{1}{4}(\beta_1 - \beta_2)^2 + k^2]^{1/2} \tag{2.21}$$

$$\text{where } k = \sqrt{k_{12}k_{21}} \tag{2.22}$$

In the coupling region, there are two independent modes called as even and odd modes propagating with propagation constant β_e and β_o respectively The suffixes e and o represent even and odd mode respectively. The general solutions are written as [14],

$$a(z) = a_e e^{-j\beta_e z} + a_o e^{-j\beta_o z} \tag{2.23}$$

$$b(z) = \{(\beta_e - \beta_1)/k_{12}\}a_e e^{-j\beta_e z} + (\beta_o - \beta_1)/k_{12}\}a_o e^{-j\beta_0 z} \tag{2.24}$$

where a_e and a_0 are amplitudes of even and odd mode, respectively. The equations (2.23) and (2.24) are coupled wave fields in waveguide-1 and 2 respectively. The behavior of the coupled waves can be determined by obtaining propagation constants. Since the waves in two waveguides are propagated in same direction in case of directional coupler, the propagation constants, $\beta_1>0$ and $\beta_2>0$ respectively.

The solutions of the coupled mode equations are given by [23]

$$a(z) = (a_e e^{-j\sqrt{k^2+\delta\beta^2}z} + a_o e^{j\sqrt{k^2+\delta\beta^2}z})e^{j\beta_{av}z} \tag{2.25}$$

$$b(z) = [\{(\beta_e - \beta_1)/k_{12}\}a_e e^{-j\sqrt{k^2+\delta\beta^2}z} + (\beta_o - \beta_1)/k_{12}\}a_0 e^{-j\sqrt{k^2+\delta\beta^2}z}]\, a_a e^{-j\beta_{av}z} \tag{2.26}$$

where, $2\delta\beta = \beta_1 - \beta_2$ and $2\beta_{av} = \beta_1 + \beta_2$. The constants a_e and a_o for even and odd mode are determined by boundary conditions. We assume that at z=0, the mode is launched in waveguide-1 with unit power and there is no power in waveguide-2. By considering boundary conditions, the power flows in waveguide-2 and 1 are given by

$$P_4 / P_1 = |A(z)|^2 = 1 - \frac{k^2}{k^2 + \delta\beta^2} \sin^2[(k^2 + \delta\beta^2)^{1/2} z] \tag{2.27}$$

$$P_3 / P_1 = |B(z)|^2 = \frac{k^2}{k^2 + \delta\beta^2} \sin^2[(k^2 + \delta\beta^2)^{1/2} z] \tag{2.28}$$

where, $k = \sqrt{k_{12}k_{21}}$

The powers of waves propagating along two guides vary periodically. The maximum power transfer occurs at a distance L_π is obtained as

$$P_{4,\max} / P_1 = \frac{1}{1 + (\delta\beta / k)^2}. \tag{2.29}$$

where, $$L_\pi = \frac{\pi}{2\sqrt{k^2 + \delta\beta^2}}$$

As, $\delta\beta \to 0$, the maximum power transfer increases. At $\delta\beta = 0$ there is a complete power transfer between two waveguides. This is called as Synchronous or symmetric directional coupler (DC) ($\beta_1 = \beta_2$).

2.3.3. Coupling Coefficient

The coupling coefficient of asymmetric directional coupler with gap h between the coupling waveguides (2D model) derived by Marcuse [30] is written as,

$$k_{mercuse} = |\ k\ | = \frac{2K_2 K_4 \gamma_3 e^{-h\gamma_3}}{k_0^2 \beta \{(n_2^2 - n_3^2)(n_4^2 - n_3^2)(w_1 + 1/\gamma_1 + 1/\gamma_3)(w_2 + 1/\gamma_1 + 1/\gamma_3)\}^{1/2}} \tag{2.30}$$

where, $K_2 = \sqrt{n_2^2 k_0^2 - \beta^2}$, (2.31)

$K_4 = \sqrt{n_4^2 k_0^2 - \beta^2}$, (2.32)

$\gamma_1 = \sqrt{\beta^2 - n_1^2 k_0^2}$,

$\gamma_3 = \sqrt{\beta^2 - n_3^2 k_0^2}$, 2.33)

$k_0 = 2\pi/\lambda$. (2.34)

The coupling coefficient in the equation (2.30) is rewritten as follows

$$k_{mercuse} = C_{mercuse}(\Delta n, w, \lambda)\ e^{-h\gamma_3} \qquad (2.35)$$

where,

$$C_{mercuse}(\Delta n, w, \lambda) = \frac{2K_2K_4\gamma_3}{k_0^2\beta\{(n_2^2 - n_3^2)(n_4^2 - n_3^2)(w_1 + 1/\gamma_1 + 1/\gamma_3)(w_2 + 1/\gamma_1 + 1/\gamma_3)\}^{1/2}} \qquad (2.36)$$

$C_{mercuse}(\Delta n, w, \lambda)$ depends on waveguide parameters and wavelength. It is independent of spacing, h between two waveguides in coupling region.

The coupling co-efficient between two coupled wave guides derived by Digonnet [31] is given as follows

$$|k| = k_{dig} = \frac{\lambda}{2\pi n_2} \cdot \frac{u^2}{d^2V^2} \frac{K_0(vH/d)}{K_1^2(v)} \qquad (2.37)$$

where d = w/2 = half width of the wave guide,

H= gap between two waveguide axes = h + w

K_0, K_1 = modified Bessel function of second kind and order 0, 1 respectively,

$$\left.\begin{aligned} u &= d\sqrt{k_0^2n_2^2 - \beta^2} \\ v &= d\sqrt{\beta^2 - k_0^2n_2^2} \end{aligned}\right\} \qquad 2.38(a)$$

V = normalized frequency = $(2\pi w/\lambda)\sqrt{(n_2^2 - n_3^2)}$ (2.38b)

and n_2, n_3 = core and cladding refractive index respectively.

The coupling coefficient in the equation (3.33) can be rewritten as

$$k_{dig} = C_{dig}(\Delta n, w, \lambda)\, k_0(vH/d) \qquad (2.39)$$

where, $$C_{dig}(\Delta n, w, \lambda) = \frac{\lambda}{2\pi n_2} \cdot \frac{u^2}{d^2V^2} \frac{1}{K_1^2(v)} \qquad (2.40)$$

The $C_{dig}(\Delta n, w, \lambda)$ depends on waveguide parameters and wavelength. It is independent of gap between central axes of waveguides, H in coupling region.

2.3.4. Numerical Calculation

For numerical calculation, we have taken the following waveguide parameters [31],

n_1=n_3=1.4551, n_2=n_4=1.458, t_1= t_2=w_1=w_2= w=6 μm and λ=1.15 μm.

The normalized frequency, V obtained from the equation (2.38b) is 3.0116. We have calculated the propagation constant β= 7.95143 using effective index method. So we, have calculated u and v using the equation (2.38a) as follows,

u = 1.2274 and v = 0.8723

The modified Bessel functions K_0(vH /d) and K_1 (v) are approximately written in asymptotic form as follows,

$$\left.\begin{aligned} K_1(v) &= \sqrt{\pi/2v}\,\exp\left[-(8v+3)/8\right] \\ K_0(vH/d) &= \sqrt{\pi d/2vH}\,\exp[-(8vH/d-1)/8] \end{aligned}\right\} \quad (2.41)$$

Using the equation (2.33), we have calculated K_0 and K_1 as follows,

$K_1(v) = 0.3854$

Putting the value of $K_1(v)$ and other waveguide parameters in the equation (2.40), we have calculated $C_{dig}(\Delta n, w, \lambda)$ for wavelength, λ=1.15 μm as follows,

$C_{dig}(\Delta n, w, \lambda)$=0.015608

For calculation of $C_{mercuse}(\Delta n, w, \lambda)$ we have determined k_2, and γ_3 using the equations (2.31) and (2.33) as follows,

k_2 = 0.40911 and γ_3 = 0.290782

The $C_{mercuse}(\Delta n, w, \lambda)$ for wavelength λ=1.15 μm is obtained using the equations (2.31)-(2.36) as follows

$C_{mercuse}(\Delta n, w, \lambda) \sim 0.0037$

Using same method, we have calculated $C_{mercuse}(\Delta n, w, \lambda)$ and $C_{dig}(\Delta n, w, \lambda)$ for other wavelengths λ =0.7 μm, and 1.55 μm.

By knowing these $C_{mercuse}(\Delta n, w, \lambda)$ and $C_{dig}(\Delta n, w, \lambda)$, we have calculated the variation of coupling coefficient with H for other wavelength 0.7 μm and 1.55 μm respectively. For calculation of k_{dig}, we have determined modified Bessel function, $k_0(vH/d)$ for different H values. For H = 6 μm,

$$K_0(vH/d) = \sqrt{\pi d/2vH}\ \exp[-(8vH/d-1)/8] = 0.1877876$$

So the k_{dig} is determined by using the equation (2.39) as follows

$$k_{dig} = C_{dig}(\Delta n, w, \lambda)k_0(vH/d) = 0.00293$$

Whereas the $k_{mercuse}$ calculated using the equation (2.35) as follows

$$k_{mercuse} = C_{mercuse}(\Delta n, w, \lambda)e^{-h/\gamma_3} = 0.0037$$

where, γ_3=0.40911 and h=H-w=0. Similarly, we have calculated the variation of $k_{mercuse}$ and k_{dig} with increase of H for wavelength λ= 0.7 μm, 1.15μm and 1.55 μm.

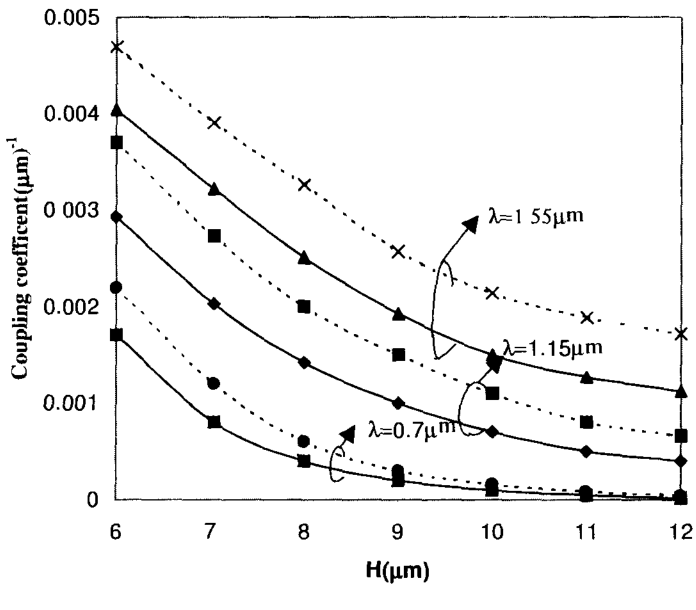

Fig-2.4(c): Variation of k_{dig} (solid line) and $k_{mercuse}$ (dashed line) with H for λ=1.55 μm, 1.15 μm and 0.7 μm respectively.

Fig-2.4(c) compares the variation of coupling coefficient with H at wavelengths 0.7 μm, 1.15 μm and 1.55 μm respectively. In the figure, the solid line represents plot of Digonnet's coupling coefficient versus H, whereas the dashed line represents plot of Mercuse's coupling coefficient, $k_{mercuse}$ versus H. It is evident from the figure that for lower wavelength there is little difference between two coupling coefficients and this difference increases with increase of wavelength.

The propagation constants for even and odd modes are given by

$$\left.\begin{aligned} \beta_e &= \beta + k \\ \beta_0 &= \beta - k \end{aligned}\right\} \tag{2.42}$$

2.3.5. Directional couplers reported by previous authors

Table-2.1 shows results of directional couplers demonstrated by different authors. In this section, only DC with different Δn and coupling gap are mentioned as demonstrated by different authors. The table also shows TMI coupler and MMI coupler which are discussed later in this chapter. The figures, Fig-2.5(a), 2.5(b) and 2.5(c) show the different waveguide structures used by different authors as mentioned in the table. It is found that most of the authors have used embedded and rib waveguide for demonstration of DC, TMI and MMI couplers.

R. Kasahara et al. [10] demonstrated directional coupler with embedded waveguide of core size~7x7 $(\mu m)^2$ using $SiO_2/SiO_2\text{-}GeO_2$ material with Δn=0.75 % for the application of thermooptic MZ switch of 22 mm. The propagation constant is determined by using dispersion equation [1] as 5.8909 $(\mu m)^{-1}$ and the coupling coefficient $k_{mercuse}$ of DC with coupling gap h=2 μm is obtained by using the equation (2.35)-(2.36) as 0.0016 $(\mu m)^{-1}$. The detail of calculation of $k_{mercuse}$ is described in section-2.3.4. The 3 dB coupling length is calculated as

$$L = \pi/4k_{mercuse} = 481.6\ \mu m$$

Table-2.1: DC, TMI and MMI couplers (MZI=Mach Zehnder Interferometer, DC= Directional Coupler, TOMZ=Thermooptic Mach Zehnder, DOS=Digital Optical Switch and TMI=Two Mode Interference)

Material	Δn taken by different authors	Device Structure	Beat length	Device length /width (mm)	Application
SiON// SiO_2 Index range~ (1.45 – 1.98) Available Δn ~53%	3.3%[1] 0.46% [2] 1.92% [3] 10.1% [4] 10 % [5] 5.42% [6] 10.3% [7]	DC(Embedded)*** DC(Embedded) MMI** MMI (Rib)**** TMI (Embedded)* MMI(Rib)**** MMI(Embedded)* *	…… 1960 μm 1920 μm 74.1 μm ….. 467 μm 23 μm	~75 / 5.6 ~50 / 0.25 …… 0.667mm 74.5 μm …. 145 μm	Add/drop mux Add/drop mux 3dB coupler Wavelength Demux WDM Power coupler Demux
GeO_2 -SiO_2/ SiO_2 Index range~ (1.45 – 1.47) Available Δn ~2%	1% [8] 0.45%[9] 0.75%[10] 0.7%[11] 1.5 % [12]	MMI(Embedded) DC (Embedded) DC(Embedded) DC(Embedded) DC (Embedded)	1000μm …. ….. ….. …..	5mm ….. 22 / 0.5 ~80/25 40/0.25	TOMZ switch WDM TOMZ switch EDFA gain equalizer TOMZ switch
InP/GaAsInP Index range~ (3.13 - 3.5) Available Δn ~33%	16.7%[13] 15% [14] 16.7%[15] 13%[16] 15%[17]	MMI (Ridge) MMI(Embedded) DC &MMI(Ridge) MMI(Ridge) MMI(buried)	35 μm 41μm 35μm 432μm 400μm	~105μm 20.5μm ….. 1296μm ~200μm	Power splitter 3dB coupler Mode filter MMI Switch 50:50 splitter

Table-2.1(Continue): DC, TMI and MMI couplers (MZI=Mach Zehnder Interferometer, DC=Directional Coupler, TOMZ=Thermooptic Mach Zehnder, DOS=Digital Optical Switch and TMI=Two Mode Interference)

Material	Δn taken by different authors	Device Structure	Beat length	Device length /width (mm)	Application
Ti $LiNbO_3$ Index range~ (2 15- 2 21) Available Δn ~6%	1%[19] 0 6%[20] 0 6%[22] 0 6%[25] 1% [21]	TMI (Embedded) TMI(Embedded) Y junction DC (Embedded) DC(Embedded)	135μm 139μm 135μm	5mm 6mm	Optical bifurcation Wavelength Mux DOS Photonic switch Optical DC
Polymer Index range~ (1 44-1 65) Available Δn ~21%	2 54%[26] 0 3%[27]	DC DC	256 μm	 ~30mm	TOMZ switch TOMZ switch

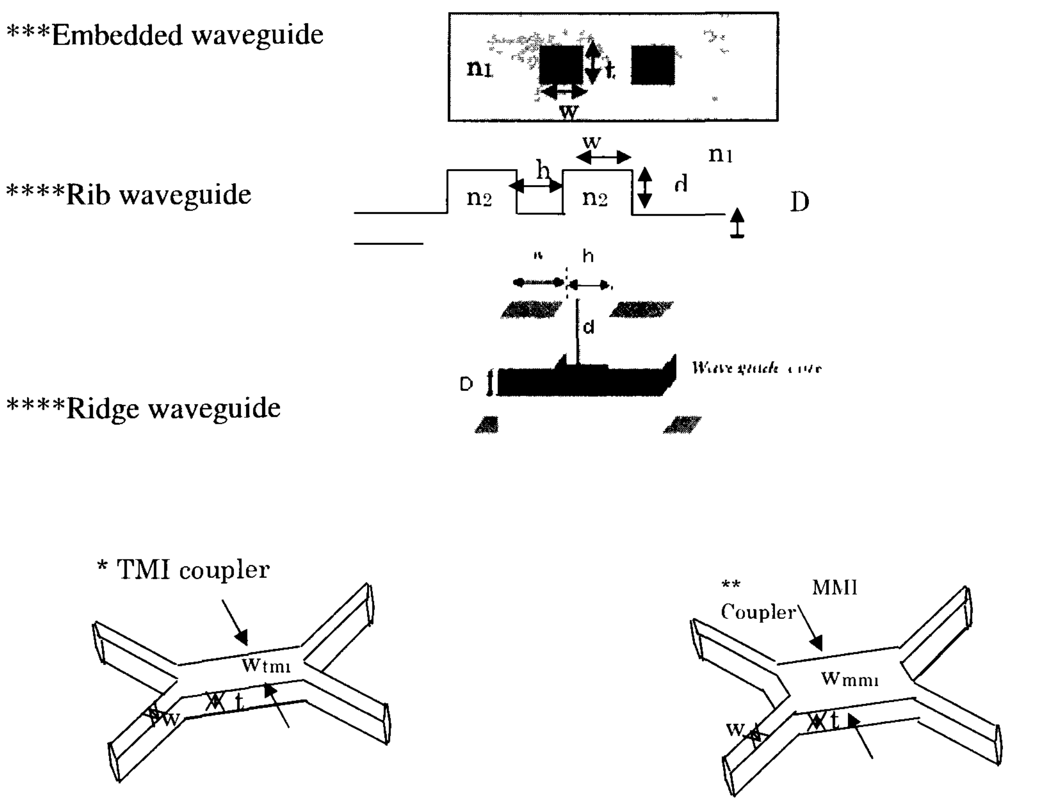

Fig-2.5: Different device structures (a) cross section of DC with embedded rectangular waveguide (b) DC with Rib waveguide (c) DC with Ridge waveguide (d) TMI coupler (e) MMI coupler

B. J. Offrein et al. [1] has demonstrated directional coupler with embedded waveguide using SiO_2/SiON material with Δn=3.3 % for the application of Add/drop multiplexer of device length of 75 mm. Y. Hida et al. [9] demonstrated directional coupler with embedded waveguide using SiO_2/SiO_2-GeO_2 material with Δn=0.45 % for the application of wavelength division multiplexer. Scilipf et al. [11] demonstrated directional coupler with embedded waveguide using SiO_2/SiO_2-GeO_2 material with Δn=0.7 % for the application of EDFA gain equalizer of length~80 mm. Sohma et al. [12] demonstrated directional coupler with embedded waveguide using SiO_2/SiO_2-GeO_2 material with Δn=1.5 % for the application of thermooptic MZ switch. M.K. Chin et al. [13] has demonstrated directional coupler of very small gap h=0.2 μm with ridge waveguide using InP/GaAsInP waveguide for wavelength and power splitting. D. Mercuse [30] has reported directional coupler with small gap h=0.5 μm using InP/GaAsInP with index contrast (Δn) of 10 %.

M. Papuchan et al. [19] has demonstrated optical directional coupler of coupling gap h=2 μm and 3 μm with corresponding coupling length 0.5 mm and 1mm using Ti:$LiNbO_3$ material with index contrast of 0.5% for switching of wavelength 514.2 nm. H. A. Haus et al. [21] has reported optical directional coupler using Ti: $LiNbO_3$ waveguide with index contrast of 1% and has tapered the same with maximum and minimum coupling gap of 3.54 μm and 2.97 μm for elimination of crosstalk. H. S. Hinton [25] has reported directional coupler using Ti:$LiNbO_3$ waveguide for photonic switching. Y. Hida et al. [27] reported polymeric directional coupler with Δn=0.3 % for demonstration of TOMZ switch of device length ~30 mm. M. Digonnet et al. [31] has demonstrated single mode fiber coupler of core center to center spacing (H), 4.75 μm with index contrast of ~0.75% for wavelength multiplexer with channel separation of 35 nm. E. A. J. Marcatali [32] has reported rectangular waveguide directional coupler of coupling gap h~1 μm and coupling length ~149 μm with index contrast of ~1.5% for 3 dB coupling of wavelength, 1.13 μm. So most of previous authors have investigated directional coupler with coupling spacing h≥1 μm. In our works discussed in chapter-4, we have studied directional coupler with coupling gap both h ≥1 μm and h<1 μm

2. 4. MMI Coupler

Fig-2.6(a) shows the schematic diagram of MMI device in which the central structure is a multimode waveguide designed to support a large number of modes (typically≥3). In order to launch light into and recover light from the multimode waveguide, a number of access waveguides (usually single mode waveguides) are placed at its beginning and end of central structure of width w_{mmi} and thickness t respectively. Such devices are generally called as MxM MMI couplers where, M is the number of input/out put access waveguides The refractive index of MMI core and cladding are considered as n_2 and n_1 respectively

The principle of operation of MMI is based on self imaging by which the input field is reproduced in single or multiple images at periodic intervals along the propagation direction of the waveguide There are number of methods to describe the self imaging phenomena—ray optics approach [33], hybrid methods [34], guided mode propagation analysis [35] etc The guided mode propagation analysis is probably most comprehensive method to analyze the self imaging in multimode waveguide because it not only supplies basis for the numerical modeling and design but it also explains the mechanism of multimode interference

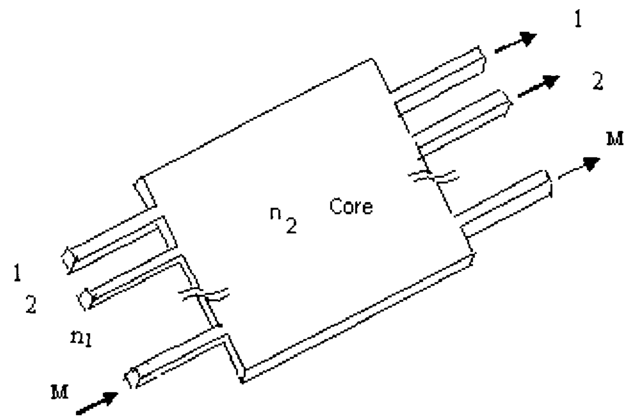

Fig.-2.6(a): 3D view of MxM MMI coupler

In MMI waveguide for wide width, the electric filed is present along Y direction in TE mode and for TM mode the electric field is present along X direction [15] This follows the field distribution of TE and TM mode in Fig-2 2(c) and Fig-2 3(a) respectively

2.4.1 Guided mode propagation analysis

The self imaging phenomenon of 3D MxM multimode structure is analyzed as shown in the Fig-2.6(a). As the lateral dimensions are much larger than the transverse dimensions, it is justified to assume that the modes have same transverse behavior everywhere in the waveguide. So the problem can be analyzed using two dimensional (lateral and longitudinal) structures, as shown in Fig-2.6(b). The analysis based on 2D representation of the multimode waveguide can be obtained from the actual 3D physical multimode waveguide by effective index method.

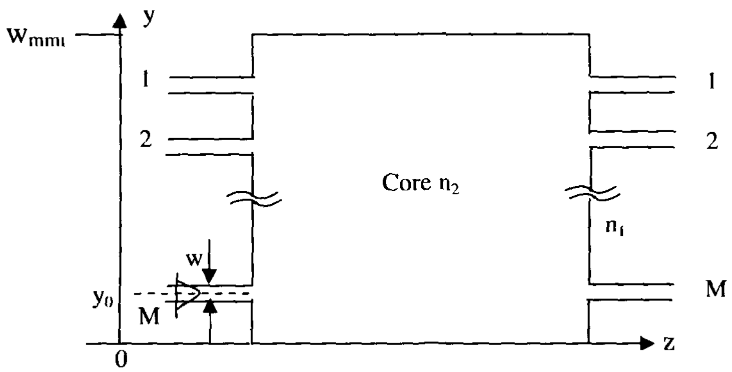

Fig-2.6(b): 2D representation of MxM MMI coupler

The input field profile H(y, 0) incident on MMI coupler is summation of mode field distribution of all modes in 2D approximation as follows,

$$H(y,0) = \sum_i b_i H_i(y) \tag{2.43}$$

where b_i is mode field excitation coefficient which can be estimated using overlap integrals based on the field orthogonal relations and $H_i(y)$= mode field distribution of i^{th} mode.

The composite mode field profile at a distance, z inside multimode coupler can be represented in 2D representation as a superposition of all the guided modes:

$$H(y,z) = \sum_{i=0}^{m-1} b_i H_i(y) \exp[j(\beta_0 - \beta_i)z] \tag{2.44}$$

where, m is total number of guided modes and β_i is the propagation constant of i[th] mode. For high index contrast, it is approximately written as [35]

$$\beta_i \approx k_0 n_r - \frac{(i+1)^2 \pi \lambda}{4 n_r w_e^2} \tag{2.45}$$

where, $w_e = w_{mmi} + w_p$ = equivalent width or effective width (2.46)

w_{mmi} = physical width of MMI coupler

$w_p = \frac{\lambda}{\pi}\left(\frac{n_l}{n_r}\right)^{2\sigma}\left(n_r^2 - n_l^2\right)^{-1/2}$ = lateral penetration depth related to Goos-Hahnchen shift (2.47)

n_r is effective index of the MMI core, w_{mmi} is width of multimode wave guide, n_l is the refractive index of multimode wave guide cladding, λ is the wavelength and $k_0=2\pi/\lambda$. σ =0 for TE mode and σ=1 for TM mode. Defining L_π as the beat length of the two lowest order modes, it is given in [35]

$$L_\pi = \frac{\pi}{\beta_0 - \beta_1} \approx \frac{4 n_r w_e^2}{3\lambda} \tag{2.48}$$

where β_0=propagation constant of fundamental mode and β_1=propagation constant of 1[st] order mode.

As for example, Ridder et al. [3] reported device parameters, n_l=1.45, Δn =0.0192, w_{mmi}=35 μm, w=3 μm λ=1.55 μm and for these parameters, penetration depth is obtained by using the equations (2.46)-(2.47) for TE mode as,

$$w_e = 35 + \frac{1.55}{3.14}\left(1.4559^2 - 1.45^2\right)^{-1/2} \approx 35+3.76=38.76\ \mu m$$

Using dispersion equation n_r is calculated as 1.4559.

The beat length is calculated as,

$$L_\pi = \frac{4\times 1.4559 \times 38.76^2}{3\times 1.55} \approx 1880\ \mu m$$

The estimated value of L_π proves good agreement of experimental value which is shown later on in Fig-2.10(a). The estimated value of L_π proves good agreement of experimental value which is shown in Fig-2.10(a). Rajarajan et al. [6] reported device parameters, n_l=1.45, Δn=0.0542, w_{mmi}=18 μm, w=3 μm λ=1.55 μm and for these parameters, penetration depth is obtained by using the equations (2.46)-(2.47) for TE mode as,

$$w_e = 18 + \frac{1.55}{3.14}\left(1.496^2 - 1.45^2\right)^{-1/2} \approx 18+1.3=19.3\ \mu m$$

Using dispersion equation n_r for TE mode is calculated as 1.496.

The beat length is calculated as,

$$L_\pi = \frac{4\times 1.496\times 19.3^2}{3\times 1.55} \approx 479\ \mu m$$

Darmawan et al. [15] reported device parameters, n_l=3.17, Δn =0.167, w_{mmi}=3.5 μm, w=1.5 μm, λ=1.55 μm and for these parameters, penetration depth is obtained by using the equation (2.46)-(2.47) for TE mode as,

$$w_e = 3.5 + \frac{1.55}{3.14}\left(3.2221^2 - 3.17^2\right)^{-1/2} \approx 3.55\ \mu m$$

Using dispersion equation n_r for TE mode is calculated as ~ 3.222.

The beat length is calculated as,

$$L_\pi = \frac{4\times 3.222\times 3.55^2}{3\times 1.55} \approx 34.9\ \mu m$$

Z. Wang et al. [44] reported device parameters, n_l=1.45, Δn=2 %, w_{mmi}= 20 μm, w=4 μm, λ=1.55 μm and for these parameters, penetration depth is obtained by using the equations (2.46)-(2.47) for TE mode as,

$$w_e = 20 + \frac{1.55}{3.14}\left(3.317^2 - 1.45^2\right)^{-1/2} \approx 20+0.165=20.165\ \mu m$$

Using dispersion equation n_r for TE mode is calculated as 1.496.

The beat length is calculated as,

$$L_\pi = \frac{4\times 3.317\times 20.165^2}{3\times 1.55} \approx 2300\ \mu m$$

Table-2.2: Comparison between Calculated and other author's reported value of L_π

Materials	Author's Name	Δn (%)	w_{mmi} (μm)	w_e (Calculated)	% of w_p in w_e	n_r (reported)	L_π (Calculated)	L_π (reported)
SiO_2/SiON	Ridder et al. [3]	1.92	35	38.76 μm	10.7%	1.4559	1880 μm	1881 μm
SiO_2/SiON	Rajarajan et al. [6]	5.42	18	19.3 μm	7.2%	1.496	479 μm	467 μm
InP/GaAsInP	Dharmawan et al. [15]	16.7	3.5	3.55 μm	1.4%	3.222	34.9 μm	35 μm

Table-2.2 compares beat length L_π calculated using the equation (2.48) and that reported by other authors. It is seen that L_π values are almost same for all Δn values mentioned in the table. The table also shows that as Δn increases, penetration depth w_p decreases. For Δn=16.7 %, $w_e \approx w_{mmi}$ which agrees with the result demonstrated by Darmawan et al. [15].

The propagation spacing can be written as

$$\beta_0 - \beta_i \approx \frac{i(i+2)\pi}{3L_\pi} \qquad (2.49)$$

The phase of i^{th} mode with respect to mode 0 (fundamental mode) at the end of MMI section of length, L is given by,

$$\Phi_i = (\beta_0 - \beta_i)L \approx \frac{i(i+2)\pi L}{3L_\pi} \qquad (2.50)$$

So the composite mode field profile in simplified form at a distance z=L, is written as

$$H(y,z) = \sum_{i=0}^{m-1} b_i H_i(y) \exp[j \frac{i(i+2)\pi L}{3L_\pi}] \qquad (2.51)$$

where b_i =mode field excitation coefficient which can be estimated from sinusoidal mode analysis [36].

2. 4. 2. Power transferred to the output waveguides

At the end of the MMI section, optical power is either transferred to the output waveguide or lost out at the end of multimode waveguide. Again the mode field at the access waveguide of same width, w is assumed to be mode, 0. Each mode of the MMI coupler contributes to the mode 0 at the output access waveguide. The mode field of the output waveguide is the sum of the contribution of all the modes guided in MMI section. So, the mode field at M^{th} waveguide can be written as

$$H_M(y,L)=\sum_{i=0}^{M-1} c_{M,i} H_i(y)\exp[j\frac{i(i+2)\pi L}{3L_\pi}] \tag{2.52}$$

where $c_{M,i}$ =measure of field contribution of i^{th} mode to M^{th} output waveguide. The $c_{M,i}$ is evaluated from simple sinusoidal mode analysis [36].

In MMI coupler, there are two types of interference–general interference and restricted interference. In case of general interference, the self imaging mechanism is independent of modal excitation and the single image is formed at a distance

$$L = p(3L_\pi) \tag{2.53}$$

where p=even for direct image and p=odd for mirror image. The multiple images are formed at

$$L=\frac{p}{2}(3L_\pi) \tag{2.54}$$

where, p = 1, 3, 5...........

In case of restricted interference, there is a restriction of excitation of some selected modes. There are two types of restricted interference– paired and symmetric. In case of paired interference [37],

$$b_i = 0, \quad \text{for } i=2, 5, 8....... \tag{2.55}$$

and N fold images are formed at a distance, $L=\frac{p}{N}(L_\pi)$ where $p\geq 0$ and $N\geq 1$ are integers having no common divisor. In case of symmetric interference,

$$b_i = 0, \quad \text{for } i=1, 3, 5....... \tag{2.56}$$

and N fold images are formed at a distance, $L = \frac{p}{N}(3L_{\pi}/4)$ where p≥0 and N≥1 are integers having no common divisor. The N images are formed with equal spacing of w_{mmi}/N. The N-way splitter can be realized in this principle [36]. The transition from DC structure to MMI structure with Ridge structure by reducing etches depth in between two coupling waveguides of DC are reported by Darmawan et al. [15].

2.4.3 MMI couplers demonstrated by previous authors

Although, Table-2.1 mentions MMI and TMI couplers as demonstrated by different authors, for more details we have used Table-2.3 in which waveguide parameters and Δβ of these couplers are also mentioned. In Table-2.3, we have considered only Ti:$LiNbO_3$, InP/InGaAsP and SiO_2/SiON materials because very limited literature for TMI and MMI couplers using SiO_2/SiO_2-GeO_2 and polymeric materials are available. Moreover, large index contrast waveguides can be made using InP/InGaAsP and SiO_2/SiON waveguide materials for compactness of these components. For comparison, we have included Ti:$LiNbO_3$ material in the table. Leuhold et al. [38] has reported MMI coupler of Δn~13% and w_{mmi} of 11.3 μm (w_{mmi}=width of MMI coupler) using InP/GaAsInP waveguide for tunable power splitter respectively. Levy et al. [39] has demonstrated 2x2 MMI coupler using same material with Δn~13 % and w_{mmi} of 9.3 μm for 3dB power splitting. M. Yagi et al. [16] has reported 3x3 MMI coupler of beat length L_{π}~432 μm using InP/GaAsInP with Δn~16.7 % for versatile switching with partial index modulation. Yong Ma *et al.* [14] has demonstrated MMI coupler with coupling length~20.5 μm and Δn~13 % using InP/GaAsInP waveguide for 3 dB coupler. Darmawan et al.[15] has reported MMI coupler of lower L_{π} ~35 μm using same material with Δn~16.7 % for mode filtering. M. Rajaranjan *et al.*[6] has reported MMI coupler of w_{mmi}~18 μm and beat length L_{π}~467 μm using SiON/SiO_2 technology with Δn~5.42 %. Janz *et. al.* [7] and Paiam *et al.*[4], have reported MMI coupler of same material with Δn~10 % and different w_{mmi} values. MMI coupler using same material with $\Delta n \sim 10$ % reported by Janz *et al.* [7] has lower L_π than that with same Δn and higher w_{mmi} reported by Paiam *et al.* [4] and former is bent waveguide device. Ridder *et al.* [3] has reported MMI coupler of $L_\pi \sim 1881$ μm using $SiON/SiO_2$ waveguide with $\Delta n \sim 1.92$ % and higher w_{mmi}. From the studies of the above authors, it is seen that for higher index contrast and lower w_{mmi}, the beat length is reduced.

Table-2.3: Different TMI/MMI based devices with device length

w_{mmi} = width of Mulitmode region, $\Delta\beta$=difference between propagation constant, $L_\pi = \pi/\Delta\beta$, L_c= coupling length, λ= wavelength. P=number of modes

Materials & available range of Δn	Author's name	Waveguide parameters (h=0)			λ (μm)	Δβ $(\mu m)^{-1}$	L_π (μm)	L_c	Devices (type)
		Δn $=n_1-n_2$	w_{mmi} (μm)/P	D/D/w/T (μm)					
Ti: $LiNbO_3$ (index range ~2.15-2.21)	A. Neyer [20] (Embedded structure) (Fig-3.5)	0.6%	2.7 P=2	w=1.35 T=1.35	0.58	0.0226	~ 139	43 L_π ~6mm	Wavelength multiplexer (TMI)*
	M. Papucahon et al. [19] (Embedded structure)	1%	4 P=2	w =2 T=2	0.514	0.0232	~135	37L_π ~5mm	Optical Bifurcation (TMI)

Materials & available range of Δn	Author's name	Waveguide parameters (h=0)			λ (μm)	Δβ $(\mu m)^{-1}$	L_π (μm)	L_c	Devices (type)
		Δn $=n_1-n_2$	w_{mmi} (μm)/P	D/D/w/T (μm)					
InP/GaAsInP (index range ~3.17- 3.5)	D. S. Levy et al. [39] (Rib structure) (Fig-3.5)	13%	9.3	W = 2 d =1 D=0.5	1.55	0.01136	277	L_π /2 ~ 138 μ	3 dB coupler (MMI)**
	M. Yegi et al.[16] (Ridge structure) (Fig-3.5)	13%	12	w=1 d=1 D=0.53	1.55	0.00727	~432	3L_π ~ 1296 μ	Switch (MMI)
	Darmawan et al. [15] (Ridge structure) (Fig-3.5)	16.7%	3.5 P=3	D=1 D=0.5 w=1.5	1.55	0.089	~35	3L_π ~ 105μm	Power splitter (MMI)
	Leuthold et al. [37] (Buried hetero structure)	15%	11.3	w=1.3 T=0.26	1.55	0.00787	~400	L_π /2 ~ 200μm	50:50 splitter (MMI)
	Yong Ma et al. [14] (Embedded structure) (Fig-3.5)	15%	3.2	W =0.4 T=0.65	1.55	0.0768	~41	L_π/ 2 ~ 20.5μ	3 dB coupler (MMI)

Materials & available range of Δn	Author's name	Waveguide parameters (h=0)			λ (μm)	$\Delta\beta$ $(\mu m)^{-1}$	L_π (μm)	L_c (μm)	Devices (type)
		Δn $=n_1-n_2$	w_{mmi} (μm)/P	D/D/w/T (μm)					
SiO_2/SiON Technology (index range ~1.45-1.98)	M. Rajaranjan et al. [6] (Rib structure) (Fig-3.5)	5.42%	18 P~20	w =3 d=2 D=1	1.55	0.00655	~479	~479	(MMI)
	Janz et al. [7] (Embedded structure) (Fig-3.5)	10.3%	6	W=3 d=3	1.55	0.0785	~40 (eqn 3.55b) ~ 63 (eqn 3.44)	~145	Demultiplex (TMI)
	Ridder et al. [3] (Embedded structure)	1.92%	35	W=3 T=2.5	1.55	0.00167	1881	940	3 dB coupler (MMI)
	Paiam et al. (Rib)[4] (Fig-3.5)	10.1%	6.5	W=2.8 d=0.35 D=1.2	1.55	0.04237	74.1	667	Wavelength Demultiplex (MMI)
	Tzong et al. (Embedded structure) [5] (Fig-3.5)	10%	1 P=2	W=0.5 w_g=1.1 T=0.5	1.538 & 1.578	....	....	75.4	WDM (TMI based on tooth-shaped grating))

2.5. TMI coupler

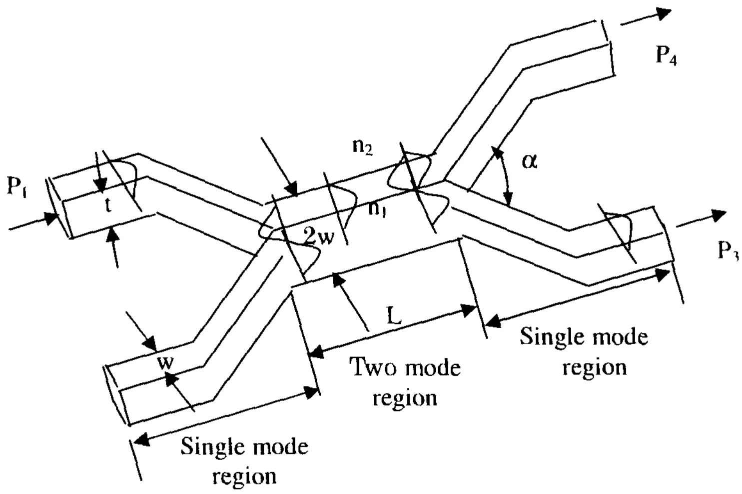

Fig-2.7: Schematic diagram of a TMI coupler of coupling length L

Fig-2.7 shows the schematic diagram of TMI coupler consisting of two single mode entrances of core width w and thickness, t and exit waveguides of same size and TMI core of width 2w and length L. The operating principle of the TMI coupler is based on two-mode interference (TMI) in coupling region. When the light is launched into one of the input waveguides, only fundamental and first order mode with propagation constants β_{00} and β_{01}, respectively, are excited in the coupling region [19]-[20]. These two modes interfere with each other while propagating along the direction of propagation. Depending on the relative phase differences $\Delta\phi$ at the end of the coupling region, the light powers are coupled into the two output waveguides.

2.5.1. Power transferred to output waveguides

Like DC, in case of TMI directional coupler, we have to use the same coupled mode equations for the calculation of power transfer to the out put waveguides. So, the powers coupled into two single mode identical waveguides of TMI coupler are approximately given by [20],

$$\frac{P_3}{P_1} = \sin^2(\Delta\phi/2) \tag{2.57a}$$

$$\frac{P_4}{P_1} = \cos^2(\Delta\phi/2) \tag{2.57b}$$

where, $\Delta\phi = \Delta\beta.L$, L= length of multimode region and $\Delta\beta = \beta_{00} - \beta_{01}$ (2.58)

The coupling length for maximum power transfer from waveguide-1 to waveguide-2 is written as,

$$L_{co}=\pi n/\Delta\beta = nL_{\pi} \tag{2.59a}$$

where n is odd integer and $L_{\pi}=\pi/\Delta\beta$ (2.59b)

2.5.2. Numerical calculation

We have taken the following waveguide parameters (which are taken by Neyer et al. [20]) for verification of our numerical calculation, $n_1=n_3=2.15$, $n_2=2.156$, 2w= width of coupling region=2.7 μm, Δn =0.6 % and λ =0.58 μm.

The normalized frequency, V_I obtained from the equation (3.34b) is $V_I= \frac{2\pi(w)}{\lambda}\sqrt{n_2^2 - n_1^2}$ =2.35. Knowing V_I, we have calculated propagation constant of fundamental mode β_{00} and propagation constant of first order mode β_{01} are calculated using effective index method [18] as follows

<u>β_{00} calculation of TE polarization:</u>

For the fundamental mode, mode indices p=0 and q=0, we have calculated b_I from the following dispersion equation [18],

$$V_I\sqrt{1-b_I} = (p+1)\pi - 2\tan^{-1}\sqrt{\frac{1-b_I}{b_I}} \tag{2.60}$$

where a_I=0 because symmetric waveguide.

$b_I \sim 0.525$

Putting b_I in the following equation N_I is calculated as follows

$$N_I = \sqrt{n_1^2 + b_I\left(n_2^2 - n_1^2\right)} \tag{2.61}$$

$$N_I = 2.15315$$

Therefore $V_{II} = \dfrac{2\pi(2w)}{\lambda}\sqrt{N_I^2 - n_1^2} = 3.404$ (2.62)

We have calculated b_{II} from the following dispersion equation [18]

$$V_{II}\sqrt{1-b_{II}} = (q+1)\pi - 2\tan^{-1}\sqrt{\frac{1-b_{II}}{b_{II}}} \tag{2.63}$$

$b_{II} = 0.6778$

Putting b_{II} in the following equation, we have calculated effective index for fundamental mode, N_{eff0} as follows,

$$N_{eff0} = \sqrt{n_1^2 + b_{II}\left(N_I^2 - n_1^2\right)} \tag{2.64}$$

$$N_{eff0} = 2.15226$$

So, $\beta_{00} = \dfrac{2\pi}{\lambda} N_{eff0} = 23.3024$

<u>β_{01} calculation of TE polarization:</u>

For the first order mode, mode indices p=0 and q=1, we have calculated b_I using the equation (2.60)

$b_I = 0.525$

Putting b_I in the equation (2.53), N_I is calculated as follows

$N_I = 2.15315$

Therefore, V_{II}=3.405 [using the equation (2.62)]

We have calculated b_{II} for the first order mode using the equation (2.63)

$b_{II} = 0.0145$

Putting b_{II} in the following equation, we have calculated effective index for fundamental mode, N_{eff1} as follows,

$$N_{eff1} = \sqrt{n_1^2 + b_{II}\left(N_I^2 - n_1^2\right)} \tag{2.65}$$

$$N_{eff1} = 2.15004587 \qquad \text{So,} \quad \beta_{01} = \frac{2\pi}{\lambda} N_{eff1} = 23.2798$$

The propagation constant difference, $\Delta\beta$ is calculated as follows

$$\Delta\beta \,|_{0.58} = \beta_{00} - \beta_{01} = 0.0226$$

Therefore, L_π is calculated as follows,

$$L_\pi = \frac{\pi}{\Delta\beta} \sim 139\mu m$$

In similar way, we have calculated propagation constant of the fundamental and first order mode for wavelength 0.59μm as follows

$$\beta_{00} \sim 22.906879 \text{ and } \beta_{01} \sim 22.884804$$

The $\Delta\beta$ of the wavelength 0.59 μm is given by

$$\Delta\beta \,|_{0.59} = \beta_{00} - \beta_{01} = 0.022075$$

So, the required coupling length for separating two wavelengths 0.58 μm and 0.59 μm is given by [20]

$$L_c = \frac{\pi}{\Delta\beta|_{0.58} - \Delta\beta|_{0.59}} = \frac{3.14}{0.000515} \sim 6mm$$

Knowing $\Delta\beta$ using above methods, we have calculated coupled power (P_4/P_1) for the wavelength varying for 0.57 μm to 0.59 μm using the equation (2.57a). Fig-2.8 shows variation of P_4/P_1 with wavelength for coupling length of ~6 mm, n_1=n_3 =2.15, n_2 =2.156 and 2w=2.7 μm respectively. The solid line represents theoretical curve. The black dots represent the experimental points of cross state power demonstrated by A. Neyer [20], showing good agreement with the theoretical results.

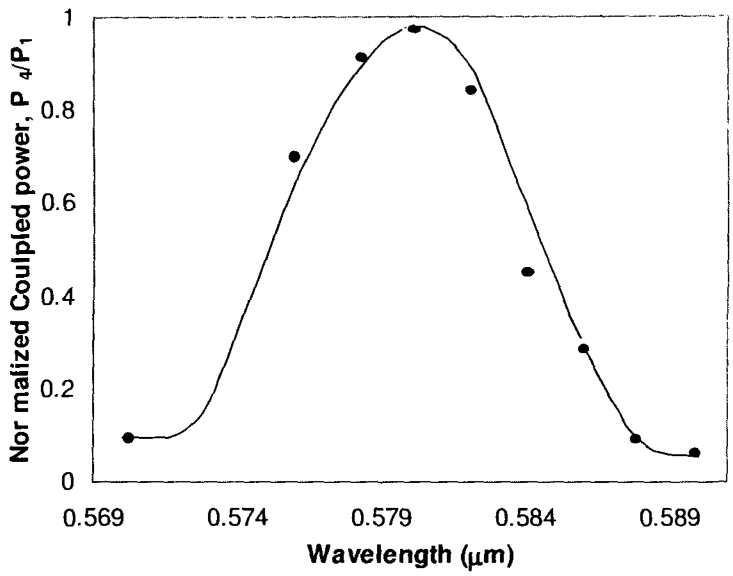

Fig-2.8: Variation of P_4/P_1 with wavelength for coupling length of ~6 mm, $n_1=n_3=2.15$, $n_2=2.156$ and $2w = 2.7$ μm respectively.

Beat length calculation of TMI coupler

Janz et al. reported TMI coupler with n_1=1.459, n_2=1.562, 2w=width of coupling region=6 μm, Δn=10.3 % and λ =1.55 μm. Using the equations (2.60)-(2.64) (applying effective index method), we get β_{01} and β_{00} of TE polarization as 6.2355 and 6.314 $(\mu m)^{-1}$ respectively and corresponding Δβ=0.0785 $(\mu m)^{-1}$ and the beat length is calculated as

$$L_\pi = \pi/\Delta\beta = 3.14/\ 0.0785 \approx 40\ \mu m$$

However, beat length is calculated by using the equation (2.48) as follows:

$$w_e = 6 + \frac{1.55}{3.14}\left(1.549^2 - 1.459^2\right)^{-1/2} \approx 6 + 0.94 = 6.94\,\mu m$$

$$L_\pi = \frac{4n_r w_e^2}{3\lambda} = \frac{4\times1.549\times6.9\times6.9}{3\times1.55} = 63\,\mu m$$

The difference of L_π values is due to assuming beat length of TMI coupler as beat length of MMI coupler.

TM polarization (using effective index method):

For n_1=1.459, n_2=1.562, 2w=width of coupling region=6 μm, Δn=10.3 % and wavelength, λ=1.55 μm.

V_I=6.78

For fundamental mode, p=0 and q=0

Dispersion equation for TM polarization is given by

$$V_I\left(\sqrt{q_s}\right)\left(n_2/n_1\right)\sqrt{1-b_M} = (p+1)\pi - 2\tan^{-1}\sqrt{\frac{1-b_M}{b_M}} \tag{2.65a}$$

where a_I=0 because symmetric waveguide.

$$b_M = \left(\frac{N_M^2 - n_1^2}{n_2^2 - n_1^2}\right)\left(\frac{n_2}{n_1 q_s}\right)^2$$

$$q_s = \left(\frac{N_M^2}{n_2^2}\right) + \left(\frac{N_M^2}{n_1^2}\right) - 1$$

From the above dispersion equation b_M is calculated as ~ 0.88.

Putting b_M in the following equation N_I is calculated as follows

$$N_M = \sqrt{n_1^2 + b_M\left(n_2^2 - n_1^2\right)} \tag{2.65b}$$

$$N_M \approx 1.55$$

$$\text{Therefore, } V_{II} = \frac{2\pi(6)}{\lambda}\sqrt{N_M^2 - n_1^2} = 12.72 \tag{2.65c}$$

We have calculated b_{MI} from the following dispersion equation [18]

$$V_{II}\left(\sqrt{q_s}\right)\left(n_2/n_1\right)\sqrt{1-b_{MI}} = (q+1)\pi - 2\tan^{-1}\sqrt{\frac{1-b_{MI}}{b_{MI}}} \tag{2.65d}$$

b_{MI} = 1.0225

Putting B_{II} in the following equation, we have calculated effective index for fundamental mode, N_{eff0} as follows,

$$N_{eff0} = \sqrt{n_1^2 + b_{MI}\left(N_M^2 - n_1^2\right)} \tag{2.65e}$$

$$N_{eff\,0} = 1.5494$$

So, $$\beta_{00} = \frac{2\pi}{\lambda} N_{eff\,0} = 6.2775\,(\mu m)^{-1}$$

Similarly we can get $N_{eff\,1} = 1.5335$ for first order mode (β_{01}) of TM polarization by taking p=0, q=1 and β_{01} for TM polarization as 6.21342 $(\mu m)^{-1}$ and corresponding $\Delta\beta$=0.06408 $(\mu m)^{-1}$. The beat length is calculated as

$$L_\pi = \pi/\Delta\beta = 3.14/\,0.06408 \approx 49\ \mu m$$

The difference between beat lengths of TE and TM for TMI coupler with Δn=10.3% is 9 μm.

2.5.3. TMI couplers demonstrated by different authors

In the table-2.3, we have mentioned TMI couplers (coupling length<<1 mm) reported by previous authors [7], [19]-[20]. A. Nayer et al. [20] has reported TMI coupler with coupling length ~6 mm, Δn~0.6% and w_{mmi}~2.7 μm using Ti:$LiNbO_3$ technology for wavelength multiplexer/demultiplexer device with wavelength range 0.57 μm-0.59 μm. M. Papuchon et al. [19] has implemented TMI coupler of coupling length ~5 mm, Δn~0.6 % and w_{mmi}~2.7 μm using Ti:$LiNbO_3$ technology for optical bifurcation device with operating wavelength~ 0.5145 μm. Veerman et al.[40] has demonstrated passive TMI coupler using silica waveguide with Δn=0.23 for 3dB coupling with 0.5 dB loss at wavelength 1550 nm. Tzong et. al [5] has reported ultra short TMI coupler based on toothed grating structure using SiO_2/SiON material with Δn~10 %.

2.6 Grating Assisted Geometry

The schematic diagram of the grating assisted (GA) structure [72] is shown in Fig.-2.9. A periodic perturbation, having period Λ and length L and arbitrary index profile, is placed on the slab waveguide, being the depth and the length direction.

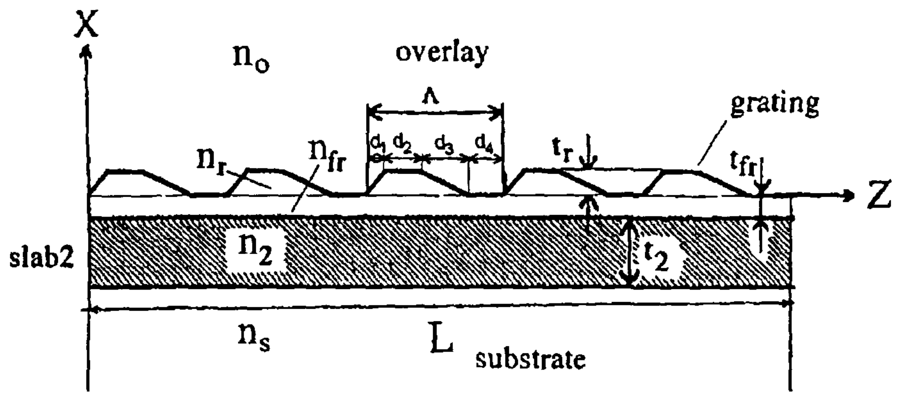

Fig-2.9: Grating assisted geometry

The refractive index parameters of GA structure are overlay n_o, grating n_r, under layer n_{fr}, slab n_2, substrate n_s refraction indices, whereas the profile thickness of GA are upper slab t_1, gap t_g, grating t_r=t, under layer t_{fr}, lower slab t_2 and thicknesses d_1, d_2, d_3, d_4. Each layer of the structure is assumed isotropic, homogeneous, lossless and two dimensional. In the figure, the $d_1=d_3=0$ and $d_2 \neq d_4 \neq 0$ corresponds to rectangular GA structure, *the $d_1=d_3=0$ and $d_2=d_4 \neq 0$ corresponds to square GA structure and the* $d_1 \neq 0$, $d_3=0$, $d_2 = d_4 = 0$ corresponds to saw tooth shaped GA structure and the $d_1=d_3 \neq 0$ and $d_2=d_4=0$ corresponds to triangular GA structure.

2.6.1 Analysis of Grating Assisted Directional Coupler (GADC)

Fig-2.10 shows grating assisted directional coupler [72] consisting of two slab waveguide in which the grating assisted structure is attached with lower waveguide. The refractive index parameters of GA structure are overlay n_o, upper slab n_1, gap n_g, grating n_r, under layer n_{fr}, lower slab n_2, substrate n_s refraction indices, whereas the profile thickness of GA are upper slab t_1, gap t_g, grating t_r=t, under layer t_{fr}, lower slab t_2 and thicknesses d_1, d_2, d_3, d_4. Each layer of the structure is assumed isotropic, homogeneous, lossless and two dimensional.

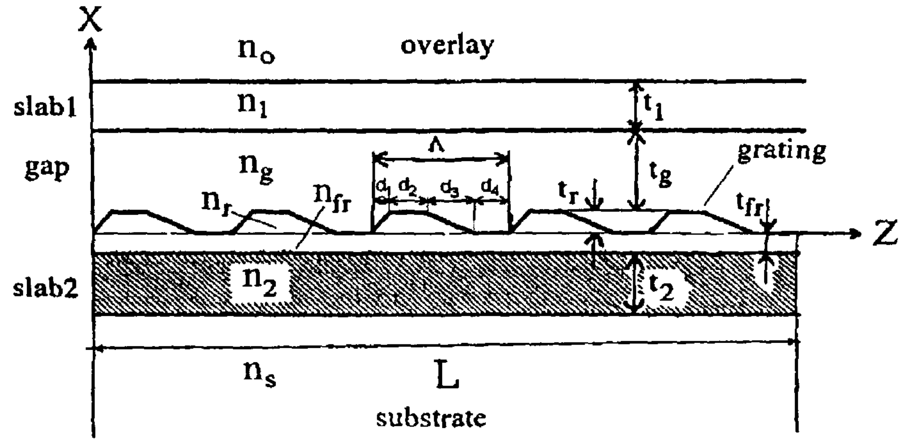

Fig-2.10: Schematic diagram of the GADC structure with arbitrary profile. GADC parameters: overlay n_o, upper slab n_1, gap n_g, grating n_r, under layer n_{fr}, lower slab n_2, substrate n_s refraction indices, and upper slab t_1, gap t_g, grating t_r=t, under layer t_{fr}, lower slab t_2, thicknesses d_1, d_2, d_3, d_4 are the profile parameters, Λ the grating period and L is the grating length.

The scalar wave equation of the GADC is given by [72],

$$d^2F_i(x,z)/dx^2 + d^2F_i(x,z)/dz^2 + k_0^2\varepsilon_i(x,z)F_i(x,z) = 0 \tag{2.66}$$

where F_i is the appropriate electric or magnetic field y-component (i.e., $F_i = E_y$ for transverse electric (TE) and $F_i = H_y$ for transverse magnetic (TM) polarization), k0 is the free space wave number, i designates the generic homogeneous layer, i= 0,1,g,r,fr,3,s, and $\varepsilon_i(x,z)$ is the relevant permittivity. The permittivity function is periodical along only in the grating region, i.e., $\varepsilon_r(x, z)$ and it can be written according to the Fourier series expansion as

$$\varepsilon_r(x,z) = \sum_n \varepsilon_n(x)\exp(j2\pi nz/\Lambda) \tag{2.67}$$

where n denotes the n-th space harmonic, and

$$\varepsilon_n(x) = (1/\Lambda)\int_{-\Lambda/2}^{\Lambda/2} \varepsilon(x,z)\exp(-j2\pi nz/\Lambda)dz \qquad ; 0 \le x \le t_r \tag{2.68}$$

is the nth series coefficient. Thus, the solution of (2.66) in the grating region, according to the Floquet space harmonics expansion [73], is

$$F_r(x,z) = \sum_n f_n(x)\exp(jk_{zn}z) \qquad 0 \le x \le t_r \tag{2.69}$$

where $f_n(x)$ is the r-th space harmonic amplitude function and k_{zn} is the component along of the relevant propagation vector. It is well known that the nth component is related to the fundamental harmonic (n=0) by the Floquet phase relationship [73], i.e. $k_{zn}=k_{z0}+2\pi n/\Lambda$, where k_{z0} refers to the zeroth-order mode of the perturbed structure. Therefore, the field in the grating region assumes the form of a superposition of space harmonics. In order to completely describe the electromagnetic field in the GADC structure, we denote *as* the z–component of the e. m. field (G_r-H_z for TE and G_r-E_z for TM polarization, respectively). Similarly to (2.69), it results in the grating region

$$G_r(x,z) = \sum_n g_n(x)\exp(jk_{zn}z) \qquad 0 \le x \le t_r \tag{2.70}$$

Where $g_n(x)$ is the relevant nth harmonic amplitude function. Moreover, the relationships between the $f_n(x)$ and $g_n(x)$ field component amplitudes have been determined by using the Maxwell equations

$$\begin{aligned} df_n(x)/dx &= \sum_l q_{nl}g_l(x) \\ dg_n(x)/dx &= \sum_n p_{nm}f_m(x) \end{aligned} \tag{2.70a}$$

where q_{nl} and p_{nm} are elements of two squared matrices, each one depending on the permittivity coefficients. In case of TE polarization, we have

$$\begin{aligned} g_{nl}(x) &= -j\omega\mu_0\delta_{nl} \\ p_{nm}(x) &= j\omega\varepsilon_0\left[(k_{zn}/k_0)^2\delta_{nm} - \varepsilon_{m-n}(x)\right] \end{aligned} \tag{2.70b}$$

being δ_{nm} , δ_{nl} Kronecker's delta functions, and ε_{m-n} (x) the appropriate coefficient of Floquet series expansion. The solution of (2.70), together with the continuity conditions applied to each longitudinal interface between different layers, allows finding the propagation constants and the field distributions of all the field space harmonics retained in the analysis. In particular, the continuity conditions can be summarized for TE-polarized mode [72] as

$$df_n(0)/dx + j\left[1 - r_n^{(fr)}\right]/\left[1 + r_n^{(fr)}\right]k_{xn}^{fr} f_n(0) = 0 \tag{2.71}$$

$$df_n(t_r)/dx - jk_{xn}^{(g)} f_n(t_r)\left[1 - r_n^{(g)} \exp\left(j2k_{xn}^{(g)} t_r\right)\right]/\left[1 + r_n^{(g)} \exp\left(j2k_{xn}^{(g)} t_r\right)\right] = 0 \tag{2.72}$$

where x= t_r=t is the grating thickness, $k_{xn}^{(fr)}$, $k_{xn}^{(g)}$ are the nth harmonic x-components of the wave vector in the layers f_r and g, respectively, and the coefficients $r_n^{(fr)}$, depend on the propagation constant components in the same layers. It must be noted that the condition (2.70b) includes a dependence of the solutions in the grating region on the equivalent permittivity

$$\varepsilon_{eq}(x) = (k_{zn}/k_0)^2 \partial_{nm} - \varepsilon_{m-n}(x)$$

which is a function of both the space harmonic order and the grating profile. This has important consequences, as it will be better clarified in the following. From the equation system (2.71) it is clear that an arbitrary but finite number of harmonics, say 2N+1 , has to be taken for numerical integration, having the complex wave-number of the GADC composite guided mode as unknown variable, where $\alpha>0$ is the mode amplitude attenuation coefficient (leakage factor). In other words, the LMP approach explains the radiating effect produced by the grating in terms of leaky modes, having field space harmonics which radiate power in the semi-infinite regions. In order to numerically integrate the system (2.70a), a four order Runge–Kutta algorithm has been used, which gives accurate results also for large grating depths when a large enough number of iterations is used (up to 50 iterations have been used for 0.15 m). Moreover, the complex eigenvalue k_{zo} has been found by the Muller's method. After finding k_{zo}, the amplitude coefficients of each space harmonic and k_{zn}, $k_{xn}^{(i)}$, $f_n(0)$, $f_n(t_r)$have been determined. Details of numerical procedure can be found in [80]. Strong attention must be paid to the choice of the starting point, i.e., the approximated propagation constant, in order to avoid double roots. The problem is well described in [72].

Grating resonance condition

The GADC structure already presented by Marcuse [74] and considered by Sun *et al.* [75] has been largely investigated. It consists in a InP–In_x Ga_{1-x} AsP–InP–In_xGa_{1-x}AsP–In_yGa_{1-y}AsP–InP multilayered structure, having parameters n_o=3.18, n_1=3.282, n_g=3.18, n_{fr}=3.282, n_s=3.18, t_1=0.2 μm, and t_g+t_r+t_{fr}=2 μm. The mono modal condition $2t_2\sqrt{n_2^2-3.18^2}+0.8119=\lambda_0$ allows obtaining as a function of, being the free-space optical wavelength. The choice to have only two ideal composite modes is similar to the TMM approach, in which only two local normal modes are considered at each grating section [12]. As a first step, we have calculated the composite modes of the same structure as above, but unperturbed (t_g=1.5 μm, t_r=0, t_{fr}=0.5 μm, n_2=3.45, t_2=0.257 μm) at λ_0=1.5 μm. Results give $n_{eff}^A\sim 3.2974545$ and $n_{eff}^B\sim 3.1906012$, being mode A (even) mainly confined in the lower slab and B (odd) in the upper one.

Then, a similar structure with a grating depth of t_r=t=0.1 μm (t_g=1.45 μm, t_{fr}=0.45 μm) has been investigated. It is well known that the grating period, needed to have a high-efficiency power transfer between the ideal composite modes of the structure, depends on the effective index difference between the two guided modes exchanging power along z. The conventional CMT method determines the grating period in an approximated form

$$\Lambda=\lambda_0/\left[n_{eff}^{(even)}-n_{eff}^{odd}\right]=14.038 \qquad (2.73)$$

The TMM approach [72] gives in this case (strongly asymmetric) a much more approximated value of the grating period

$$\Lambda=\Lambda^-+\Lambda^+=\lambda o/\left[n_{eff}^{(1,inf)}-n_{eff}^{(2,inf)}\right]+\lambda o/\left[n_{eff}^{(1,sup\,p)}-n_{eff}^{(2,sup)}\right]=40.258\ \mu m \qquad (2.74)$$

being "inf" and "sup" the local sections of the grating period. In the LMP approach, the optimal grating period is found at the resonance condition [75], i.e., when the deviation $\delta = \beta_0^A - \beta_0^B - K$ from the exact synchronization condition between the modes and B, i.e., $\delta = \beta_0^A - \beta_0^B - K$ is minimized, being the grating wave vector and β_0^A, β_0^B, the real parts of the fundamental (zeroth-order) harmonic propagation constants of mode and , respectively. Since $\beta_{-1}^A = \beta_0^A - K$, where β_{-1}^A is the real part of -1 harmonic propagation constant of mode A, the resonance condition implies also that the electromagnetic field distribution of -1 harmonic of mode is more similar to that of 0 harmonic of mode or, in other words, the difference of their phase velocities is minimal. The resulting coupling length, allowing the maximum power transfer between the lower and upper slabs, is given by the well-known formulation

$$L_c = \frac{\pi}{\delta} \tag{2.75}$$

which is used in the CMT approach, too [72]. The presence of the grating in the GADC structure causes three fundamental effects. The first is that each guided mode generates infinite space harmonics (with n<-1 for mode A and n<0 for mode B), radiating power in the substrate and in the overlay. The second is that only two space harmonics ("fundamental") carry significant guided power in the upper and lower slabs (with n= -1 and n=0 for mode A and n=0, n=1 for mode B). The third effect implies that the electromagnetic fields of space harmonics having $\varepsilon_{eq}(x)>0$ are confined in the grating region (here in after "spurious" harmonics). This circumstance occurs for the harmonics having n>0 (mode A) or n>1 (mode B) for the structures considered in this paper. These confinements depends on the permittivity coefficients of the Fourier series expansion of the grating profile, which are contained in $\varepsilon_{eq}(x)$, and cause a distortion of electromagnetic field distribution of fundamental harmonics from "ideal" condition in absence of grating, i.e., δ=0. As a consequence, at the resonance the influence of spurious harmonics is minimal since their amplitudes, depending on the equivalent permittivity, are globally minimized.

The amplitudes of spurious harmonics have been calculated at the resonance and near the resonance for different profiles (D=saw tooth, S=sinusoidal, T=triangular, Q=squared, TR=trapezoidal) Table-2 4 summarizes these amplitudes for both modes A and B for saw tooth profile at 14 029 μm and 14 031 μm respectively; and also shows the percentage difference of the amplitudes of other profiles with respect to the saw tooth D, as calculated at 14 029 μm The alternating signs in some cases are due to the relevant coefficients of Fourier series expansion of grating profile

In case of sinusoidal profile, the amplitudes of the real part of field component of spurious harmonics for n=1 (mode A) and (mode B) are dominant (in absolute value) with respect to the other harmonics, and are at least two orders of magnitude lower than the amplitudes of fundamental harmonics In fact, when n=1 (mode A) and (mode B), the equivalent permittivity assumes a minimum value because the sinusoidal profile admits only one spatial frequency, i.e., $\varepsilon_0>0$, $\varepsilon_n=0$, $n\neq0$ Therefore, the guided spurious harmonics are weaker in the grating region for n=0 than n>0, giving stronger guiding, less coupling with the two slabs and much lower amplitudes with increasing n. In a similar way, the resonance condition (Λ=14 031 μm) for saw tooth profile arises when the spurious harmonics in the grating region have minimum amplitudes This can be seen in Table 2 4 by comparing the amplitudes for saw tooth profile calculated at 14 029 μm and 14 031 μm

Since the Fourier series expansion of saw tooth profile has its permittivity components in rigorously decreasing order, the space harmonic amplitudes are in decreasing order with increasing n , too (Table 2.4) This can be clearly seen from the amplitudes of space harmonics for mode A and mode B, as changed with respect to those of sawtooth profile (Table 2 4 [72]) Amplitudes larger than those occurring in saw tooth, sinusoidal, triangular or trapezoidal profile have been obtained Therefore, the resonance condition occurs with a larger deviation wave number

Table-2.4: Amplitudes of spurious harmonics for various profiles [72]

n	GADC with n_2 =3.45, t = 0.1 μm		Mode A			
	(S)	(T)	(D) (14.029 μm)	(TR)	(Q)	(D) (14.031 μm)
1	+29.3%	+4.18%	0.01746	-99.5%	-266%	0.01726
2	-120.7%	-79.4%	0.006837	-60.1%	-41.1%	0.006738
3	-97.5%	-67.6%	0.003792	-33.6%	-248.6%	0.003732
4	-102.2%	-86%	0.002444	-75.5%	-33%	0.002403
5	-99.8%	-80.2%	0.001716	-99.6%	-244.2%	0.001687
6	-99.9%	-89%	0.001275	-86.8%	-29.9%	0.001253
7	-99.9%	-85.5%	0.0009857	-68.6%	-242.3%	0.0009682
8	-99.9%	-90.8%	0.0007847	-83.8%	-28.4%	0.0007706
9	-99.9%	-88.3%	0.0006387	-99.7%	-242.1%	0.0006271
			Mode B			
	(S)	(T)	(D)	(TR)	(Q)	(D)
2	-230.6%	-197.2%	0.06504	+64.7%	+111.6%	0.06086
3	-77.1%	-74.8%	0.02357	-65.5%	-147.8%	0.02211
4	-102.8%	-134.2%	0.01270	-152.9%	+104.2%	0.01195
5	-99.6%	-83.3%	0.008103	-99.9%	-155%	0.007624
6	-100.2%	-121.2%	0.005654	-64.5%	+99.3%	0.005322
7	-99.9%	-87.2%	0.004182	-88.3%	-158.1%	0.003938
8	-100.1%	-115.7%	0.003224	-125%	+96.8%	0.003037
9	-100%	-89.3%	0.002566	-99.9%	-161.2%	0.002417

Fig.-2.11 shows the coupling length obtained for different grating profiles at (quasi-symmetric GADC) with groove depth ranging from 0.01 to 0.15 μm. The curves have been determined by evaluating the resonance condition versus the groove depth by using the sinusoidal profile. The symmetric profiles exhibit higher efficiency with respect to the asymmetric ones with increasing the groove depth, but the best condition (lowest coupling length) is obtained again with the optimized rectangular profile (42%),

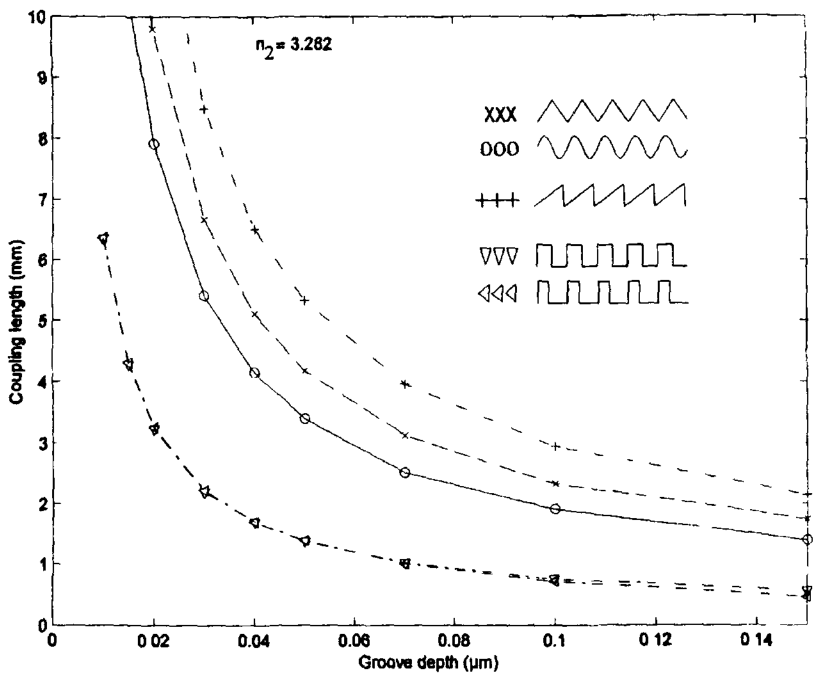

Fig.-2.11: Coupling length (mm) versus grating depth (μm) [72] for different index profiles, +++: sawtooth, XXX: symmetric triangular, 000: sinusoidal. GADC parameters: n_0=3.18, n_1=3.282, n_g=3.18, n_r=n_{fr}=3.282, n_s=3.18, t_1=0.2 μm, t_2=0.4238 μm, t_g=1.5-t_r /2 μm, t_{fr} = 0.5-t_r /2 μm, t ranging from 0.01 to 0.15 μm.

It is seen from the figure that the lower coupling length is obtained at rectangular grating geometry and the same of rectangular grating assisted structure is almost close to that of square grating assisted structure. This is due to having more number of reflections in rectangular or square grating assisted structure than other structures and multiple refection increases phase difference between excited modes in these structures. It is also seen that the coupling length slowly varied with groove depth at groove depth ~0.04 μm. This rectangular grating assisted structure is also called as tooth shaped grating assisted structure. Fig-2.12 shows the coupling efficiency obtained for rectangular, square and saw tooth grating assisted structures of GADC with groove depth ranging from 0.01 to 0.15 μm.

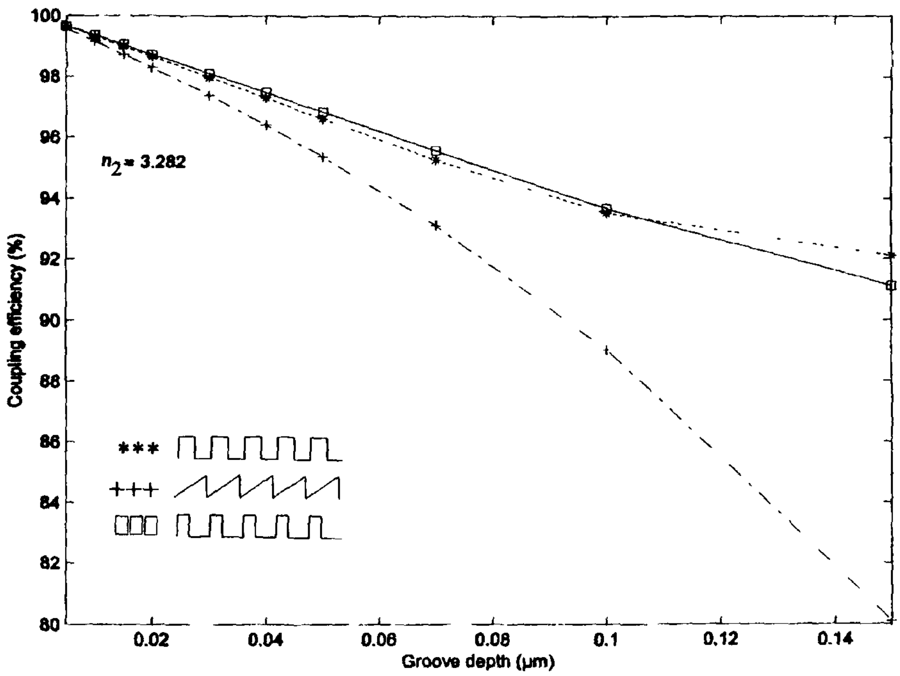

Fig-2.12: Coupling efficiency (%) versus grating depth (μm) for different index profiles, ***: squared (50%), +++: sawtooth, boxes: optimized rectangular (42%). GADC [72] parameters: n_0 = 3.18, n_1=3.282, n_g=3.18, n_r=n_{fr}=3.282, n_s=3.18, t_1=0.2 μm, t_2=0.4238 μm, t_g =1.5–t_r/2 μm, t_{fr}=0.5– t_r/2 μm, t_r ranging from 0.01 to 0.15 μm.

It is seen that the coupling efficiency for rectangular structure is almost close to that of the square structure but it is grater than that of saw tooth structure. So it is confirmed from the curve of coupling efficiency and coupling length that the rectangular or square grating assisted structure performs better than other structures. So we have chosen same tooth shaped grating assisted structure for DC, TMI coupler and MMI coupler, as studied in chapter-4 and 5 for compactness of photonic integrated device (PID).

2.6.2 Tooth shaped grating assisted TMI coupler

As discussed in section-2.6.2, tooth shaped grating assisted geometry has already been studied by previous authors [76]-[77] for compactness of two mode interference coupler. Fig-2.13 shows a 2x2 two-mode-interference multiplexer using a tooth-shaped grating structure.

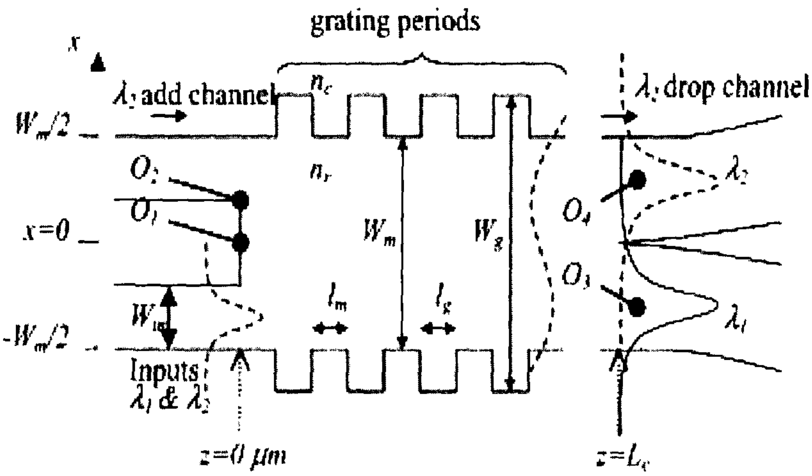

Fig-2.13: Schematic design of an ultra compact TMI wavelength division multiplexer using a tooth shaped grating structure [76]-[77].

The two-moded waveguide where TMI occurs had a width W_m, and a width of the grating W_g. The lengths of the alternating sections of the grating were l_m and l_g, n_c and n_r were the refractive indexes of the cladding and waveguides, respectively. Observation points O_1 and O_2 were located at (x=0, z=0) and (x=W_m/4, z=0), respectively, for detecting the mode-related reflection spectrum of the grating. Two observations points O_3 and O_4 were located at the lower and upper single-mode output waveguides, respectively, to detect the transmission spectra. The widths of the single-moded input and output waveguides were W_{in} and W_{out}.

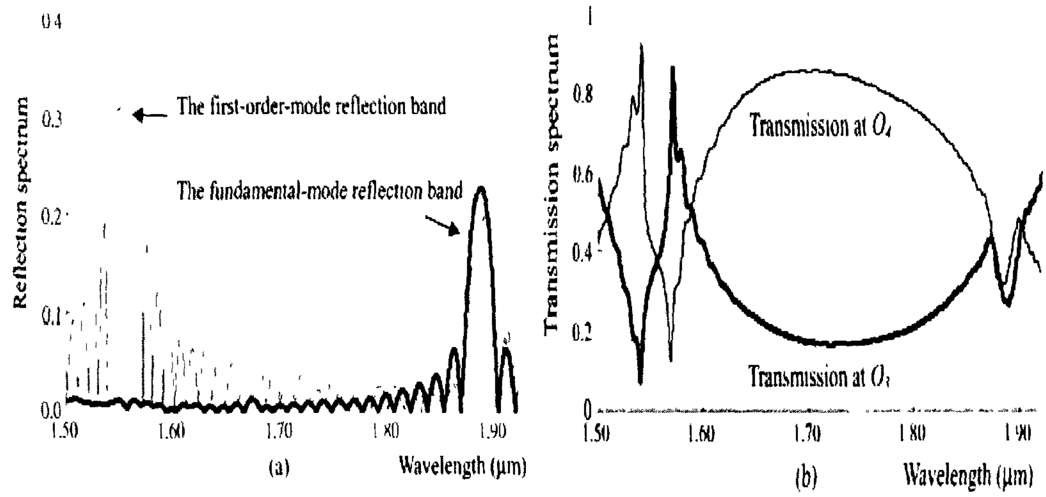

Fig- 2.14: Mode-dependent E-field spectra of the toothed-grating TMI multiplexer. (a) The bold line was detected at the observation point O_1(x=0, z=0) and the thin one at O_2(x=W_m/4, z=0). (b) The bold line was detected at O_3 and the thin one at O_4.

Two symmetric S-bend output waveguides of radius R located at the end of the TMI waveguide are not shown in the figure. It was assumed that the transverse guided dimension (y-axis) was much smaller than the lateral and longitudinal ones (x and z) such that all the EM guided modes discussed here were uniformly single-mode in the y dimension. Thus, TMI wavelength (de)multiplexing could be reasonably analyzed and discussed using two-dimensional (2-D) FDTD simulation. The structural factors were designed as: W_m=1 μm, W_g=1.1 μm, W_{in}=0.25 μm, n_c=1, n_r=1.5, l_m=0.347 μm and l_g=0.334 μm. The number of grating periods was 100. The mode-dependent forbidden bands contributed by the toothed grating were obtained using an ultra short TE-mode pulsed excitation of FWHM 1×10^{-15} second and central wavelength 1.55 μm, followed by taking Fourier transform of the temporal responses. Fig.-2.14(a) shows two reflection spectra that were detected at the observation points O_1 and O_2 and are represented by a bold line and a thin one, respectively. Because of the location of O_1, the bold line only corresponds to the reflection spectrum of the fundamental (even) mode, indicating that the reflection band over 1.5–1.6 m was mainly for the first-order guided mode. The central wavelength of the first-order-mode reflection band was arranged to be [76] at 1550 nm by setting the values of l_m and l_g to be $l_m = \frac{\lambda_0}{4 \times n_{j,m}}$ and $l_g = \frac{\lambda_0}{4 \times n_{j,g}}$, where λ_g = 1550 nm, $n_{j,m}$ and $n_{j,g}$ were the effective indexes of the j^{th} order guided modes of λ_0 (here j^{th} is first) in the guiding widths W_m and W_g , respectively. The central wavelength of the band gap λ_0 is determined by $\lambda_0 = 2(l_m \times n_{j,m} + l_g \times n_{j,g})$. If the sum of l_m and l_g is a constant, which should be achievable in manufacture, the shift of the central wavelength $\delta\lambda_0$ caused by the conjugate variations of Δl_m and Δl_g can be obtained by [76],

$$\frac{\delta\lambda_0}{\lambda_0} \sim \frac{n_{j,g} - n_{j,m}}{n_{j,g} + n_{j,m}} \times \frac{\Delta l_m}{l_m} \tag{2.76}$$

The wavelengths of 1538 and 1572 nm, which were the first zero-reflection points near the reflection band, were chosen for the WDM demonstration, because of the relatively low reflection losses and high dispersion. Notice that wavelength demultiplexing of 1538 nm and 1572 nm could also be implemented using the fundamental-mode reflection band blue-shifted from 1.88 to 1.55 μm by replacing effective indexes $n_{0,m}$ and $n_{0,g}$. Nevertheless, using the first-order mode reflection band for wavelength demultiplexing always contributed stronger dispersion effects, a shorter coupler length of wavelength multiplexing and narrower add–drop channel widths than using the fundamental mode one. The reason was that the effective index of the first-order guided mode was more sensitive to the variation of guiding width. That is to say, with the fixed W_m and W_g, ($n_{1,g}$- $n_{1,m}$) was larger than ($n_{0,g}$-$n_{0,m}$). Thus, the first-order mode reflection band had a wider bandwidth and stronger dispersion effect than the fundamental mode. In addition, the reflection bandwidths were related to the difference between and which could be slightly adjusted in a range where only two modes could be guided. The second or higher order modes excited in a large would contribute higher scattering losses and degradation of channel contrasts. Fig.-2.14(b) shows two transmission spectra of electrical fields that were detected at the observation points and are represented by a bold line and a thin one, respectively. Clearly the wavelengths near the first-order reflection band were separated by the grating dispersion. The band gap dispersion decreases quickly for the wavelengths away from the band gap, giving rise to narrow add-drop channel widths. The corresponding channel contrasts could be evaluated by squaring the E-field transmission values. For contrast values larger than 10 dB, the add-drop channel widths were about 5–10 nm. Notice that there are a variety of three-dimensional (3D) waveguide structures whose performances could be quite different. For the waveguides of low index contrast between the guides and claddings, the difference between the effective indices and could be much smaller than that in the 2-D case analyzed here. It is expected that the band gap widths and the add-drop channel widths are narrower and the device lengths are longer in these 3D cases than the 2-D analyzed results.

Analysis of GA-TMI Coupling

A guided mode $\beta_{j,\lambda}$ in the grating-assisted TMI waveguide actually having periodic variation of its effective refractive index when propagating in alternating guiding widths W_m and W_g. The situation could be considered as a plane wave normally incident upon a periodic multilayered medium. For a given wavelength λ_0, the effective permittivity tensor in a tooth-shaped grating illustrated in Fig.-2.13 can be defined by,

$$\varepsilon_j(z) = \varepsilon_0 n_j^2(z) = \varepsilon_0 \left(\frac{\beta_j(z)}{2\pi / \lambda_0} \right)^2 \tag{2.77}$$

where $n_j(z)$ is the effective index of the j^{th} order guided mode, alternating between $n_{j,m}$ and $n_{j,g}$ in the guiding widths W_m and W_g, respectively. The quantity ε_0 is the permittivity in vacuum. The permittivity in the waveguide as a function of distance $\varepsilon_j(z)$ can be further expressed in terms of Fourier coefficients as [76]

$$\varepsilon_j(z) = \sum_p \varepsilon^f_{j,p} \exp(jpG_0 z) \tag{2.78}$$

where $G_0=2\pi/\Lambda$, and Λ is the grating period, equal to the sum of l_m and l_g. The symbol $\varepsilon^f_{j,p}$ denotes the corresponding p^{th} Fourier coefficient of $\varepsilon_j(z)$. Assuming that the difference between W_g and W_m is very small, the fundamental and first order propagation modes would mainly retain their guided lateral shapes while propagating in the grating. Therefore, the electrical field of guided waves in the grating could be modeled by the Bloch wave equation, modified as [76]

$$E_{j,K} = \hat{e}.\, g_j(x,y)\, u_{j,K}(z) \exp(iK_j z)$$

where $g_j(x,y)$ presents the lateral guided form of the j^{th} order guided mode; $u_{j,K}$ a function of z of the period Λ; K_j the guided Bloch wave number. When the grating is removed (i.e., $W_g=W_m$), both $u_{j,K}$ and εj are constants and K_j becomes the guided propagation constant β_j. The βs is the propagation constants in the TMI waveguide of no grating. The $\beta_{1,1}$ and $\beta_{1,2}$ are transformed to Bloch wave numbers $K_{1,1}$ and $K_{1,2}$, both equal to $K=\pi/\Lambda$. The beat lengths $l_{\pi,1}$ increases and $l_{\pi,2}$ decreases. The coupling length is shortened to be

$$L_c = \frac{\pi}{(\beta_{0,2} - \beta_{0,1})} \tag{2.79}$$

where, $\beta_{1,1} < K_{1,1} < (\pi/\Lambda) < K_{1,2} < \beta_{1,2}$ in most cases. Besides, because a grating of infinite periods is ideally assumed in the Bloch theorem, such an ideal value is difficult to achieve with a grating of finite periods. The theory tells us at what length the wavelengths are separated inside an infinite grating. In practice, the grating length should be only long enough to separate the wavelengths right after the grating. Then the grating dispersion is limited by the optimal gating length. Nonetheless, as shown in the later simulation, L_c was still be significantly shortened by such a dispersion effect of the grating. The corresponding frequencies ω_1 and ω_2 on the band gap edges are mainly related to the first two Fourier coefficients $\varepsilon^f_{j,0}$ and $\varepsilon^f_{j,1}$, and can be approximated by [76],

$$\omega_1 = \frac{\pi/\Lambda}{\sqrt{\mu\left(\varepsilon^f_{j,0} + \left|\varepsilon^f_{j,1}\right|\right)}} \tag{2.80a}$$

$$\omega_2 = \frac{\pi/\Lambda}{\sqrt{\mu\left(\varepsilon^f_{j,0} - \left|\varepsilon^f_{j,1}\right|\right)}} \tag{2.80b}$$

Because $\varepsilon^f_{j,1}$ in most cases is much smaller than $\varepsilon^f_{j,0}$, the band gap width $\Delta\lambda$ of the central wavelength λ_0 could be further simplified as [76],

$$\Delta\lambda \sim \frac{\left|\varepsilon^f_{j,1}\right|}{\varepsilon^f_{j,0}}\lambda_0$$

With a given constant W_m=1 μm and a few sets of variables l_m, l_g and W_g, some forbidden band gap widths were calculated and listed in Table-I. The bandwidths $\Delta\lambda_{1,1550}$ and $\Delta\lambda_{1,1880}$ were from the original design discussed above and were the first-order mode and zero order mode reflection bandwidths located at 1550 and 1880 nm, respectively. The bandwidth was blue-shifted to be $\Delta\lambda_{1,1550}$ (from 1880 to 1550 nm) by adjusting the factors l_m and l_g. Furthermore, the blue-shifted $\Delta\lambda_{1,1550}$ was broadened to be $\Delta\lambda'_{0,1550}$ by increasing W_g from 1 to 1.3 μm. Note that there are still two guided modes in a guiding width of 1.3 μm. The bandwidths $\Delta\lambda_{1,1550}$ and $\Delta\lambda'_{0,1550}$ (the first column and the last one in Table-2.5) were the first-order mode and fundamental mode reflection bands of the central wavelengths located at 1550 nm. They will be used to separate the wavelengths of 1538 nm and 1572 nm in the later simulation for purposes of comparison.

Table-2.5: Designed parameters used for grating assisted TMI multiplexer by [76]

W_g=1.1, l_m=0.347, l_g=0.334 (a)				W_g=1.1, l_m=0.276, l_g=0.274 (b)		W_g=1.3, l_m=0.276, l_g=0.268 (c)	
$n_{1,m}$	1.116	$n_{0,m}$	1.035	$n_{0,m}$	1.403	$n_{0,m}$	1.403
$n_{1,g}$	1.16	$n_{0,g}$	1.073	$n_{0,g}$	1.415	$n_{0,g}$	1.433
$\Delta\lambda_{1,1550}$	37.8 nm	$\Delta\lambda_{1,1880}$	13.4 nm	$\Delta\lambda_{1,1550}$	8.4 nm	$\Delta\lambda'_{0,1550}$	20.9 nm

Using the set (a) of schematic factors designed in the Table-2.5, continuous TE waves of 1538 nm and 1572 nm that were single-moded in the input waveguide entered and excited the two-moded waveguide at z=0. Their individual TMI patterns are shown in Fig.-2.15(a), respectively. By comparing the TMI patterns inside and after the grating, the results showed that the 1572 nm imaging period was significantly broadened and the 1538 nm one was on the contrary slightly shortened in the grating. Both wavelengths were nearly separated after the 68 μm long grating. The best z position for locating the output waveguides could be accurately determined by plotting the intensity contrast defined by [76].

$$\text{Contrast} = 10 \log \left(\frac{\int_0^a S_z(z).dx}{\int_{-a}^0 S_z(z).dx} \right) \quad (dB) \tag{2.81}$$

where S_z is the Poynting vector propagating in the z direction. The contrasts of 1538 nm and 1572 nm are shown in Fig.-2.15(b), by a bold line and a thin one, respectively. After passing through the grating region, the maximum contrast difference occurred at z=75.4 μm, indicating the optimum position of the output waveguides for wavelength separation. For 1572 nm (λ_1) and 1538 nm (λ_2) propagating in a 2-D waveguide of 1 μm width and no grating, the propagation constants $\beta_{0,2}$, $\beta_{0,1}$, $\beta_{1,2}$ and $\beta_{1,1}$ were $5.74\text{x}10^6$, $5.6\text{x}10^6$, $4.58\text{x}10^6$and $4.44\text{x}10^6$ (unit: rad/m), respectively. By (2.79), $\Delta\beta$ was $2.88\text{x}10^3$ (rad/m) giving rise to a required L_c

about 1.1 mm, which is about fourteen times the L_c obtained above for the tooth-shaped grating. The theoretical optimum (shortest) L_c predicted is about 22.4 μm. The ideal value is obtained based on the assumption that both λ_1 and λ_2 are right on the edges of the forbidden bandgap contributed by a grating of infinite periods.

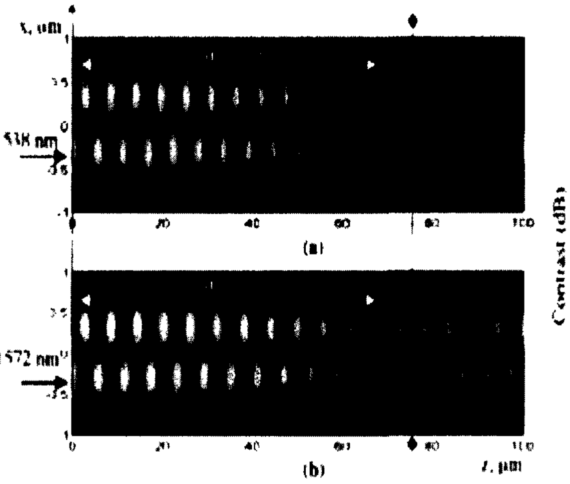

Fig-2.15(a): Mode independent patterns of 1538 nm and 1572 nm in GA-TMI coupler.

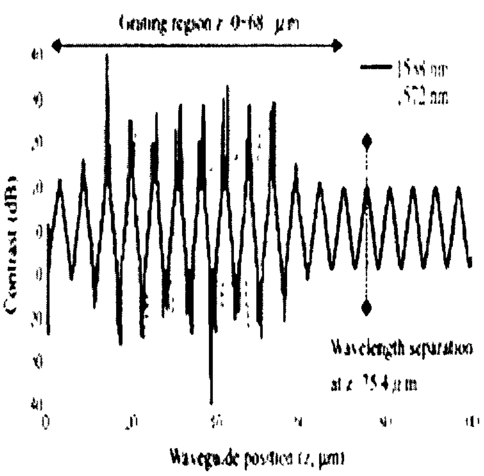

Fig-2.15(b): Intensity contrasts of 1538 nm and 1572 nm in GA-TMI coupler.

The insertion loss is an important factor to be considered, defined as [76],

$$Insertion\ \ loss = -10\ \log\left(\frac{\int_{-a}^{a} S_z(z).dx}{\int_{-a}^{a} S_z(z=0,t=0).dx}\right) \quad (dB) \tag{2.82}$$

where $S_z(z=0,\ t=0)$ is the initial input before the waves are reflected by the grating. The corresponding insertion losses of 1572 nm and 1538 nm are shown in Fig.-2.16. In the FDTD software (optiFDTD produced by the Optiwave Corp.), the input source could be embedded right on the interface between the single moded input waveguide and the two-moded waveguide. The input coupling losses were neglected in the simulation. Then the initial losses of about 0.2 dB at z=0 indicate the reflection losses caused by the grating. The major losses are the scattering losses mainly caused by the toothed structure of the grating. The insertion losses are slightly increased by the S-bend output waveguides.

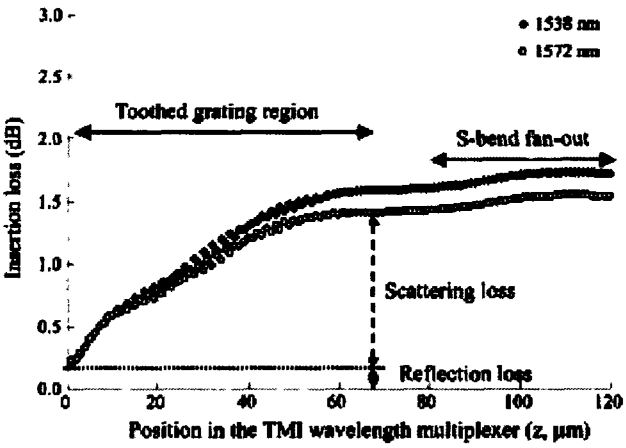

Fig-2.16: Insertion loss of 1538 nm and 1572 nm wavelengths in GA-TMI coupler

Although intensity contrast and insertion loss of tooth shaped grating assisted structure of TMI coupler has been studied by previous authors, for accurate design of GA-TMI coupler, it is required to study accurate estimation of coupling power along with polarization dependence property and fabrication tolerance. The FDTD method has some limitation to study the above performance analysis accurately. In this direction, the simple effective index method is useful to study the above performance accurately. So we have attempted in chapter-4 to design GA-TMI coupler with detail analysis of polarization fabrication tolerance and coupling behavior by using simple effective index method based sinusoidal modes.

2.7 Bend Waveguide Structure

Waveguide bends are important parts of integrated waveguide type devices because they are used to obtain directional changes in the devices such as Mach-Zehnder Interferometer (MZI) type device, Directional coupler, ring lasers, modulators etc. Such waveguide bends are also widely used in arrayed waveguide filters and optical delay lines and to interconnect different photonic devices within integrated optic circuit (IOC). The small radius or sharp bends are essential to achieve a higher packaging density of optical components in integrated optical circuit to improve their functionality and reliability in optical networks. Mass production at an economic cost and reduction of overall device size is a key parameter. In this direction, considerations of sharp bends are most important. These waveguide bends are inherently lossy and increase the overall loss which is also dependent on waveguide parameters. The radiation loss suffered at a bend can be reduced by increasing the modal confinement in the plane of the bending. Many authors have studied the waveguide bend of the device with different waveguide parameters as shown in table-2.6 [57]-[67]. D. Marcuse has studied theoretically the bending of the waveguide and derived the formula for loss coefficient of the bending [57]. T. Kitoh et al. [58] has demonstrated PLC (planar lightwave circuit) type directional coupler (DC) with $\Delta n \sim 0.25\%$ and $SiO_2/GeO_2\text{-}SiO_2$ waveguide by taking bending radius of 15 mm and 40 mm with bending loss of 0.32 dB and 0.05 dB respectively and reduced the bending loss using lateral offset. M. Kawachi et al. [61] has reported DC with $\Delta n \sim 0.25\%$, 0.45%, 0.75%, and 1.5% using bending radius of 25 mm, 15 mm, 5mm and 2 mm respectively with bending loss of ~ 0.1 dB.

From these studies by previous authors, it is clear that bending loss can be reduced with either increase of bending radius or index contrast. But the requirement of compactness of IOC is small radius bends. Keeping bending loss within 0.1 dB/90^0, some of the previous authors [5]-[7] have reduced bending radius up to 2 mm by taking $\Delta n \sim 1.5\%$ and 2 % with $SiO_2/GeO_2\text{-}SiO_2$ material. $SiO_2/GeO_2\text{-}SiO_2$ waveguide has maximum available Δn of ~2%. Using with SiO_2/SiON material, E. Fluck et al. [8] and B. J. Offrein et al. [66]-[67] have reduced bending radius to 1.5 mm with $\Delta n \sim 3.3$ % for thermo optical space switch, wavelength tunable add after drop filter and adaptive gain equalizer devices.

2.7.1. Single Bending Loss

D. Marcuse has derived bending loss coefficient formula of slab dielectric waveguide using cylindrical polar coordinate system [57]. Fig.-2.17(a) shows the wave front, transverse amplitude distribution and pointing vector of the fundamental modes in straight and 90^0 arc bent waveguide of radius of curvature, R. The refractive index of waveguide core and cladding are n_2 and n_1, respectively. At the straight waveguide, the centre of gravity of the light distribution in the beam coincides with the waveguide axis and at the curved waveguide, the beam axis shifts in the plane of the curvature to the outside of the bend. The phase velocity inner side of the bend is smaller than that of outside of the beam axis. So, the wave fronts are retarded on the inner side of the bend, while following the curved path and on outer side of the bend, the wave fronts are split and radiated from the waveguide.

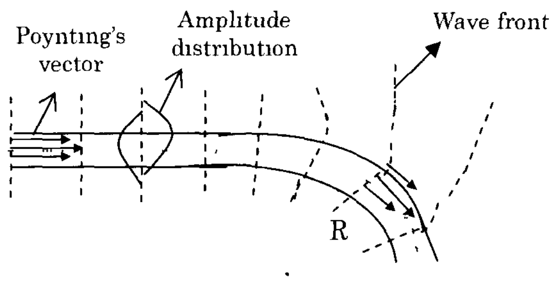

Fig-2.17(a): Amplitude distribution, wave fronts, time averaged poynting vector of fundamental mode on a straight and a bent waveguide section

To find the bending loss, it is required to know the mode field outside the bent waveguide. The mode field outside the bent waveguide can be expressed by the solution of the Maxwell's equations in the region R+ w/2 < r < α (where R= radius of curvature). The mode field at (r,ϕ) coordinate from the center of the curvature is given by [57]

$$E_y = BH_{\gamma}^{2}(n_1 k_0 r)\exp(-j\gamma\phi) \quad (2.83)$$

where, $H_{\gamma}^{2}(n_1 k_0 r)$ = Henkel function of the second kind of order, γ

β=propagation constant, $k_0=2\pi/\lambda$, (2.84)

$$z=R.\phi \quad (2.85)$$

Considering approximate Hankel function for R >> λ and substituting the same in the equation (2.83), we can write the radiated field as follows [57],

$$E_y= B.\sqrt{\{2/(\pi n_1 k_0 r)\}}exp(-jn_1 k_0 r).exp\{j(2\gamma+1)\pi/4\}. exp(-j\beta z) \quad (2.86)$$

where,

$$B = 2jK_1 exp(\upsilon d).\sqrt{[(\pi/2)\omega\mu_0 P.\upsilon.R/\{\beta(2d+2/\upsilon)(K_1^2 + \upsilon^2)\}]}.exp(-U/2) \quad (2.87)$$

$$\upsilon=\sqrt{\{(\beta)^2-(n_1k_0)^2\}} \quad (2.88a)$$

$$K_1 = \sqrt{\{(n_2k_0)^2-(\beta)^2\}} \quad (2.88b)$$

$$U=(2/3).(\upsilon^3/\beta).R \quad (2.89)$$

P= input power of the bent waveguide.

The radiated power is calculated by poynting vector which is given by

$$S_r = \tfrac{1}{2} n_2.\sqrt{(\varepsilon_0/\mu_0)}.|E_y|^2$$

$$= \tfrac{1}{2} n_2.\sqrt{(\varepsilon_0/\mu_0)}.|B|^2\{2/(\pi n_1 k_0 r)\} \quad (2.90)$$

Putting S_r and B from the equations (2.90), the power loss coefficient of bending is written as [78],

$$\alpha = (r/R).S_r/P$$

$$= (1/R)\sqrt{(\varepsilon_0/\mu_0)}.|B|^2(1/k_0)(1/P)$$

$$= \upsilon^2.K_1^2 exp(2\upsilon d).(exp(-U)/\{\beta(d.\upsilon+1)(K_1^2+\upsilon^2)\}] \quad (2.91)$$

$$\alpha = C_1 exp(-C_2R) \quad (2.92)$$

where, $C_1 = \upsilon^2.K_1^2 exp(2\upsilon d)./\{\beta(d.\upsilon+1)(K_1^2+\upsilon^2)\}]$ (2.93)

$$C_2 = (2/3).(\upsilon^3/\beta) \quad (2.94)$$

The constants C_1 and C_2 depend mainly on index contrast (Δn) and wavelength (λ).

The attenuation of the waveguide is usually expressed as

$$\frac{P_o}{P_i}=e^{-\alpha_t z} \quad (2.95a)$$

where P_o=out put power, P_i= input power, $\alpha_T = \alpha + \alpha_p$, α =bending loss coefficient and α_P=propagation loss coefficient. In bent waveguide, $\alpha >> \alpha_P$. So, $\alpha_T \approx \alpha$.
Loss in dB can be expressed as

$$T_B = -10\log\left(\frac{P_o}{P_i}\right) = \frac{10}{\ln 10}\alpha z \tag{2.95b}$$

For 90^0 arc bent waveguide, $z = \frac{\pi \times 90^0 \times R}{180^0} = 1.57R$ (2.95c)

So loss in dB for 90^0 arc bent waveguide can be expressed as

$$T_B(90) = 4.343\alpha \times 1.57R \tag{2.96}$$

Considering the experimental value of T_B (90) of less than 0.1 dB, reported in [60] at R =25 mm and λ=1.55μm for Δn = 0.0025, α is obtained using the equation (4.14) as 0.56 x10^{-6} $(\mu m)^{-1}$. C_1 and C_2 are determined by using the equation (2.92) as follows

C_1 =2 x10^{-5} $(\mu m)^{-1}$

C_2=14.3 x10^{-5} $(\mu m)^{-1}$

T. Kitoh et al. [58] has reported measured values of C_1 and C_2 for Δn = 0.0025 at wavelength λ=1.55 μm. These values are ~2.032 x10^{-5} $(\mu m)^{-1}$ and 7.033 x10^{-5} $(\mu m)^{-1}$ for TE mode, proving good agreement with the above values of C_1 and C_2 estimated from the experimental results in [60]. Fig-2.17(b) shows the plot of T_B versus R at wavelength λ=1.3 μm and 1.55 μm for Δn =0.0025. In the figure, the solid line is drawn by using the above values of C_1 and C_2 from experimental results in [60] for wavelength λ=1.55 μm and the equations (4.10) and (4.14). The dashed lines represent the BPM results reported in [58] for λ=1.3 μm and 1.55 μm. The difference between two results at λ=1.55 μm shown in the figure may be due to difference in waveguide parameters such as core width (w). As R increases, the bending loss decreases. The figure also shows that the bending loss at λ =1.3 μm is lower than that at λ =1.55 μm. So bending loss, T_B depends on wavelength. In this thesis work, we have taken λ=1.55 μm which is mainly used in optical communication due to lower propagation loss.

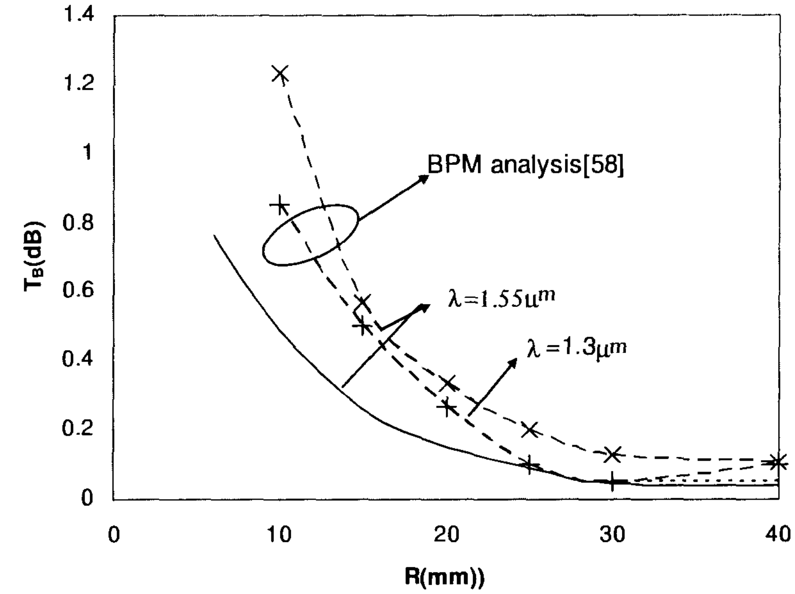

Fig-2.17(b): T_B versus R for Δn=0.0025 at λ=1.3 μm and 1.55 μm

2.7.2 S-bending loss

S-bend is one of fundamental components of the planar waveguide device such as Mach Zehnder (MZ) type devices. The transition region of MZ device can be represented by two S-bends with intersection angle, 2A as shown in Fig-2.18(a).

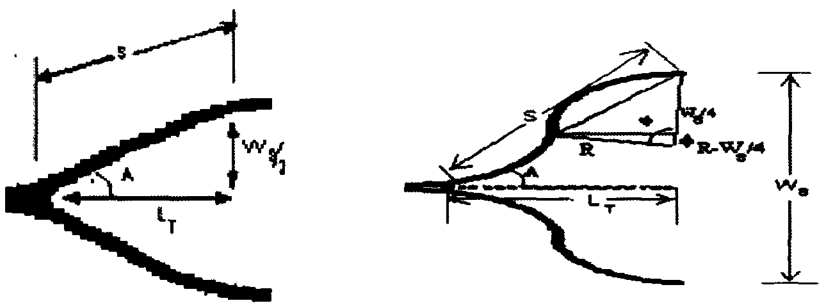

Fig-2.18(a): Transition region TOMZ switch-(a) Transition region (b) Single S-bend

Fig-2.17(b) shows single S-bend waveguide of bending radius, R. L_T is transition length of the MZ device and arc length of S-bend is S. The radius of curvature of the bending (R) depends on L_T and separation of the waveguides in MZ section, W_s.

The S-bend arc length is considered as,

$$S= (L_T + \Delta L) \quad (2.97a)$$

where ΔL = small difference between L_T and S.

From Fig-2.17(a), we can write approximately

$$S^2=(L_T +\Delta L)^2 = (W_s/2)^2 + L_T^2 \quad (2.97b)$$

From the equation (2.97b), ΔL can be approximately written as

$$\Delta L \approx W_s^2 /8L_T \quad (2.98)$$

where, $\Delta L << L_T$.

From the geometry of Fig-2.17(b),

$$S=2 R\phi. \quad (2.99)$$

$$Cos (\phi) =(R-W_s/4)/ R = (1 - W_s/4R)$$

$$\phi= Cos^{-1} (1-W_s/2R) \quad (2.100)$$

Substituting ϕ in the equation (2.99), S can be written as

$$S= 2R\, Cos^{-1}[1- W_S /(4 R)] \quad (2.101)$$

The S-bend loss in dB is given by

$$T_s = -10 \ln [\exp \{-\int (\alpha ds)\}] \quad (2.102a)$$

$$= 4.343\ \alpha S$$

The equation (2.100) can be written approximately by using Taylor's series as follows

$$1- \phi^2/2 \ldots\approx [1-W_s /(4R)] \quad (2.102b)$$

Putting the value of ϕ from the equation (2.99) in the equation (2.102b), we get

$$R= S^2/2 W_s$$

$$= (L_T+ \Delta L)^2/2 W_s$$

$$= (L_T+ W_s^2 /8L_T)^2/2 W_s \quad (2.103)$$

The intersection angle between two S-bends denoted by 2A is obtained from the geometry of Fig-2.17(a) as given below:

$$2A = 2Sin^{-1}(W_s/2S) \tag{2.104}$$

Substituting S in the equation (2.104), we get A as follows

$$\text{Sin}\, A = W_s/4R\ Cos^{-1}[1 - W_S/(4R)] \tag{2.105}$$

Transition length, L_T is an important parameter in controlling chip area in which chip area reduces with decrease of L_T. L_T is determined by the following equation, knowing W_s and intersection angle 2A.

$$L_T = \frac{W_s}{2\tan A} \tag{2.106}$$

T. Kitoh et al. [58] has reported S-bend of radius 15 mm and 40 mm with W_s =50 μm. The half intersection angle is calculated as follows:

For R= 40 mm and W_s=50 μm [58]

$$SinA = \frac{50}{4\times 40000\times \cos^{-1}(1 - \frac{50}{4\times 40000})} = 0.02042$$

A= 0.716^0,

2A=1.432^0.

$$L_T = \frac{W_s}{2\tan A} = \frac{50}{2\times \tan\ 0.716} = 2000\mu m$$

For R=15 mm and W_s= 50 μm [58]

$$\text{Sin A} = \frac{50}{4\times 15000\times \cos^{-1}(1 - \frac{50}{4\times 15000})} = 0.0125$$

A= 1.17^0, 2A=2.34^0

$$L_T = \frac{W_s}{2\tan A} = \frac{50}{2\times \tan\ 1.17} = 1224\mu m$$

The above estimated values of A and L_T shows that lower R values make the waveguide device compact.

Loss coefficient versus R for different values of Δn:

In order to find out loss coefficient with C_1 and C_2 for different values of Δn we had the experimental results reported by M. Kawachi [60] as mentioned in table-2.6. Using measured values of C_1 and C_2 reported by T. Kitoh et al.[58] and M. Kawachi [60] for Δn=0.0025 at λ=1.55 µm, $T_B(90)$ for different values of R are determined by using the equations (2.92) and (2.96) and plotted by solid curve in Fig-2.18(b). M. Kawachi [60] reported that T_B of less than 0.1dB for Δn=0.0025, 0.0045, 0.0075 and 0.015 are obtained experimentally at R=25 mm, 15 mm, 5 mm and 2 mm respectively and represented by crossed points (x) in the figure. The dotted line (B) is made parallel to R axis passing the crossed point on the solid curve at R= 25 mm and T_B of 0.098 dB for Δn=0.0025. The experimental point for Δn=0.0045 [60] is found at R=15 mm on the dotted line (B) and made the dotted curve (T_B (90) versus R) of similar nature passing through this point. In order to find C_1 and C_2 for Δn=0.0045, we have chosen two points at R = 15 mm and 20 mm on the dotted lines. Taking T_B (90) at R=15 mm and 20 mm, we have determined loss coefficients as 0.97×10^{-6} $(\mu m)^{-1}$ and 0.208×10^{-6} $(\mu m)^{-1}$ respectively.

$$C_1 \exp(-C_2 \times 15000) = 0.97\times10^{-6}$$

$$C_1 \exp(-C_2 \times 20000) = 0.208\times10^{-6}$$

Using the above equations, we have estimated C_1 and C_2 as follows

$$C_1 = 10\times10^{-5}\ (\mu m)^{-1}$$

$$C_2 = 30.9\times10^{-5}\ (\mu m)^{-1}$$

Similarly, we have drawn the curves of same nature passing through crossed points at R = 5 mm and 2 mm for Δn 0.0075 and 0.015 respectively. Taking T_B (90) at R=5 mm and 10 mm for Δn=0.0075 we have determined loss coefficients as 2.9×10^{-6} $(\mu m)^{-1}$ and 0.025×10^{-6} $(\mu m)^{-1}$ respectively.

$$C_1 \exp(-C_2 \times 5000) = 2.9\times10^{-6}$$

$$C_1 \exp(-C_2 \times 10000) = 0.025\times10^{-6}$$

Using the above equations, we have estimated C_1 and C_2 as follows

$C_1 = 35\times10^{-5}\ (\mu m)^{-1}$

$C_2 = 95\times10^{-5}\ (\mu m)^{-1}$

Loss coefficients at R=2 mm and 5 mm for Δn=0.015 are found to be $7.2\times10^{-6}\ (\mu m)^{-1}$ and $0.0075\times10^{-6}\ (\mu m)^{-1}$ respectively and estimated values of C_1 and C_2 are $70\times10^{-5}\ (\mu m)^{-1}$ and $229\times10^{-5}\ (\mu m)^{-1}$.

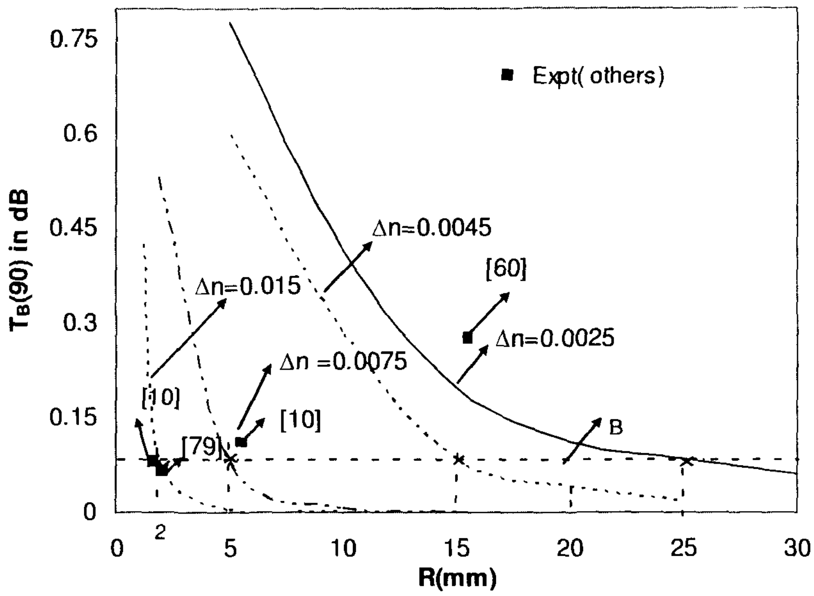

Fig-2.18(b): T_B (90) vs R for Δn=0.0025, 0.0045, 0.0075 and 0.015 at λ=1.55 μm

The calculated values of C_1 and C_2 for Δn =0.0025, 0.0045, 0.0075 and 0.015 are tabulated in table-2.6. From the figure and table-4.2, it is seen that considering permissible value of 90^0 arc bend loss T_B of 0.1 dB as used by different authors [10], [60], [79] radius of bending can be reduced with increase of Δn.

Table-2.6: C_1 and C_2 for different Δn values for the experiments [60]

V= normalized frequency=2.4, Wavelength λ=1.55 μm

Material used	I Δn (%)	Minimum Bending Radius R(mm)	Intersection angle (2A)	W_s (μm)	Bending Loss in dB for 90^0 arc	α $(\mu m)^{-1}$	C_1 $(\mu m)^{-1}$	C_2 $(\mu m)^{-1}$
SiO_2/GeO -SiO	0.25	25 mm (reported)	1.8^0 (Calculated) 1.4^0 (Calculated)	50 (assumed) 30 (assumed)	<0.1dB (reported)	0.58x 10^{6} (Calculated)	2x 10^{5} (Calculated)	14x 10^{5} (Calculated)
	0.45	15 mm (reported)	2.34^0 (Calculated) 1.8^0 (Calculated)	50 (assumed) 30 assumed	<0.1 dB (reported)	0.97x 10^{6} (Calculated)	10x 10^{5} (Calculated)	30.9x 10^{5} (Calculated)
	0.75	5 mm (reported)	4.04^0 (Calculated) 3.14^0 (Calculated)	50 (assumed) 30 (assumed	<0.1 dB (reported)	2.9x 10^{6} (Calculated)	35x 10^{5} (Calculated)	95x 10^{5} (Calculated)
	1.5	2 mm (reported)	6.4^0 (Calculated) 4.96^0 (Calculated)	50 (assumed) 30 (assumed)	<0.1 dB (reported)	7.2x 10^{6} (Calculated)	70 x 10^{5} (Calculated)	229x 10^{6} (Calculated)

The experimental results demonstrated by other authors [10], [60], [79] using same material are shown in Fig-2.18(a) proving good agreement with these fitted curves. The half intersection angle are determined for W_s=30 μm and 50 μm by using the equation (4.23) and tabulated.

In order to determine C_1 and C_2 for other Δn values at V~2.4, we have plotted C_1 and C_2 versus Δn as shown in Fig-2.18(c). In the figure, black rectangle and black dots represent the experimental points of C_1 and C_2 respectively. The solid line indicates the curve passing through these experimental points of C_1 with minimum deviation whereas the dashed line represents the curve passing through experimental points of C_2. It is seen from the figure that both the curves of C_1 and C_2 are approximately linear. From these linear curves we can express C_1 and C_2 in terms of Δn as follows,

$$C_1 = m_1\Delta n + p_1 \quad (2.107a)$$

$$C_2 = m_2\Delta n + p_2 \quad (2.107b)$$

where, fitted values of m_1, p_1, m_2 and p_2 calculated from the linear curves are given below:

$m_1=0.04$, $p_1= - 8x\ 10^{-5}$, $m_2=0.0835$ and $p_2 = - 6.775\ x10^{-5}$.

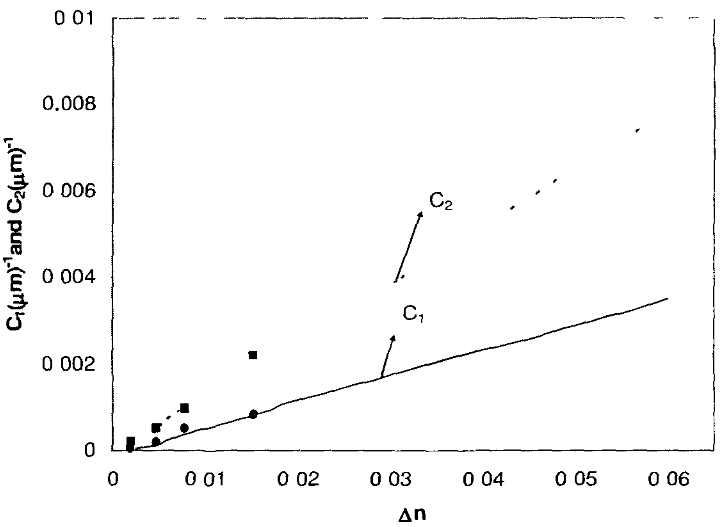

Fig-2.18(c): C_1 and C_2 versus index contrast (Δn) for V ~2.4

Fig-2.18(d) show the plot of Loss coefficient (α) versus R obtained using equation (2.96) and (2.92) for different Δn values. It is seen from the figure that bending loss coefficient decreases with Δn and it also decreases with R for all values of Δn. In the figure, the rectangle shows the experimental points demonstrated by previous authors, proving good agreement with the curves in the figure.

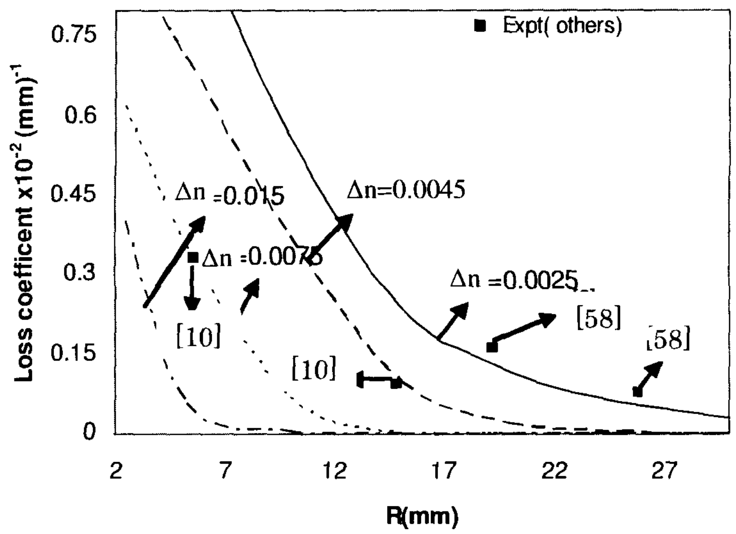

Fig-2.18(d): Loss coefficient versus R for Δn =0.0025, 0.0045, 0.0075 and 0.015

As discussed in sections-2.3, 2.4, 2.5 and 2.6, we have seen that one of important part of DC, TMI and MMI coupler is bent input and output access waveguides. The bending portion of access waveguides plays an important role for change of direction of signal propagation in PID. The compact design of PID requires proper design of the bending portion. In our work, we have studied the compact design of the bent access waveguides to reduce total device length, as mentioned in Chapter-5.

2.8. Motivation and Advantages of SiO_2/SiON Material as a Waveguide Material

Table-2.7 mentions the optical properties and processing steps of different waveguide materials used for fabrication of PID's. These materials are compared in terms of advantages and disadvantages. It is seen form the table that the fabrication steps of waveguide devices used for silicon based materials are as same as those used for conventional IC technology but those are not the same for other waveguide materials as mentioned in the table. The fabrication steps of silicon based materials can easily be adapted in mass production which is commercially viable. Since

InP/GaAsInP waveguide materials uses Molecular Beam Epitaxial (MBE) growth technique, the fabrication cost of InP/GaAsInP waveguide is more than other materials. The basic fabrication steps for polymeric waveguide materials is LASER writing which is cheaper therefore, it is difficult to use the same technology for mass production. Moreover LASER writing technique is time consuming.

The table shows that high index contrast are available in SiO_2/SiON, InP/GaAsInP, SOI and Polymeric waveguide materials to compact waveguide device components, compared to Ti:$LiNbO_3$ and SiO_2/SiO_2-GeO_2 materials having lower index contrast. In addition, these materials show polarization insensitive property in comparison to Ti:$LiNbO_3$ material because of crystal structure. Actually, polymeric and silicon based materials show thermo optic properties. Although, polymeric materials have higher thermo optic coefficient and easy processing of devices, but silicon based materials are highly stable and compatible to conventional IC processing technology. In our work, we have studied thermo optic device structures, as available for the fabrication of some optical devices which are studied in Chapter-6 and Chapter-7 respectively.

Although SOI has higher index contrast of fixed value~2, but wide variation of the index contrast (maximum up to 0.53) can be achieved by varying nitrogen and oxygen content in SiON material. In case of SOI waveguide device, the reported propagation losses of SOI waveguides is 0.1 dB/cm [59] and the fiber to chip coupling loss are of the order of 2-5 dB/facet [59], whereas in case of SiO_2/SiON, the propagation losses are same as SOI materials but fiber to chip coupling loss (order of 1 dB per facet) is lower than that of SOI material [59]. The SiO_2/SiON material also shows more chemical inertness property than SOI material. More over, the processing system of SiO_2/SiON waveguide device is available with us for fabrication of waveguide devices. Because of the above reasons, we have chosen SiO_2/SiON material in which SiON material is used as waveguide core and SiO_2 as waveguide cladding for fabrication of DC with small gap and TMI coupler in section -5.7.

Table-2.7: Optical properties of some materials for waveguide type integrated devices

Materials with range of refractive index	Δn (max)	Δn taken by previous authors	Properties				Basic Steps of fabrication	Material cost/ processing cost
			Thermo-optic coefficient $\alpha = \frac{dn}{dT}$	Electro-optic coeff (r_{33})	Stability	Polarization sensitivity /Birefringence		
SiO_2/SiON Index range~ (1.45 - 1.98)	~ 0.53	0.033 [1] 0.103 [7]	10^{5} / ^{0}C [54]	- ---	High [54]	Polarization Insensitive [54]/10^{6}	i) Formation of SiO_2 lower cladding layer on Si-Substrate ii)Formation of SiON layer on SiO_2 layer iii) Fabrication of SiON core with photolithography iv) Formation of Top cladding SiO_2 layer	Mode-rate/ High
GeO_2 SiO_2/ SiO_2 Index range~ (1.45 - 1.47)	~ 0.02	0.0075 [10] 0.0025 [55]	10^{5} / ^{0}C [54]	---	High [54]	Polarization Insensitive [54]/10^{5}	i) Formation of SiO_2 lower cladding layer on Si-Substrate ii)Formation of SiO_2-GeO_2 layer on SiO_2 layer iii) Fabrication of SiO_2-GeO_2 core with photolithography and RIE iv) Formation of Top cladding SiO_2 layer	Moderate/ High

Silicon on insulator (SOI) (3.4767)	2.026	--	1.84 x 10^{-4}/ ^{0}C [54]	----	High [54]	Polarization insensitive /10^{-4}	i) Formation of SOI wafer by using Bond and etch back method or Separated by implanted oxygen method ii) Fabrication of Si core with photolithography and RIE ii) Formation of Top cladding SiO_2 layer	Mode rate/ High
Ti $LiNbO_3$ Index range~ (2.15- 2.21)	~0.06	0.006 [20] 0.01 [19]	---	30.8 pm/V [56]	High [56]	Polarization sensitive[56] /10^{-2}	i) Formation of Ti $LiNbO_3$ using thermal Ti diffusion ii) Fabrication of waveguide core with photolithography and etching	High/high
InP/GaAsInP Index range~ (3.13 - 3.5)	~0.33	0.13 [16] 0.167 [15] 0.15 [14], [37]	----	-- --	Stable [16]	Polarization Insensitive [16] / 2.5x10^{-4}	i) Formation of GaAsInP layer by using molecular beam epitaxial growth (MBE) ii) Formation of InP layer by using MBE iii) Fabrication of waveguide core with photolithography and etching	High/ High

Polymer Index range~ (1.44 - 1.65)	~0.21	0.03 - 0.1 [47]	10^{-4} /°C [47]	10 – 200 pm/V	Low	Polarization Insensitive / 10^{-2}- 10^{6}	i) Fabrication of polymer layers by using chemical processing polymerization ii) Fabrication of polymeric waveguide by using LASER writing	Low/low

2.9 Previously Reported TMI, MMI Coupler Based Photonic Integrated Devices for Applications in Optical Networks

Optical networks have become essential to fulfill the huge demands of bandwidth required for skyrocketed increase of number of users and services in present day's communication networks. In fact, Nation wide communication networks requires optical backbone in USA, India etc, In this direction, USA already has optical backbone named as NSFNET T1 backbone [67] as shown in Fig-2.19(a) whereas Indian optical back bone connecting major cities of India has been reported and studied by previous authors [67]-[68] as shown in Fig-2.19(b). In these networks, flexible operation such as routing, restoration and reconfiguration are provided by the nodes where wavelength division multiplexer (WDM)/de-multiplexer, optical matrix switches and add/drop multiplexer are key devices. Fig-2.19(c) shows 3x3 node architecture having three incoming and out going fiber links. It consists of three 4x4 wavelengths Multiplexer (W-MUX) and de-multiplexer (W-DMUX), add/drop multiplexer and 3x3 Thermo Optic Mach Zehnder (TOMZ) switch. In the figure, after de multiplexing of wavelength channels λ_1, λ_2.... λ_4 , these wavelength are switched to particular out going fiber as per routing block and finally wavelength channels are multiplexer by W-MUX .

These devices are implemented by using photonic integrated device (PID) technology due to having immunity to vibration, electromagnetic interference, low transmission loss, small size and light weight. In this section, we have reviewed these devices (based on PID) using basic components such as DC, TMI and MMI coupler. Table-2.8 shows these devices reported by previous authors.

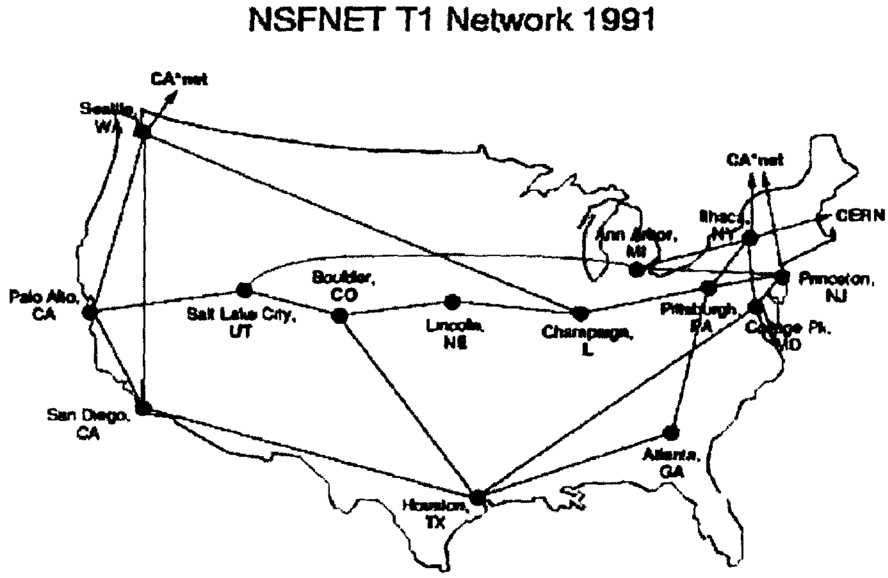

Fig-2.19 (a): Nation wide optical backbone: NSFNET T1 [67]-[68]

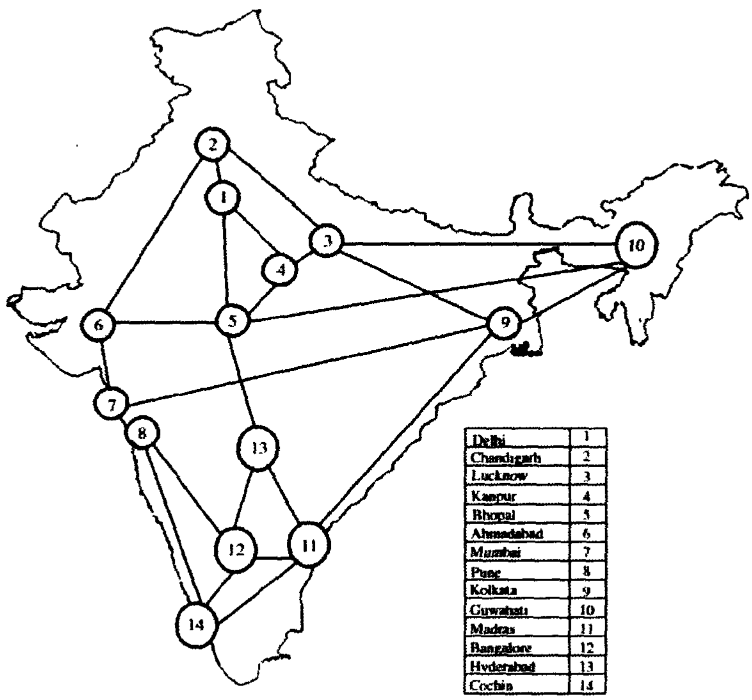

Fig-2.19 (b): Nation wide optical back bone: Indian network [67]-[68]

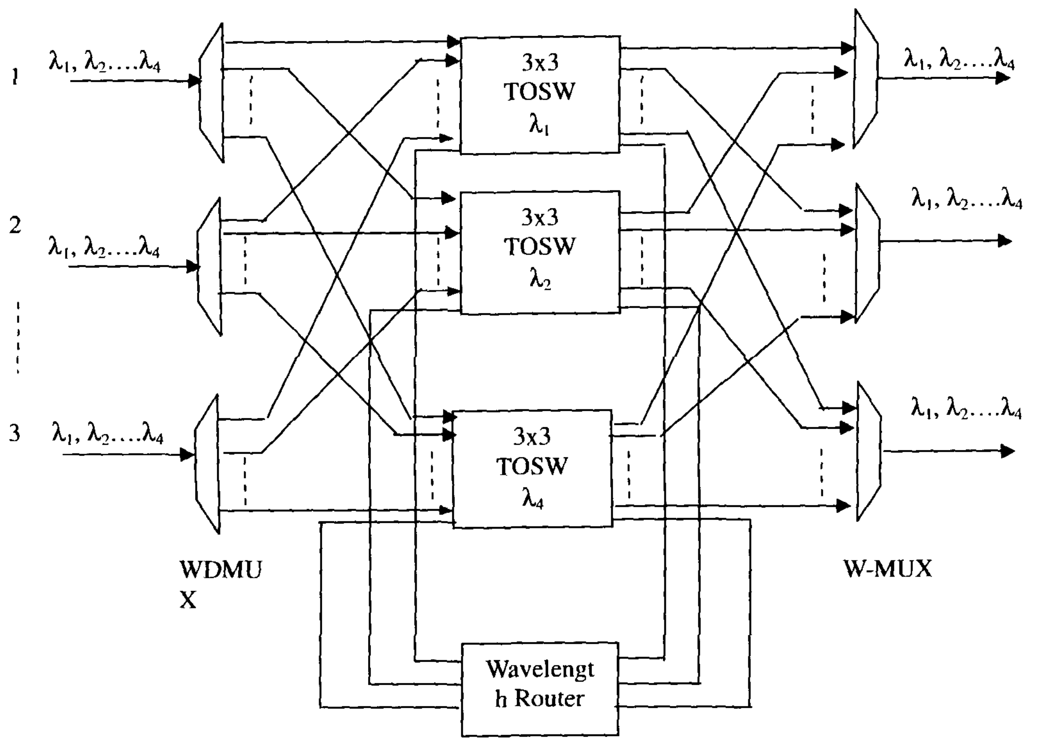

Fig-2.19(c): Schematic block diagram of reconfigurable node consisting of 3x3 TOSW, W-MUX and W-DMUX

R. Kasahara et al. [10] demonstrated silica based thermooptic mach zehnder (TOMZ) switch having DC as one of basic component with power consumption of 90 mW and response time of 4.9 to achieve a core temperature change of 15^0 C for switching [10].

Fig-2.20(a) shows layout of 8x8 optical matrix of chip area of 85x85 $(mm)^2$ demonstrated by Kasahara et al. [10]. In the figure, there are eight switching stages and each stage consists of eight switching unit arranged in eight rows, as shown in Fig-2.20(b), giving 64 switching units. Fig-2.20(c) shows the length of each TOMZ switching unit is determined from the layout of the matrix switch, as ~22.3 μm. Z.

Wang et al. [44] reported SOI thermooptic MZ switch based MMI coupler with power consumption of 330 mW and response time ~30 µsZ.

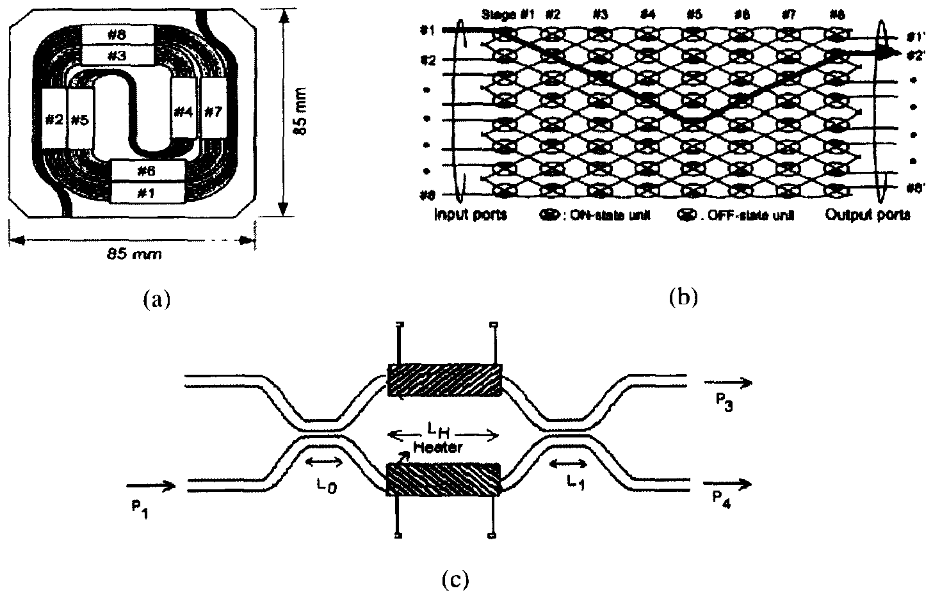

Fig-2.20(a): Lay out of 8x8 optical matrix switch demonstrated by Kasahara et. al [10] using SiO_2/SiO_2-GeO_2 waveguide.(b) Arrangement of eight switching units in each stage giving 64 units for eight stages (c) single TOMZ unit.

Wang et al. [44] has also demonstrated 4x4 SOI thermo-optic MZ switching matrix based MMI coupler with arrangement of five switches, as shown in Fig-2.21. Total length (L_S) of matrix switch is 50 mm and the length of each TOMZ switching unit is estimated as,

$$L_t = 50/3 = 16.67 \text{ mm}.$$

The length of TOMZ switch unit based on DC structure demonstrated by Kasahara et.al is higher than that reported by Z. Wang et al. Firstly it is due to higher heater length of 5 mm used by Kasahara et al. in comparison to that used by Z. Wang et al. Secondly it is due to higher Δn used by Z. Wang et al. in comparison to that by

R. Kasahara et al.[10]. We have considered both TOMZ device (DC) demonstrated by Kasahara et al. and TOMZ device (MMI coupler) by Z. Wang et al.

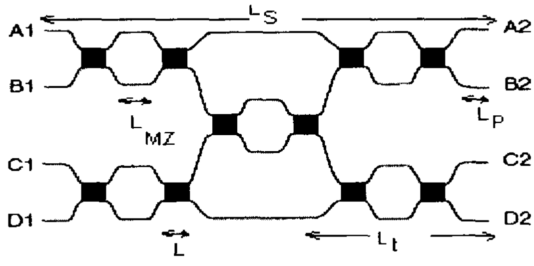

Fig-2.20(d): Architecture of SOI 4x4 optical matrix switch demonstrated by Z. Wang et. al [44] (L_P= length of input /output waveguide, L=length of 3dB coupler, L_{MZ}=MZ section length=L_H=heater length, L_S=length of 4x4 optical matrix switch)

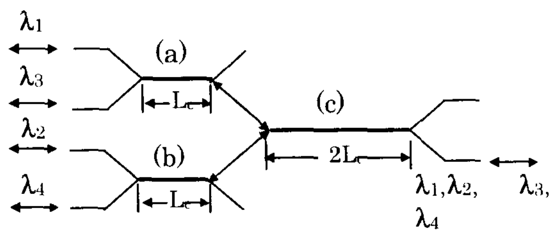

Fig-2.20(e): 4 channel cascaded multiplexer/demultiplexer

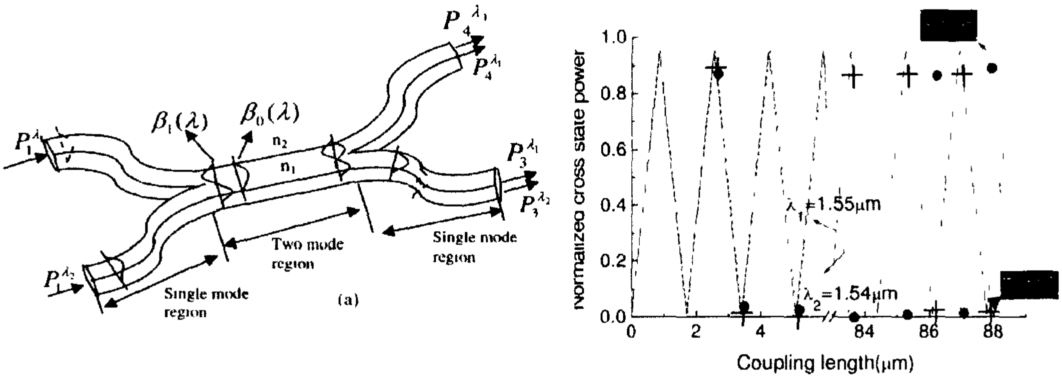

Fig-2.21: (a) Two wavelength channel 2x2 TMI coupler based W-MUX (b) coupling characteristics of W-MUX

A. Neyer [20] reported 4 wavelength channel wavelength multiplexer/de-multiplexer based TMI coupler using Ti:$LiNbO_3$ with device length ~6 mm as shown in Fig-2.20(e). Sahu [69] has demonstrated Compact W-MUX and W-DMUX based on TMI coupler using SOI waveguide as shown in Fig-2.21 and from its transmission characteristics the coupling length for multiplexing wavelengths 1540 nm and 1550 nm was obtained as 86 μm.

B. J. Offrein et al. [47] has demonstrated Adaptive EDFA gain equalizer based on Delay line coupler with DC using SiO_2/SiON material with thermooptic heater which has phase shift response time of less than 1ms and sensitivity of 2π rad./440 mW/heater. Compact Add/drop multiplexer using delay line based on TMI coupler has been reported [70] with device length ~3 mm as shown in Fig-2.22 and from transmission characteristics it confirms polarization independence.

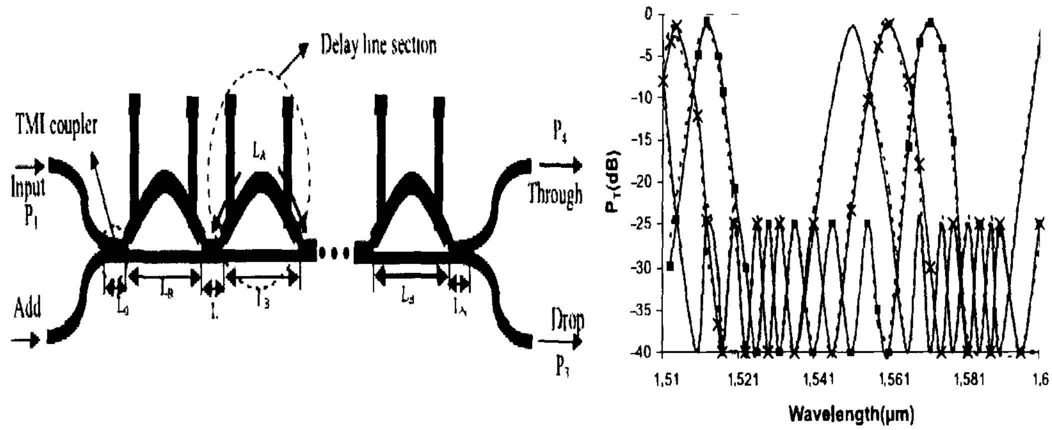

Fig-2.22: (a) Polarization independent thermooptic add/drop multiplexer and (b) Transmission characteristics

Thermooptic MZ device based on TMI coupler has been reported by previous author [71] using SiO_2/SiON waveguide having fast response time of 180 μs and from Fig-2.23(b), it is confirmed that for getting bar state the heating power is required as ~ 180 mW

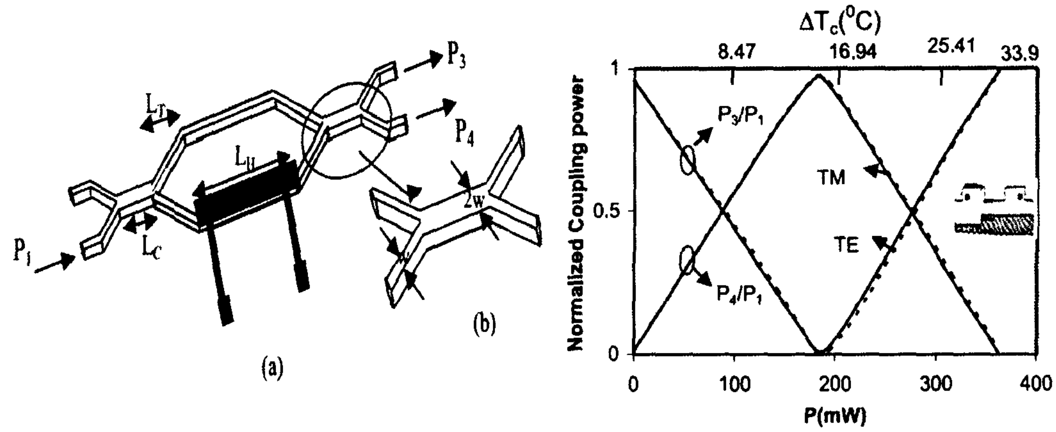

Fig-2.23: (a) Polarization independent thermooptic MZ device and (b) Coupling characteristics

R. L. Espinola et al. [43] has reported DC based TOMZ switch using SOI with less switching power consumption of 50mW, less switching time of 35 μs and higher fiber to chip loss of 32 dB and insertion loss of 4dB for device operation. Z. Wang et al. [44] reported SOI thermooptic MZ switch based on MMI coupler with power consumption of 330 mW and switching time~30 μs. A. Sugita et al. [50] has demonstrated silica based bridge-suspended structure for TOMZ switch with lower heating power of 45 mW resulting longer response time. B. J. Offrein et al.[42] has demonstrated DC based TOMZ switch using $SiO_2/SiON$ material with switching power of 220 mW and response rime<100 μs. M. Okuno et al. [53] has reported TOMZ switch using $SiO_2/SiO_2\text{-}GeO_2$ material with switching power of 45 mW and response rime of 3ms. Q. Lai et al. [52] has demonstrated 2x2 TOMZ switch based on MMI coupler using Silica on silicon geometry with switching power of 110 mW and response rime of~180 μs. R. Kasahara et al. [51] has reported TOMZ switch based on DC using $SiO_2/SiO_2\text{-}GeO_2$ material with switching power of 134 mW and response rime<2 ms. M.C. Oh et al. [44] has demonstrated X-junction polymeric TOMZ switch with power consumption of ~10 mW and response time of 2 ms respectively for switching operation. The lower value of heating power requirement is due to larger value of thermooptic coefficient of polymeric material.

Table-2.8: Characteristics of DC, TMI and MMI based device reported by different authors.

Author's Name/ material used	Δn (%) used	Type of Structure	Coupling length	Core size (μm)² and cladding width(μm)	Device length	Heating power (mW)	Response time	Loss per MZ switch	Application
R Kasahara et al [10] SiO_2/GeO_2-SiO_2	0.75 %	MZ based on DC (Fig-3.11)	$L_\pi/2$ = 963.2 μm	7x7 (μm)² /60μm	22.3 mm	90 mW (proposed) 360 mW (conventional)	4.9 ms	1.5 dB	TOMZ switch
Z Wang et al [44] SOI	200 %	MZ based on MMI Coupler (Fig-3.13(d))	$L_\pi/2$ = 2400 μm	1x4 (μm)² /60μm	16.67 mm	330 mW	30μs	3.3 dB	TOMZ Switch
B J Offrein et al [47] $SiO_2/SiON$	3.3 %	MZ with Unequal Arms based on DC		1.3x3 (μm)²	75 mm	440 mW / heater for 2π phase shift	<1 ms	2 dB	EDFA Gain equalizer
R L Espinhola et al [43] SOI	200 %	MZ based on DC (Fig-3.11)	-	0.26x0.6 (μm)² /2.26μm		50 mW	35μs	32 dB	TOMZ switch
P P Sahu [70] $SiO_2/SiON$	5 %	TMI coupler based Add/drop multiplexer	L_π= 45 μm	w = 1.5 μm t =1.5μm λ= 1.55 μm	~ 3 mm	53 mW per delay line	180 μs		Thermooptic Add /drop MUX
A Sugita et al[50] GeO_2-SiO_2/SiO_2	0.75 %	Bridge suspended MZ on DC (Fig 3.11)		7x7(μm)²		40 mW	> 5ms	1.5 dB	TOMZ Switch

B J Olfrein et al [42] $SiO_2/SiON$	3 3 %	MZ based On DC (Fig-3 11)		2x3 $(\mu m)^2$		200 mW	<100 µs	2 dB	TOMZ switch
Q Lai et al [52] silica on Silcon	1%	MZ based on MMI coupler (Fig-13(d)	L_π = 1000 µm	4 5x4 5 $(\mu m)^2$ /60µm	5 mm	110 mW	180 µs	1 dB	TOMZ Switch
P P Sahu [69] SOI	~	TMI coupler based MUX	L_c= 86 µm	w = 1 5 µm t =1 5µm λ= 1 55 µm	~ 92 µm	--	--	~ 7 dB	2 wave length channel MUX/DMUX
R Kasahara et al [51] GeO_2-SiO_2	0 75 %	MZ based on DC	$L_\pi/2$ = 963 2 µm	7x7 $(\mu m)^2$ /60µm	22 3 mm	134 mW	<2ms	1 5 dB	
P P Sahu [71] $SiO_2/SiON$	~5 %	TMI based MZ device	L_π= 45 µm	w_{tmi}= 3 µm w = 1 5 µm t =1 5µm λ= 1 55 µm	9 85 mm	177 mW	180 µs		TOMZ device
M Yegi et al [16] InP/GaAs InP	~ 16 %	MMI coupler	L_π=432 µm	w_{mmi}=12 µm w = 1µm t =1 µm λ= 1 55 µm	~ 1 3 mm				MMI based switch
A Neyer [20] Ti $LiNbO_3$	0 6 %	TMI coupler based device	L_π=139 µm	w_{tmi}=2 7 µm w = 1 35 µm t =1 35µm λ= 0 58 µm	6 mm	--			4 wavelength W-MUX W-DMUX

From Table-2.8, it is seen that for TOMZ device, W-MUX/DMUX, Add/drop multiplexer reported by previous authors [20], [69]-[70] it is confirmed that basic components of these devices are DC, MMI and TMI coupler. It is also seen that these devices using SOI waveguides are more compact than the devices using other material mentioned in the table. But SOI based devices has more fiber to chip loss than devices using other materials shown in the table. As mentioned in section-2.7, The $SiO_2/SiON$ waveguide materials has more advantages such chemical inertness, variable index contrast, low propagation loss etc. Because of the above, we have chosen SiO_2/SiON materials. For large scale integration of PID devices for optical networks, it is required to design and implement compact device components for these devices. In this work, we tried to design and propose compact geometry for these devices as reported in chapter-4 and 5.

2.10. Conclusion

In this chapter, we have reviewed directional coupler/MMI couplers/TMI couplers and Mach-Zender type devices demonstrated by different authors. It is seen that the coupling length required for full transfer of the power for TMI coupler is smaller than that of directional coupler and MMI coupler. We have also mentioned grating assisted geometries for compactness of the above devices. We have discussed of advantages of waveguide material SiO_2/SiON over other materials such as SOI, SiO_2/SiO_2-GeO_2, InP/GaAsInP, Ti: LiNbO3 and polymeric materials. The brief review of key devices such as wavelength division multiplexer/de-multiplexer, optical matrix switch and add/drop multiplexer for optical networks have been mentioned. It is found that for the basic components of these devices are DC, TMI and MMI coupler. For large scale integration of PID in optical networks, it is required to make these basic components more compact.

References:

1. Offrein, B. J., et. al. Wavelength tunable optical Add after drop filter with flat pass band for WDM networks, *IEEE Photonics Tech. Lett.* **11**, 239-241, 1999.
2. Sahu, P. P., & Das, A.K. Reduction of crosstalk and loss of compact distributed cascaded Mach-Zehnder filter using lateral offset in Proceedings of Conference on Computer Networking and Multimedia (COMNAM-2000), Jadavpur University, Calcutta, India, 43-48.

3. Ridder, R. M., et al. Silicon Oxynitride Planar Waveguiding Structures for Application in Optical Communication, *IEEE J. Sel Top. Quant. Elect.* **4**, 930-937, 1998.
4. Paiam, M. R., et al. Polarization insensitive 980/1550 nm wavelength de multiplexer using MMI couplers, *IEE Electron. Lett.* **33**, 1219-1220, 1997.
5. Tzong-Yow, Tsai et al., A novel ultrashort two mode interference wavelength division multiplexer for 1.5 μm operation, *IEEE J. Quantum Electron.* **41**, 741-746, 2005.
6. Rajaranjan, M., et al. A rigorous comparison of the performance of directional couplers with multimode interference devices, *IEEE J. Lightwave Tech.* **17,** 243-248, 1999.
7. Janz, F., et al. Bent waveguide couplers for Demultiplexing of arbitrary broadly separated wavelengths using two mode interference, *IEEE Photonics Tech. Lett.* **7**, 1037-1039, 1995.
8. Lai, Q., et al. Tunable wavelength selection switch and multiplexer/ demultplexer based on asymmetric silica on silicon Mach Zehnder interferometer, *IEEE Electron. Lett.* 34, 266-267, 1998.
9. Hida, Y., et al. Wavelength division multiplexer with wide passband and stop band for 1.3μm /1.5μm using silica planar light wave circuit, *IEEE Electron. Lett.*, **31**, 1377-1378, 1995.
10. Kashahara, R., et al. New structures of silica-based planar light wave circuits for low power thermooptic switch and its application to 8x8 optical matrix switch, *J. Light wave Tech* .**20**, 993-1000, 2002.
11. Scilipf, T.R., et al. Design and anlsysis of a control system for optical line circuit used as reconfigurable gain equalizer, *IEEE J. of Lightwave Tech.* **21,** 1944-1952, 1995.
12. Sohma, S. Low switching power silica based super high delta thermo optic switch with heat insulating grooves, *IEEE Electron. Lett.* **38**, 127-128, 2002.

13. Chin, M.K., et al. High index contrast waveguides and devices, *Applied optics*, **44,** 3077-3086, 2005.
14. Ma, Y., et al. Ultracompact Multimode Interference 3-dB Coupler with Strong Lateral Confinement by Deep Dry Etching, *IEEE Photonics Lett.* **12,** 492-494, 2000.
15. Darmawan, S., et al. A Rigorous Comparative Analysis of Directional Couplers and Multimode Interferometers Based on Ridge Waveguides, *IEEE J. of Sel. topics of Quant. Electron.* **11**, 466-475, 2005.
16. Yagi, M., et.al. Versatile multimodes interference photonic switches with partial index modulation regions, *IEEE Electron. Lett.* **36**, 533-534, 2000.
17. Spiekman, L.H., et.al. Extremely small multimode interference coupler and utra short bends on InP by deep etching, *IEEE Photonics Tech. Lett.* **6**, 1008-1010, 1994.
18. Nishihara, H., Haruna, M. and T. Suhara, *Optical Integrated circuits*, Mc. Graw Hill book company, New York, 1985.
19. Papuchon, M., et al. Electrically active optical bifurcation: BOA, *Applied physics letter* **31**, 266-267, 1977.
20. Neyer, A. Integrated optical multichannel wavelength multiplexer for monomode system, *IEEE Electron. Lett.* **20**, 744-746. 1984.
21. Haus, H.A. & Whitaker, N. A. Elimination of cross talk in optical directional couplers, *Applied physics letters* **46**, 1-2, 1985.
22. Krahenbuhl, R., et al. Performance and modeling of advanced Ti:$LiNbO_3$ digital optical switches, *IEEE J. of Light wave Tech.* **20**, 92-99, 2002.
23. Ghatak, A. K. & Thyagarajan, K. *Optical Electronics*, Cambridge University press, 1993.
24. Taylor, H. F. Optical switching and modulation in parallel dielectric waveguides, *J. Applied Physics* **44**, 3257-3264, 1973.
25. Hinton, H. S. Photonic switching using directional coupler using directional couplers, *IEEE communication Magazine* **25**, 16-25, 1987.

26. Cheng, S. Y., et al. Polarization dependence in polymer waveguide directional couplers, *IEEE Photonic Tech. Lett.* **17**, 1465-1467, 2005.
27. Hida, Y. et al. Polymer waveguide thermooptic switch with low electric power consumption at 1.3μm, *IEEE Photonics Tech. Lett.* **5**, 782-784, 1993.
28. Janz, F., et al. Bent waveguide couplers for Demultiplexing of arbitrary broadly separated wavelengths using two mode interference, *IEEE Photonics Tech. Lett.*, **7**, 1037-1039, 1995.
29. Sharma, M., et al. Optical circuits for equalizing group dely dispersion of optical fibers, *IEEE J. of Lightwave Tech.* **12**, 1759-1764, 1994.
30. Mercuse, D. Directional coupler made of nonidentical asymmetric slabs, part-I: Synchronous coupler, *IEEE J. of Lightwave Tech.*, **5**, 113-118, 1987.
31. Digonnet, M. J. F. et al. Analysis of tunable single mode optical fiber coupler, *IEEE J. of Quantum Electronics* **QE-18**, 746-754, 1982.
32. Marcatili, E. A. J. Dielectric rectangular waveguides and directional coupler for integrated optics, *Bell system technical J.* 2071-2099, 1969.
33. Utrich, R., et al. Self imaging in homogeneous planar optical waveguides, *Appl. Phy. Lett.* **27**, 337-339, 1975.
34. Chang, D. C., et al. A hybrid method of paraxial beam propagation in multimode optical waveguides, *IEEE Trans Microwave theory and tech.* **MTT-29,** 923-933, 1981.
35. Soldano, L. B., et al. Optical multimode interference devices on self imaging: principle and applications, *IEEE. J. of lightwave tech.* **13**, 615-627, 1995.
36. Hill, M.T., et al. Optimizing Imbalance and loss in 2x2 3dB multimode interference couplers via access waveguide width, *IEEE J. of Lightwave Tech.* **21**, 2305-2313, 2003.
37. Leothold et al. Multimode Interference couplers with tunable power splitter ratios, *IEEE J. of Lightwave Tech.* **19**, 700-707, 2001.

38. Chinni, V. R., et al. Crosstalk in a lossy directional coupler switch, *IEEE J. of Lightwave Tech.* **13**, 1530-1535, 1995.
39. Levy, D. S., et al. Fabrication of ultracompact 3-dB 2x2 MMI power splitters, *IEEE Photonics Tech. Lett.*, **11**,1009-1011, 1999.
40. Veerman, F. B., et al. An optical passive 3-dB TMI coupler with reduced fabrication tolerance sensitivity, *IEEE J. of Lightwave Tech.* **10**, 306-311, 1992.
41. Inoue, Y., et al. Polarization sensivity of a silica waveguide thermooptic phase shifter for planar lightwave circuits, *IEEE Photonics Tech. Lett.* **4**, 36-38, 1992.
42. Offrein, B. J. et al. Polarization independent thermooptic phase shifter in silicon oxinitride waveguides, *IEEE Photonics Tech. Lett.* **16**, 1483-1485, 2004.
43. Espinola, R. L. et al. Fast and low power thermoptic switch on thin silicon on insulator, *IEEE Photonics Lett.* **15**, 1366-1368, 2003.
44. Wang, Z., et al. Rearrangable nonblocking thermooptic 4x4 switching matrix in silicon on insulator, *IEE proc optoelectron.* **152**, 160-162, 2005.
45. McEwan, I. et al. A high performance optical photopolymer for planar lightwave circuits, in Proceedings of 2002 IEEE/LEOS Workshop on Fibre and Optical Passive Components, 2002, 133-139, 2002.
46. Eldada, L. et al. Advances in polymer integrated optics, *IEEE J. of selected topics in quantum electron.* **6**, 54-67, 2000.
47. Offrein, B. J., et al. Adaptive gain equalizer in high index contrast SiON technology, *IEEE Photonics technology lett.* **12**, 504-506, 2000.
48. Moosburger, R., et al. Digital optical switch based on oversized polymer rib waveguides, *IEEE Photonics Tech. Lett.* **32**, 544-545, 1996.
49. Chan, H. P., et al. A wide angle X-junction polymeric thermooptic digital switch with low crosstalk, *IEEE Photonics Tech. Lett.* **15**, 1210-1212, 2003.
50. Sugita, A., et al. Bridge-suspended silica wave-guide thermooptic phase shifter and its application to Mach-Zehnder type optical switch, *Trans. IEICE.* **E73**, 105-109, Jan, 1990.

51. Kasahara, R., et al. Low power consumption Silica based 2x2 thermooptic switch using trenched silicon substrate, *IEEE Photonics Tech. Lett.* **11**, 1132-1134, September, 1999.
52. Lai, Q., et al. Low power compact 2x2 thermooptic silica on silicon waveguide switch with fast response time, *IEEE Photonics Tech. Lett.* **10**, 681-683, 1998.
53. Okuno, M., Highly integrated PLC type optical switches for OADM and OxC systems in IEEE Optical Fiber Communications Conference (OFC'2003), 2003, Kanagawa, Japan, 169-170.
54. Zappe, H. P. *Introduction to Semiconducor Integrated Optics*, Artech House, Boston, 1995.
55. Takato, N., et al. Silica based Integrated Optic Mach Zehnder Multi/Demultiplexer family with channel spacing of 0.01-250 nm, *IEEE selected areas of comm.* **8**, 1120-1127, 1990.
56. Nishihara, H., Haruna, M. & Suhara, T. *Optical Intagrated Circuits*, McGraw-Hill, New York, 1989.
57. Mercuse, D. Bending losses of the asymmetric slab waveguide, Bell system technical J. **50**, 2551-2563, 1971.
58. Kitoh, T. et al. Bending loss reduction in silica-based waveguides by using lateral offsets, *IEEE J. of Lightwave Tech.* **13**, 555-562, 1995.
59. Kashahara, R., et al. New structures of silica-based planar light wave circuits for low power thermooptic switch and its application to 8x8 optical matrix switch, *IEEE J. light wave Tech.* **20**, 993-1000, 2002.
60. Kawachi, M. Recent progress in silica based planar lightwave circuits on silicon, in IEE Proceedings, Optoelectron. **43**, 257-261, 1996.
61. Okuno, M. Highly integrated PLC type optical switches for OADM and OXC systems in IEEE Optical Fiber Communication Conference (OFC-2003), Kanagawa, Japan, 2003.
62. Earnshaw, M.P., et al. Highly integrated wavelength selective switch, *IEEE Electronics lett.* 39, 1397-1398, 2003.

63. Sohma, S., et al. Low switching power silica based super high delta thermooptic switch with high insulating grooves, *IEE Electronics lett.* **38**, 127-128, 2002.

64. Fluck, E. et al. Compact Versatile thermooptical space switch based on beam steering by a waveguide array, *IEEE Photonics Tech. Lett.* **11**, 1399-140, 1999.

65. Offrein, B. J., et al. Wavelength tunable optical Add after drop filter with flat passband for WDM networks, *IEEE Photonics lett.* **11**, 239-241, 1999.

66. Offrein, B. J., et al. Adaptive gain Equalizer in high-index- contrast SiON Technology, *IEEE Photonics Technology Lett.* **12**, 504-506, 2000.

67. Chatterjee, B. C., et al. Priority based Routing and Wavelength Assignment with Traffic Grooming for Optical Networks, *IEEE/OSA Journal of Optical Communications and Networking.* **4**, 480-489, 2012,

68. Chatterjee, B. C., et al. A Heuristic Priority based Wavelength Assignment Scheme for Optical Networks, *Optik-International Journal for Light and Electron Optics.* **123**, 1505-1510, 2012,

69. Sahu, P. P. Compact optical multiplexer using silicon nano-waveguide, IEEE *J. of selected topics in Quantum electronics.* **15**, 1537-1541, 2009.

70. Sahu, P. P. Polarization insensitive thermally tunable Add/Drop multiplexer using cascaded Mach Zehnder coupler, *Applied Physics: Lasers and optics.* **B92**, 247-252, 2008.

71. Sahu, P. P. & Das, A. K. Polarization-Insensitive Thermo-Optic Mach Zehnder Device Based on Silicon Oxinitride Waveguide with Fast Response Time, Fiber and integrated optics. **29**, 10-20, 2010.

72. Passaro, V. M. N. Optimal Design of Grating-Assisted Directiona Couplers, *J. light wave Tech.* **18**, 973-985, 2000.

73. Chang, K. C., et al. Scattering and guiding of waves by dielectric gratings with arbitrary profiles, *J. Opt. Soc. Amer.* 70, 804–813, 1980.

74. Marcuse, D. Radiation loss of grating-assisted directional coupler, *IEEE J. Quantum Electron.* **26**, 675–684, 1990.

75. Sun, N. H., et al. Analysis of grating-assisted directional couplers using the floquest-bloch theory, *IEEE J. Lightwave Technol.* **15**, 2301–2314, 1997.

76. Tsai, T. Y., et al. A novel ultra compact two mode interference wavelength multiplexer for 1.5 μm operation, *IEEE J. Quantum Electron.* 41, 741–746, 2005.

77. Parker, M. C. & Walker, S. D. Design of arrayed waveguide gratings using hybrid Fourier Fresnel transform techniques, *IEEE J. Sel. Topics Quantum Electron.*, **5**, 1379–1384, 1999.

78. Das, A. K. & Sahu, P. P. Polymeric directional coupler with lateral offset, in Proceeding. of International Conference on Fiber Optics, Calcutta, 744-746, 2000.

79. Hadley, G. R. Transparent boundary condition for the beam propagation method, *J. Quantum Electron.* **28**, 363-370, 1992.

80. Passaro, V. M. N., & Armenise, M. N. Analysis of radiation loss in grating-assisted codirectional couplers, *IEEE J. Quantum Electron.* **31**, 1691–1697, 1995.

81. Rahman, B. A. M. & Davies, J. B. Finite element analysis of optical and microwave problems, *IEEE Trans. Microwave Theory Tech.* **MTT-32**, 20-28, 1983.

82. Koshiba, M., et al., Improved finite element formulation in terms of the magnetic fields vector for dielectric waveguides, IEEE Trans. Microwave Theory Tech. **MTT-33**, 227-233, 1985.

83. Lee, J. F., et al. Full wave analysis of dielectric waveguides using tangential finite elements, *IEEE Trans. Microwave Theory Tech.* **MTT-39**, 1262-1271, 1991.

84. Yee, K. S. Numerical solution of initial boundary value problems involving Maxwell's equations in isotropic media, *IEEE Trans. Antennas Prop.* **AR-14**, 302-307, 1966.

85. Taflov, A. Computational Electrodynamics: The Finite Difference Time Domain Method, Artech House, MA, 1995.

86. Strang, G. On the construction and comparison of difference schemes, *SIAM J. Numerical Analysis*, **5**, 506-517, 1968.

87. Shang, J. S. Characteristic based methods for the time-domain Maxwell equations, *IEEE Ant. Prop. Magazine*, **37**, 15-25, 1995.

88. Colella, P. & Woodward, P. R. The piecewise parabolic method (PPM) for gas dynamical simulations, *J. Comp. Phys.* 54, 174-201, 1984.

89. Marcatili, E. A. J. Dielectric rectangular waveguide and directional coupler for integrated optics, *Bell Syst. Tech. J.* **48,** 2071-2102, 1969.

90. Knox, R. M. & Toulios, P. P Integrated circuits for the millimeter through optical frequency range in, Proceeding M.R.I. Symp. Submillimeter waves, Fox J. Ed. Brooklyn, N.Y.: Polytechnic Press, 1970.

****

Chapter-3:

Transformation Relationship of Directional Coupler with Two Mode Interference (TMI) Coupler and Multimode Interference (MMI) Coupler by using Simple Effective Index Method (SEIM)

3.1. Introduction

As reviewed in chapter -1 and -2, the Photonic Integrated Devices (PID) have become essential devices in application of all optical networks due to its reliability, immunity to vibration and electromagnetic interference, low loss transmission, small size, light weight and low power consumption. Further, in comparison to fiber devices, PID's are more compact and of low cost due to its capability of mass production. The basic components of these PIDs are Directional Coupler (DC) [1]-[4], Two Mode Interference (TMI) coupler [5]-[8], Multimode Interference (MMI) coupler [9]-[12], X-branches [13], Y-branches [13] and Mach-Zhender (MZ) structure [13]-[14] etc. Further, directional coupler [15]-[16], MMI coupler [17]-[19] and TMI coupler [20]-[21] based devices have been widely used in the applications of optical networks due to its attractive properties such as compactness, tolerance to a range of fabrication parameters, an inherent balance and low optical loss.

In this chapter, a mathematical model using Simple Effective Index Method (SEIM) [3][4],[22]-[25] based on sinusoidal modes have been developed for theoretical analysis of coupling characteristics of directional coupler, TMI coupler and MMI coupler with embedded rectangular core waveguide. In section-3.2, coupling behavior of DC and its coupling characteristics has been discussed using SEIM. Further, theoretical analysis of coupling characteristics of TMI coupler using the SEIM based numerical model is mentioned and the results of TMI coupler reported by different authors are also reviewed. Section-3.4 describes the mathematical model based on SEIM, coupling characteristics of MMI coupler and results demonstrated by previous authors. The coupling characteristics of DC, TMI couplers and MMI couplers are also compared. It is found that the TMI coupler provides the lower coupling length than the other two couplers. The normalized coupling power at the cross state and bar state of TE polarized light for these devices are also discussed and analyzed. Finally, the SEIM based results are compared with the other numerical techniques such as Marcuse theory [26] and Beam Propagation Method (BPM) [27]-[28] results obtained by using commercially available software based on finite difference time domain method (FDTD).

3.2. Directional Coupler (DC)

Directional Coupler (DC) consists of two dielectric waveguides placed in close proximity to each other for coupling of guided power based on phase difference of two guided modes– even mode and odd mode. As discussed in the chapter-2, the basic principle of a directional coupler is based on the coupled mode theory which describes the coupling of evanescent lightwave that occurs between two adjacent parallel waveguides through the overlapping of the evanescent waves of the propagating modes. In order to study the above, a mathematical model has been derived using Simple Effective Index Method (SEIM) based on sinusoidal modes for accurate estimation of coupling power. The Effective Index Method (EIM) is used to find approximate solutions for the propagation constants of three dimensional waveguides as details are discussed in following sections.

3.2.1 Mathematical Model Based on SEIM for DC

Fig-3.1 shows the schematic three dimensional (3D) view of a 2x2 conventional directional coupler with coupling gap ~h consisting of a coupling region of length L, two single mode input access waveguides and two single mode output access waveguides. The coupling region consists of two parallel identical waveguides of core width 'a' and thickness 'b' placed close to each other showing small coupling separation gap 'h'. The separation between center of cores is 2d (where 2d=a+h) and n_1, n_3 are the refractive indices of the core and coupling gap's cladding region respectively whereas n_2 is refractive index of cladding region other than coupling gap cladding region. The input single mode field of propagation constant β, incident through the access waveguide-2 excites even and odd modes in coupling region where these modes propagate with propagation constants β_e and β_o (where $\beta_e=\beta+C$, $\beta_o=\beta-C$, C=coupling coefficient). P_1 is the input incident power in waveguide-2 and output power for output access waveguide-3 and waveguide-4 are

P_3 and P_4 respectively.

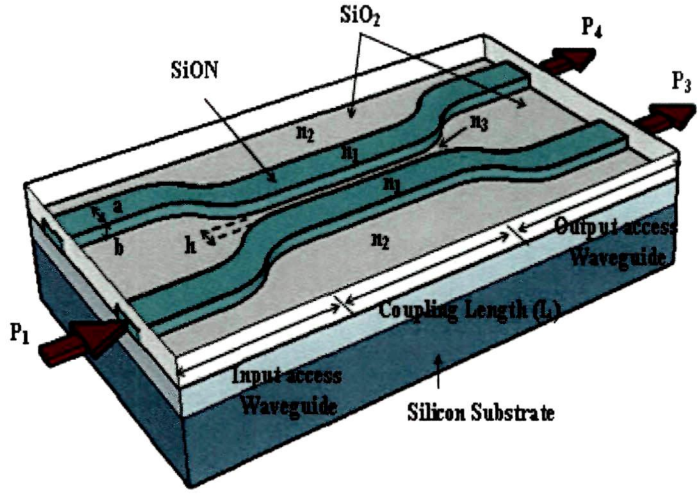

(a)

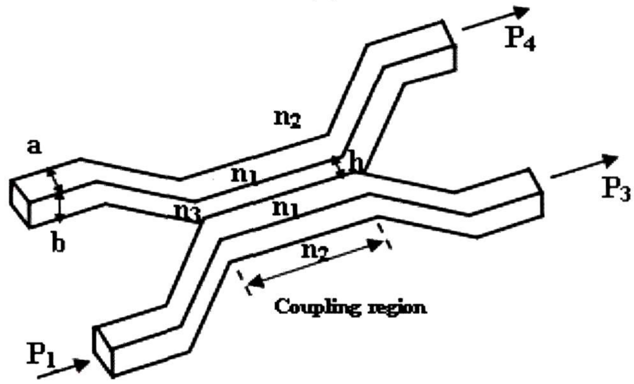

(b)

Fig-3.1: Schematic 3D view of 2x2 conventional directional coupler (a) device layout and (b) waveguide layer

If the coupling takes place in the region $0<z<L$, in which the even mode and odd mode are propagate with propagation constants β_e and β_o respectively. When the phase shift between the even and odd modes become 180^0 (or π), the propagation distance L_π (also known as the beat length) is defined by [14],

$$L_{\pi} = \frac{\pi}{\beta_e - \beta_o} \tag{3.1}$$

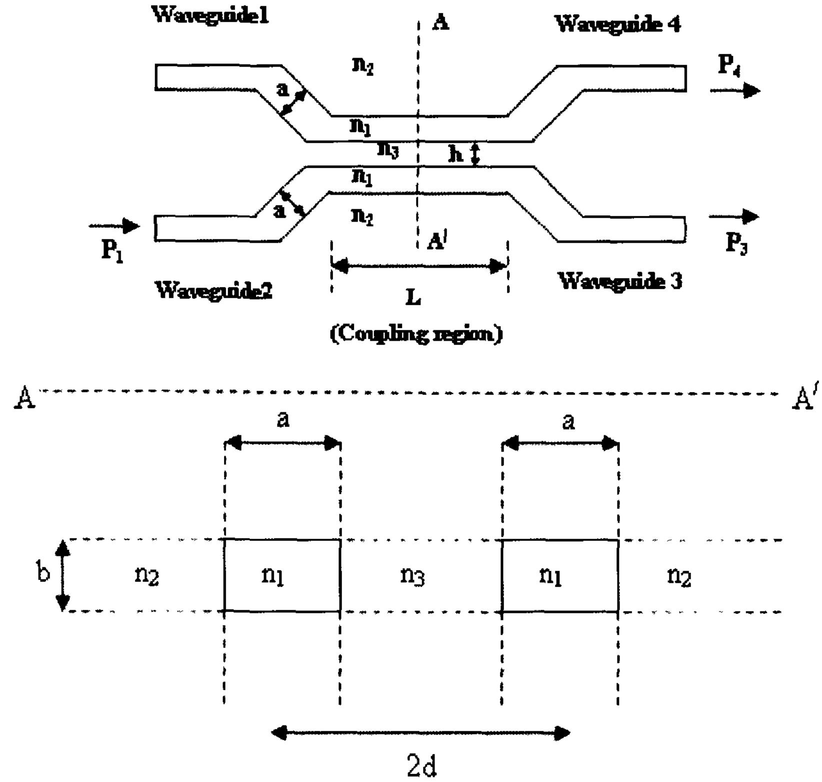

Fig-3.2: Schematic directional coupler with coupling gap, h and coupling length L (a) 2D top view (b) Cross sectional view along line AA$^{/}$

Fig-3.2(a) shows the two dimensional (2D) schematic top view of guiding (core) layer as shown in Fig-3.1 of a conventional directional coupler with coupling gap ~h, whereas Fig-3.2(b) shows the cross sectional view along line AA$^{/}$ with core and cladding refractive indices respectively.

As reviewed in section-2.2.1 of previous chapter-2, the basic idea of the simple effective index method (SEIM) is to approximate a 2D waveguide by a one dimensional one with an effective index profile of the original structure. Considering effective index method, 3D waveguides of DC is divided in to two 2D waveguides: firstly with light confinement along x axis and then 2D waveguides with light confinement along y-axis as shown in Fig-3.3(a).

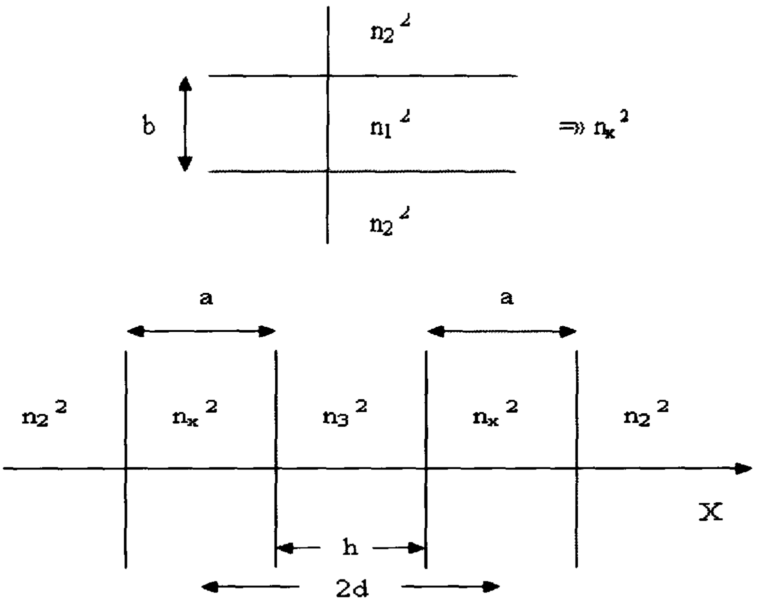

Fig-3.3 (a): Effective index method solving a single slab for effective refractive index n_x and resulting in an array of two slabs with refractive index, n_x

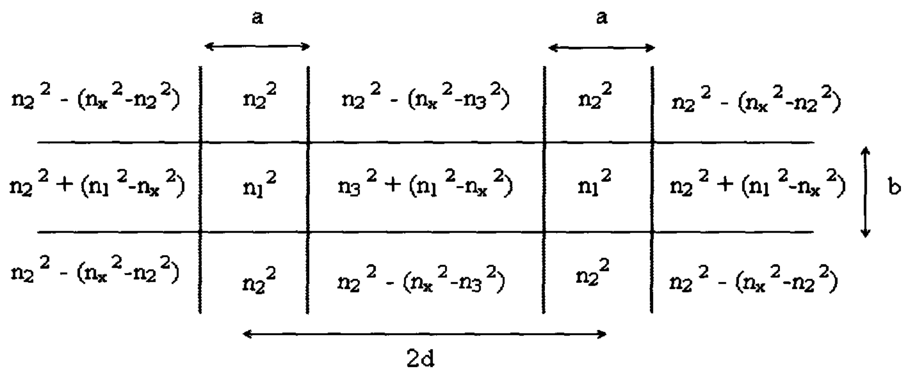

Fig-3.3 (b): Cross sectional view of SEIM applies to the directional coupler consisting of two parallel rectangular waveguide cores

In order to approximate a non-separable mode field of the original structure of the DC into separable mode field along different axis, there must be existence of a separate refractive index profile. Such separable refractive index profile can be defined by using the simple effective index method (SEIM-X) along x-direction to the original structure as shown in Fig-3.3(a). Fig-3.3(b) shows a cross sectional view of SEIM-X applies to the directional coupler along with the refractive index profile. The refractive index in the cladding region at both sides of the waveguide cores is increased by an amount of $\left(n_1^2 - n_x^2\right)$ whereas at the corner region of both waveguides, it is decreased by an amount of $\left(n_x^2 - n_2^2\right)$. Considering asymptotic approximation [3], the mode field (based on sinusoidal) of a single rectangular core waveguide can be defined in terms of the function $\psi_0(x, y)$ for the core and different cladding region as

Cladding Region:

$$\psi_0(x,y) = \begin{cases} \dfrac{\pi b}{2aV_1} Sin\left[\dfrac{\pi\left(y+\frac{b}{2}\right)}{b}\right] \exp\left[-V_1\left(\dfrac{|x|-\frac{a}{2}}{\frac{b}{2}}\right)\right] & ; -\infty \le x \le -\dfrac{a}{2},\ -\dfrac{b}{2} \le y \le \dfrac{b}{2} \\ \dfrac{\pi b}{2aV_2} Sin\left[\dfrac{\pi\left(y+\frac{b}{2}\right)}{b}\right] \exp\left[-V_2\left(\dfrac{|x|-\frac{a}{2}}{\frac{b}{2}}\right)\right] & ; \dfrac{a}{2} \le x \le \infty,\ -\dfrac{b}{2} \le y \le \dfrac{b}{2} \\ \dfrac{\pi^2 b}{4aV_1^2} \exp\left[-V_1\left(\dfrac{|x|-\frac{a}{2}}{\frac{b}{2}}\right)\right] \exp\left[-V_1\left(\dfrac{|y|-\frac{b}{2}}{\frac{b}{2}}\right)\right] & ; \begin{array}{l} -\infty < x < -\dfrac{a}{2},\ \dfrac{b}{2} \le y < \infty \\ -\infty < x < -\dfrac{a}{2},\ -\infty < y \le -\dfrac{b}{2} \end{array} \\ \dfrac{\pi^2 b}{4aV_2^2} \exp\left[-V_2\left(\dfrac{|x|-\frac{a}{2}}{\frac{b}{2}}\right)\right] \exp\left[-V_2\left(\dfrac{|y|-\frac{b}{2}}{\frac{b}{2}}\right)\right] & ; \begin{array}{l} \dfrac{a}{2} \le x < \infty,\ \dfrac{b}{2} \le y < \infty \\ \dfrac{a}{2} \le x < \infty,\ -\infty < y \le \dfrac{b}{2} \end{array} \\ \dfrac{\pi}{2V_1} Sin\left[\dfrac{\pi\left(x+\frac{a}{2}\right)}{a}\right] \exp\left[-V_1\left(\dfrac{|y|-\frac{b}{2}}{\frac{b}{2}}\right)\right] & ; \begin{array}{l} -\dfrac{a}{2} \le x \le \dfrac{a}{2},\ -\dfrac{b}{2} \le y < \infty \\ -\dfrac{a}{2} \le x \le \dfrac{a}{2},\ -\infty < y \le -\dfrac{b}{2} \end{array} \end{cases} \quad (3.2)$$

Core Region:

$$\psi_0(x,y) = Sin\left[\frac{\pi\left(x+\frac{a}{2}\right)}{a}\right] Sin\left[\frac{\pi\left(y+\frac{b}{2}\right)}{b}\right] \quad ; -\frac{a}{2}\langle x \langle \frac{a}{2} \text{ and } -\frac{b}{2}\langle y \langle \frac{b}{2} \tag{3.3}$$

where $V_1 = \frac{b}{2}k(n_1^2 - n_2^2)^{1/2}$, $V_2 = \frac{b}{2}k(n_1^2 - n_3^2)^{1/2}$

3.2.2 Coupling Coefficient of Directional Coupler

According to the coupled mode theory, the normalized coupling coefficient can be defined as [26][29]-[30],

$$\frac{C}{C_0} = \frac{V\int_{-b/2}^{b/2}\int_{d-\frac{a}{2}}^{d+\frac{a}{2}} \psi_0(x+d,y)\psi_0(x-d,y)\,dxdy}{2\int_{-\infty}^{\infty}\int_{-\infty}^{\infty}\psi_0^2(x,y)\,dxdy} \tag{3.4}$$

where $V = \frac{b}{2}k(n_{core}^2 - n_{clad}^2)^{1/2}$

Applying coupled mode theory for directional coupler (as shown in Fig-3.3(b)); the Eq. (3.4) can be express as,

$$\frac{C}{C_0} = \frac{V_1\int_{-b/2}^{b/2}\int_{d-\frac{a}{2}}^{d+\frac{a}{2}} \psi_0(x+d,y)\psi_0(x-d,y)dxdy}{2\int_{-\infty}^{\infty}\int_{-\infty}^{\infty}\psi_0^2(x,y)dxdy} + \frac{V_2\int_{-b/2}^{b/2}\int_{d-\frac{a}{2}}^{d+\frac{a}{2}} \psi_0(x+d,y)\psi_0(x-d,y)dxdy}{2\int_{-\infty}^{\infty}\int_{-\infty}^{\infty}\psi_0^2(x,y)dxdy} \tag{3.5}$$

$$\text{where } V_1 = \frac{b}{2}k(n_1^2 - n_2^2)^{1/2} \text{ and } V_2 = \frac{b}{2}k(n_1^2 - n_3^2)^{1/2} \tag{3.6}$$

Applying the boundary conditions from Eq. (3.2) and Eq. (3.3) in the Eq. (3.5) and taking integration with respect to different boundary limits, finally we obtain,

$$\frac{C}{C_0}=\frac{V_1}{2ab}\times\int_{-b/2}^{b/2}\int_{d-\frac{a}{2}}^{d+\frac{a}{2}}\psi_0(x+d,y)\psi_0(x-d,y)dxdy+\frac{V_2}{2ab}\times\int_{-b/2}^{b/2}\int_{d-\frac{a}{2}}^{d+\frac{a}{2}}\psi_0(x+d,y)\psi_0(x-d,y)dxdy$$

where the resultant integrand values of the denominator is $\int_{-\infty}^{\infty}\int_{-\infty}^{\infty}\psi_0^{\,2}(x,y)dxdy=ab$.

$$\frac{C}{C_0}=\frac{V_1}{2ab}\times\int_{-b/2}^{b/2}\int_{d-\frac{a}{2}}^{d+\frac{a}{2}}\left(\frac{\pi b}{2aV_1}\right)^2\sin^2\left[\frac{\pi\left(y+\frac{b}{2}\right)}{b}\right]\exp\left[-V_1\left(\frac{|x+d|-\frac{a}{2}}{b/2}\right)\right]\exp\left[-V_1\left(\frac{|x-d|-\frac{a}{2}}{b/2}\right)\right]dxdy$$

$$+\frac{V_2}{2ab}\times\int_{-b/2}^{b/2}\int_{d-\frac{a}{2}}^{d+\frac{a}{2}}\left(\frac{\pi b}{2aV_2}\right)^2\sin^2\left[\frac{\pi\left(y+\frac{b}{2}\right)}{b}\right]\exp\left[-V_2\left(\frac{|x+d|-\frac{a}{2}}{b/2}\right)\right]\exp\left[-V_2\left(\frac{|x-d|-\frac{a}{2}}{b/2}\right)\right]dxdy$$

$$\frac{C}{C_0}=\frac{V_1}{2ab}\times\left(\frac{\pi b}{2aV_1}\right)^2\times\int_{-b/2}^{b/2}\sin^2\left[\frac{\pi\left(y+\frac{b}{2}\right)}{b}\right]\int_{d-\frac{a}{2}}^{d+\frac{a}{2}}\left\{\exp\left[-V_1\left(\frac{|x+d|-\frac{a}{2}}{b/2}\right)\right]\exp\left[-V_1\left(\frac{|x-d|-\frac{a}{2}}{b/2}\right)\right]\right\}dxdy$$

$$+\frac{V_2}{2ab}\times\left(\frac{\pi b}{2aV_2}\right)^2\times\int_{-b/2}^{b/2}\sin^2\left[\frac{\pi\left(y+\frac{b}{2}\right)}{b}\right]\int_{d-\frac{a}{2}}^{d+\frac{a}{2}}\left\{\exp\left[-V_2\left(\frac{|x+d|-\frac{a}{2}}{b/2}\right)\right]\exp\left[-V_2\left(\frac{|x-d|-\frac{a}{2}}{b/2}\right)\right]\right\}dxdy$$

$$\frac{C}{C_0}=\frac{V_1}{2ab}\times\left(\frac{\pi b}{2aV_1}\right)^2\times\frac{b}{2}\times\frac{-b}{4V_1}\left[\exp\left\{\frac{-4V_1d}{b}\right\}-\exp\left\{\frac{-4V_1(d-a)}{b}\right\}\right]$$

$$+\frac{V_2}{2ab}\times\left(\frac{\pi b}{2aV_2}\right)^2\times\frac{b}{2}\times\frac{-b}{4V_2}\left[\exp\left\{\frac{-4V_2d}{b}\right\}-\exp\left\{\frac{-4V_2(d-a)}{b}\right\}\right]$$

$$\frac{C}{C_0}=\left(\frac{-\pi^2b^3}{64a^3V_1^2}\right)\times\left[\exp\left\{\frac{-4V_1d}{b}\right\}-\exp\left\{\frac{-4V_1(d-a)}{b}\right\}\right]$$

$$+\left(\frac{-\pi^2b^3}{64a^3V_2^2}\right)\times\left[\exp\left\{\frac{-4V_2d}{b}\right\}-\exp\left\{\frac{-4V_2(d-a)}{b}\right\}\right]$$

$$\frac{C}{C_0}=\left(\frac{\pi^2 b^3}{64a^3V_1^2}\right)\times\left[\exp\left\{\frac{-4V_1(d-a)}{b}\right\}-\exp\left\{\frac{-4V_1 d}{b}\right\}\right]$$
$$+\left(\frac{\pi^2 b^3}{64a^3V_2^2}\right)\times\left[-\exp\left\{\frac{-4V_2(d-a)}{b}\right\}-\exp\left\{\frac{-4V_2 d}{b}\right\}\right]$$

$$\frac{C}{C_0}=\left(\frac{\pi^2 b^3}{64a^3V_1^2}\right)\times\left[\exp\left\{\frac{-2V_1(2d-2a)}{b}\right\}-\exp\left\{\frac{-2V_1(h+a)}{b}\right\}\right]$$
$$+\left(\frac{\pi^2 b^3}{64a^3V_2^2}\right)\times\left[-\exp\left\{\frac{-2V_2(2d-2a)}{b}\right\}-\exp\left\{\frac{-2V_2(h+a)}{b}\right\}\right]$$

From the Fig.-3.3(b), substituting 2d=a + h $\Rightarrow$h=2d-a, we have

$$\frac{C}{C_0}=\left(\frac{\pi^2 b^3}{64a^3V_1^2}\right)\times\left[\exp\left\{\frac{-2V_1(h-a)}{b}\right\}-\exp\left\{\frac{-2V_1(h+a)}{b}\right\}\right]$$
$$+\left(\frac{\pi^2 b^3}{64a^3V_2^2}\right)\times\left[-\exp\left\{\frac{-2V_2(h-a)}{b}\right\}-\exp\left\{\frac{-2V_2(h+a)}{b}\right\}\right]$$

$$\frac{C}{C_0}=\left(\frac{\pi^2 b^3}{64a^3V_1^2}\right)\times\exp\left\{\frac{-2V_1 h}{b}\right\}\times\left[\exp\left\{\frac{2V_1 a}{b}\right\}-\exp\left\{\frac{-2V_1 a}{b}\right\}\right]$$
$$+\left(\frac{\pi^2 b^3}{64a^3V_2^2}\right)\times\exp\left\{\frac{-2V_1 h}{b}\right\}\times\left[-\exp\left\{\frac{2V_2 a}{b}\right\}-\exp\left\{\frac{-2V_2 a}{b}\right\}\right]$$

Thus, using the asymptotic analysis of SEIM model of DC [shown in Fig-3.3(a)] and equation (3.4), the normalized coupling coefficient is approximated as

$$\frac{C}{C_0}=\frac{\pi^2 b^3}{64a^3}\left[\begin{array}{l}\frac{1}{V^2_1}\exp\left(\frac{-2V_1}{b}h\right)\left\{\exp\left(\frac{2V_1 a}{b}\right)-\exp\left(\frac{-2V_1 a}{b}\right)\right\}\\+\frac{1}{V^2_2}\exp\left(\frac{-2V_2}{b}h\right)\left\{\exp\left(\frac{2V_2 a}{b}\right)-\exp\left(\frac{-2V_2 a}{b}\right)\right\}\end{array}\right] \quad (3.7)$$

Considering a=b for square embedded channel waveguide and substituting the values of V_1, V_2 from Eqn. (3.6) in Eqn. (3.7) we obtain,

$$\frac{C}{C_0}=\frac{\pi^2 b^3}{64a^3}\times\frac{\exp\left\{-\frac{2h}{b}\times\frac{b}{2}k\left(n_{eff}^2-n_2^2\right)^{1/2}\right\}}{\left(\frac{b}{2}\right)^2 k^2\left(n_1^2-n_2^2\right)}\times\left[\exp\left\{\frac{2a}{b}\times\frac{b}{2}k\left(n_1^2-n_2^2\right)^{1/2}\right\}-\exp\left\{-\frac{2a}{b}\times\frac{b}{2}k\left(n_1^2-n_2^2\right)^{1/2}\right\}\right]$$

$$+\frac{\pi^2 b^3}{64a^3}\times\frac{\exp\left\{-\frac{2h}{b}\times\frac{b}{2}k\left(n_1^2-n_3^2\right)^{1/2}\right\}}{\left(\frac{b}{2}\right)^2 k^2\left(n_1^2-n_3^2\right)}\times\left[\exp\left\{\frac{2a}{b}\times\frac{b}{2}k\left(n_1^2-n_3^2\right)^{1/2}\right\}-\exp\left\{-\frac{2a}{b}\times\frac{b}{2}k\left(n_1^2-n_3^2\right)^{1/2}\right\}\right]$$

$$\begin{aligned}\frac{C}{C_0}&=\frac{\pi^2}{16b^2k^2\left(n_1^2-n_2^2\right)}\exp\left\{-hk\left(n_{eff}^2-n_2^2\right)^{1/2}\right\}\left[\exp\left\{bk\left(n_1^2-n_2^2\right)^{1/2}\right\}-\exp\left\{-bk\left(n_1^2-n_2^2\right)^{1/2}\right\}\right]\\&+\frac{\pi^2}{16b^2k^2\left(n_1^2-n_3^2\right)}\exp\left\{-hk\left(n_1^2-n_3^2\right)^{1/2}\right\}\left[\exp\left\{bk\left(n_1^2-n_3^2\right)^{1/2}\right\}-\exp\left\{-bk\left(n_1^2-n_3^2\right)^{1/2}\right\}\right]\end{aligned} \tag{3.8}$$

where $$C_0=\frac{0.4}{(1+0.2h)}\times\frac{\left(n_1^2-n_{eff(TE)}^2\right)\sqrt{n_{eff(TE)}^2-n_2^2}}{n_{eff(TE)}\left(n_1^2-n_3^2\right)\left[W+\frac{2}{k_0\sqrt{n_{eff(TE)}^2-n_2^2}}\right]}\text{ ; for TE mode} \tag{3.9}$$

$$C_0=\frac{0.4}{(1+0.2h)}\times\frac{\left(n_1^2-n_{eff(TM)}^2\right)\sqrt{n_{eff(TM)}^2-n_2^2}}{n_{eff(TM)}\left(n_1^2-n_3^2\right)\left[W+\frac{2}{k_0\sqrt{n_{eff(TM)}^2-n_2^2}}\right]}\text{ ; for TM mode} \tag{3.10}$$

$$\left.\begin{aligned}n_{eff(TE)}&=\beta_{TE}\left(\frac{\lambda}{2\pi}\right)\\n_{eff(TM)}&=\beta_{TM}\left(\frac{\lambda}{2\pi}\right)\end{aligned}\right\} \tag{3.11}$$

where β_{TE}, β_{TM} are the propagation constants of TE and TM mode respectively that are determined from dispersive relations as discussed in section-2.3.2 of chapter-2.

In this directions, the propagation constants β_{TE}, β_{TM} for TE or TM modes as discussed above, are estimated using dispersion relations [14] of a 3D waveguide (shown in Fig-3.4) as follows:

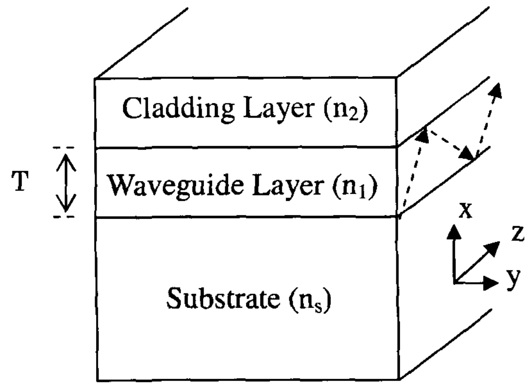

Fig-3.4: Basic Optical Waveguide Structure with three layers: Cladding layer, Waveguide Core layer (thickness T) and Substrate layer of refractive indices n_2, n_1 and n_s respectively.

The dispersion equation of TE modes for a two dimensional asymmetric step index planar waveguide along x-axis as shown in Fig-3.4, can be written as

$$V_I\sqrt{1-b_I} = (m+1)\pi - \tan^{-1}\sqrt{\frac{1-b_I}{b_I}} - \tan^{-1}\sqrt{\frac{1-b_I}{b_I+a_I}} \tag{3.12}$$

where m is an integer, a_I asymmetric factor for the waveguide structure with normalized guide index, $b_I = (N^2-n_s^2)/(n_1^2-n_s^2)$ and normalized frequency, $V_I = k_0 T\sqrt{(n_I^2-n_s^2)}$ with $k_0 = 2\pi/\lambda$.

The above dispersion equation (3.12) for a two dimensional symmetric step index planar waveguide reduces to,

$$V_I\sqrt{1-b_I} = (m+1)\pi - 2\tan^{-1}\sqrt{\frac{1-b_I}{b_I}} \tag{3.13}$$

where m is an integer and a_I=0 for symmetric waveguide and normalized frequency,

$$V_I = k_0 T\sqrt{(n_I^2-n_s^2)}, \quad k_0 = 2\pi/\lambda.$$

Now, substituting the values of b_I that satisfying the equation (3.13) in the following equation, N_I is calculated as follows

$$N_I = \sqrt{n_1^2 + b_I\left(n_2^2 - n_1^2\right)} \tag{3.14}$$

The dispersion equation for the 2D waveguide as shown in Fig-3.4 along y-axis, can be written as,

$$V_{II}\sqrt{1-b_{II}} = (n+1)\pi - 2\tan^{-1}\sqrt{\frac{1-b_{II}}{b_{II}}} \tag{3.15}$$

where n is an integer, normalized guide index, $b_{II} = (n_{eff}^2 - n_2^2)/(N_I^2 - n_1^2)$ and normalized frequency, $V_{II} = k_0 b\sqrt{(N_I^2 - n_1^2)}$; $k_0 = \frac{2\pi}{\lambda}$ respectively.

Further, substituting the values of b_{II} that satisfying the equation (3.15) in the following equation, n_{eff} is calculated.

$$n_{eff} = \sqrt{n_2^2 + b_{II}\left(N_I^2 - n_1^2\right)} \tag{3.16}$$

Thus by calculating effective refractive index (n_{eff}) using simple effective index method for a three dimensional waveguide, the propagation constant is estimated as,

$$\beta = k_0 n_{eff\,(TE)} = \left(\frac{2\pi}{\lambda}\right) n_{eff\,(TE)} \tag{3.17}$$

Similarly for TM modes, $n_{eff\,(TM)}$ can be estimated from dispersion equation of TM mode [14] and propagation constant can be estimated as,

$$\beta = k_0 n_{eff\,(TM)} = \left(\frac{2\pi}{\lambda}\right) n_{eff\,(TM)} \tag{3.18}$$

Again, the coupling takes place in the $0<z<L$ region of directional coupler in which the even and odd modes are propagated with propagation constants β_e and β_o. The phase shift between the even and odd modes becomes π when the propagation distance L_π is given by

$$L_\pi = \frac{\pi}{\beta_e - \beta_o} = \frac{\pi}{2C} \tag{3.19}$$

The coupling coefficients (C) for the SEIM model of directional coupler are estimated using equation (3.8)-(3.18) for both TE/TM polarizations.

3.2.3 Coupling Characteristics of DC

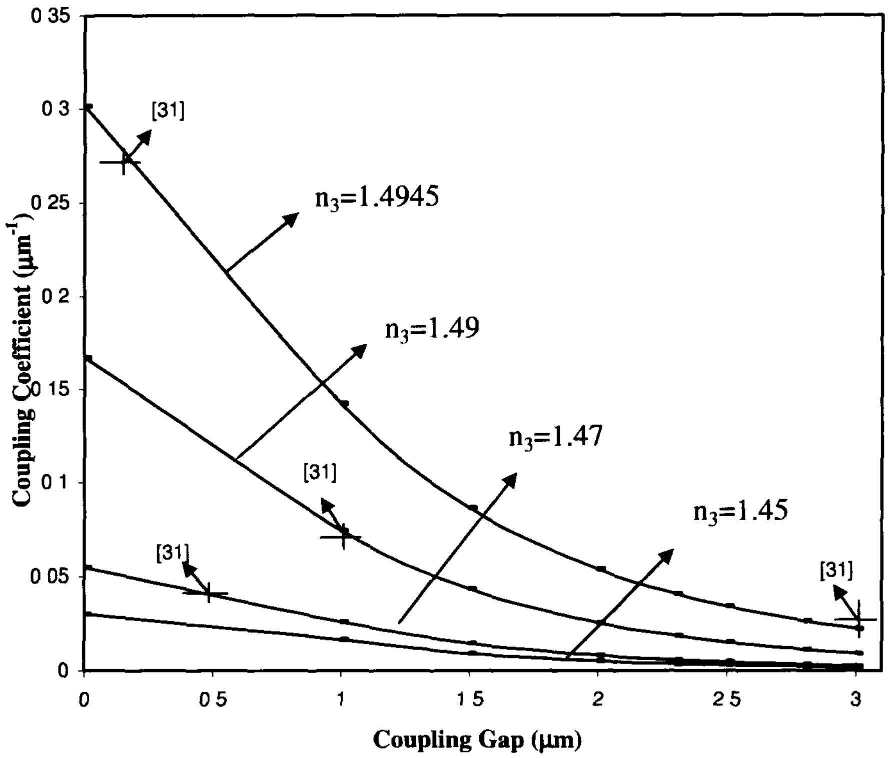

Fig-3.5: Coupling characteristics of DC using SEIM with n_3=1.45, 1.47, 1.49, 1.4945 with a=b=1.5 μm, n_1=1.5, n_2=1.45 and Δn=5%

Fig-3.5 shows the coupling characteristics versus coupling gap ~h of directional coupler (DC) obtained by using simple effective index method (SEIM) based on sinusoidal mode for different coupling gap refractive indices n_3=1.45, 1.47, 1.49, 1.4945 with a=b=1.5 μm, n_1=1.5, n_2=1.45 and Δn=5% respectively. It is found that the coupling coefficient of DC decreases as the coupling gap increases and the rate of decrease of coupling coefficient with respect to h increases as coupling gap refractive index n_3 increases. The cross point in the figure represents the experimental point demonstrated by previous authors [31]-[32] with SiON/SiO_2 matching well with the theoretical curves.

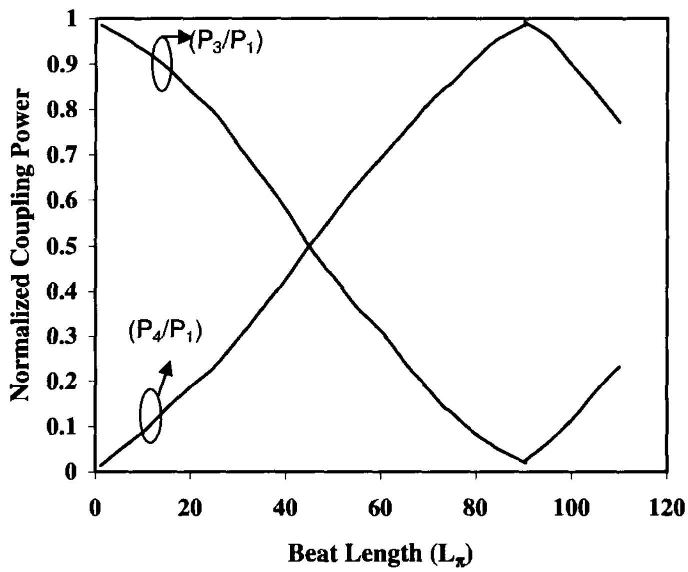

Fig-3.6: Normalized coupled power versus beat length for DC with coupling gap h~0.5 μm, a=b=1.5 μm, n_2=1.45, Δn=5 % and λ=1.55 μm.

The coupled power to the output access waveguide of directional coupler can be estimated using coupled mode theory [29] as discussed in Section-2.3.2 of Chapter-2 which can be defined as,

$$\frac{P_3}{P_1} = \cos^2(CZ) \tag{3.20}$$

$$\frac{P_4}{P_1} = \sin^2(CZ) \tag{3.21}$$

where P_3 and P_4 are the output power in the bar state and cross state respectively whereas P_1 is the incident power. The coupling coefficient (C) is determined by using the equation (3.8) and (3.11) where Z is the length along the direction of propagation.

Fig-3.6 shows the normalized coupled power for the bar coupling (P_3/P_1) state and the cross coupling (P_4/P_1) state versus beat length (L_π) obtained by using the equations (3.17)-(3.18), (3.20) and (3.21) for directional coupler with coupling gap, h~0.5 μm, a=b=1.5 μm, n_2=1.45 and Δn =5 % respectively. It is seen from the figure that the peak cross-coupling power (P_4/P_1) is obtained at beat length ~91 μm for the conventional directional coupler with n_2=1.45, λ=1.55 μm and Δn = 5 % respectively.

3.2.4 Beat Length of DC

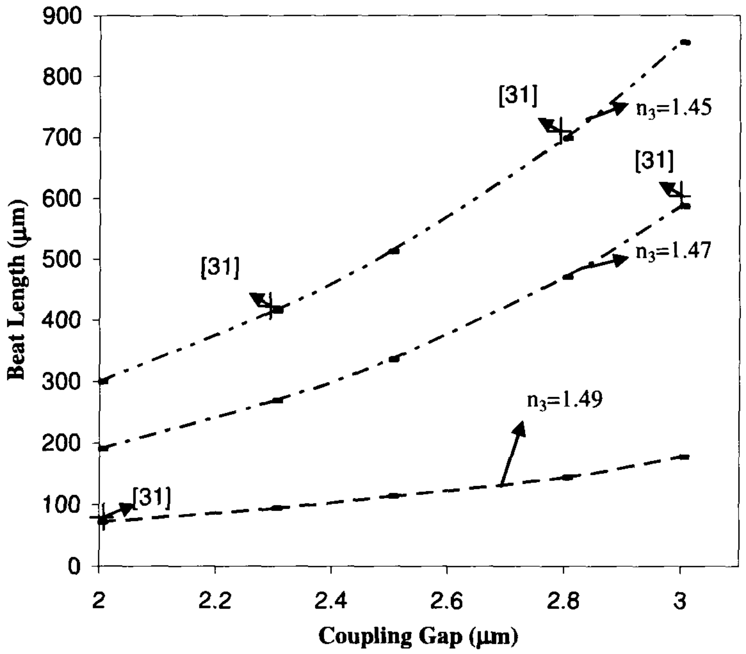

Fig-3.7: Beat length (L_π) vs coupling gap (h) for directional coupler with n_3=1.45, 1.47 and 1.49 with n_2=1.45, a=b=1.5 μm, Δn =5 % and λ=1.55 μm.

Fig-3.7 shows the beat length (L_π) vs coupling gap (h) of directional coupler for different coupling gap refractive index n_3=1.45, 1.47 and 1.49 with a=b=1.5 μm, n_2=1.45, Δn=5% and λ=1.55 μm respectively. From the graph, it is seen that beat length increases as h increases. The cross signs in the figure indicates the previously reported experimental results [31] that are matching well with the theoretical results as discussed in section-3.2.2.

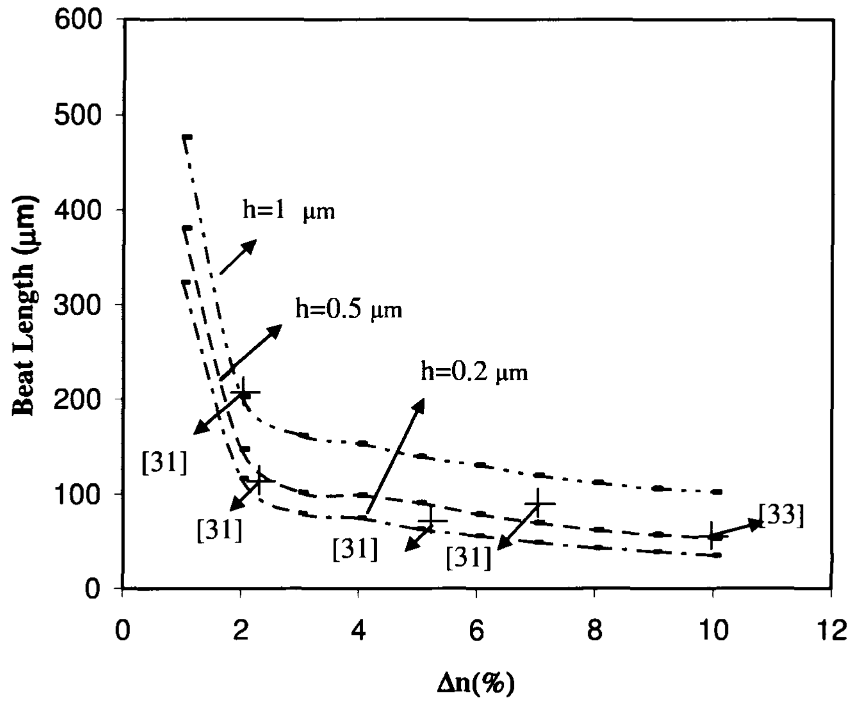

Fig-3.8: Beat length (L_π) versus index contrast (Δn) of conventional DC with h=1 μm, 0.5 μm, 0.2 μm with a=b=1.5 μm, Δn =5 %, n_2=1.45 and λ=1.55 μm.

The Beat length (L_π) versus index contrast (Δn) of directional coupler for different waveguide separation gap h=1 μm, 0.5μm, 0.2 μm with a=b=1.5 μm, Δn=5%, n_2=1.45 and λ=1.55 μm is shown in the Fig-3.8. The cross points in the figures indicate the experimental results of previous authors [31][33], which are matching well with the curves that obtain by using simple effective index method (SEIM) based on sinusoidal mode. It is seen from the figure that the beat length of directional coupler for index contrast (Δn)~5 % with a=b=1.5 μm, n_2=1.45, λ=1.55

μm are obtained as 45 μm, 91 μm, and 140 μm for different coupling gaps (h) of 0.2 μm, 0.5 μm and 1 μm respectively.

3.2.5 Comparison of Coupling Characteristics Obtained by SEIM and Marcuse Theory

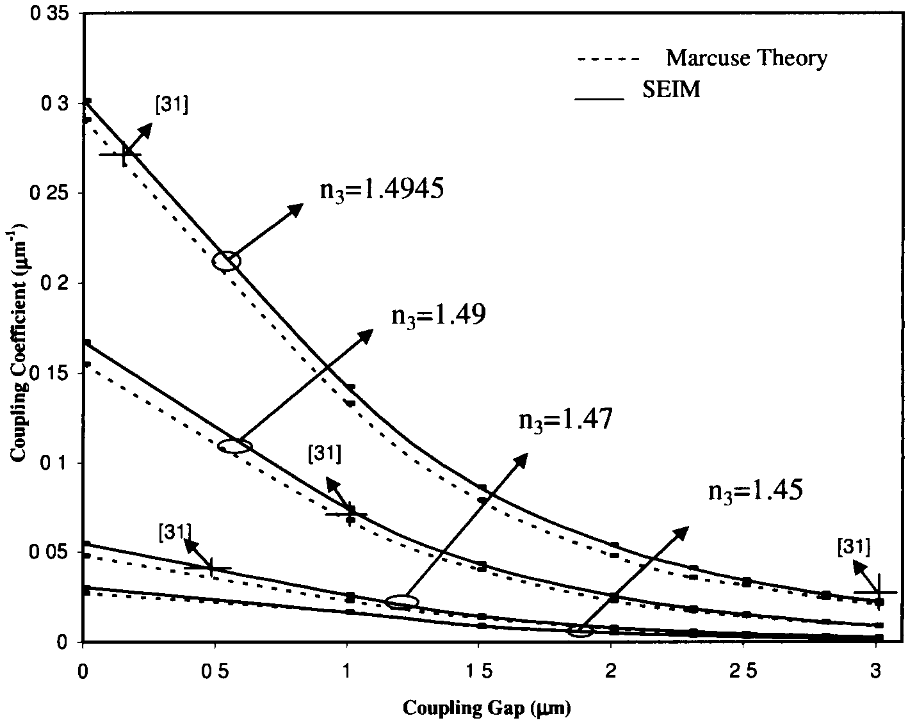

Fig-3.9: Coupling characteristics of DC using SEIM and Marcuse theory for n_3=1.45, 1.47, 1.49, 1.4945 with a=b=1.5 μm, n_1=1.5, n_2=1.45 and Δn =5 %.

Fig-3.9 shows the coupling coefficient versus coupling gap ~h for TE polarization of DC obtained by using the equation (3.8)-(3.15) of SEIM and Marcuse theory [as details are discussed in section-2.2.2 of chapter-2] for coupling gap refractive index, n_3=1.45, 1.47, 1.49 and 1.4945 with a=b=1.5 μm, n_1=1.5, n_2=1.45 and Δn=5 % (where $\Delta n=n_1-n_2$) are compared. It is evident from the figure that the coupling coefficient of DC decreases as the coupling gap increases and the rate of decrease of coupling coefficient with respect to h increases as coupling gap refractive index n_3 increases. The figure also shows that the curve obtained by SEIM is close to the same obtained by using Marcuse relations as details are mentioned in chapter-2.

The cross point in the figure represents the experimental point demonstrated by previous authors [31] with $SiON/SiO_2$, matching well with the theoretical curves. The coupling coefficients of directional coupler obtain by using SEIM are compared with Marcuse theory for different coupling gaps (h) ranges from 0 μm to 3 μm and n_3=1.45, 1.47, 1.49, 1.4945 with a=b=1.5 μm, n_2=1.45 and Δn =5 % which is shown in the Table-3.1.

Table-3.1: Comparison of Coupling Coefficients obtained by using SEIM and Marcuse theory

Coupling gap, h (μm)	**Calculated Coupling Coefficient (μm^{-1}) for Δn=5 %**		**Experimental results reported by previous authors [31]**
	SEIM	Marcuse theory	
0	0.30152	0.291	
0.5	0.2258	0.2106	0.4975 (Δn=3%)
1.0	0.14232	0.1331	0.07821 (Δn=1%)
1.5	0.08645	0.079	
2.0	0.05387	0.048	
2.5	0.034408	0.0314	
3.0	0.0212	0.0209	0.03109 (Δn=5%)

3.2.6 Beam Propagation Method (BPM) Simulation Results of Directional Coupler

From the above studies and as mentioned in the previous chapters, it is necessary to study the lightwave beam propagation with the designed device parameters before fabrication. In this direction, the design waveguide device components are studied for beam propagation with the help of commercially available optiBPM software (version 9.0) which is based on beam propagation method (BPM) and these results are compared with results obtained by SEIM.

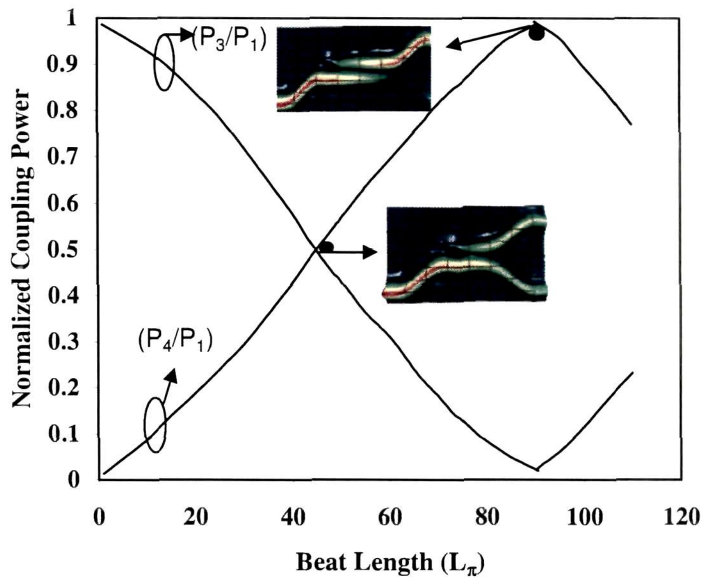

Fig-3.10: Normalized coupled power versus beat length for DC with coupling gap h~0.5 μm, n_2=1.45, Δn =5 %, λ=1.55 μm respectively and the BPM output results at beatlength~91 μm and 3 dB coupling length ~ 45 μm respectively.

Fig-3.10 shows normalized coupled power distribution for the bar coupling (P_3/P_1) state and the cross coupling (P_4/P_1) state versus beat length (L_π) for directional coupler with coupling gap, h~0.5 μm, a=b=1.5 μm, n_2=1.45 and Δn=5 % respectively as details are discussed in section-3.2.3. The figure also shows the lightwave propagation at half coupling point (3 dB) and cross coupling point of directional coupler obtained by optiBPM software matching well with the results obtained by SEIM model. It is seen from the figure that the peak cross-coupling power (P_4/P_1) is obtained at beat length ~91 μm whereas 3dB coupling power is obtained at beat length ~45.1 μm for the directional coupler with a=b=1.5 μm, h=0.5 μm, n_2=1.45 Δn=5 % respectively.

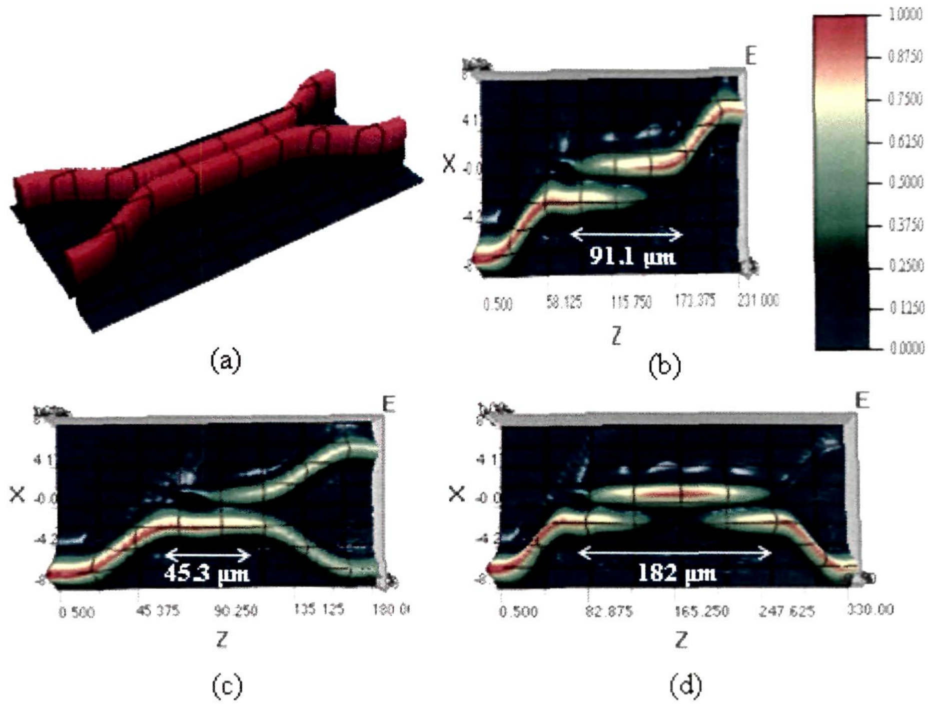

Fig-3.11 : BPM results of Conventional Directional Coupler for (a) Layout structure (b) Cross state (c) 3-dB coupler and (c) bar state

The Beam Propagation Method (BPM) results of conventional directional coupler (DC) obtained by using optiBPM software at the cross state, bar state and 3-dB directional coupler are shown in Fig-3.11. From the BPM output results, it is found that the beat length of conventional directional coupler at cross point~ 91.1 μm, 3 dB state ~45.3 μm and bar point~182 μm with a=b=1.5 μm, n_2=1.45, h=0.5 μm and Δn=5% respectively which are analogous with the theoretical results obtained by SEIM.

3.2.7 Fabrication Tolerances and Polarization Dependence of Directional Coupler

Since it may be difficult for precise fabrication of device structure with exact designed parameters, it is necessary to study its performance degradation with small unwanted variation of waveguide parameters Therefore, the effect of fabrication tolerances (δw) of DC width on power imbalance of directional coupler has been studied Fig-3 12 shows plot for power imbalance [=10 $\log_{10}$ (P_3/P_4)] versus fabrication tolerances ($\pm\delta w$) of DC width with cladding index~1 45, n_2=1 45, index contrast ~5 %, a=1 5 μm and wavelength ~1 55 μm It is seen from the figure that power imbalance increases almost symmetrically in both sides of minimum power imbalance obtained at δw~0 μm as 3 dB directional coupler is designed for this The rate of increase of power imbalance (dB) with respect to width tolerance for the conventional directional couplers is approximately obtained as $\frac{\partial}{\partial(\delta w)}$[Power Imbalance (dB)] ~0 15 dB/μm respectively

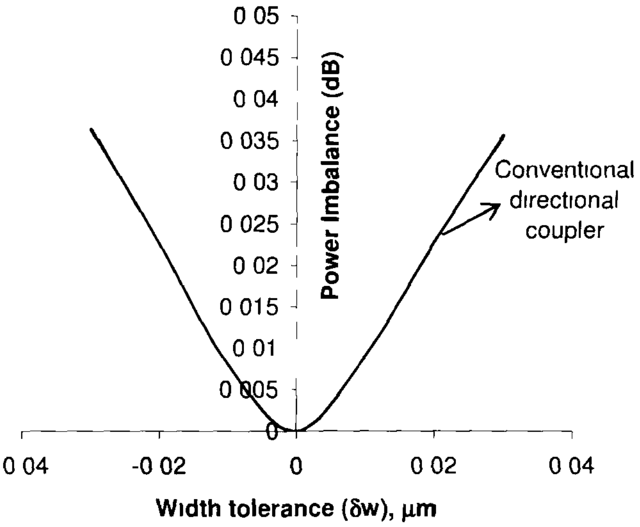

Fig-3.12 Power imbalance characteristics versus width tolerance ($\pm\delta w$) of conventional directional coupler with cladding index~1 45, index contrast ~5 %, a=b=1 5 μm and wavelength~1 55 μm

Fig-3 13 shows the dependence of power Imbalance on wavelength for 3 dB conventional directional coupler with a=1 5 μm, b=1 5 μm, index contrast ~5 % and cladding index~1.45. It is seen from the graph that power imbalance increases almost symmetrically in both sides of minimum power imbalance obtained at λ~1.55 μm as 3dB directional coupler is designed for this wavelength.

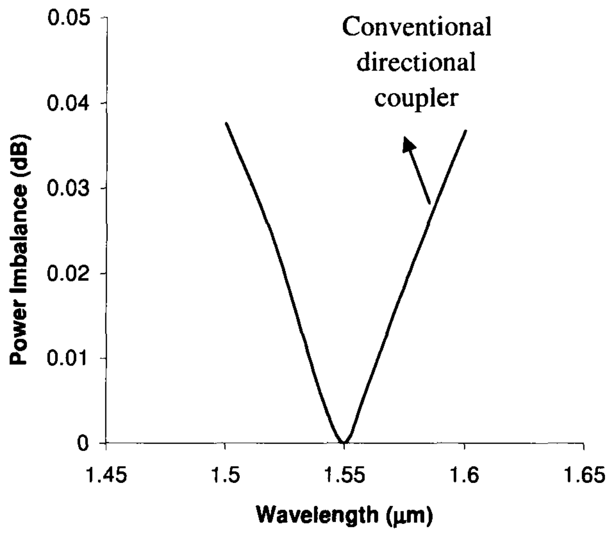

Fig-3.13: Power Imbalance characteristics versus wavelength variation for conventional directional coupler with a=1.5 μm, b=1.5 μm, index contrast ~5 % and cladding index~1.45.

Further the polarization dependence of coupling characteristics are also studied for conventional directional coupler. Fig-3.14 shows the normalized coupling power distribution versus beat length of conventional directional coupler for both TE-mode and TM-mode with h=0.5 μm, a=1.5 μm, b=1.5 μm, cladding index~1.45, Δn=5 % and λ~1.55 μm respectively. It is found that for TM-polarization the value of beat length (L_π) is ~0.22 % more than that of the TE-polarization.

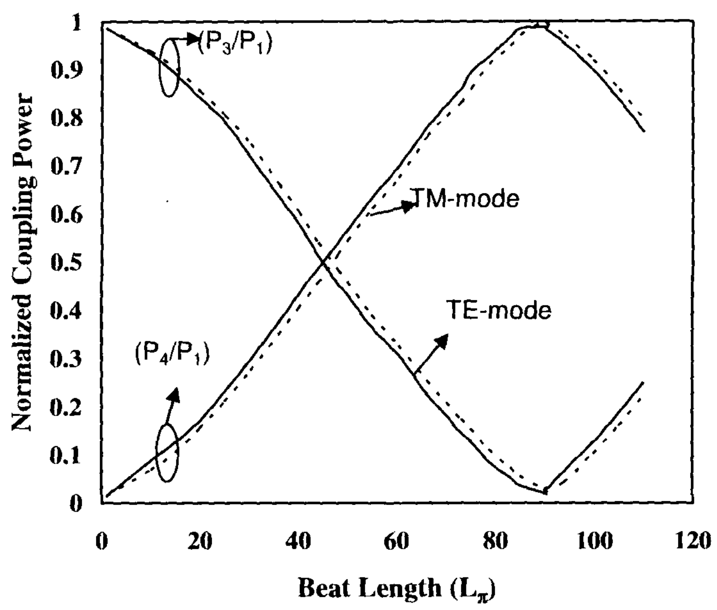

Fig-3.14: Normalized coupling power distribution of conventional directional coupler for both TE-mode (solid line) and TM-mode (dashed line) with h=0.5 μm, a=1.5 μm, b=1.5 μm, cladding index~1.45, Δn = 5 % and λ~1.55 μm respectively.

3.3. Two Mode Interference (TMI) Coupler

The Two Mode Interference (TMI) coupler is based on two mode interference phenomena, where the input field excites two modes–fundamental and first order modes and interfered with each other along the direction of propagation [31]. Two mode interference (TMI) coupler are consist of two single mode waveguides placed with zero separation gaps where due to the coupling and depending upon the phase difference between two excited modes, light propagates along the direction of propagation. Depending upon the phase difference at the end of coupling region, light signal can be obtained at the cross state or bar state output access waveguides respectively.

3.3.1 Mathematical Model of TMI Coupler Using SEIM

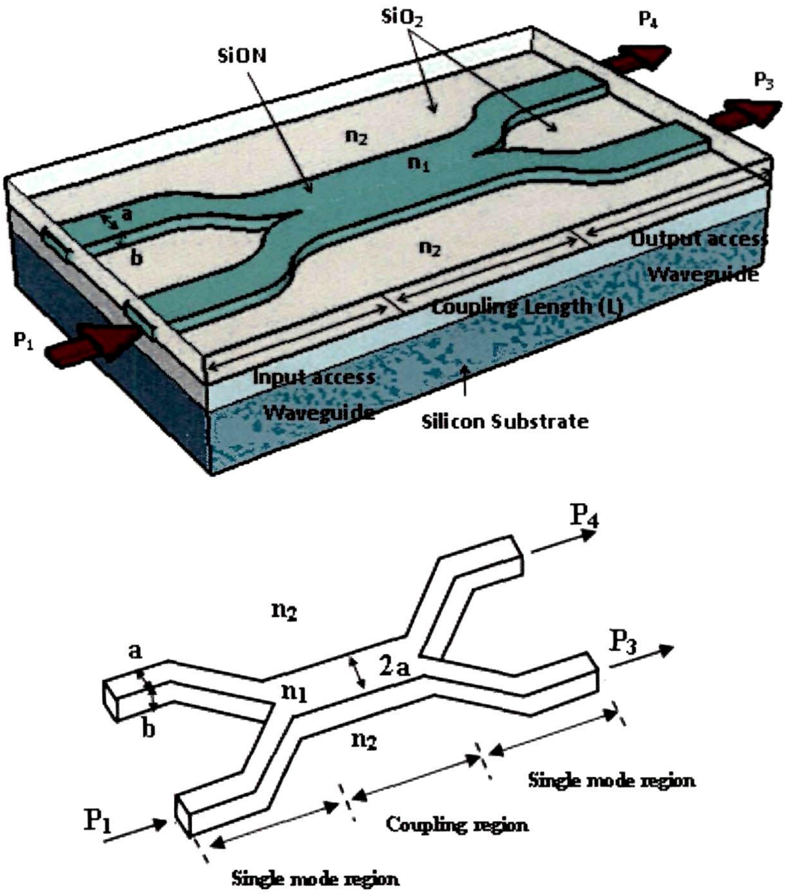

Fig-3.15: 3D Schematic view of TMI coupler (h=0 μm) based general interference

Fig-3.15 shows the three dimensional (3D) schematic view of the basic geometry of a two-mode interference (TMI) coupler with coupling gap (~h) zero. It consists of two-mode coupling region of width 2a and coupling length L with four single mode access waveguides of core width a and core thickness b. n_1 and n_2 are the refractive index of the core and cladding region respectively, whereas the single mode access waveguides— (Waveguide-1 & Waveguide-2) are attached to the input portion of the TMI region and the other two access waveguides (Waveguide-3 &

Waveguide-4) are attached to the output portion.

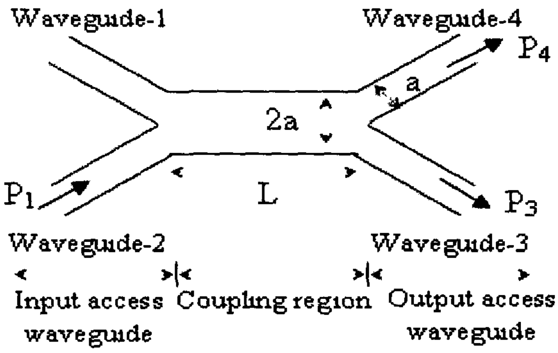

Fig-3.16: 2D schematic cross-sectional view of TMI coupler

Fig-3.16 shows the two dimensional (2D) schematic view of a 2x2 two-mode interference coupler as shown in Fig-3.15. When the input light signal is launch into one of the input access waveguides, only fundamental and first order modes of propagation constant β_{00} and β_{01} respectively are excited in the coupling region [14]. At the end of the coupling region, depending upon relative phase differences between these two excited modes, light power is either coupled into two output waveguides or vanishes.

The beat length is obtained by introducing the π (or 180^0) phase differences between two modes (fundamental and first order mode) and it is written as

$$L_\pi = \frac{\pi}{\beta_0 - \beta_1} = \frac{\pi}{2C} \tag{3.22}$$

where β_0, β_1 are the propagation constants of fundamental and first order modes, whereas coupling coefficient (C) for two-mode interference coupler (h~0 μm) can be estimated using equation (3.8)-(3.11).

The normalized coupling coefficient for two-mode interference (TMI) coupler can be derived using the following equation (3.23) of asymptotic analysis of SEIM model of DC as already discussed in the previous section-3.2.1, with a consideration as coupling gap (h) tends to zero, we have

$$\frac{C}{C_0}=\frac{\pi^2 b^3}{64a^3}\left[\begin{array}{l}\frac{1}{V^2{}_1}\exp\left(\frac{-2V_1}{b}h\right)\left\{\exp\left(\frac{2V_1 a}{b}\right)-\exp\left(\frac{-2V_1 a}{b}\right)\right\}\\+\frac{1}{V^2{}_2}\exp\left(\frac{-2V_2}{b}h\right)\left\{\exp\left(\frac{2V_2 a}{b}\right)-\exp\left(\frac{-2V_2 a}{b}\right)\right\}\end{array}\right] \quad (3.23)$$

where $V_1=\frac{b}{2}k(n_1{}^2-n_2{}^2)^{1/2}$ and $V_2=\frac{b}{2}k(n_1{}^2-n_3{}^2)^{1/2}$

3.3.2 Coupling Coefficient of TMI Coupler

For TMI coupler (h⟶0), as h tends to zero the value of the exponential term contains 'h' in equation (3.22) will be 1. Since there is no separation gap between the two cores (n_3 does not exist and $n_1 \approx n_3$), V_2 will be vanishes. Finally the equation (3.22) for TMI coupler can be approximate as,

$$\frac{C}{C_0}=\frac{\pi^2 b^3}{64a^3}\left[\frac{1}{V^2{}_1}\left\{\exp\left(\frac{2V_1 a}{b}\right)-\exp\left(\frac{-2V_1 a}{b}\right)\right\}\right] \quad (3.24)$$

Similar to the directional coupler as mentioned in section-3.2.2, considering square embedded channel waveguide (a=b, h⟶0) and substituting the values of V_1, V_2 from equation (3.2) and (3.3) in the above equation (3.24) we have,

$$\frac{C}{C_0}=\frac{\pi^2 b^3}{64a^3}\times\frac{1}{\left(\frac{b}{2}\right)^2 k^2\left(n_1^2-n_2^2\right)}\times\left[\exp\left\{\frac{2a}{b}\times\frac{b}{2}k\left(n_1^2-n_2^2\right)^{1/2}\right\}-\exp\left\{-\frac{2a}{b}\times\frac{b}{2}k\left(n_1^2-n_2^2\right)^{1/2}\right\}\right]$$

$$\frac{C}{C_0}=\frac{\pi^2}{16b^2k^2\left(n_1^2-n_2^2\right)}\times\left[\exp\left\{bk\left(n_1^2-n_2^2\right)^{1/2}\right\}-\exp\left\{-bk\left(n_1^2-n_2^2\right)^{1/2}\right\}\right] \quad (3.25)$$

where $C_0=\frac{0.4}{(1+0.2h)}\times\frac{\left(n_1^2-n_{eff(TE)}^2\right)\sqrt{n_{eff(TE)}^2-n_2^2}}{n_{eff(TE)}\left(n_1^2-n_3^2\right)\left[W+\frac{2}{k_0\sqrt{n_{eff(TE)}^2-n_2^2}}\right]}$; for TE mode (3.26)

$$C_0 = \frac{0.4}{(1+0.2h)} \times \frac{\left(n_1^2 - n_{eff(TM)}^2\right)\sqrt{n_{eff(TM)}^2 - n_2^2}}{n_{eff(TM)}\left(n_1^2 - n_3^2\right)\left[W + \dfrac{2}{k_0\sqrt{n_{eff(TM)}^2 - n_2^2}}\right]} \quad ; \text{for TM mode} \qquad (3.27)$$

$$n_{eff(TE)} = \beta_{TE}\left(\frac{\lambda}{2\pi}\right)$$

$$n_{eff(TM)} = \beta_{TM}\left(\frac{\lambda}{2\pi}\right)$$

β_{TE}, β_{TM} are the propagation constants of TE and TM mode respectively which can be estimated for two mode interference coupler from dispersive relation as discussed in section-3.2.2 of the current chapter.

3.3.3 Coupling Characteristics of TMI Coupler

For the calculation of power transfer to the output access waveguides of TMI coupler, the same coupled mode relations to that of the directional coupler as discussed in section-3.2.3 are used. The coupled power into the single mode output access waveguides of TMI coupler can be approximate as,

$$\frac{P_3}{P_1} = \cos^2(\Delta\phi / 2) \qquad (3.28)$$

$$\frac{P_4}{P_1} = \sin^2(\Delta\phi / 2) \qquad (3.29)$$

where, $\Delta\phi = \Delta\beta . L$ and $\Delta\beta = \beta_{00} - \beta_{01}$; and β_{00}, β_{01} are the propagation constant of fundamental and first order modes respectively.

The coupling length for maximum power transfer ($\Delta\phi = \pi$) can be defined as,

$$L = \frac{\Delta\phi}{\Delta\beta} = \frac{\pi}{\Delta\beta} \qquad (3.30)$$

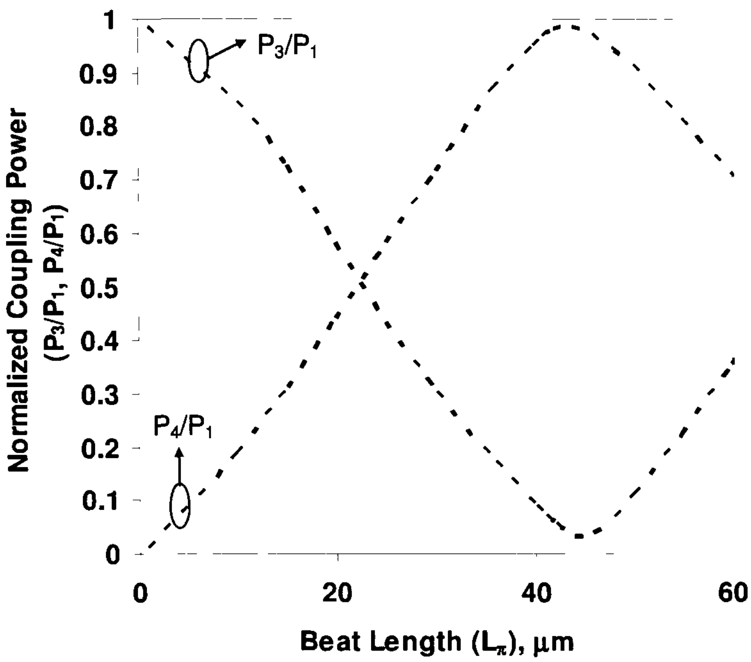

Fig-3.17: Normalized coupled power versus beat length with Δn=5 % for two mode interference (TMI) coupler with coupling gap h~0 μm, 2a=3 μm.

Fig-3.17 shows normalized coupled power (P_3/P_1 and P_4/P_1) obtained by using the equations (3.28) and (3.29) for two mode interference (TMI) coupler with coupling gap, h~0 μm, 2a=3 μm, n_2=1.45 and Δn=5 % respectively. It is seen that the normalized coupled power of two mode interference (TMI) coupler is transferred to the cross state at the beat length which can be determined using equation (3.30). It is found that the beat length of the TMI coupler with Δn=5 %, h=0 μm, n_2=1.45, a=b=1.5 μm are obtained as ~ 45 μm.

3.3.4 Beat Length of TMI Coupler

The Beat length (L_π) with respect to the index contrast (Δn) for TMI coupler with a separation gap of h=0 μm and a=b=1.5 μm, Δn =5 %, n_2=1.45, λ=1.55 μm has been shown in the Fig-3.18. It is evident from the figure that the beat length of TMI coupler decreased with the increase of index contrast (Δn). It is found that the beat length of TMI coupler for index contrast (Δn)~5 % with a=b=1.5 μm, n_2=1.45, λ=1.55 μm are obtained as ~45 μm. The results obtained by using simple effective index method (SEIM) based on sinusoidal mode are also compared with beam propagation method that is discussed later in this chapter.

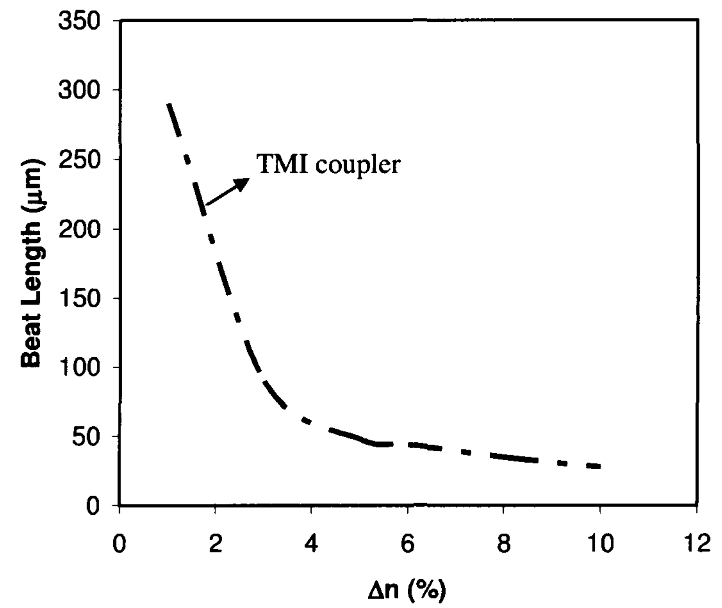

Fig-3.18: Beat length versus index contrast (Δn) of two mode interference (TMI) coupler with a=b=1.5 μm, n_2=1.45 and λ~1.55 μm.

3.3.5 Beam Propagation Method (BPM) Simulation Results of TMI Coupler

The normalized coupled power (P_3/P_1 and P_4/P_1) obtained by using the equations (3.28) and (3.29) for SEIM based two mode interference (TMI) coupler with coupling gap, h~0 μm, 2a=3 μm, n_2=1.45 and Δn=5 % has been shown in Fig-3.19. The figure also indicates the light wave propagation at half coupling point (~22.3 μm) and cross coupling point (~45 μm) of TMI coupler obtained (by optiBPM version 9.0), matching well with the results obtained by SEIM model.

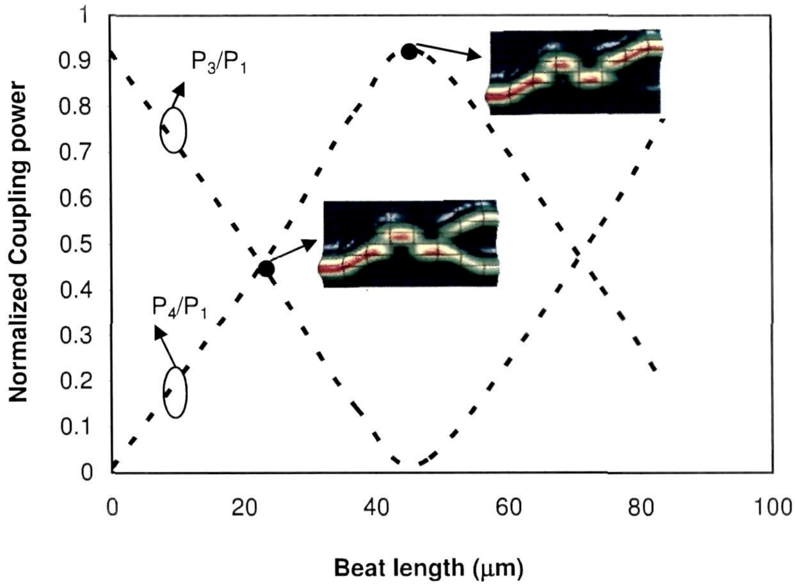

Fig-3.19: Normalized coupled power versus beat length with Δn=5 % for two mode interference (TMI) coupler with coupling gap h~0.5 μm, 2a=3 μm.

The beam propagation method (BPM) results of conventional Two-Mode Interference (TMI) coupler obtained by using optiBPM software for cross state, bar state and 3-dB TMI coupler have been shown in the Fig.-3.20. The results obtained by SEIM based model of TMI coupler is matching well with the BPM results. From the BPM simulation results, it is found that the beat lengths of conventional TMI coupler at the cross point, 3 dB coupling point and bar point are obtained as ~45 μm, 22.1 μm and 90.2 μm respectively.

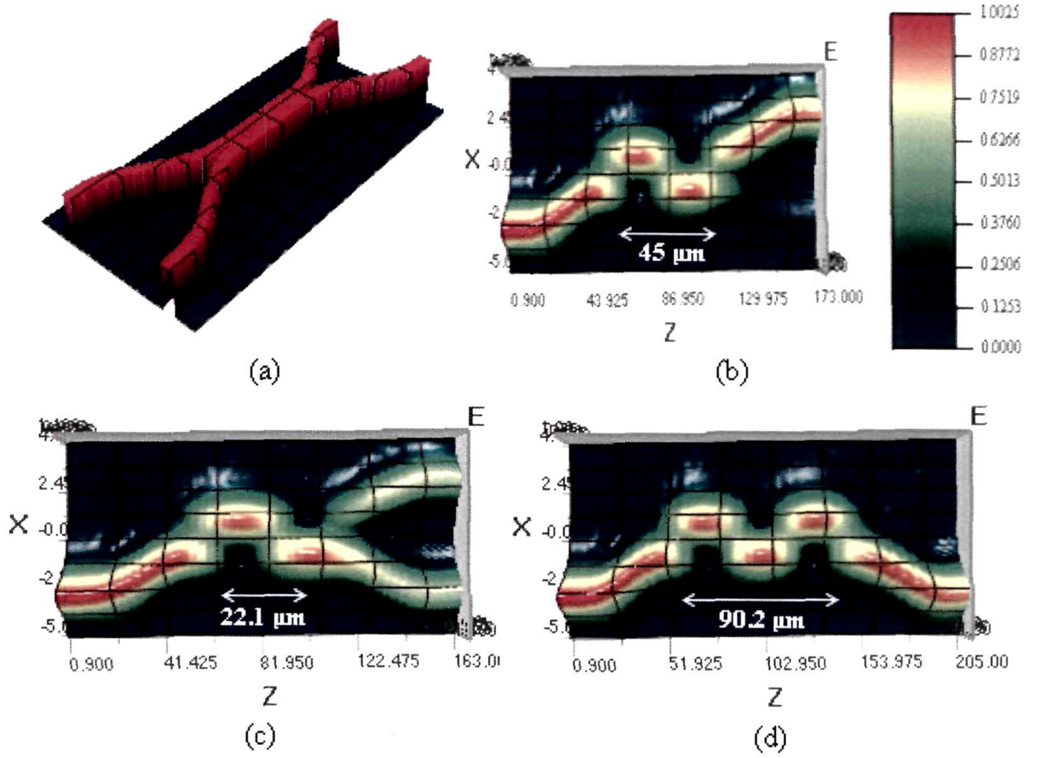

Fig-3.20 : BPM results of Conventional Two-Mode Interference (TMI) Coupler for (a) Layout structure (b) Cross state (c) 3-dB coupler and (d) bar state

3.3.6 Fabrication Tolerances and Polarization Dependence of TMI Coupler

As already mentioned the necessity to study the performance degradation of designed devices with small unwanted variation of waveguide parameters due to difficulties in realization of precise fabrication of device structure with exact designed parameters; the effect of fabrication tolerances (δw) of TMI width on power imbalance of designed TMI coupler also has been studied. Fig-3.21 shows the plot for power imbalance [$=10 \log_{10} (P_3/P_4)$] versus fabrication tolerances (±δw) of TMI width with cladding index~1.45, n_2=1.45, index contrast ~5 %, a=b=1.5 µm and wavelength ~ 1.55 µm respectively.

The graph shows that the power imbalance is increases almost symmetrically in both sides of minimum power imbalance obtained at δw~0 µm as 3 dB TMI coupler is designed for this. The rate of increase of power imbalance (dB) with respect to width tolerance for conventional TMI coupler is approximately obtained as $\frac{\partial}{\partial(\delta w)}$ [Power Imbalance (dB)] ~0.18 dB/μm respectively.

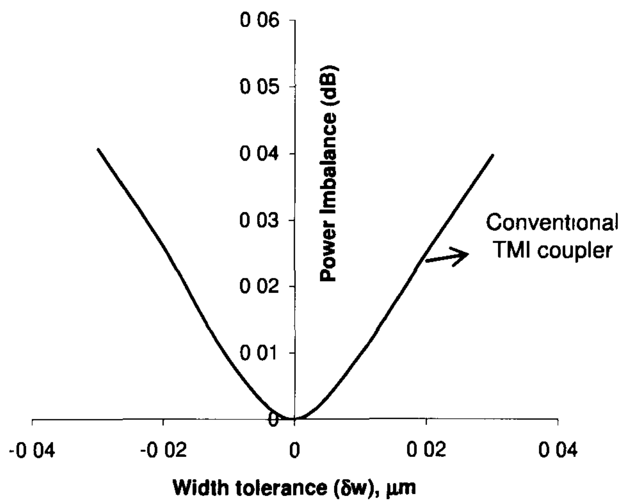

Fig-3.21: Power imbalance characteristics versus width tolerance (±δw) of conventional 3-dB TMI coupler with cladding index~1.45, index contrast ~ 5 %, a=b=1.5 μm and wavelength~ 1.55 μm.

The dependence of power imbalance on wavelength for 3 dB conventional TMI coupler with a=1.5 μm, b=1.5 μm, index contrast ~5 % and cladding index~1.45 also have been studied which is shown in Fig-3.22. It is found that power imbalance increases almost symmetrically in both sides of minimum power imbalance obtained at λ~1.55 μm as 3 dB TMI coupler is designed for this wavelength.

Fig-3.23 shows the normalized coupling power distribution versus beat length of conventional TMI coupler for both TE-mode and TM-mode with h=0 μm, a=1.5 μm, b=1.5 μm, cladding index~1.45, Δn=5 % and λ~1.55 μm respectively. From this polarization dependences plot, it is obtained that for TM-polarization the value of beat length (L_π) is ~0.25 % more than that of the TE-polarization.

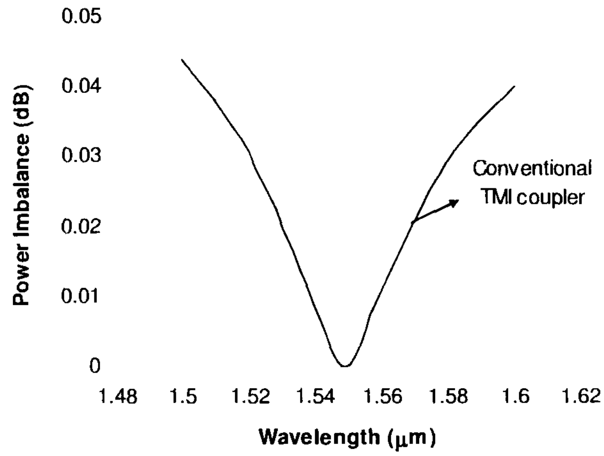

Fig-3.22: Power Imbalance characteristics versus wavelength variation for conventional TMI coupler with a=b=1.5 μm, index contrast ~5 % and cladding index~1.45.

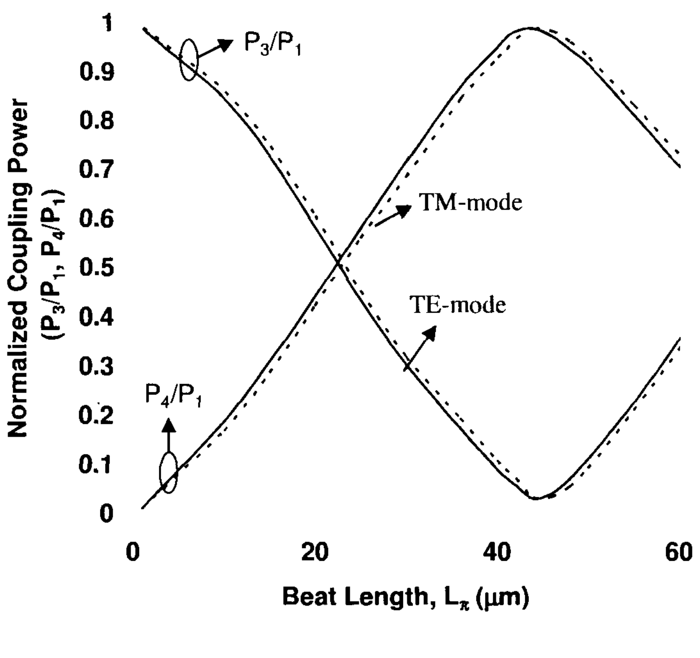

Fig-3.23: Normalized coupling power distribution of conventional TMI coupler for both TE-mode (solid line) and TM-mode (dashed line) with h=0 μm, a=1.5 μm, b=1.5 μm, cladding index~1.45, Δn=5 % and λ~1.55 μm respectively.

3.4. Multimode Interference (MMI) Coupler

The MMI coupler is based on self-imaging phenomena where the input excited field profile is reproduced in single or multiple images of the exciting field at a periodic interval along the direction of wave propagation. The MMI coupling length depends on consideration of structure based on either restricted interference (where, there is a restriction of excitation of some selected modes) or general interference (where, self imaging mechanism is independent of modal excitation). The conventional MMI structures based on general interference and restricted interference has been studied by previous authors as details are reviewed in chapter-2. In case of MMI coupler, the input field excites higher order modes in addition to the fundamental mode and first order mode and interfered with each other along the direction of propagation. Based on self imaging principles, there will multiple images.

3.4.1 Mathematical Model of MMI Coupler Using SEIM

Multi mode interference (MMI) couplers are basically consisting of two single mode waveguides placed with a gap and gap is filled with same core material. When light is launched to one of the input waveguide, more than two modes are excited. Due to the coupling and depending upon the phase difference between excited modes propagated along the direction of propagation, at the end of coupling region light signal can be obtain at the cross state or bar state output access waveguides

Fig-3.24 shows the three dimensional (3D) schematic view of the basic geometry of a multimode interference (MMI) coupler that is consisting of multimode coupling region of width (2a+h) and coupling length L with four single mode access waveguides of core width a and core thickness b whereas h represents the coupling waveguide separation gap. n_1 and n_2 are the refractive index of the core and cladding region respectively. A pair of single mode access waveguides is attached to the input portion of the MMI region and the other pair of single mode access waveguides is attached to the output portion.

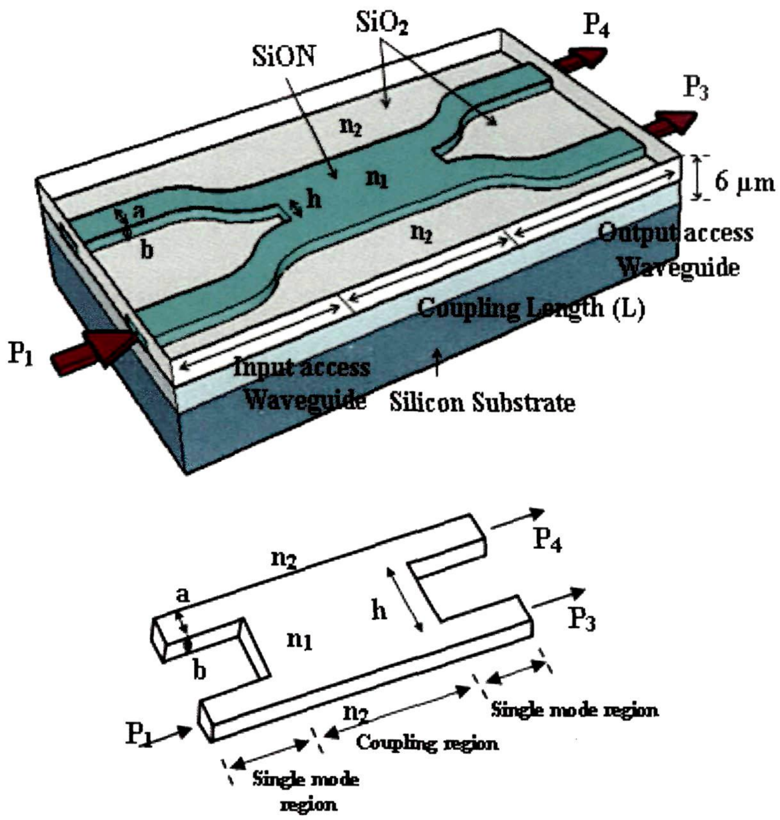

Fig-3.24: 3D schematic view of 2x2 MMI coupler based general interference

Fig-3.25 shows the two dimensional (2D) schematic view of multimode interference coupler as shown in Fig-3.24. When the input signal light is launch into one of the input access waveguides, higher order modes are excited in addition to the fundamental and first order modes of propagation constant β_{00} and β_{01} respectively are excited in the coupling region. At the end of the coupling region, depending upon relative phase differences between these excited modes, light power is either coupled into two output waveguides or vanishes.

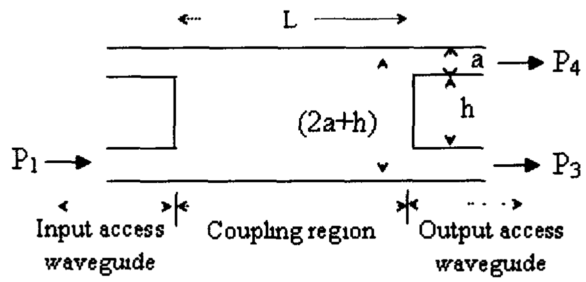

Fig-3.25: 2D schematic view of 2x2 MMI coupler based general interference

The beat length (length required for π phase difference) of the MMI coupler is written as

$$L_\pi = \frac{\pi}{\beta_{oo} - \beta_{01}} \tag{3.31}$$

where β_{00}, β_{01} =propagation constant of fundamental and first order mode that can be obtained by using dispersion equations[14].

The normalized coupling coefficient for multimode interference (MMI) coupler can be derived using the following relation (3.32) of asymptotic analysis of SEIM model of DC with the assumption ($a=b$, $n_3 \rightarrow n_1$) as discussed in previous section-3.2.2,

$$\frac{C}{C_0} = \frac{\pi^2 b^3}{64a^3}\left[\begin{array}{l}\frac{1}{V^2{}_1}\exp\left(\frac{-2V_1}{b}h\right)\left\{\exp\left(\frac{2V_1 a}{b}\right)-\exp\left(\frac{-2V_1 a}{b}\right)\right\} \\ +\frac{1}{V^2{}_2}\exp\left(\frac{-2V_2}{b}h\right)\left\{\exp\left(\frac{2V_2 a}{b}\right)-\exp\left(\frac{-2V_2 a}{b}\right)\right\}\end{array}\right] \tag{3.32}$$

where $V_1 = \frac{b}{2}k(n_1{}^2 - n_2{}^2)^{1/2}$ and $V_2 = \frac{b}{2}k(n_1{}^2 - n_3{}^2)^{1/2}$.

3.4.2 Coupling Coefficient of MMI Coupler

The MMI coupler consists of two waveguides having a separation gap (h) of refractive index (n_3) similar to that of the core refractive index (n_1). As discussed in the previous sections for a 2x2 directional coupler, the coupling gap between the access waveguides should be filled with same refractive index to that of the core refractive index. As the coupling gap refractive index, n_3 tends to the waveguide's core refractive index, n_1 of a directional coupler as discussed in previous section; the equation (3.32) can be approximated as follows.

$$\frac{C}{C_0}=\frac{\pi^2 b^3}{64a^3}\left[\frac{1}{V^2_1}\exp\left(\frac{-2V_1}{b}h\right)\left\{\exp\left(\frac{2V_1 a}{b}\right)-\exp\left(\frac{-2V_1 a}{b}\right)\right\}\right] \quad (3.33)$$

Similar to the directional coupler as mentioned in section-3.2.2, considering square embedded channel waveguide for MMI coupler (a=b, $n_3 \rightarrow n_1$) and substituting the values of V_1, V_2 from equation (3.2) and (3.3) in the above equation (3.33) we have,

$$\frac{C}{C_0}=\frac{\pi^2 b^3}{64a^3}\times\frac{1}{\left(\frac{b}{2}\right)^2 k^2\left(n_1^2-n_2^2\right)}\times\exp\left\{-hk\left(n_1^2-n_2^2\right)^{1/2}\right\}\times\left[\exp\left\{\frac{2a}{b}\times\frac{b}{2}k\left(n_1^2-n_2^2\right)^{1/2}\right\}-\exp\left\{-\frac{2a}{b}\times\frac{b}{2}k\left(n_1^2-n_2^2\right)^{1/2}\right\}\right]$$

$$\frac{C}{C_0}=\frac{\pi^2}{16b^2k^2\left(n_1^2-n_2^2\right)}\times\exp\left\{-hk\left(n_1^2-n_2^2\right)^{1/2}\right\}\times\left[\exp\left\{bk\left(n_1^2-n_2^2\right)^{1/2}\right\}-\exp\left\{-bk\left(n_1^2-n_2^2\right)^{1/2}\right\}\right]$$

(3.34)

where $$C_0=\frac{0.4}{(1+0.2h)}\times\frac{\left(n_1^2-n_{eff(TE)}^2\right)\sqrt{n_{eff(TE)}^2-n_2^2}}{n_{eff(TE)}\left(n_1^2-n_3^2\right)\left[W+\frac{2}{k_0\sqrt{n_{eff(TE)}^2-n_2^2}}\right]}$$; for TE mode (3.35)

$$C_0=\frac{0.4}{(1+0.2h)}\times\frac{\left(n_1^2-n_{eff(TM)}^2\right)\sqrt{n_{eff(TM)}^2-n_2^2}}{n_{eff(TM)}\left(n_1^2-n_3^2\right)\left[W+\frac{2}{k_0\sqrt{n_{eff(TM)}^2-n_2^2}}\right]}$$; for TM mode (3.36)

$$n_{eff(TE)}=\beta_{TE}\left(\frac{\lambda}{2\pi}\right)$$

$$n_{eff(TM)}=\beta_{TM}\left(\frac{\lambda}{2\pi}\right)$$

β_{TE}, β_{TM} = Propagation constants of TE and TM mode respectively which are determined from dispersive relations [14].

3.4.3 Coupling Characteristics of MMI Coupler

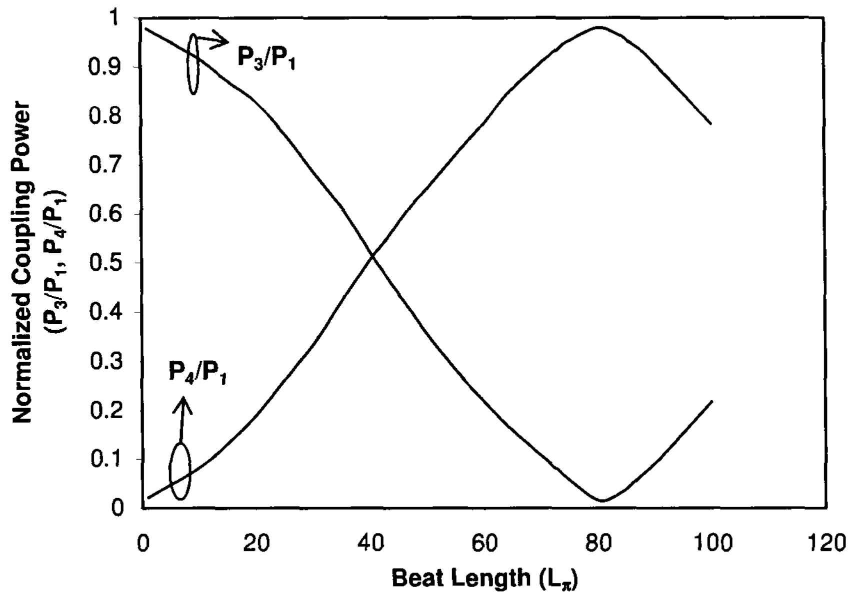

Fig-3.26: Normalized coupled power versus beat length with Δn=5 % for MMI coupler with h~4 μm.

The normalized coupled power (P_3/P_1 and P_4/P_1) obtained by using the equations (3.25) and (3.26) applying for conventional multimode interference (MMI) coupler with coupling gap, h~4 μm, w_{mmi}=7 μm, n_2=1.45 and Δn=5 % is shown in the Fig-3.26. It is observed that the normalized coupled power of MMI coupler is transferred to the cross state at the beat length which can be determined using equation (3.31). It is found that the beat length of the MMI coupler for TE-mode with Δn=5 % with h=4 μm, n_2=1.45, a=b=1.5 μm are obtained as ~ 80 μm.

3.4.4 Beat Length of MMI Coupler

The beat length (L_π) for TE polarization obtained by using the equation (3.31) for coupling gap (h) varying for 2 μm to 3 μm of MMI coupler is shown in Fig-3.27. For TM-polarization, the value of L_π is estimated 0.6% more than that of TE-polarization. From the figure, it is seen that beat length increases with increase of coupling separation gap due to the increase of excited modes. For h>3 μm (not shown in the figure), it is seen that the beat length increases sharply with h.

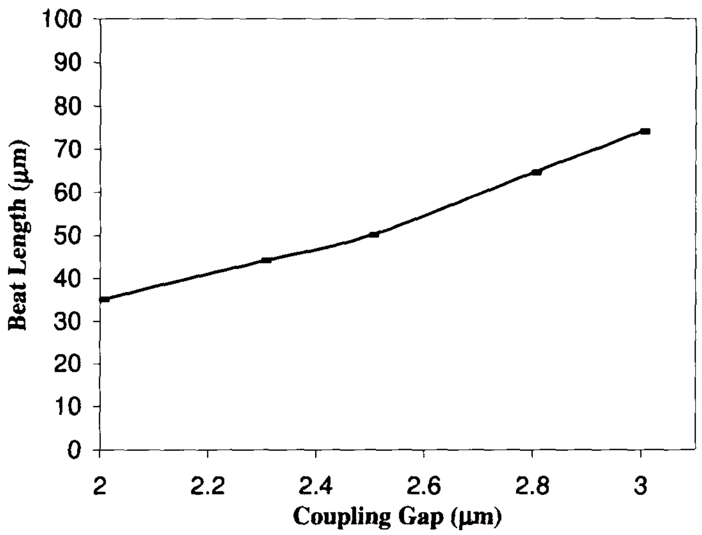

Fig-3.27: Beat length versus coupling gap of MMI coupler with a=b=1.5 μm and Δn=5 % respectively.

Fig 3.28 shows the comparison of L_π versus coupling gap for DC and MMI coupler with Δn=5 %, a=b=1.5 μm. It is seen that beat length of DC with n_3=1.45 is much more than that of MMI coupler and the rate of increase of beat length is more for n_3=1.45. As n_3 increases, the beat length of DC decreases and at n_3=1.4945, the beat of DC is almost close to that of MMI coupler. So DC with n_3= 1.4945 behaves as MMI coupler with Δn=5 %.

Fig-3.29 shows beat length (L_π) versus index contrast (Δn) for conventional MMI coupler with a=b=1.5 μm, h=4 μm, n_2=1.45 and Δn =5 % respectively. It is evident from the figure that the beat length decreases with increase of Δn and it decreases slowly with Δn for Δn≥5 %. So Δn=5 % is chosen for details study of MMI coupler.

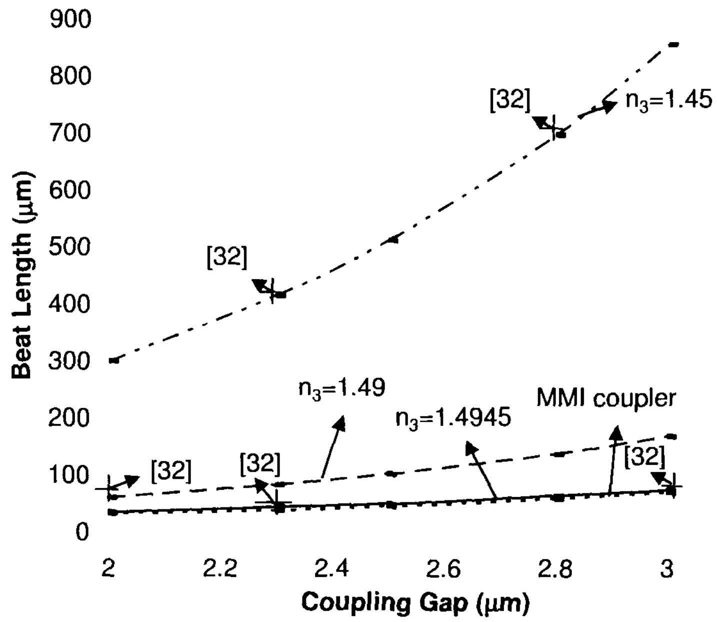

Fig-3.28: Beat length versus coupling gap of directional coupler (dashed lines) with n_3=1.45, 1.49, 1.4945 and MMI coupler (solid line) with a=b=1.5 μm and Δn =5 %.

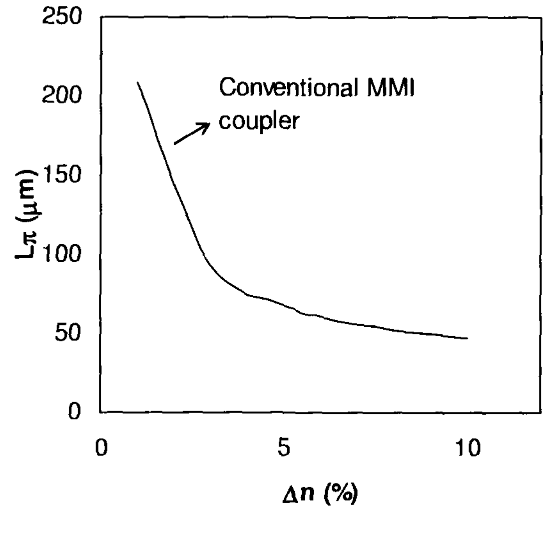

Fig-3.29: Beat length (L_π) versus index contrast (Δn) of conventional MMI coupler with a=b=1.5 μm, h=4 μm, n_2=1.45 and Δn =5 % respectively.

3.4.5 Beam Propagation Method (BPM) Simulation Results of MMI Coupler

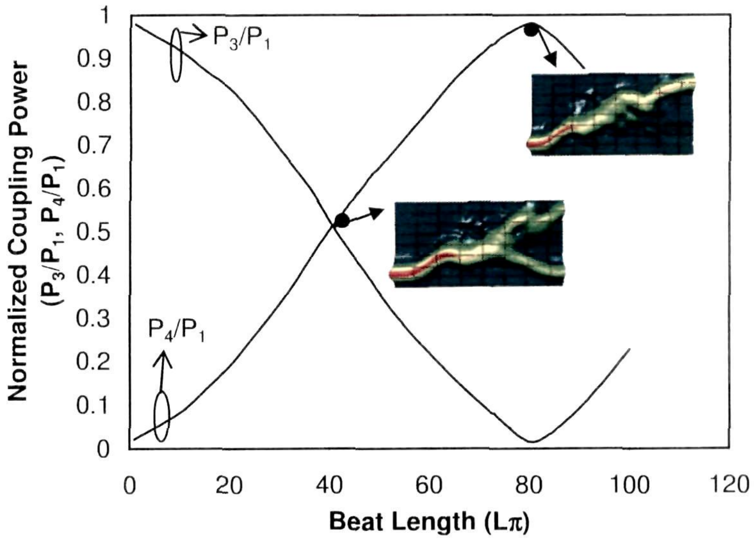

Fig-3.30: Normalized coupled power versus beat length with Δn=5 % for multimode interference (MMI) coupler with coupling gap h~4 μm.

Fig-3.30 shows normalized coupled power (P_3/P_1 and P_4/P_1) obtained by using the equations (3.25) and (3.26) for multimode interference (MMI) coupler with coupling gap, h~4 μm, n_2=1.45 and Δn=5 %. The figure also shows light wave propagation at half coupling point (39.9 μm) and cross coupling point (80 μm) of multimode interference (MMI) coupler obtained (by optiBPM version 9.0), matching well with the results obtained by SEIM model.

Fig.-3.31 shows the beam propagation method (BPM) results of multimode interference (MMI) coupler obtain by using optiBPM software for cross state, bar state and 3-dB MMI coupler respectively. It is found that the beat length of multimode interference (MMI) coupler at cross state, 3-dB MMI coupler and bar state with h=4 μm, n_2=1.45, Δn=5 % are obtained as ~80.1 μm, 40.2 μm and 160 μm respectively.

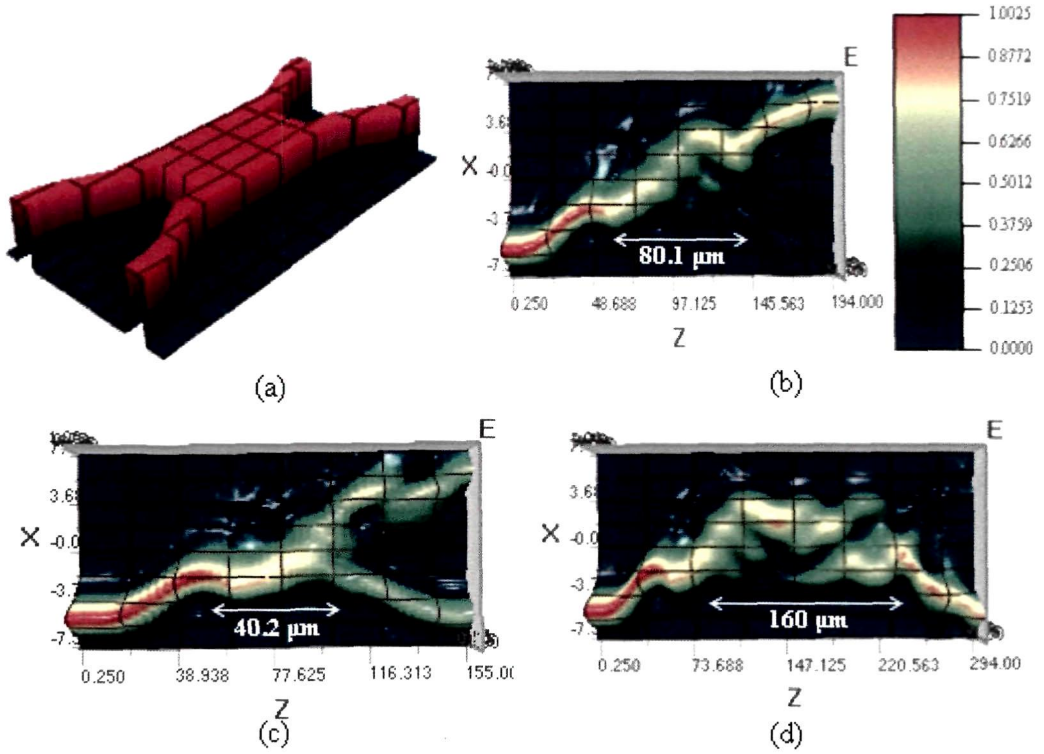

Fig-3.31 : BPM results of Conventional Multimode Interference (MMI) Coupler for (a) Layout structure (b) Cross state (c) 3-dB coupler and (d) bar state

3.4.6 Fabrication Tolerances and Polarization Dependence of MMI Coupler

In order to study the performance degradation of designed devices with a small unwanted variation of waveguide parameters during fabrication process step; the effect of fabrication tolerances (δw) of MMI width on power imbalance of conventional MMI coupler has been estimated. Fig-3.32 shows plot for power imbalance [$=10\log_{10}(P_3/P_4)$] versus fabrication tolerances (±δw) of MMI width with h~4.0 µm, a=1.5 µm, b=1.5 µm, index contrast~5 %, cladding index~1.45, and λ~1.55 µm respectively. It is found that the power imbalance increases symmetrically for both side of with ±δw=0 µm. The rate of increase of power imbalance (dB) with respect to width tolerance for conventional MMI coupler is approximately obtained as $\frac{\partial}{\partial(\delta w)}$ [Power Imbalance (dB)] ~0.13 dB/μm respectively.

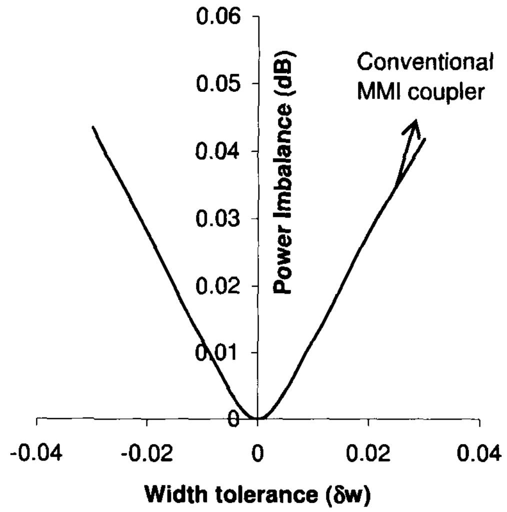

Fig-3.32: Power Imbalance characteristics versus width tolerances (δw) for conventional MMI coupler with index contrast ~5 %, cladding index~1.45, h~4.0 μm, a=1.5 μm, b=1.5 μm and λ~1.55 μm.

Since, it is also essential to study the dependence of power imbalance on wavelength; the power imbalance versus wavelength characteristics for conventional MMI coupler with a=b=1.5 μm, h~4.0 μm, index contrast ~5 % and cladding index~1.45 is shown in Fig-3.33. In the figure, the solid line indicates the curve for 3 dB conventional MMI coupler of coupling length ~40.1 μm and the minimum power imbalance is obtained at λ~1.55 μm. It is found that power imbalance is almost symmetrically increased in both sides of λ~1.55 μm.

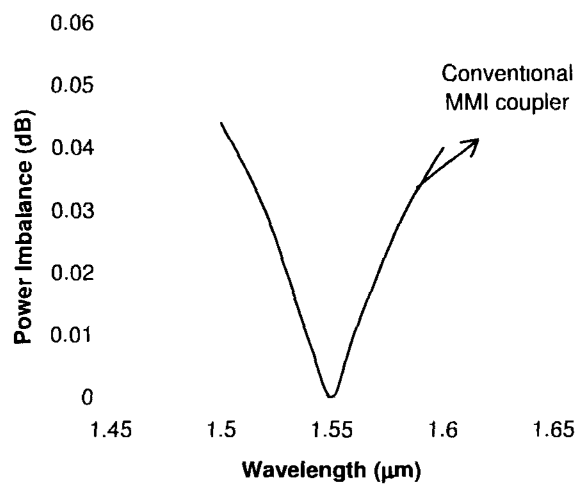

Fig-3.33: Power Imbalance characteristics versus wavelength variation for conventional MMI coupler with a=b=1.5 μm, h~4.0 μm, Δn ~5 % and n_2~1.45.

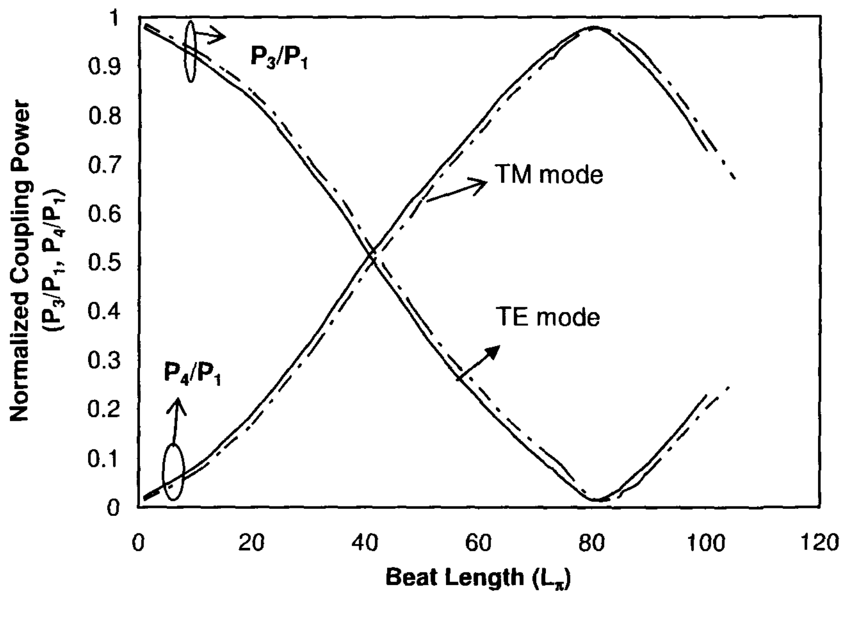

Fig-3.34: Normalized coupling power distribution of conventional MMI coupler for both TE-mode (solid line) and TM-mode (dashed line) with h=4.0 μm, a=1.5 μm, b=1.5 μm, cladding index~1.45, Δn=5 % and λ~1.55 μm respectively.

The polarization dependence characteristic for conventional MMI coupler is shown in the Fig-3.34. The figures shows the normalized coupling power distribution versus beat length of conventional MMI coupler for both TE-mode and TM-mode with h=4 μm, a=1.5 μm, b=1.5 μm, cladding index~1.45, Δn=5 % and λ~1.55 μm respectively. It is found that for TM-polarization the value of beat length (L_π) is ~0.24 % more than that of the TE-polarization.

3.5. Transformation Relationship of DC, TMI Coupler and MMI Coupler

From the above studies, transformation relationships between directional coupler, two-mode interference coupler and multimode interference coupler have been observed and details are discussed in the following two sub-sections 3.5.1 and 3.5.2 respectively.

3.5.1 Transformation from DC to TMI Coupler

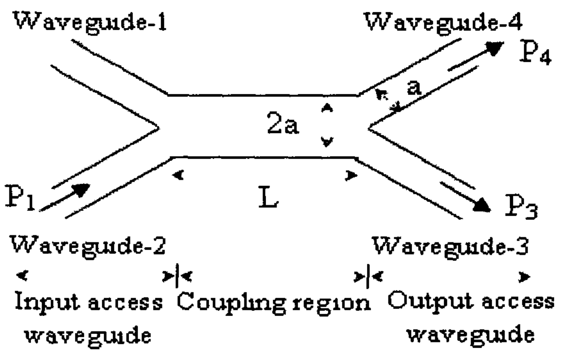

Fig-3.35: Schematic of TMI coupler (h=0) based general interference

Fig-3.35 shows a 2x2 conventional TMI coupler that is consisting of a two-mode coupling region of length L and width 2a (where h=0); and a pair of single mode input access waveguides of width a and thickness b and another pair of single mode output access waveguides of same size. Fig-3.36 shows beat length (L_π) versus index contrast, Δn (%) of DC obtained by using equation (3.17)-(3.19) for different values of coupling gap h=0.02 μm, 0.2 μm, 0.5 μm, 1μm and n_2=n_3=1.45, a=b=1.5 μm respectively. The cross points in the figure are the experimental results demonstrated by previous authors [31], [33] matching well with theoretical curves. It is found that as index contrast (Δn) increases, the beat length decreases and the rate of decrease of L_π with Δn becomes slower in lower values of h. As h becomes closer to zero coupling gap (h=0), the curves become closer and closer. For Δn≥2%, the decrease of beat length is smaller. It is obtained that the beat lengths of DC with h≤0.02 μm are almost same with those of TMI coupler.

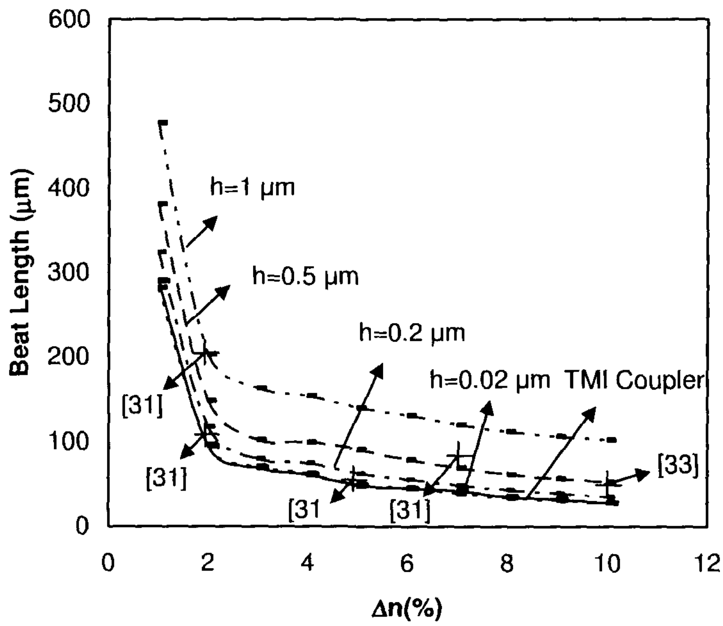

Fig-3.36: Beat length (L_π) versus index contrast (Δn) of DC (dashed line) with h=1 μm, 0.5 μm, 0.2 μm, 0.02 μm and TMI coupler (h=0 μm, solid line) respectively.

We have also estimated the beat length (L_π) of conventional TMI coupler for index contrast, Δn (%) varying from 1 to 10 obtained by using the equation (3.27) which is shown by the solid line in Fig-3.36. It is evident from the graph that the curve for the

TMI coupler is almost overlapped with that of DC with h=0.02 μm, showing the equivalence of TMI coupler with DC having coupling gap h≤0.02μm. For Δn>10% (not shown in figure), it is seen that L_π decreases slowly with Δn. As h tends to zero, the equation (3.7) is approximately written for TMI coupler as

$$\frac{C}{C_0}=\frac{\pi^2 b^3}{64a^3}\left[\frac{1}{V^2_1}\left\{\exp\left(\frac{2V_1 a}{b}\right)-\exp\left(\frac{-2V_1 a}{b}\right)\right\}\right] \tag{3.37}$$

Thus, as h tends to zero (≤0.02 μm), DC is equivalence of TMI coupler. So the coupling coefficient in the equation (3.37) estimated from the equation (3.7) is approximately equal to coupling coefficient of TMI coupler.

3.5.2 Transformation from DC to MMI Coupler

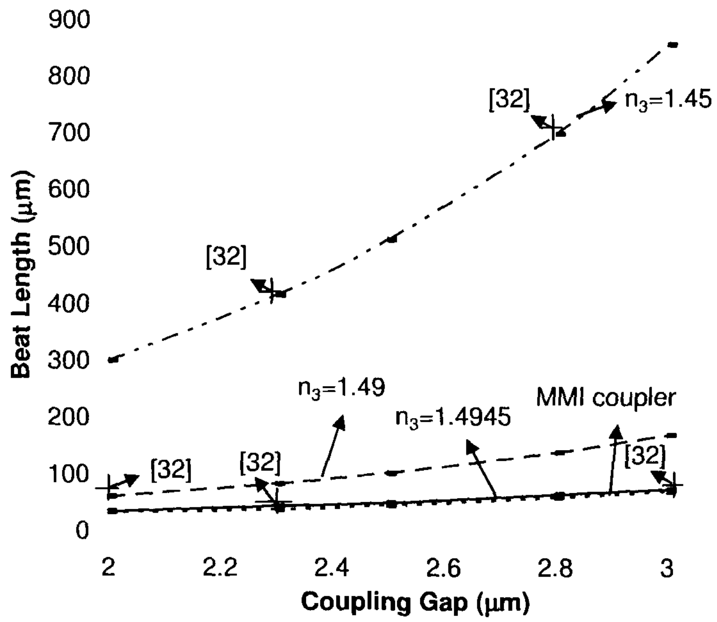

Fig-3.37: Beat length versus coupling gap of DC (dashed line) with n_3=1.45, 1.49, 1.4945 and MMI coupler (solid line) with a=b=1.5 μm and Δn=5 % respectively.

Fig-3.37 shows the beat length (L_π) versus coupling gap h of DC obtained by using the equation (3.27) for TE polarization with different values of n_3=1.45, 1.47, 1.49, 1.4945 with Δn=5 %, a=b=1.5 μm respectively. It is found that as coupling gap increases, the beat length increases and the rate of increase of L_π with h becomes slower in higher values of n_3. As n_3 becomes closer and closer to n_1, the curves also become closer and closer. We have also obtained (not shown in fig) that for $1.5>n_3>1.45945$, the curves are almost superposed. It is important to note that the values of beat length for DC with $n_3 \geq 1.4945$ are almost same with those of MMI coupler based on general inference as shown in Fig-3.37.

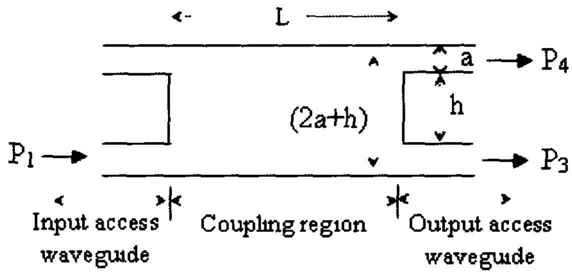

Fig-3.38: Schematic of 2x2 MMI coupler based general interference

Fig-3.38 shows a 2x2 conventional MMI coupler consisting of a multimode coupling region of length L and width (2a+h), thickness b; a pair of single mode input access waveguides of width a and thickness b and another pair of single mode output access waveguides of same dimensions. The beat length of the MMI coupler is written as

$$L_\pi = \frac{\pi}{\beta_{oo} - \beta_{01}} \tag{3.38}$$

where β_{00}, β_{01} =propagation constant of fundamental and first order mode obtained by using dispersion equations. We have determined L_π for TE polarization by using the equation (3.35) for h varying for 2 μm to 3 μm, as shown by the solid line in Fig-3.37. For TM-polarization, the value of L_π is estimated 0.6 % more than that of TE-polarization. The cross point in the figure is the experimental result demonstrated by previous authors [32], matching well with theoretical curves. The figure shows the plot of the MMI coupler is almost overlapped with that of DC with n_3~1.4945, showing the equivalence of MMI coupler with DC having n_3 close to core refractive index. For h>3 μm (not shown in the figure), it is seen that the beat length increases with h. As n_3 tends to n_1, the equation (3) is approximated as follows.

$$\frac{C}{C_0}=\frac{\pi^2 b^3}{64a^3}\left[\frac{1}{V^2_1}\exp\left(\frac{-2V_1}{b}h\right)\left\{\exp\left(\frac{2V_1 a}{b}\right)-\exp\left(\frac{-2V_1 a}{b}\right)\right\}\right] \quad (3.39)$$

From Fig-3.37, it is also shown that as n_3 tends to n_1 (n_1-n_3≤0.0055, which is ~ 0.43%), DC is equivalent to MMI coupler. So the coupling coefficient for DC with n_3 close to n_1, satisfies also the coupling coefficient formula for MMI coupler. The beat length of MMI coupler with Δn=5 % and width ~7 μm is obtained as 80 μm.

Thus form the above studies, the following two observations have notice:

(i) When the waveguide separation gap in DC decrease (<0.02 μm), DC shows the coupling characteristics equivalent to TMI couplers.

(ii) When the refractive index of the waveguide separation gap region of DC is increases and almost equivalent [(n_1-n_3) ~0.005] to the refractive index of the core region; the DC shows the coupling characteristics equivalent to MMI couplers.

3.6. Comparison of Coupling Characteristics for DC, TMI Coupler and MMI Coupler

A comparative normalized coupling characteristic of DC, TMI coupler and MMI coupler is shown in the Fig-3.39. The figure shows the normalized coupled power obtained by using the equations (3.20) and (3.21) for DC with coupling gap~0.5 μm, Δn=5 %, TMI coupler with same Δn and 2a=3 μm; and MMI coupler with h~4 μm and Δn=5% respectively. The figure also shows the light wave propagation at half coupling points and cross coupling points of DC, TMI and MMI coupler obtained (by optiBPM version 9.0), are matching well with the results obtained by SEIM model. It is also found that the peak power of MMI coupler is slightly more than that of DC and TMI coupler due to presence of bending loss of

DC and TMI coupler at bent access waveguides.

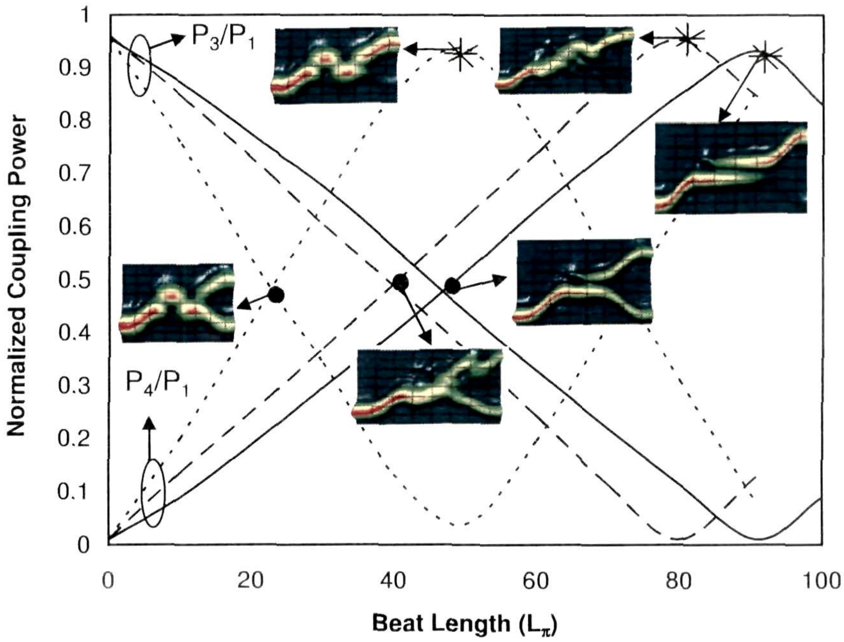

Fig-3.39: Normalized coupled power versus beat length with Δn=5 % for DC with coupling gap h~0.5 μm (solid line), TMI coupler (dotted line) with h~0 μm and MMI coupler (dashed line) with h~4 μm.

Further, it is found that the beat length of TMI coupler (h=0 μm) and MMI coupler with h=4 μm, Δn=5 % are obtained as ~45 μm and ~80 μm respectively and that for DC with h=0.5 μm and same Δn is ~91 μm respectively. The dot and star signs in the normalized coupling characteristics graph indicate the respective cross and 3 dB coupling point of DC, TMI coupler and MMI coupler respectively. The design parameters for DC, TMI coupler and MMI coupler that are considered in the above studies are summarized in the Table-3.2 as given below. The designed DC, TMI coupler and MMI coupler with these waveguide parameters are then fabricated and experimentally tested using SiON as the waveguide core material with SiO_2 cladding layer. The detail fabrication process steps and experimental results are discussed later on in the chapter-6 of this thesis.

Table-3.2: Design parameters DC, TMI coupler and MMI coupler

Design Parameters	Directional Coupler	MMI Coupler	TMI Coupler
Core waveguide width (a), μm	1.5	1.5	1.5
Core waveguide Thickness (b), μm	1.5	1.5	1.5
Index Contrast (Δn)	5%	5%	5%
Core RI (n_1) , Δn=5%	1.5	1.5	1.5
Cladding RI (n_2)	1.45	1.45	1.45
Coupling Gap Cladding RI (n_3)	1.45	1.4945	----
Coupling gap (h), μm	0.5	4	0
Wavelength (λ), μm	1.55	1.55	1.55
Beat Length (L_π), μm	91	80	45

3.7. Conclusion

In this chapter the coupling characteristics of DC, TMI and MMI are shown. Polarization dependence property and fabrication tolerance of DC, TMI and MMI couplers are discussed. For accurate estimation of these characteristics, a mathematical model using simple effective index method (SEIM) based on sinusoidal modes have been developed. Finally, a transformation relationship has been established for DC with TMI coupler and DC with MMI coupler. From the transformation relationship, it is observed that the beat length of TMI coupler is half of that of DC and 0.65 of that of MMI coupler with h=4 μm. Further, this transformation relationship of DC, TMI and MMI coupler have been used to estimate the coupling characteristics for the proposed structures of directional coupler, two mode interference (TMI) and multi mode interference (MMI) couplers as discussed in chapter 4, 5 and 7 respectively.

Reference:

1. Marcatili, E.A. J. Dielectric rectangular waveguide and directional coupler for integrated optics, *J. Bell. Syst. Tech.* **48**, 2071-2102, 1969.
2. Iizuka, K. Elements of Photonics: for fiber and integrated optics, 2nd edition, Wiley interscience, NewYork, 2002.
3. Chiang, K.S. Effective index method for the analysis of optical waveguide couplers and arrays: an asymptotic theory, *J. of Lightwave Tech.* **9**, 62-72, 1991.
4. Wang, Q., et al. Effective index method for planar lightwave circuits containing directional couplers, *J. of Optics Comm.* **259**, 133-136, 2006.
5. Rottmann, F., et al. Integrated-optic wavelength multiplerxers on lithium niobate based on two-mode interference, *J. of Lightwave Tech.* **6**, 946-952, 1988.
6. Yiling, S., et al. Integrated optical isolators based on two-mode interference couplers, *J. Opt. (IOP)* **12**, 1-5, 2010.
7. Veerman, F. B., et al. An optical passive 3-dB TMI coupler with reduce fabrication tolerance sensitivity, *J. of Lightwave Tech.* **14**, 306-311, 1996.
8. Sahu, P. P. A compact optical multiplexer using silicon nano waveguides, *IEEE J. Sel. Topics Quantum Electron.* **15**, 1537-1541, 2009.
9. A. Neyer, Integrated optical multichannel wavelength multiplexer for monomode systems, *Electron. Lett.* **20**, 744-746, 1984.
10. Paiam, M.R., & MacDonald, R.I. A 12-channel phased-array wavelength multiplexer with multimode interference couplers, *IEEE Photonic Tech. Lett.* **10**, 241-243, 1998.
11. Huang, J. Z., et al. A new design approach to large input/output number multimode interference couplers and its application to low-crosstalk WDM routers, *IEEE Photonic Tech. Lett.* **10**, 1292-1294, 1998.
12. Soldano, L. B., & Pennings, E.C M. Optical multi-mode interference devices

based on self-imaging: Principles and Applications, *J. of Lightwave Tech.* **13,** 615-627, 1995.

13. Chan, H.P., et al. A wide angle X-junction polymeric thermo optic digital switch with low crosstalk, *IEEE Photonic Tech. Lett.* **15**, 1210-1212, 2003.
14. Nishihara, H., Haruna, M., & Suhara, T. *Optical Integrated Circuits*, McGraw-Hill, New York, 1989.
15. Chatterjee, R. et al. Nanomechanical Proximity Perturbation for Switching in Silicon-Based Directional Couplers for High-Density Photonic Integrated Circuits, *J. of Microelectromechanical Syst.* **19**, 657-662, 2010
16. Sheng, W. D., et al. Numerical simulation of quantum directional couplers, *Appl. Phys.* A **64**, 167-170, 1997.
17. Zhou, J., et al. Operation principle for optical switches based on two multimode interference couplers, *J. of Lightwave Tech.* **30**, 15-21, 2012.
18. Jin, Z., & Peng, G. Designing optical switches based on silica multimode interference devices, in *Proc. of Progress in Electromagnetic Research Symposium* (PIERS 2005), Hangzhou, China, 58-61.
19. Yao, C., et al. An ultracompact multimode interference wavelength splitter employing asymmetrical multi-section structures, *Opt. Exp.* **20**, 18248-18253, 2012.
20. Chen, K., et al., Silicon oxynitride optical waveguide ring resonator utilizing a two-mode interference structure, *Int. J. Photoenergy* **Dec**, 1-5, 2012
21. Li, B., et al. Two-mode interference photonic waveguide switch, *J. of Lightwave Tech.* **21**, 1685-1690, 2003.
22. Chiang, K. S. Analysis of the effective-index method for the vector modes of rectangular-core dielectric waveguides, *IEEE Transactions on Microwave Theory and Techniq.* **44,** 692-700, 1996.
23. Kogelink, H. Guided Wave Optoelectronics, Springer-verlag, Berlin, 1998.
24. Benson, T. M., et al. Rigorous effective index method for semiconductor waveguides in, IEE Proceedings of J. optoelectronic. **139**, 67-70, 1992.

25. Kumar, A, et al. Explanation of errors inherent in the effective index method for analyzing rectangular core waveguides, *Opt. Lett.* **13**, 1129-1131, 1988.

26. Marcuse, D. Directional couplers made of non identical asymmetric slabs. Part 1: synchronous couplers, *J. of Ligthwave Tech.* **LT-5,** 113-118, 1987.

27. Tsao, S. L., et al., BPM simulation and comparision of 1x2 directional waveguide couplingand Y-junction coupling silicon-on-insulator optical couplers, *Fiber and Integrated Optics*, **21**, 417-433, 2002.

28. Lifante, G. *Integrated Photonics: Fundamentals*, John Wiley, USA, 2003.

29. Haus, H.A., et al. Coupled-mode theory of optical waveguides, *J. of Ligthwave Tech.* **LT-5,** 16-23, 1987.

30. Synder, A.W. Coupled-mode theory of optical fibers, *J. of the Optical Society of Americ.* **62,** 1267-1277, 1972.

31. Das, A. K. and Sahu, P. P. Compact integrated optical devices using high index contrast waveguides in, International conference on *Wireless and Optical Communication Network Conference*, 2006.

32. Sahu, P. P. Parabolic tapered structure for an ultracompact multimode interference coupler, *Appl. Opt.* **48**, 206-211, 2009

33. Chin, M. K., et al., High-index-contrast waveguides and devices, *Appl. Opt.* **44**, 3077-3086, 2005. Runde, D, et al. Mode-selective coupler for wavelength multiplexing using $LiNbO_3$:Ti optical waveguides, *Cent. Eur. J. Phys.* **6**, 588-592, 2008

34. Mule, A.V., et al. Photopolymer-based diffractive and MMI waveguide couplers, *IEEE Photonic Tech. Lett.* **16**, 2490-2492, 2004.

35. Ibrahim, M. H., et al. A novel 1x2 multimode interference optical wavelength filter based on photodefinable benzocyclobuene polymer, *J. of Microwave and Optical Tech. Lett.* **49**, 1024-1028, 2007.

36. Chin, M. K., et al., High-index-contrast waveguides and devices, *Appl. Opt.* **44**, 3077-3086, 2005

37. Miya, T. Silica-based planar lightwave circuits: passive and thermally active

devices, *IEEE J. Sel. Topics Quantum Electron.* **6**, 38-45, 2000.

38. Yamada, H., et al. Si photonic wire waveguide devices, *J. of IEICE Trans. Electron.* **E90-C**, 59-64, 2007.
39. Kashahara, R, et al., New structures of silica-based planar light wave circuits for low power thermooptic switch and its application to 8x8 optical matrix switch, *J. Lightwave Tech.* **20**, 993-1000, 2002.
40. Worhoff, K., et al., Design, tolerance analysis and fabrication of silicon oxynitride based planar optical waveguides for communication devices, *J. of Lightwave Tech.* **17**, 1401-1407, 1999.
41. Bona, G. L., et al. SiON high refractive-index waveguide and planar lightwave circuit, *IBM J. Res. & Dev.* **47**, 239-249, 2003.
42. Yagi, et al. Versatile multimodes interference photonic switches with partial index modulation regions, *IEE Electronics Lett.* **36,** 533-534, 2000.

****

Chapter-4:

Tooth-Shaped Grating-Assisted Geometry for Directional Coupler and Two Mode Interference Coupler

Introduction

Grating Assisted Directional Coupler

Grating Assisted Two Mode Interference Coupler

Comparative Study of Directional Coupler and Two Mode Interference Coupler with Tooth Shaped Grating Geometry

Conclusion

4.1. Introduction

As discussed in chapter-2, the compact waveguide device components have become essential for implementation of large scale photonic integrated device (PID) [1]-[6] to provide enormous bandwidth for skyrocketed increase of users in present day's communication. As mentioned in chapter-3, DC/TMI/MMI couplers with small gap have been preferred because of compactness and easy fabrication. In this direction, grating assisted geometry has growing interest and is thus introduced in these couplers for further compactness which is very much obligatory for large scale integration of PID. Apart from the above property, it has polarization insensitiveness and higher fabrication tolerances. Previous works [7]-[9] on the coupling characteristics of tooth shaped grating structure have used finite difference time domain (FDTD) method offering little inside the analysis such as fabrication tolerances and polarization insensitiveness.

In this chapter, mathematical analysis of tooth shaped grating assisted geometry for compact directional coupler and two mode interference (TMI) coupler have been carried out using a mathematical model based on sinusoidal mode simple effective index method (SM-SEIM) [2],[10]-[12] for accurate analysis of modal power. The dependence of access waveguide length on the gap between access waveguides with fixed value of S-bending loss for grating assisted directional coupler (GA-DC) and tooth shaped grating assisted two mode interference (GA-TMI) coupler are shown. The coupling behavior for both DC and TMI coupler with grating geometry are discussed and compared with conventional structures. The polarization dependence property and fabrication tolerances of grating assisted structures of these couplers are also discussed.

4.2. Tooth Shaped Grating Assisted Directional Coupler (GA-DC)

Fig-4.1 shows the three dimensional (3D) view of 2x2 tooth shaped grating assisted directional coupler having tooth shaped grating assisted coupling region of length L and coupling gap h, two input single mode access waveguides of core width a, thickness b (waveguide-1 and waveguide-2) and two output single mode access waveguides of same core dimension (waveguide-3 and waveguide-4) respectively. The grating assisted coupling region is consisting of two grating assisted waveguides placed close to each other, where the guiding layer of width W_m=2a+h and grating layer of width, $W_g=W_m+2\Delta W$ (where ΔW= tooth width of grating) are placed alternatively in the coupling region. As discussed and reviewed in the section-2.6 of chapter-2, we have chosen rectangular tooth shaped grating geometry for more compactness. The coupling region consists of N total numbers of grating period, $\Lambda = l_m + l_g$; where l_m and l_g are the length of guiding width (K=m) and grating width (K=g) in each grating period respectively. The n_1 and n_2 are refractive index of core and cladding region respectively, whereas n_3 is refractive index of the coupling cladding region. When the input power P_1 is launched into lower most input S-bent access waveguide, the output powers P_3 and P_4 are obtained as bar state and cross state respectively.

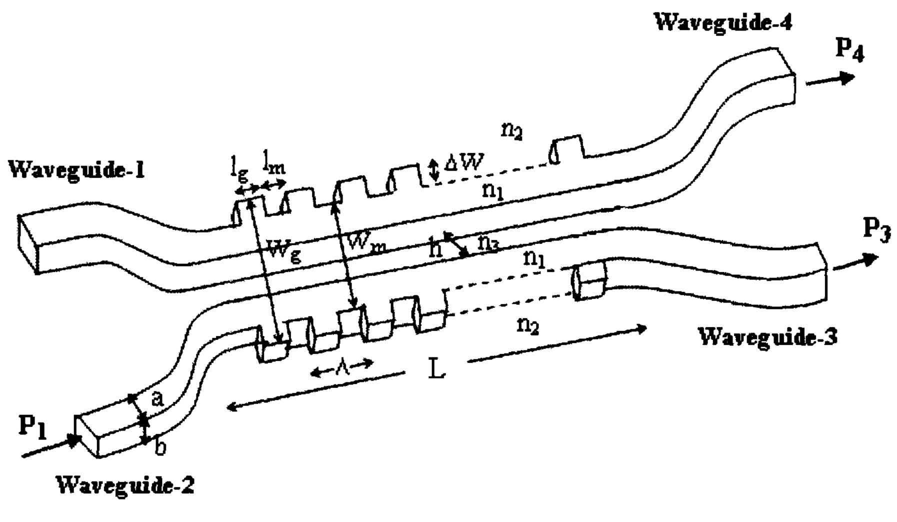

Fig-4.1: 3D Schematic of 2x2 tooth shaped grating-assisted directional coupler.

Fig-4.2 shows the two dimensional (2D) cross-sectional view of the tooth shaped grating assisted directional coupler (GA-DC) signifying the waveguide design parameters as shown in Fig-4.1.

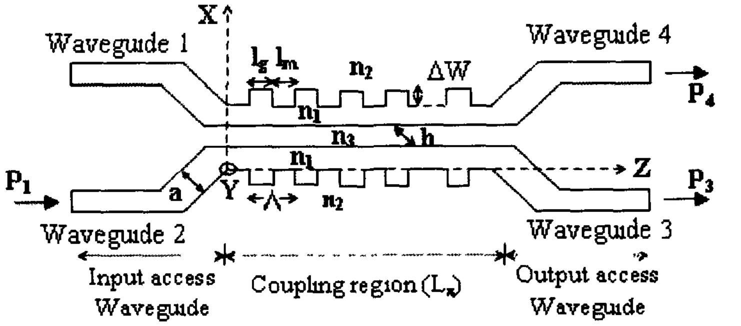

Fig-4.2: Schematic 2D cross-sectional view of tooth shaped grating-assisted directional coupler (GA-DC)

When the input signal mode field of propagation constant $\beta_i(\lambda)$ is incident in single mode S-bent access waveguide-2, two modes-(even and odd modes) are excited in the grating assisted coupling region of the directional coupler. At the end of grating assisted coupling region based on relative phase difference between these two excited modes in both guided and grating region, the light power is either coupled into the single mode S-bent output access waveguides (Waveguide-3 or Waveguide-4) or vanishes. The beat length (defined as the length required for π phase shift) of the directional coupler assisted with total N numbers of grating period is obtained as,

$$L_\pi = [(N+1)l_m + Nl_g] = \frac{\pi}{[(\beta_e^m - \beta_0^m) + (\beta_e^g - \beta_o^g)]} \quad (4.1)$$

where β_e^m, β_o^m and β_e^g, β_o^g are the propagation constants of even and odd modes in the guiding region (K=m) and grating region (K=g) respectively.

As the grating-assisted coupling region in transverse dimension (along Y-axis) is smaller than the lateral dimension (along X-axis) and have the same transverse behavior in everywhere of GA-DC coupling region, it is justified to be assumed that the waveguide structure is to be single mode in transverse dimension. So the mode fields in the grating-assisted directional couplers can be represented in 2D. The input field profile H (x, 0) launched into tooth shaped grating assisted directional coupler (GA-DC) at z=0 is composed of mode field distribution of all modes excited in grating assisted region and represented in terms of odd and even modes in 2D approximation as

$$H(x,0) = \sum_{i=0}^{1} b_i H_i(x) \tag{4.2}$$

where b_i is field contribution coefficient of tooth shaped grating-assisted directional coupler for i^{th} mode and $H_i(x)$ is mode field distribution of i^{th} mode at z=0 with i=0 corresponds to odd mode and i=1 corresponds to even mode respectively.

The composite field profile at a distance z inside GA-DC region can be represented in 2D approximation as a summation of all the guided modes.

$$H(x,z) = \sum_{i=0}^{1} H_i(x,z) = \sum_{\substack{i=0 \\ K=m,g}}^{1} b_i H_i(x) \exp\left[j\left(\beta_0^K - \beta_i^K\right)z\right] \tag{4.3}$$

where i=0, 1 denotes the order of guided modes; β_0^K is the propagation constant of zeroth order (fundamental mode) and β_i^K represents the propagation constant for i^{th} mode respectively. b_i is field contribution coefficient of tooth shaped GA-DC for i^{th} mode and $H_i(x)$ is mode field distribution of i^{th} mode at z=0. The K=m and K=g represent the guiding layer and grating layer of a grating period respectively.

Since the width of the access waveguide (a~1.5 μm) is required to be small for single mode operation of the access waveguide by keeping the normalization frequency V~2.3, the lateral penetration of the mode field outside the waveguide is negligible for the lateral high index contrast. Thus input mode field profile $H_i(x)$ for the i^{th} mode can be approximated for tooth shaped grating-assisted coupling region as,

$$H_i(x) = \sin\left[(i+1)\frac{\pi x}{W_g}\right] \tag{4.4}$$

At the end of tooth shaped grating-assisted coupling section of GA-DC, optical power is either transferred to the output S-bent access waveguide or lost out at the end of tooth shaped grating assisted channel waveguide. The mode field of output access waveguides is contributed by all guided modes propagated in grating assisted coupling region. The mode fields at Mth S-bent access waveguide can be written as

$$H_M^K(x,L) = \sum_{\substack{i=0 \\ K=m,g}}^{1} H_{M,i}^K(x,L) = \sum_{\substack{i=0 \\ K=m,g}}^{1} c_{M,i} H_i(x) \exp\left[j\left(\beta_0^K - \beta_i^K\right)L\right] \tag{4.5}$$

where L=[(N+1)l$_m$+Nl$_g$] and $c_{M,i} = \sqrt{C_{M,i}^K}$ =the ith mode's contribution coefficient (with K=m for guiding region and K=g for grating region) to the M-th access waveguide (M=3 for 3rd output access waveguide and M=4 for 4th output access waveguide), which can be determined by using the mathematical model (as discussed in chapter-3) based on sinusoidal mode simple effective index method (SEIM) as,

$$\begin{aligned}\frac{C_{M,i}^K}{C_0} &= \frac{\pi^2}{16b^2k^2\left(n_1^2-n_2^2\right)}\exp\left\{-hk\left(n_{eff}^2-n_2^2\right)^{1/2}\right\}\left[\exp\left\{bk\left(n_1^2-n_2^2\right)^{1/2}\right\}-\exp\left\{-bk\left(n_1^2-n_2^2\right)^{1/2}\right\}\right] \\ &+\frac{\pi^2}{16b^2k^2\left(n_1^2-n_3^2\right)}\exp\left\{-hk\left(n_1^2-n_3^2\right)^{1/2}\right\}\left[\exp\left\{bk\left(n_1^2-n_3^2\right)^{1/2}\right\}-\exp\left\{-bk\left(n_1^2-n_3^2\right)^{1/2}\right\}\right]\end{aligned} \tag{4.6}$$

where for TE mode,

$$C_0 = \frac{0.4}{F_C} \times \frac{\left(n_1^2 - n_{eff(TE),K}^2\right)\sqrt{n_{eff(TE),K}^2 - n_2^2}}{n_{eff(TE),K}\left(n_1^2 - n_3^2\right)\left[W_K + \dfrac{2}{k_0\sqrt{n_{eff(TE),K}^2 - n_2^2}}\right]} \tag{4.7}$$

$$F_c = \frac{3(1+0.2h)}{\left\{13.5 + 185\left(\beta_0^K - \beta_i^K\right)\right\}h} \tag{4.8}$$

$$n_{eff\,(TE),K} = \beta^{K}_{TE\,(i)}\left(\frac{\lambda}{2\pi}\right) \quad ;K = m,\ g \tag{4.9}$$

Similarly, for TM mode,

$$C_0 = \frac{0.4}{F_C} \times \frac{\left(n_1^2 - n^2_{eff(TM),K}\right)\sqrt{n^2_{eff(TM),K} - n_2^2}}{n_{eff(TM),K}\left(n_1^2 - n_3^2\right)\left[W_K + \dfrac{2}{k_0\sqrt{n^2_{eff(TM),K} - n_2^2}}\right]} \tag{4.10}$$

$$F_c = \frac{3(1 + 0.2h)}{\left\{13.5 + 185\left(\beta_0^K - \beta_i^K\right)\right\}h} \tag{4.11}$$

$$n_{eff\,(TM),K} = \beta^{K}_{TM\,(i)}\left(\frac{\lambda}{2\pi}\right) \quad ;K = m,\ g \tag{4.12}$$

The contributed power to the M[th] S-bent output access waveguide by i[th] mode is given by [13]-[14],

$$P^i_M = \left|H^K_{M,i}(x,L)\right|^2 \tag{4.13}$$

Normalized power coupled to the M[th] output access waveguide for tooth shaped grating assisted directional coupler can be approximated as,

$$\frac{P_{M,i}(x,L)}{P_{1,i}(x,o)} = \frac{\left|\sum\limits_{\substack{i=0\\K=m,g}}^{1} H^K_{M,i}(x,L)\right|^2}{\left|\sum\limits_{\substack{i=0\\K=m,g}}^{1} H^K_{1,i}(x,0)\right|^2} \tag{4.14}$$

$$\approx \sum_{\substack{i=0\\K=m,g}}^{1} C^K_{M,i}H_i^2(x) + \sum_{\substack{i=0\\K=m,g}}^{1}\ \sum_{\substack{j=i+1\\K=m,g}}^{1}\left[2\sqrt{C^K_{M,i}C^K_{M,j}}\,H_i(x)H_j(x)\times\cos\left\{\sum_{\substack{i=0,j=i+1\\K=m,g}}^{1}\left[(N+q_K)(\beta_i^K - \beta_j^K)l_K\right]\right\}\right] \tag{4.15}$$

where i, j = 0, 1 refers to even and odd modes provided j>i, q_K = 0, 1 for grating region (K=m) and guided region (K=g) respectively, N = Number of grating period and $C_{M,i}^{K}$, $C_{M,j}^{K}$ = contribution coefficients (measure of field contribution of i[th] and j[th] modes to lower output access waveguides) that are obtained using equations (4.6)-(4.12), β_i, β_j = propagation constant for i[th] and j[th] modes which are determined from dispersive equations (as discussed in section-3.2.2 of chapter-3). The length of the guiding width (l_m) and grating width (l_g) is determined by using the following relation (4.16) [8-9],

$$l_K = \frac{\lambda}{4n_{eff(j,K)}} \quad ;K = m,g \tag{4.16}$$

Thus, the normalized power coupled to the 3[rd] S-bent access waveguide by i[th] mode for tooth shaped GA-DC can be approximated as,

$$\frac{P_{3,i}(x,L)}{P_{1,i}(x,o)} = \frac{\left|\sum_{\substack{i=0\\K=m,g}}^{1} H_{3,i}^{K}(x,L)\right|^2}{\left|\sum_{\substack{i=0\\K=m,g}}^{1} H_{1,i}^{K}(x,0)\right|^2} \tag{4.17}$$

$$\approx \sum_{\substack{i=0\\K=m,g}}^{1} C_{3,i}^{K} H_i^2(x) + \sum_{\substack{i=0\\K=m,g}}^{1} \sum_{\substack{j=1+i\\K=m,g}}^{1} \left[2\sqrt{C_{3,i}^{K} C_{3,j}^{K}}\, H_i(x) H_j(x) \times \cos\left\{ \sum_{\substack{i=0,j=i+1\\K=m,g}}^{1} \left[(N+q_K)(\beta_i^K - \beta_j^K) l_K \right] \right\} \right]$$

where $C_{3,i}^{K} = \left(c_{3,i}^{K}\right)^2$ and $c_{3,i}^{K}$ = the contribution coefficient of i[th] mode (which can be calculated by using a mathematical model based on SM-SEIM) for the 3[rd] output access Waveguide. Normalized power coupled to the output access waveguide-4 by i[th] mode for tooth shaped GA-DC can be approximated as,

$$\frac{P_{4,i}(x,L)}{P_{1,i}(x,o)} = \frac{\left|\sum_{\substack{i=0\\K=m,g}}^{1} H_{4,i}^{K}(x,L)\right|^2}{\left|\sum_{\substack{i=0\\K=m,g}}^{1} H_{1,i}^{K}(x,0)\right|^2} \tag{4.18}$$

$$\approx \sum_{\substack{i=0\\K=m,g}}^{1} C_{4,i}^{K} H_i^2(x) + \sum_{\substack{i=0\\K=m,g}}^{1} \sum_{\substack{j=1+i\\K=m,g}}^{1} \left[2\sqrt{C_{4,i}^{K} C_{4,j}^{K}} H_i(x) H_j(x) \times \cos\left\{ \sum_{\substack{i=0,j=i+1\\K=m,g}}^{1} \left[(N+q_K)(\beta_i^K - \beta_j^K) l_K \right] \right\} \right]$$

where $C_{4,i} = \left(c_{4,i}^{K}\right)^2$ and $c_{4,i}$ = the contribution coefficient of ith mode (which can be calculated by using a mathematical model based on SM-SEIM) for the 4th output access Waveguide-4.

4.2.1. Coupling Characteristics of GA-DC

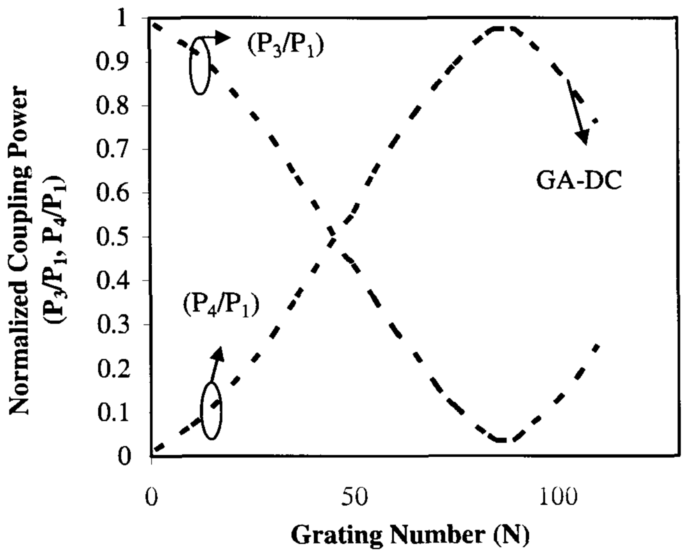

Fig-4.3: Normalized coupling power distribution of tooth shaped grating assisted structures of directional coupler with ΔW=0.25 μm, Δn=5 % and λ~1.55 μm.

Fig-4.3 shows the normalized coupling power distribution for bar coupling (P_3/P_1) state and cross coupling (P_4/P_1) state versus number of grating (N) estimated by using the equations (4.1) and (4.6)-(4.15) for the tooth shaped grating assisted directional coupler (GA-DC) with ΔW=0.25 μm, h=0.5 μm, a=1.5 μm, b=1.5 μm, l_m~0.26 μm, l_g~0.26 μm, Δn=5 %, cladding index~1.45 and wavelength (λ) ~1.55 μm respectively. From the figure, it is seen that the peak cross coupling power (P_4/P_1) is obtained at the beat length where N value is 86 for GA-DC respectively. So the beat length of GA-DC obtained by using equation (4.1) is ~45 μm respectively which is ~50% less than that of conventional directional coupler (beat length~91 μm as obtained in the chapter-3).

4.2.2. Beat Length of GA-DC

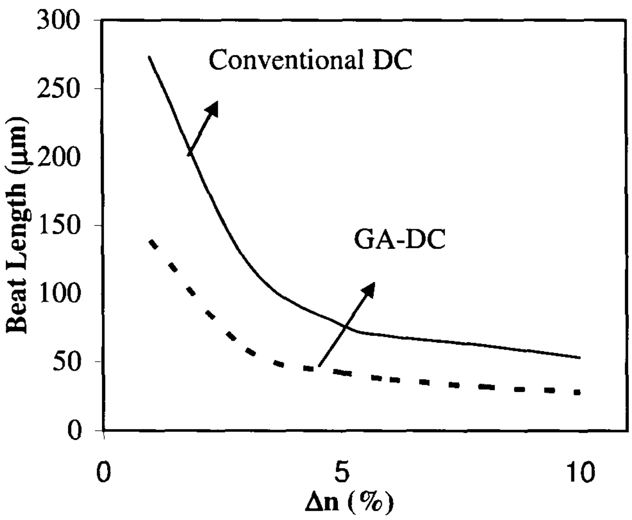

Fig-4.4: Beat length (L_π) versus index contrast (Δn) for tooth shaped GA-DC couplers (ΔW=0.25 μm) and conventional directional coupler (ΔW=0 μm).

Fig-4.4 shows the beat length (L_π) versus index contrast (Δn) of tooth shaped grating assisted directional coupler (GA-DC) with ΔW=0.25 μm and conventional directional coupler (ΔW=0 μm) with a=1.5 μm, b=1.5 μm, h=0.5 μm, W_m ~2a+h,

W_g ~W_m+2ΔW, cladding index~1.45 and λ~1.55 μm respectively. It is observed from the figure that as the index contrast (Δn) increases, the beat length decreases and for Δn>5 %, it decreases slowly. It is also seen that the beat lengths of GA-DC (with Δn=5 % and ΔW=0.25 μm) and conventional DC (with Δn=5 % and ΔW=0 μm) are obtained as ~45 μm, 91 μm respectively. So the beat length of tooth shaped grating assisted directional coupler is ~50 % lower than conventional directional coupler. The lower beat lengths in GA-DC in comparison to the conventional DC are because of multiple reflections that takes place in the tooth shaped grating geometry.

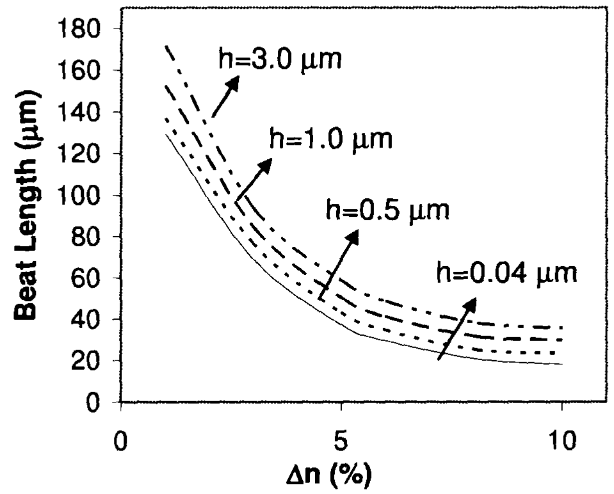

Fig-4.5: Beat length (L_π) versus Δn (%) for GA-DC with different coupling gaps, h=0.04 μm, 0.5 μm, 1.0 μm, 3.0 μm and ΔW=0.25 μm respectively.

The beat length (L_π) versus index contrast (Δn) that is estimated from coupling power distribution curves (as shown in Fig-4.3) using equations (4.1) and (4.6)-(4.15) for tooth shaped GA-DC is shown in Fig-4.5 for different values of waveguide separation gap, h=0.04 μm, 0.5 μm, 1.0 μm, 3.0 μm with ΔW=0.25 μm, a=1.5 μm, b=1.5 μm, n_1=1.5, n_2=1.45 and wavelength ~1.55 μm respectively. It is seen from the graph that the beat lengths for GA-DC decreases as Δn (%) increases. The rate of decrease of L_π is smaller for Δn>5 % and lower values of h. It is also observed that as h becomes nearer to zero coupling gap (h=0), the curves become closer and at h<0.04 μm, the curves for GA-DC almost coincides with the curve for GA-TMI coupler (h=0 μm) [not shown in the figure], which is discussed latter in this chapter.

4.2.3. Beam Propagation Method (BPM) Simulation Results

From the above studies and as already mentioned in the previous chapters, it is indispensable to study the light wave beam propagation with the designed device parameters before fabrication. So, the designed waveguide device components are studied for beam propagation with the help of commercially available optiBPM software and then compared with the results obtained from simple effective index method (SEIM).

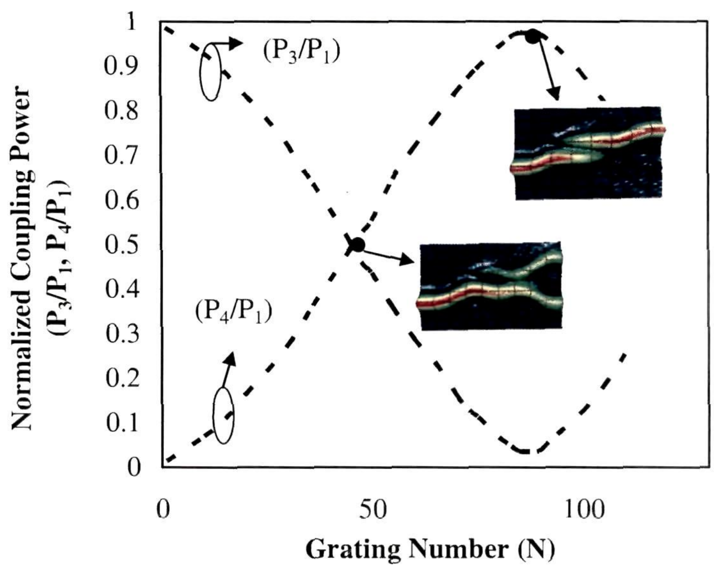

Fig-4.6: Normalized coupled power versus beat length of GA-DC and the BPM output results (cross state and 3 dB state) with coupling gap h~0.5 μm, n_2=1.45, Δn=5 % and wavelength~1.55 μm respectively.

Fig-4.6 shows the normalized coupled power distribution versus beat length (L_π) for tooth shaped grating assisted directional coupler (GA-DC) with coupling gap, h~0.5 μm, a=b=1.5 μm, n_2=1.45 and Δn=5 % respectively as details are discussed in the section-4.2.1. The figure also shows the lightwave propagation at half coupling point (3 dB) and cross coupling point of GA-DC obtained by optiBPM software, is matching well with the results obtained by SEIM model. It is seen from the figure that the peak cross-coupling power (P_4/P_1) is obtained at beat length ~45 μm whereas 3dB coupling power is obtained at beat length ~22.3 μm for the grating assisted directional coupler with a=b=1.5 μm, n_2=1.45 Δn=5% respectively. The inset figures shows the respective BPM output results at the beat length ~45 μm (cross state) and 22.3 μm (3 dB state) respectively.

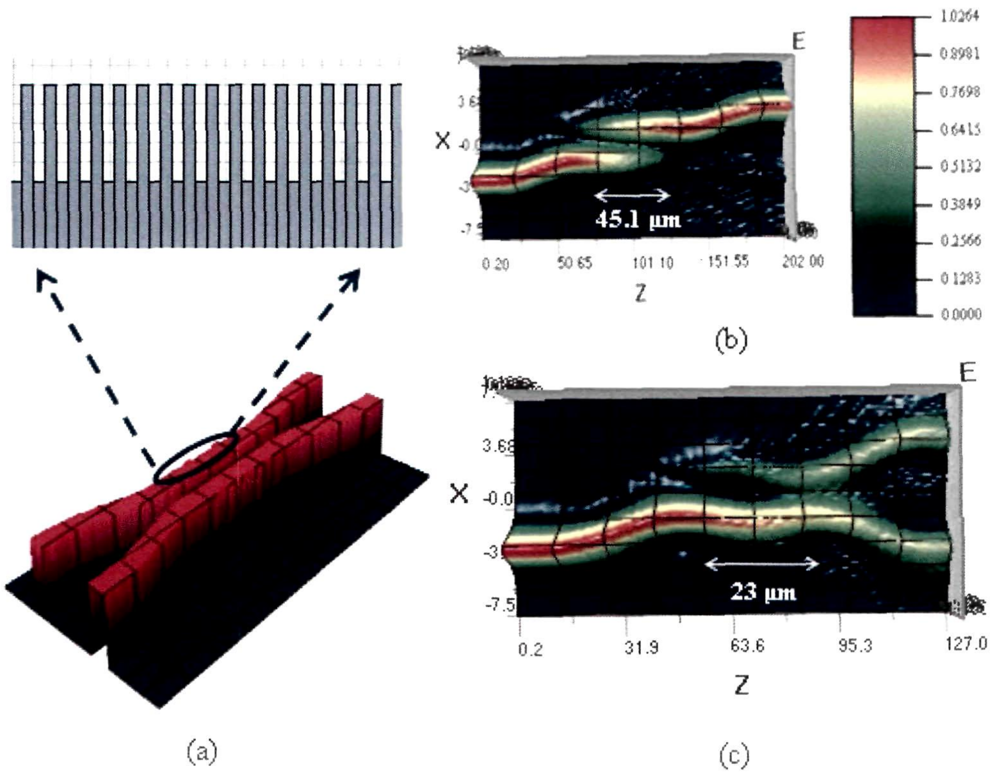

Fig-4.7: BPM results of grating assisted directional coupler (GA-DC) (a) Layout structure (b) Cross state and (c) 3-dB coupler

The Beam Propagation Method (BPM) results of GA-DC obtained by using optiBPM software at the cross state and 3-dB directional coupler are shown in Fig-4.7. From the BPM results, it is found that the beat length of tooth shaped grating assisted directional coupler at cross state~ 45.1 μm, 3 dB state ~23 μm with a=b=1.5 μm, n_2=1.45, h=0.5 μm and Δn=5 % respectively which are analogous with the theoretical results obtained by using SEIM.

4.2.4. Fabrication Tolerances and Polarization Dependence

In order to study the performance degradation with a small unwanted deviation of designed waveguide parameters during the fabrication process steps, the effect of fabrication tolerances (δw) of grating assisted channel waveguide width on power imbalance for tooth shaped grating assisted directional coupler and conventional directional coupler (ΔW=0 μm) has been studied.

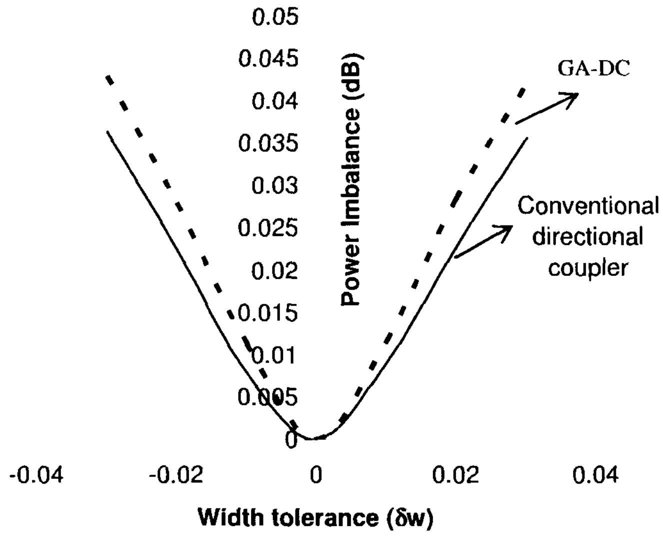

Fig-4.8: Power Imbalance characteristics versus width tolerances (δw) for tooth shaped grating assisted directional coupler (dashed line) and conventional directional coupler (solid line) with index contrast ~5%, cladding index~1.45, h~0.5 μm, a=1.5 μm, b=1.5 μm and λ~1.55 μm respectively.

Fig-4.8 shows power imbalance [=10 $\log_{10}$ (P_3/P_4)] versus fabrication tolerances (±δw) of tooth shaped grating assisted MMI width and conventional DC with h~0.5 μm, a=1.5 μm, b=1.5 μm and λ~1.55 μm respectively. It is seen from the figure that the power imbalance increases with ±δw symmetrically for both the structures and the increase of power imbalance for tooth shaped grating assisted directional coupler is slightly more than that of conventional directional coupler due to having more number of device parameters in tooth shaped grating assisted DC. The rate of increase of power imbalance (dB) with respect to width tolerance for GA-DC and conventional directional couplers are approximately obtained as $\frac{\partial}{\partial(\delta w)}$ [Power Imbalance (dB)] ~0.13 dB/μm and 0.15 dB/μm respectively.

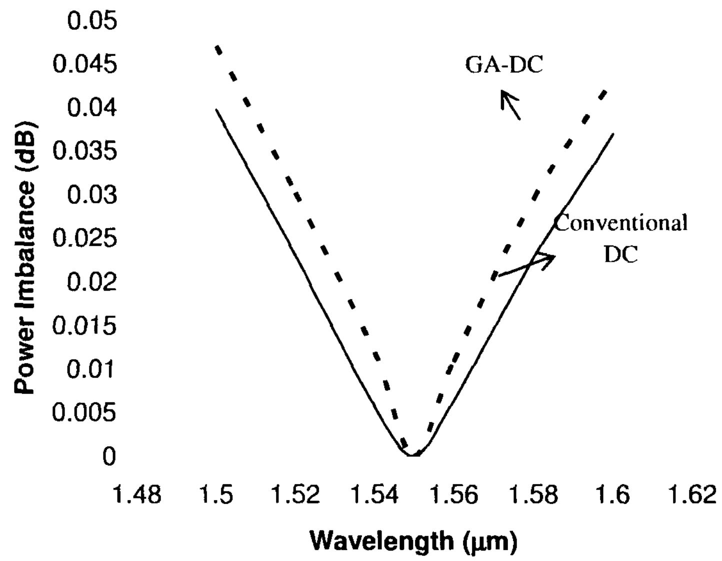

Fig-4.9: Power Imbalance characteristics versus wavelength variation for tooth shaped grating assisted DC (dashed line) and conventional DC (solid line) with a=1.5 μm, b=1.5 μm, h~0.5 μm, index contrast ~5% and cladding index~1.45 respectively.

Fig-4.9 shows the power imbalance versus wavelength for a~1.5 μm, b~1.5 μm, h~0.5 μm, index contrast ~5 % and cladding index~1.45. In the figure, the dashed line indicates the curve for 3 dB tooth shaped grating assisted directional coupler of coupling length ~22.5 μm and the solid line shows for 3 dB conventional directional coupler of coupling length ~45.5 μm respectively. It is seen from the plot that in both cases minimum power imbalance is obtained at λ~1.55 μm and it is almost symmetrically increased in both sides of λ~1.55 μm. The increase of power imbalance with wavelength for tooth shaped grating assisted DC is more than that of conventional DC. So the dependence of power imbalance on fabrication tolerance and wavelength for grating assisted geometry is slightly more as that for conventional structure.

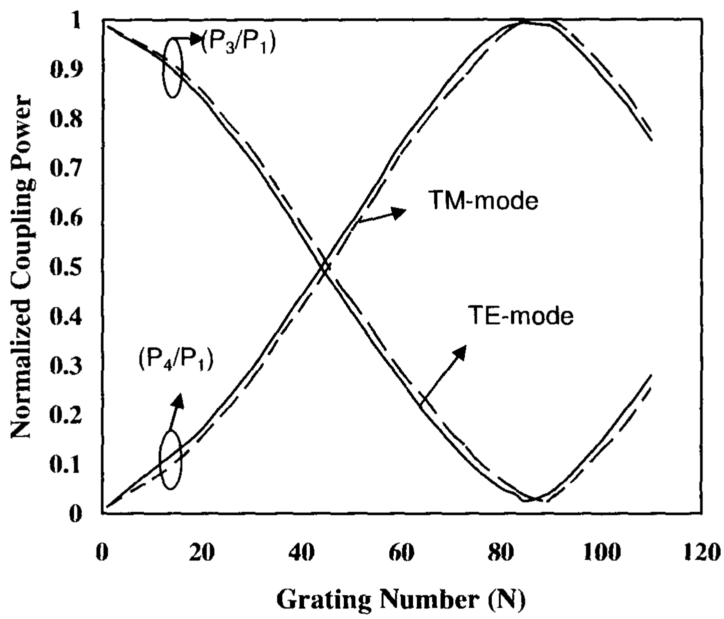

Fig-4.10: Normalized coupling power distribution of tooth shaped GA-DC for TE mode (solid line) and TM mode (dashed line) with a=b=1.5 μm, h~0.5 μm, Δn ~5% and cladding index~1.45 respectively.

From the studies, it is also found that beat length of GA-DC for TE polarization is ~0.24% more than that of the TM polarization which is shown in the Fig.-4.10. The figure shows the normalized coupling power distribution versus grating number of both TE and TM polarization for GA-DC with a~1.5 μm, b~1.5 μm, h~0.5 μm, index contrast ~5 % and cladding index~1.45 respectively. It is seen that polarization dependence of GA-DC is slightly more than that of the conventional directional coupler as the number of waveguide parameters in tooth shaped grating structure is more than that of the conventional DC.

4.3. Tooth Shaped Grating Assisted Two Mode Interference (GA-TMI) Coupler

The basic principle of grating assisted two mode interference (GA-TMI) coupler is based on the principle of coupled mode theory that describes the coupling of multiple reflected evanescent ligthwave occurs between the two adjoin grating assisted waveguides, where basically two modes (fundamental and first order) are excited through the overlapping of multiple reflected evanescent waves of the propagating modes.

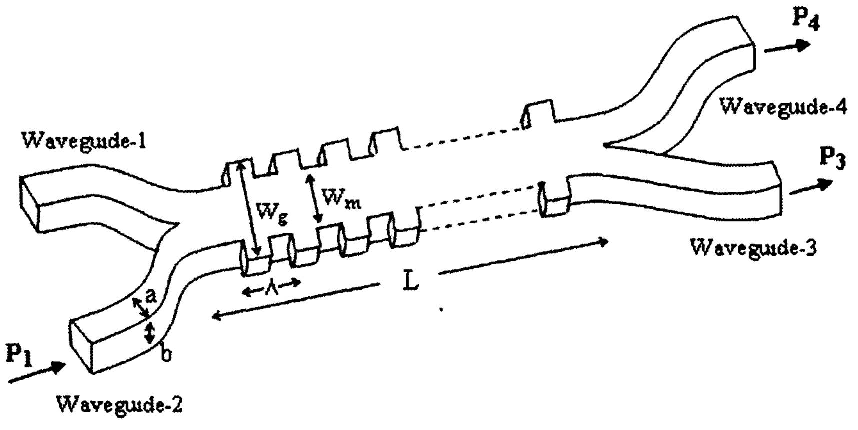

Fig-4.11: Schematic 3D diagram of GA-TMI coupler

Fig-4.11 shows the three dimensional (3D) view of an ultra compact tooth shaped grating assisted two-mode interference (GA-TMI) coupler consisting coupling region of length L with alternating guiding layer of width (W_m=2a) and grating layer of width (W_g=W_m +2ΔW). The coupling region consists of N total numbers of grating period (Λ=l_m+l_g) where l_m and l_g are the length of guiding layer and grating layer in each grating period respectively. There are two single mode input S-bent access waveguides (Waveguide-1 & Waveguide-2) and two single mode output S-bent access waveguides (Waveguide-3 & Waveguide-4) of core width a and thickness b in GA-TMI coupler. The n_1 and n_2 are the refractive indices of core and cladding region respectively whereas ΔW [~(W_g-W_m)] is the width of tooth shaped grating. The input power P_1 is incident in lower most input access waveguide when the output powers P_3 and P_4 are obtained as a bar state and cross state respectively.

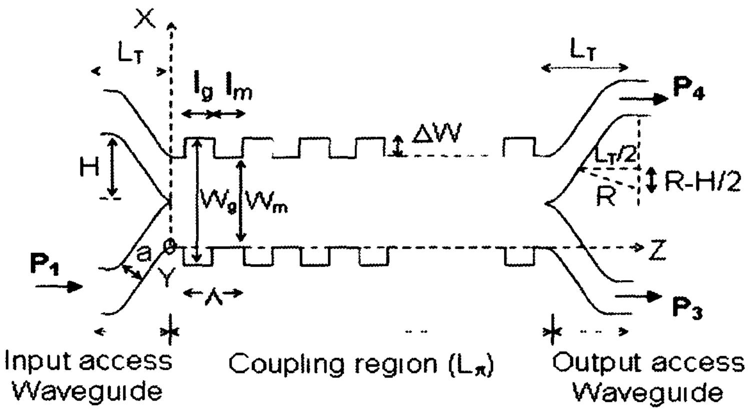

Fig-4.12: Schematic diagram of tooth shaped grating assisted two-mode interference (GA-TMI) coupler with waveguide parameters

Fig-4.12 shows the two dimensional (2D) cross-sectional view of tooth shaped grating assisted waveguide geometry of TMI coupler as shown in Fig-4.11. The input signal mode field of propagation constant β_i (λ) is launched through input single mode S-bent access Waveguide-2, excites only the fundamental mode and first order mode in the coupling region, where β_{00}^{m}, β_{01}^{m} and β_{00}^{g}, β_{01}^{g} are the propagation constants of fundamental and first order modes in the guiding region and grating region respectively. Based on relative phase difference between these modes, the light power is coupled into two single mode S-bent output access waveguides, Waveguide-3 and Waveguide-4. The beat length (defined as the length required for π phase shift) for the TMI couplers assisted with total N numbers of grating period is written as,

$$L_\pi = [(N+1)l_m + Nl_g] = \frac{\pi}{[(\beta_{00}^m - \beta_{01}^m) + (\beta_{00}^g - \beta_{01}^g)]} \tag{4.19}$$

From the device geometry, it is justified to assume that the waveguide structure is to be single mode in transverse dimension as transverse dimension of GA-TMI coupling region is smaller than that of the lateral dimension and have the same transverse behavior in everywhere of GA-TMI coupling region. So the mode fields in GA-TMI couplers can be expressed in 2D representation.

The input field profile H(x, 0) incident on tooth shaped grating assisted two-mode interference (GA-TMI) coupler is composed of mode field distribution of all modes and written as

$$H(x,0) = \sum_{i=0}^{1} b_i H_i(x) \tag{4.20}$$

where b_i is i^{th} mode field contribution coefficient of tooth shaped grating assisted TMI coupler and $H_i(x)$ is mode field distribution of i^{th} mode at z=0.

The composite mode field profile at a distance z inside grating assisted TMI region can be written in 2D approximation as a super position of all the guided modes.

$$H(x,z) = \sum_{i=0}^{1} H_i(x,z) = \sum_{\substack{i=0 \\ K=m,g}}^{1} b_i H_i(x) \exp\left[j(\beta_0^K - \beta_i^K)z\right] \tag{4.21}$$

where i=0, 1 denotes the order of guided modes; β_0^K is the propagation constant of zeroth order (fundamental mode) and β_i^K represents the propagation constant for i^{th} mode respectively. b_i is field contribution coefficient of tooth shaped GA-TMI coupler for i^{th} mode and $H_i(x)$ is mode field distribution of i^{th} mode at z=0. The guiding layer and grating layer of a grating period is denoted by K=m and K=g respectively.

Since the width of the access waveguide (a ~1.5 μm) is required to be small for single mode operation of the access waveguide for the normalization frequency V~2.3. The lateral penetration of the mode field outside the waveguide is negligible for the lateral high index contrast. Thus input mode field profile for the i[th] mode $H_i(x)$ can be approximated for tooth shaped grating assisted TMI region as,

$$H_i(x) = \sin\left[(i+1)\frac{\pi x}{W_g}\right] \tag{4.22}$$

At the end of tooth shaped GA-TMI coupling section, optical power is either transferred to the output waveguide or lost out at the end of tooth shaped grating assisted TMI waveguide. The mode field of output waveguide is sum of the contribution of all guided modes in TMI section with grating. The mode field at M-th output access waveguide can be define as

$$H_M(x,L) = \sum_{\substack{i=0\\K=m,g}}^{1} H_{M,i}^{K}(x,L) = \sum_{\substack{i=0\\K=m,g}}^{1} c_{M,i} H_i(x) \exp\left[j\left(\beta_0^K - \beta_i^K\right)L\right] \tag{4.23}$$

where L= $[(N+1)l_m+Nl_g]$ and $c_{M,i} = \sqrt{C_{M,i}^{K}}$ is the i[th] order mode's contribution coefficient (with K=m for guiding region and K=g for grating region) to the M-th access waveguide (M=3 for 3[rd] output access waveguide and M=4 for 4[th] output access waveguide), which can be determined by using the mathematical model of directional coupler based on sinusoidal modes and simple effective index method (SEIM) as discussed in the previous section-4.2.1, with a consideration h→0 in the equation (4.6); where h is the waveguide separation gap (for TMI coupler h=0 μm), we have

$$\frac{C_{M,i}^{K}}{C_0} = \frac{\pi^2}{16b^2k^2\left(n_1^2 - n_2^2\right)}\left[\exp\left\{bk\left(n_1^2 - n_2^2\right)^{1/2}\right\} - \exp\left\{-bk\left(n_1^2 - n_2^2\right)^{1/2}\right\}\right] \tag{4.24}$$

where for TE mode,

$$C_0 = \frac{0.4}{F_C} \times \frac{\left(n_1^2 - n_{eff(TE),K}^2\right)\sqrt{n_{eff(TE),K}^2 - n_2^2}}{n_{eff(TE),K}\left(n_1^2 - n_3^2\right)\left[W_K + \frac{2}{k_0\sqrt{n_{eff(TE),K}^2 - n_2^2}}\right]} \tag{4.25}$$

$$F_c = \frac{3(1+0.2h)}{\left\{13.5 + 185\left(\beta_0^K - \beta_i^K\right)\right\}h} \tag{4.26}$$

$$n_{eff\,(TE),K} = \beta_{TE\,(i)}^K\left(\frac{\lambda}{2\pi}\right) \quad ; K = m,\ g \tag{4.27}$$

Similarly, for TM modes,

$$C_0 = \frac{0.4}{F_C} \times \frac{\left(n_1^2 - n_{eff(TM),K}^2\right)\sqrt{n_{eff(TM),K}^2 - n_2^2}}{n_{eff(TM),K}\left(n_1^2 - n_3^2\right)\left[W_K + \frac{2}{k_0\sqrt{n_{eff(TM),K}^2 - n_2^2}}\right]} \tag{4.28}$$

$$F_c = \frac{3(1+0.2h)}{\left\{13.5 + 185\left(\beta_0^K - \beta_i^K\right)\right\}h} \tag{4.29}$$

$$n_{eff\,(TM),K} = \beta_{TM\,(i)}^K\left(\frac{\lambda}{2\pi}\right) \quad ; K = m,\ g \tag{4.30}$$

The contributed power to the Mth S-bent output access waveguide by ith order mode is given by,

$$P_M^i = \left|H_{M,i}^K(x,L)\right|^2 \tag{4.31}$$

Normalized power coupled to the Mth output access waveguide for tooth shaped grating assisted TMI coupler can be approximated as,

$$\frac{P_{M,i}(x,L)}{P_{1,i}(x,o)} = \frac{\left|\sum_{\substack{i=0 \\ K=m,g}}^{1} H_{M,i}^K(x,L)\right|^2}{\left|\sum_{\substack{i=0 \\ K=m,g}}^{1} H_{1,i}^K(x,0)\right|^2} \tag{4.32}$$

$$\approx \sum_{\substack{i=0\\K=m,g}}^{1} C_{M,i}^{K} H_i^2(x) + \sum_{\substack{i=0\\K=m,g}}^{1} \sum_{\substack{j=1+i\\K=m,g}}^{1} \left[2\sqrt{C_{M,i}^{K} C_{M,j}^{K}}\, H_i(x) H_j(x) \times \cos\left\{ \sum_{\substack{i=0,j=i+1\\K=m,g}}^{1} \left[(N+q_K)(\beta_i^K - \beta_j^K) l_K \right] \right\} \right] \quad (4.33)$$

where i, j = 0, 1 refers to fundamental and first order modes provided j>i, q_K= 0, 1 for grating region (K=m) and guided region (K=g) respectively, N= Number of grating period and $C_{M,i}^{K}$, $C_{M,j}^{K}$=contribution coefficients (measure of field contribution of ith and jth modes to lower output access waveguides) that are obtained using equations (4.24)-(4.30), β_i^K, β_j^K = propagation constants for ith and jth modes at the guided region (K=m) and grating region (K=g) which are determined from dispersive equations (as discussed in section-3.2.2 of chapter-3). The lengths of the guiding width (l_m) and grating width (l_g) are determined by using the following relation (4.34) [8-9],

$$l_K = \frac{\lambda}{4 n_{eff(j,K)}} \quad ; K = m, g \quad (4.34)$$

Thus, the contributed power to the 3rd S-bent access waveguide of GA-TMI coupler by ith order mode is given by,

$$P_3^i = \left| H_{3,i}^K(x, L) \right|^2 \quad (4.35)$$

Similarly, normalized power coupled to the 3rd S-bent access waveguide by ith order mode for tooth shaped GA-TMI coupler can be approximated as,

$$\frac{P_{3,i}(x,L)}{P_{1,i}(x,o)} = \frac{\left| \sum_{\substack{i=0\\K=m,g}}^{1} H_{3,i}^K(x,L) \right|^2}{\left| \sum_{\substack{i=0\\K=m,g}}^{1} H_{1,i}^K(x,0) \right|^2} \quad (4.36)$$

$$\approx \sum_{\substack{i=0\\K=m,g}}^{1} C_{3,i}^{K} H_i^2(x) + \sum_{\substack{i=0\\K=m,g}}^{1} \sum_{\substack{j=1+i\\K=m,g}}^{1} \left[2\sqrt{C_{3,i}^{K} C_{3,j}^{K}}\, H_i(x) H_j(x) \times \cos\left\{ \sum_{\substack{i=0,j=i+1\\K=m,g}}^{1} \left[(N+q_K)(\beta_i^K - \beta_j^K) l_K \right] \right\} \right]$$

where $C^{K}_{3i} = \left(c^{K}_{3i}\right)^{2}$ and $c^{K}_{3,i}$ = the contribution coefficient of i[th] mode (which can be calculated by using a mathematical model based on SM-SEIM) for the 3[rd] output access Waveguide.

Normalized power coupled to the 4[th] S-bent access waveguide of tooth shaped GA-TMI coupler by i[th] order mode can be approximated as,

$$\frac{P_{4,i}(x,L)}{P_{1,i}(x,o)} = \frac{\left|\sum_{\substack{i=0\\K=m,g}}^{1} H^{K}_{4,i}(x,L)\right|^{2}}{\left|\sum_{\substack{i=0\\K=m,g}}^{1} H^{K}_{1,i}(x,0)\right|^{2}} \tag{4.37}$$

$$\approx \sum_{\substack{i=0\\K=m,g}}^{1} C^{K}_{4,i} H^{2}_{i}(x) + \sum_{\substack{i=0\\K=m,g}}^{1} \sum_{\substack{j=1+i\\K=m,g}}^{1} \left[2\sqrt{C^{K}_{4,i} C^{K}_{4,j}}\, H_{i}(x) H_{j}(x) \times \cos\left\{ \sum_{\substack{i=0,j=i+1\\K=m,g}}^{1} \left[(N+q_{K})(\beta^{K}_{i} - \beta^{K}_{j}) l_{K}\right] \right\}\right]$$

where $C^{K}_{4} = \left(c^{K}_{4}\right)^{2}$ and $c^{K}_{4,i}$ = contribution coefficient of i[th] mode that is estimated by using a mathematical model based on SM-SEIM for the 4[th] output access waveguide.

4.3.1. Coupling Characteristics of GA-TMI Coupler

Fig-4.13 shows the normalized coupling power (P_3/P_1 and P_4/P_1) versus number of grating (N) estimated by using equation (4.20)-(4.38) with $W_m(=2a)=3.0$ μm, $\Delta n=5\%$, $l_m=0.264001$ μm, $l_g=0.263943$ μm and cladding index~1.45 for $\Delta W=0.05$ μm and 0.25 μm respectively. It is seen from the figure that peak cross coupling power (P_4/P_1) for $\Delta W=0.05$ μm and 0.25 μm is obtained at N=41 and 42 respectively which are almost close to each other. So we have considering $\Delta W=0.25$ μm for further study. The beat length for GA-TMI with $\Delta W=0.25$ μm is given by $[(N+1)l_m + Nl_g] = 22.4$ μm which is ~50% less than that of conventional TMI coupler ($\Delta W=0$ μm). The lower beat length in grating assisted geometry of two mode interference (GA-TMI) coupler is due to multiple reflections occurred in the tooth shaped grating region.

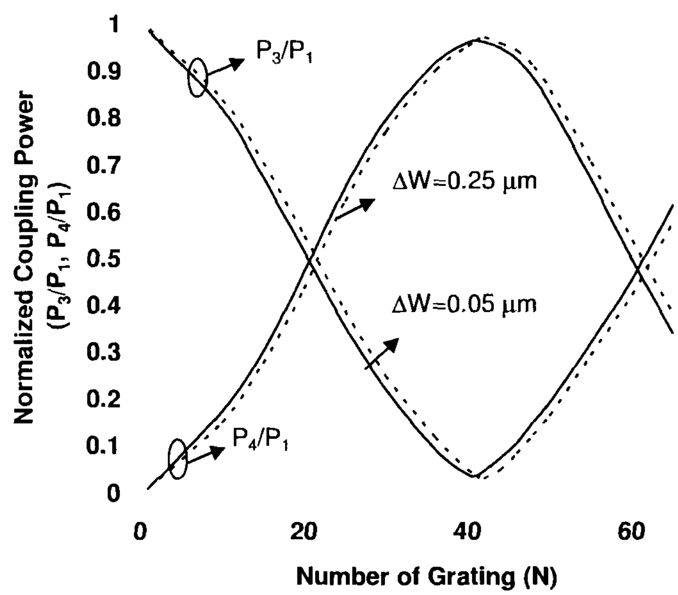

Fig-4.13: Normalized coupling power distribution of tooth shaped GA-TMI coupler with W_m=3.0 μm, a=b=1.5 μm, Δn=5%, λ ~1.55 μm for ΔW=0.05 μm (solid line) and ΔW=0.25 μm (dashed line) respectively.

It is also observed that for TM mode, the theoretical value of L_π is estimated to be 0.22% more than that of the TE mode which is discussed latter in this chapter. The lowering of peak normalization power (0.96) is mainly due to radiation loss at bending portion of access waveguide. The bending loss at the access waveguide is estimate as $4.343\alpha S$= 0.2 dB (where α = loss coefficient that mainly depends on bending radius R [15] and $S = 2R\cos^{-1}\left[1-\frac{H}{2R}\right]$, R=358 μm and H = height of access waveguide as shown in Fig-4.12). The transition length L_T is obtained as $\sqrt{H(4R-H)}$ =132 μm. Total length of cross coupling GA-TMI coupler is obtained as $2L_T+L_\pi$ =286 μm.

Fig-4.14 shows the normalized coupling power (P_3/P_1 and P_4/P_1) vs. number of grating period (N) calculated using eqn. (4.24)-(4.37) for the tooth shaped grating assisted TMI coupler (h=0 μm) with ΔW=0.25 μm, Δn=5%, a=1.5 μm, b=1.5 μm, $l_m \approx l_g$ ~0.27 μm, n_1=1.5, n_2=1.45 and wavelength ~1.55 μm respectively. From the plot, it is seen that the peak normalized coupling power (P_4/P_1) is obtained at beat lengths (calculated using equ. (4.19)) ~22.9 μm respectively, with the corresponding values of N are 43 for grating assisted TMI coupler respectively.

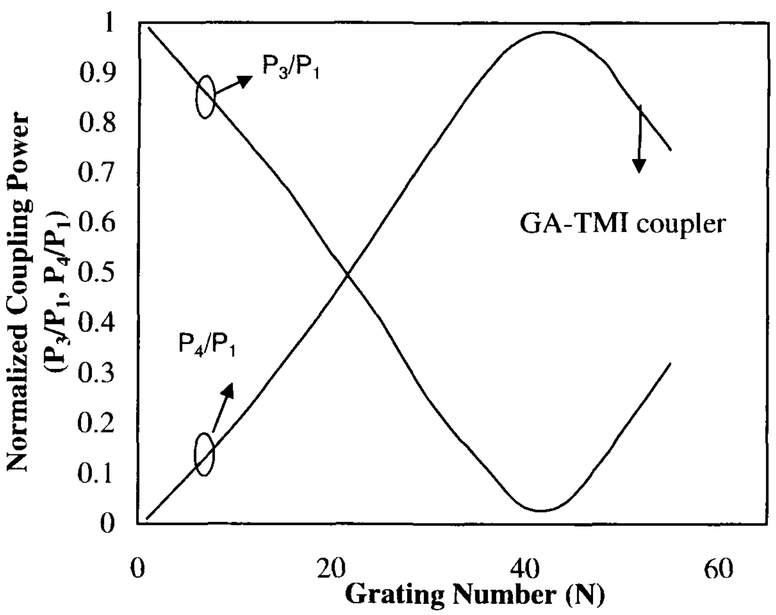

Fig-4.14: Normalized coupling power vs. number of grating period (N) for GA-TMI coupler with Δn =5 %, ΔW=0.25 μm, a=1.5 μm, b=1.5 μm, $l_m \approx l_g$ ~0.27 μm, n_1=1.5, n_2=1.45 and λ~1.55 μm respectively.

4.3.2. Multiple Reflection in Grating Assisted TMI Coupler

Fig.-4.15 shows the schematic ray diagram of multiple reflections that take place in the tooth shaped grating geometry. The light path shown in red colour gives the light reflections that occurs at the guiding width (K=m) (without grating region) whereas the yellow colour rays are getting multiple reflections in the grating width (K=g). It is observed that the path travelled by the rays in grating assisted structure is more than that obtained in conventional structures (i. e. without grating region). Thus the path difference between any two rays or excited modes in grating assisted geometry is more that in conventional structures.

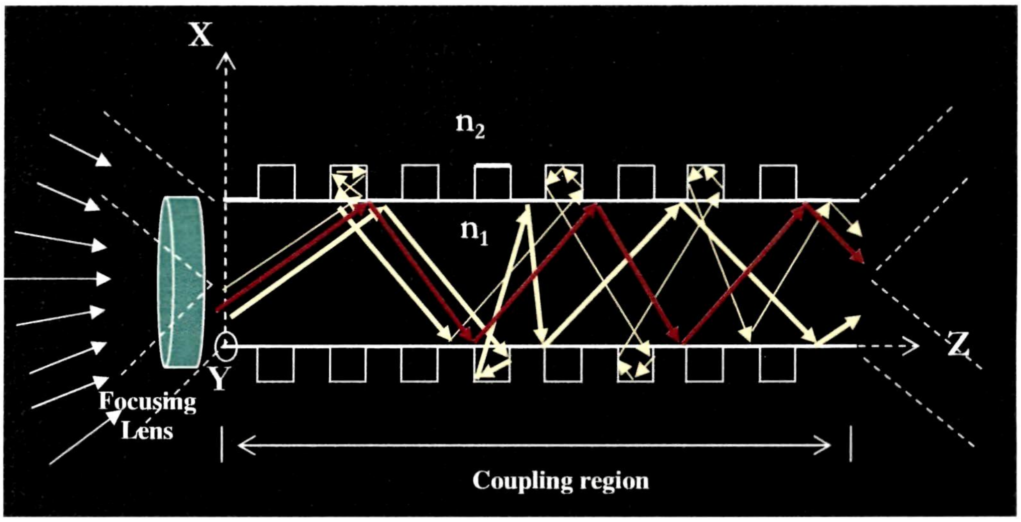

Fig-4.15: Schematic ray diagram showing the multiple reflections occur in the tooth shaped grating structures

4.3.3. Beat Length of GA-TMI Coupler

Fig-4.16 shows the plot for beat length (L_π) versus Δn (%) estimated from coupling power distribution curves (Fig-4.13) for ΔW=0.5 μm, 0.25 μm and conventional TMI coupler (with ΔW=0 μm) respectively. It is obtained from the figure that at Δn=5 %, the beat length decreases slowly with ΔW. As Δn increases the beat length reduces and for ΔW<0.05 μm, the curves becomes overlapped. So we have chosen Δn=5 % and ΔW=0.25 μm respectively for the further details study. It found that at Δn=5 %, the beat lengths are ~21.9 μm, 22.4 μm with ΔW=0.5 μm (solid line), 0.25 μm (dotted line) respectively whereas beat length of conventional TMI coupler (with ΔW=0 μm, dashed line) is 45 μm.

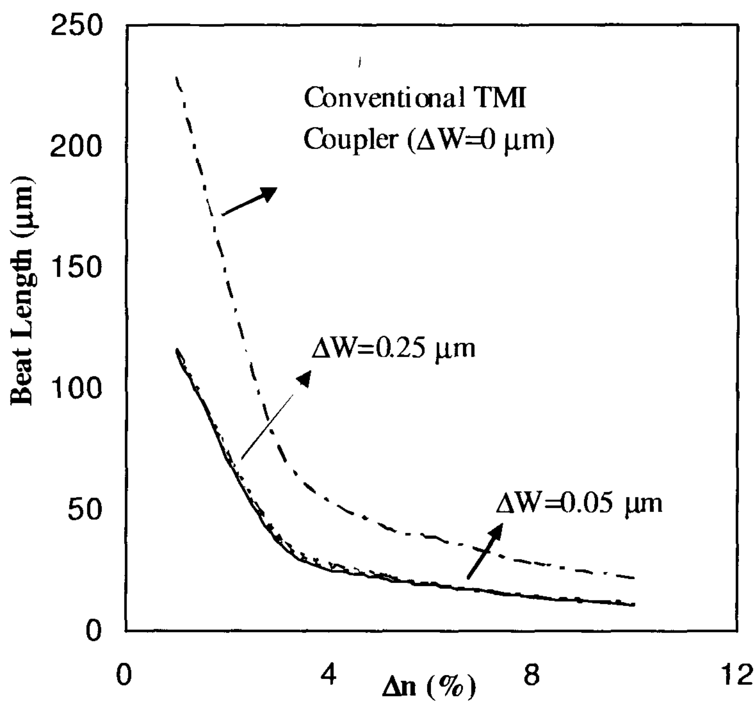

Fig-4.16: Beat length versus index contrast of tooth shaped grating assisted two mode interference (GA-TMI) coupler with ΔW=0.05 μm (solid line), 0.25 μm (dotted line) and conventional TMI coupler (ΔW=0 μm, dashed line) respectively.

4.3.4. Beam Propagation Method (BPM) Simulation Results for GA-TMI Coupler

The design waveguide device components are studied for beam propagation analysis with the designed device parameters before fabrication with the help of commercially available optiBPM software and then compared with sinusoidal mode simple effective index method (SEIM) based results. Fig-4.17 shows the normalized coupled power distribution for the bar coupling (P_3/P_1) state and the cross coupling (P_4/P_1) state versus beat length (L_π) for tooth shaped grating assisted TMI (GA-TMI) coupler obtained by SEIM and the BPM output results with zero coupling gap, W_m=3.0 μm, a=1.5 μm, b=1.5 μm, Δn=5 %, λ ~1.55 μm, ΔW= 0.25 μm respectively.

The figure shows the lightwave propagation at half coupling point (3 dB) and cross coupling point of GA-TMI coupler obtained by optiBPM software which is matching well with the results obtained by SEIM model.

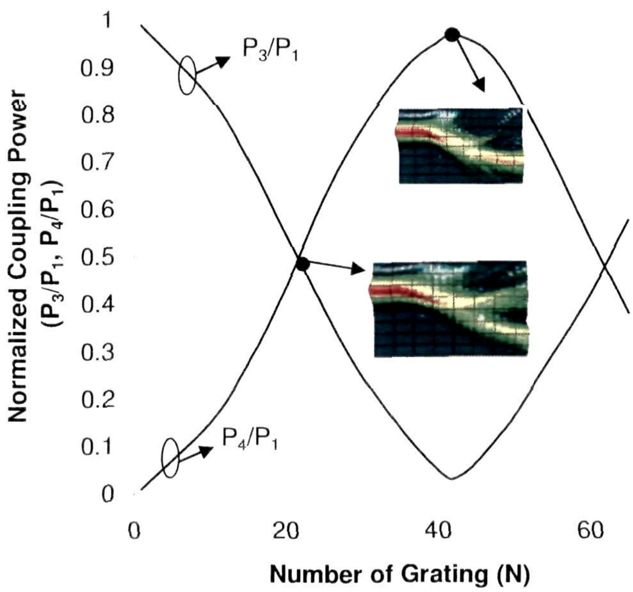

Fig-4.17: Normalized coupling power distribution of tooth shaped grating assisted two mode interference (GA-TMI) coupler with W_m=3.0 μm, a=1.5 μm, b=1.5 μm, Δn=5 %, λ ~1.55 μm, ΔW= 0.25 μm and the BPM output results at the cross and 3 dB state obtained by using optiBPM software respectively.

From the above figure, the peak cross-coupling power (P_4/P_1) is obtained at beat length ~22.4 μm whereas 3dB coupling power is found at beat length ~11.2 μm for the tooth shaped GA-TMI coupler with a=b=1.5 μm, n_2=1.45 Δn=5 % respectively. The inset figures shows the respective BPM output results at the beat length ~22.3 μm and 11.5 μm respectively.

The beam propagation method (BPM) results of GA-TMI coupler obtained by using optiBPM software at the cross state and 3-dB directional coupler respectively are shown in Fig-4.18. From the BPM results, it is found that the beat length of tooth shaped grating assisted TMI (GA-TMI) coupler at cross point~ 22.3 μm, 3 dB state ~ 11.5 μm and bar point~ 45 μm with a=b=1.5 μm, n_2=1.45 and Δn=5% respectively, matching well with the theoretical results obtained by SEIM.

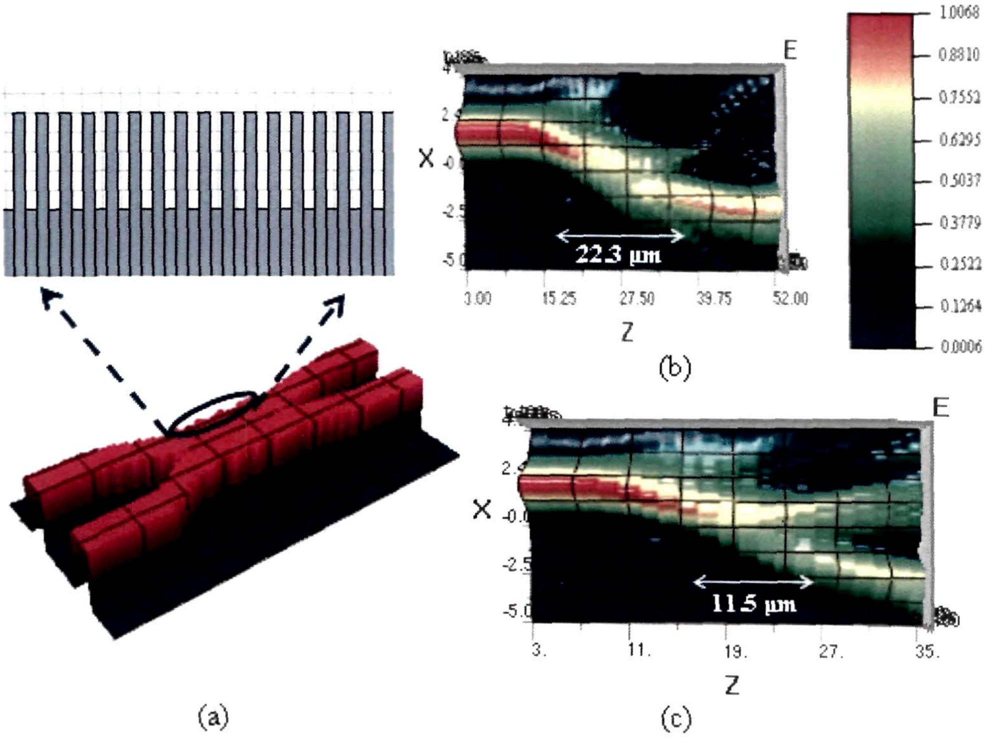

Fig-4.18 : BPM results of grating assisted TMI (GA-TMI) coupler for (a) Layout structure (b) Cross state (c) 3-dB coupler

4.3.5. Fabrication Tolerances and Polarization Dependence of GA-TMI Coupler

Since it may be difficult for precise fabrication of device structure with exact designed parameters, it is indispensable to study its performance with unwanted variation of designed waveguide parameters. Here, the effect of fabrication tolerances (δw) of TMI width on power imbalance of tooth shaped GA-TMI coupler and TMI coupler without grating (ΔW=0 μm) has been studied. Fig-4.19 shows the power imbalance [$=10\log_{10}(P_3/P_4)$] characteristics versus fabrication tolerances (±δw) of tooth shaped grating geometry of TMI width with cladding index~1.45, index contrast ~ 5 %, a=1.5 μm and wavelength~1.55 μm. It is seen that the increase of power imbalance for GA-TMI coupler is slightly more than that of conventional TMI coupler because TMI coupler with tooth shaped grating geometry has more number of device parameters than the conventional TMI coupler. The rate of increase of power imbalance (dB) with respect to width tolerance for GA-TMI coupler and conventional TMI coupler are approximately obtained as $\frac{\partial}{\partial(\delta w)}$ [Power Imbalance (dB)] ~0.16 dB/μm and 0.18 dB/μm respectively.

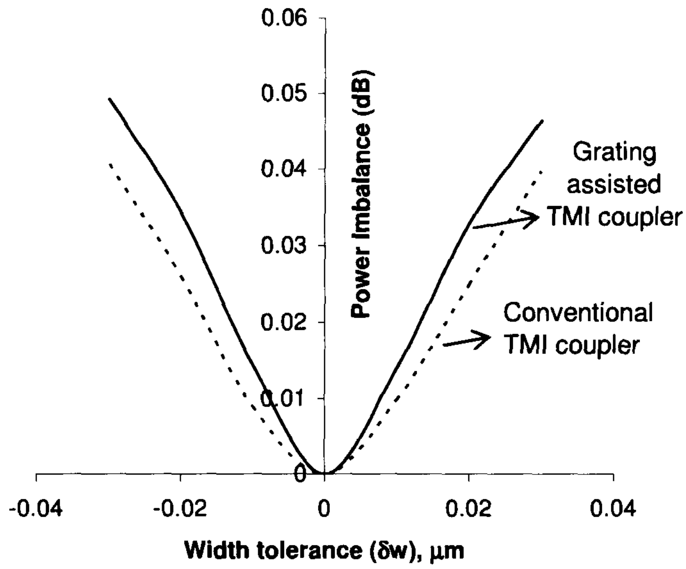

Fig-4.19: Power imbalance characteristics versus width tolerance (δw) of tooth shaped grating assisted TMI coupler (dotted line) and conventional TMI coupler (solid line), 3-dB TMI coupler with cladding index~1.45, index contrast ~5 % , a=1.5 μm and wavelength~ 1.55 μm.

Fig-4.20 shows the dependence of power Imbalance on wavelength for 3 dB TMI coupler with tooth shaped grating geometry (dotted line) and 3 dB conventional TMI coupler (solid line) with a=1.5 μm, b=1.5 μm, index contrast ~5 % and cladding index~1.45. It is seen from the graph that increase of power imbalance for GA-TMI coupler is slightly more than that of conventional TMI coupler (ΔW=0 μm) and in both cases, the power imbalance increases almost symmetrically in both sides of minimum power imbalance obtained at λ~1.55 μm as 3 dB coupler is designed for this wavelength. So 3dB TMI coupler with tooth shaped grating geometry is more wavelength sensitive than 3 dB conventional TMI coupler.

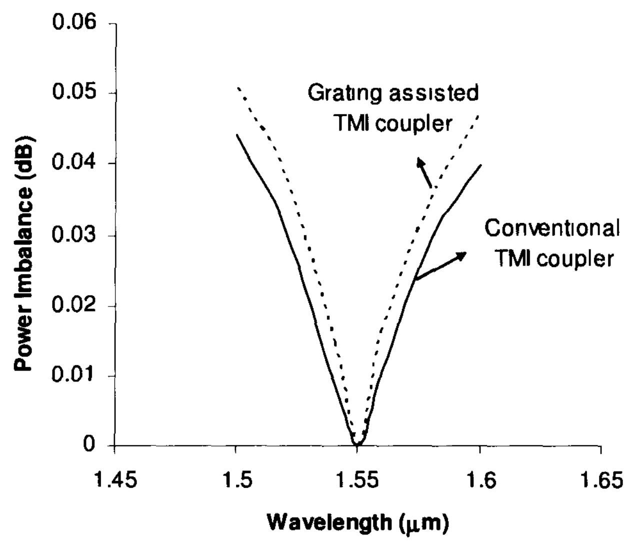

Fig-4.20: Power Imbalance characteristics versus wavelength variation for tooth shaped grating assisted TMI coupler (dashed line) and conventional TMI coupler (solid line) with a=1.5 μm, b=1.5 μm, index contrast ~5% and cladding index~1.45.

Fig-4.21 shows the normalized coupling power distribution versus longitudinal coupling length of GA-TMI coupler for both TE-mode and TM-mode with ΔW=0.25 μm, h=0 μm, a=b=1.5 μm, cladding index~1.45, Δn=5 % and λ~1.55 μm respectively. It is found that for TM-polarization the value of longitudinal beat length is ~0.22 % more than that of the TE-polarization. It is also observed that the polarization dependence of GA-TMI coupler is slightly more than conventional TMI couplers because the number of waveguide parameters in the grating geometry is more than that of conventional structures.

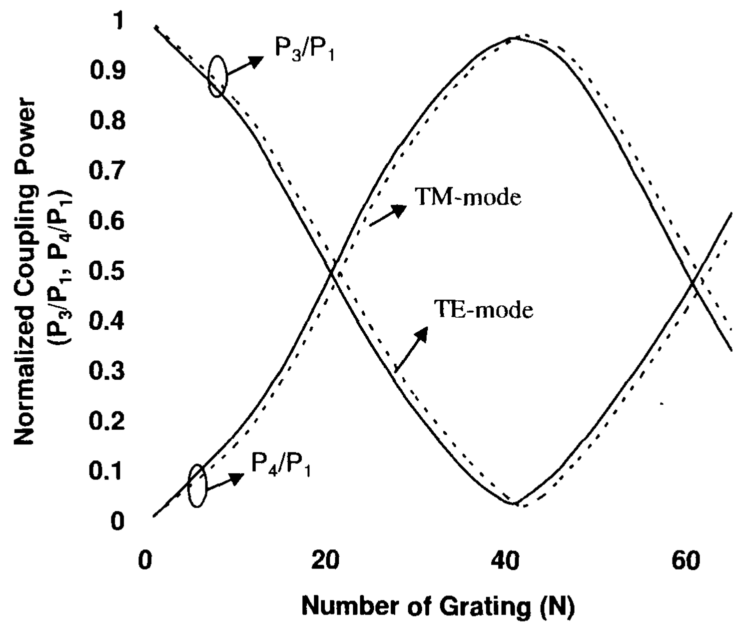

Fig-4.21: Normalized coupling power distribution of GA-TMI coupler for both TE-mode (solid line) and TM-mode (dotted line) with ΔW=0.25 μm, h=0 μm, a=b=1.5 μm, cladding index~1.45, Δn=5 % and λ~1.55 μm respectively.

4.4. Comparison Between GA-DC and GA-TMI Coupler

Fig-4.22 shows the normalized coupling power (P_3/P_1 and P_4/P_1) vs. number of grating period (N) calculated by using eqn. (4.6)-(4.37) for the tooth shaped grating assisted directional coupler (h=0.5 μm) and grating assisted TMI coupler (h=0 μm) with ΔW=0.25 μm, Δn=5%, a=b=1.5 μm, $l_m \approx l_g$ ~0.26 μm, n_1=1.5, n_2=1.45 and wavelength ~1.55 μm. From the plot, the peak normalized coupling power (P_4/P_1) is obtained at beat lengths (calculated using equ. (4.20)) ~22.4 μm and 45 μm respectively which corresponds to N values 42 and 86 for grating assisted TMI coupler (solid line) and grating assisted DC (dashed line) respectively.

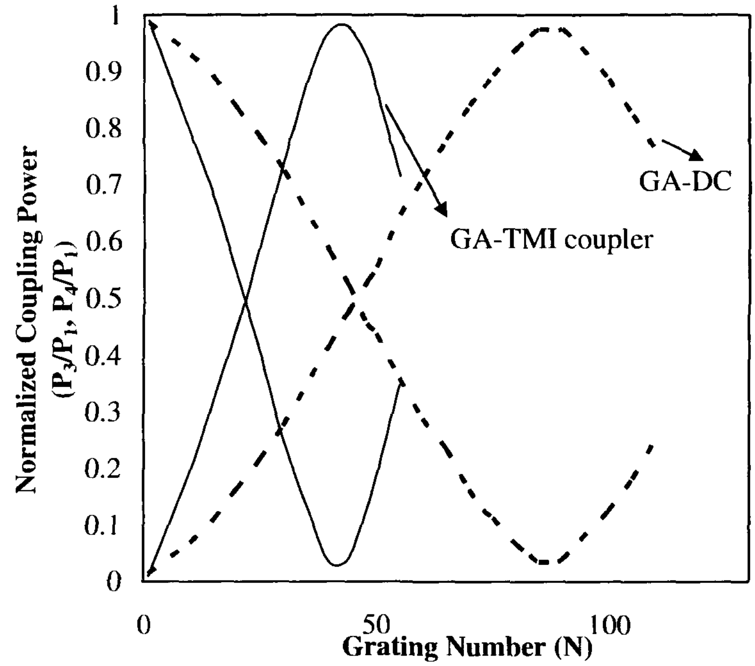

Fig-4.22: Normalized coupling power vs. number of grating period (N) for GA-DC (dashed line) and GA-TMI coupler (solid line) with Δn=5 %, ΔW=0.25 μm and λ~1.55 μm respectively.

Fig-4.23 shows the plot for beat length (L_π) versus Δn (%) estimated from coupling power distribution curves (Fig-4.22) for grating assisted geometry (with ΔW=0.25 μm) and a comparison to that of the conventional structures (with ΔW=0 μm). It is found from the figure that as Δn increases the beat length reduces and grating assisted TMI (GA-TMI) coupler has the lower beat length compared to that of the other couplers.

Further the beat length (L_π) versus index contrast (Δn) for different values of waveguide separation gap (h) is also studied. Fig-4.24 shows the L_π versus Δn

estimated from coupling power distribution curves (as shown in Fig-4.22) for tooth shaped GA-TMI coupler (h=0 μm) and tooth shaped GA-DC with different values of waveguide separation gap, h=0.04 μm, 0.5 μm, 1.0 μm, 3.0 μm and ΔW=0.25 μm, a=1.5 μm, b=1.5 μm, n_1=1.5, n_2=1.45, wavelength~1.55 μm respectively.

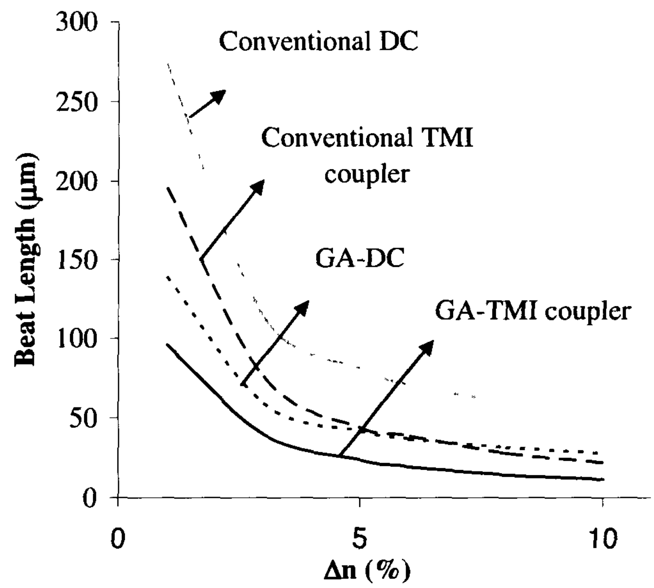

Fig-4.23: Beat length versus index contrast of tooth shaped grating assisted geometry for directional coupler (GA-DC), two mode interference (GA-TMI) coupler with ΔW=0.25 μm and conventional structure of directional coupler, TMI coupler with ΔW=0 μm respectively.

From the Fig-4.24, it is seen that for both grating assisted directional coupler (GA-DC) and grating assisted two-mode interference (GA-TMI) coupler, the beat lengths decreases as index contrast (Δn) increases. The rate of decrease of L_π is smaller for Δn>5 % and lower values of h. As h becomes nearer to zero coupling gap (h=0), the curves become closer and at h<0.04 μm, the curves for GA-DC almost coincide with the curve (solid line) for GA-TMI coupler (h=0 μm). Thus, it is observed that for very small value of coupling gap (h~0.04 μm), GA-DC shows equivalent behavior as that of GA-TMI coupler.

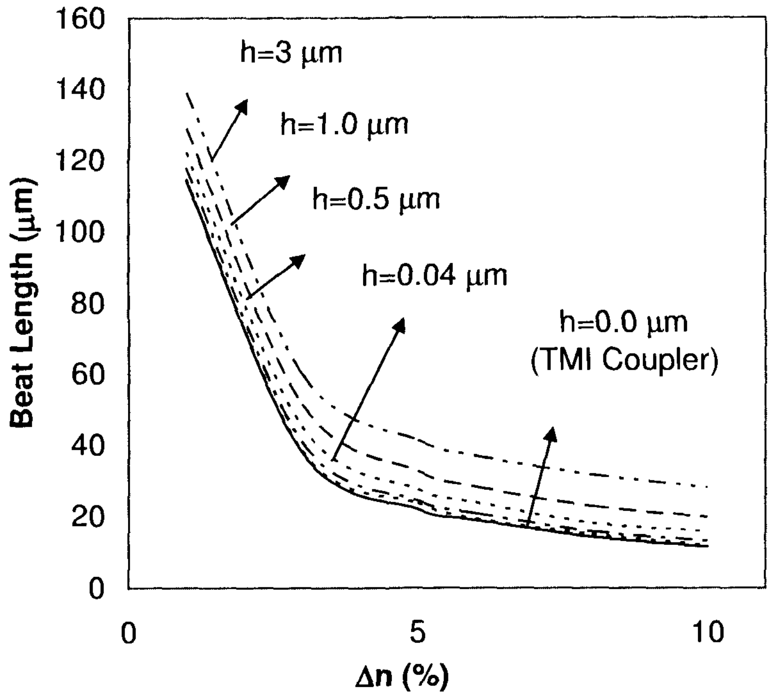

Fig-4.24: Beat length (L_π) versus Δn (%) for GA-DC (dashed lines) with different gap (h≠0) and GA-TMI coupler (h=0, solid line) with ΔW=0.25 μm.

4.5. Design Device Parameters

Table-4.1 shows the design parameters that is considered for the designed of tooth shaped grating assisted directional coupler (GA-DC) and grating assisted two mode interference (GA-TMI) coupler as discussed in the current chapter. The device length ($2L_T+L_\pi$) of GA-DC and GA-TMI coupler is obtained as ~295 μm and 286.4 μm respectively.

Table-4.1 Device Design Parameters

Design Parameters	GA-DC	GA-TMI Coupler	Conventional DC	Conventional TMI Coupler
Core waveguide width (a), μm	1 5	1 5	1 5	1 5
Core waveguide Thickness (b), μm	1 5	1 5	1 5	1 5
Index Contrast (Δn)	5%	5%	5%	5%
Core RI (n_1) , Δn=5%	1 5	1 5	1 5	1 5
Cladding RI (n_2) , Δn=5%	1 45	1 45	1 45	1 45
Coupling Gap Cladding RI (n_3) , Δn=5%	1 45	--	1 45	---
Coupling gap (h), μm	0 5	0	0 5	0
Grating teeth width (ΔW), μm	0 25	0 25	0 25	0 25
Guiding region length (l_m), μm	0 27	0 27	0 27	0 27
Grating region length (l_g), μm	0 27	0 27	0 27	0 27
Wavelength (λ), μm	1 55	1 55	1 55	1 55
Beat length (L_π), μm	45	22 4	91	45
Access Waveguide length (L_T), μm	125	132	132	141
Total device length (L_π+2 L_T), μm	295	286 4	355	327

4.6. Conclusion

In this chapter, 2x2 compact tooth shaped grating assisted geometry for compact directional coupler (DC) and two mode interference (TMI) coupler have been studied using a mathematical model based on sinusoidal mode simple effective index method (SEIM). In the designed structures, each tooth shaped grating periods (^) consist of a guiding region (K=m) of length l_m~0.26 μm and a grating region (K=g) of length l_g~0.26 μm respectively. The fabrication of such compact photonic integrated devices with dimensions<1 μm require processes such as electron beam, focused ion beam (FIB) method etc The process is expensive and due to our limited access/availability of these process/techniques, the fabrication of tooth shaped grating assisted structures which essentially requires electron beam technique could not be done. And as such the designs without grating (specifically conventional structures and structures with double S-bend) with dimensions≥1 μm as discussed in preceding chapter-6 and chapter-7 respectively have been fabricated with standard photolithography process only. In the above study, it found that the beat length of GA-TMI coupler is 22.4 μm, which is half of that for conventional TMI coupler and is ¼ that for conventional DC. But the increase of power imbalance with fabrication tolerance is slightly more than that of TMI coupler without grating. It is observed that TMI coupler with tooth shaped grating geometry is more wavelength sensitive than 3 dB conventional TMI coupler.

References:

1. Chin, M. K., et al., High-index-contrast waveguides and devices, *Appl. Opt.* **44**, 3077-3086, 2005.
2. Nishihara, H., Haruna, M., & Suhara, T. *Optical Integrated Circuits*, McGraw-Hill, New York, 1989.
3. Das, A. K. and Sahu, P. P. *IEEE Wireless and Optical Communication Network Conference*, Digital No- 01666673, **1**, 2006.
4. Sahu, P. P. Parabolic tapered structure for an ultracompact multimode interference coupler, *Appl. Opt.* **48**, 206-211, 2009
5. Chan, H.P., et al. A wide angle X-junction polymeric thermo optic digital switch

with low crosstalk, *IEEE Photonic Tech. Lett.* **15**, 1210-1212, 2003.

6. Passaro, V. M. N. Optimal design of grating-assisted directional couplers, *J. of Lightwave Tech.* **18**, 973-984, 2000.
7. Hardy, A. Exact Derivation of the Coupling Coefficient in Corrugated Waveguides with Rectangular Tooth Shape, *IEEE J. Quantum Electron.* **20**, 1132-1139, 1984.
8. Tsai, T. Y., et al., A novel wavelength-division-multiplexer using grating assisted two-mode interference, *IEEE Photonic Tech. Lett.* **16**, 2251-2253,2004
9. Tsai, T. Y., et al., A novel ultra compact two-mode-interference wavelength division multiplexer for 1.5 μm operation, *IEEE J. Quantum Electron.* **41**, 741-746, 2005.
10. Chiang, K.S. Effective index method for the analysis of optical waveguide couplers and arrays: an asymptotic theory, *J. of Lightwave Tech.* **9**, 62-72, 1991.
11. Wang, Q., et al. Effective index method for planar lightwave circuits containing directional couplers, *J. of Optics Communications* **259**, 133-136, 2006.
12. Deka, B., et al., Transformation relationship of directional coupler with multimode interference coupler and two mode interference coupler, *J. Optics* **38**, 75-87, 2009.
13. Sahu, P. P. A tapered structure for compact multimode interference coupler, *IEEE Photonic. Technol. Lett.* **20**, 638-640, 2008.
14. Sahu, P. P. Compact multimode interference coupler with tapered waveguide geometry, *Optics Communications.* **227**, 295-301, 2008.
15. Sahu, P. P. A compact optical multiplexer using silicon nano waveguides, *IEEE J. Sel. Topics Quantum Electron.* **15**, 1537-1541, 2009.

****

Chapter-5:

Tooth Shaped Grating Assisted Geometry for Compact Multimode Interference Coupler

Introduction

Mathematical Model of Grating Assisted Multimode Interference (GA-MMI) Couplers

Results and Discussion

Conclusion

5.1. Introduction

Since total length of photonic integrated device (PID) component is contributed by beat length and access waveguide length; the compactness of device requires reduction of access waveguide length having S-bend. As discussed in chapter-4, the reduction of beat length has been considered in the components as the length of large scale integrated optic devices such as wavelength division multiplexer/demultiplexer, optical matrix switches etc. for all optical networks. For the reduction of total device length it is very much essential to study the longitudinal access waveguide length (also known as transition length) for Two Mode Interference (TMI) coupler as well as Multimode Interference (MMI) coupler with other potential structures such as grating assisted geometry and also in the conventional structures. In this direction, Multimode Interference (MMI) coupler [1]-[5] based devices have become attractive due to having lower access waveguide bending losses than that of TMI coupler. As per our knowledge no study is made on surface relief grating assisted structure of multimode interference coupler. So, tooth shaped grating assisted geometry has been proposed for the reduction of device length of MMI coupler and studied the same structure for MMI coupler in this chapter. The coupling behavior of grating assisted MMI (GA-MMI) coupler have been analyzed theoretically using the mathematical model based on sinusoidal mode Simple Effective Index Method (SEIM) [6]-[10] as mentioned in chapter-3 and chapter-4. The coupling characteristics, beat length and fabrication tolerances for GA-MMI coupler have been compared with GA-TMI coupler. It is observed that, although beat length of GA-TMI coupler with grating width (ΔW) =0.25 μm is ~1.6 times less than that of GA-MMI coupler with grating width (ΔW)=0.25 μm, but the total device length of GA-MMI coupler by inclusion of access waveguide length with permissible bending loss of 0.01 dB is ~7.5 % less than GA-TMI coupler. The dependence of access waveguide length on h with fixed value of S-bending loss for grating assisted MMI (GA-MMI) structure and tooth shaped grating assisted two-mode interference (GA-TMI) structure are discussed. The effect of fabrication tolerance on power imbalance of GA-MMI coupler is also studied whereas these SEIM results are compared with the results obtained by commercially available beam propagation method (BPM) [11]-[12] based optiBPM software (V 9.0).

5.2. Grating Assisted MMI (GA-MMI) Coupler

Like conventional MMI coupler the tooth shaped grating assisted multimode interference (GA-MMI) coupler is based on the principle of self imaging principles[9]. When light is launched through access waveguide of MMI coupler, higher order modes are excited with fundamental and first order modes. These excited modes are interfered with each other along the direction of propagation where multiple reflections of evanescent ligthwave occur within the grating geometry.

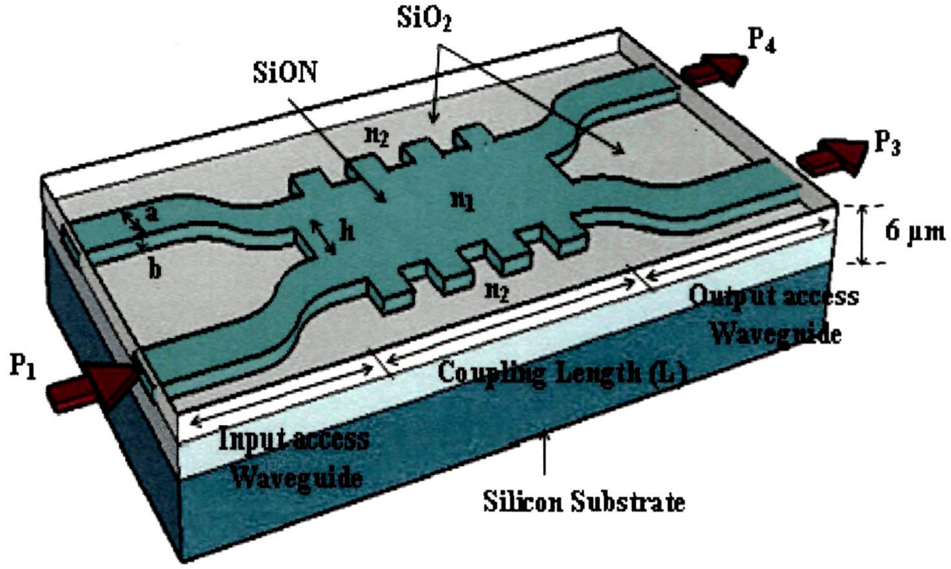

Fig-5.1: Schematic 3D diagram of 2x2 tooth shaped grating assisted multimode interference (GA-MMI) coupler

Fig-5.1 shows the schematic three dimensional (3D) diagram of a 2x2 compact tooth shaped grating assisted multimode interference (GA-MMI) coupler with a channel waveguide consisting of two single mode input S-bent access waveguides of core width a and thickness b (Waveguide-1 & Waveguide-2), two single mode output S-bent access waveguides of same core size (Waveguide-3 & Waveguide-4) and a coupling region of length L with guiding width, W_m=2a+h (h=the gap between two input access waveguides) and grating width, $W_g=W_m+2\Delta W$ (where ΔW=tooth width of grating) placed alternatively. As mentioned in the previous chapter-4, tooth shaped rectangular grating geometry has been considered for the case study due to better compactness and simpler for applications. The coupling region consists of N total numbers of grating period ($\Lambda= l_m+ l_g$, where l_m and l_g are the length of guiding width (K=m) and grating width (K=g) in each grating period respectively. The n_1 is the refractive index of core whereas n_2 is the refractive index of the cladding region. When the input power P_1 is launched into lower most input S-bent access waveguide (Waveguide-2), the output powers P_3 and P_4 are obtained as bar state and cross state respectively.

When the input signal mode field of propagation constant β_i (λ) is incident through input single mode S-bent access waveguide (Waveguide-2), multiple modes are excited in the grating assisted MMI coupling region. At the end of GA-MMI region based on relative phase difference between these modes in the region, the light power is coupled into two single mode S-bent output access waveguides (Waveguide-3 and Waveguide-4). Since fundamental and first order modes carry most of signal power, the beat length (defined as the length for π phase shift) for the MMI couplers assisted with total N numbers of grating period is obtained as,

$$L_\pi = [(N+1)l_m + Nl_g] = \frac{\pi}{[(\beta_{00}^m - \beta_{01}^m) + (\beta_{00}^g - \beta_{01}^g)]} \quad (5.1)$$

where $\beta_{00}^m, \beta_{01}^m$ and $\beta_{00}^g, \beta_{01}^g$ are the propagation constants of fundamental and first order modes in the guiding region and grating region respectively.

Fig-5.2(b) shows a two dimensional (2D) cross sectional schematic view of 2x2 tooth shaped grating assisted multimode interference (GA-MMI) coupler of Fig-5.1

whereas Fig-5.2(a) shows the 3D view of the guided layer. As GA-MMI coupling region in transverse dimension (along Y-axis) is smaller (minimum two times as mentioned later in this chapter) than the lateral dimension (along X-axis) and have the same transverse behavior in everywhere of GA-MMI coupling region (in the XZ-plane), it is justified to be assumed that the waveguide structure is to be single mode in transverse dimension. So the mode fields in grating assisted MMI couplers can be represented in two dimensionally.

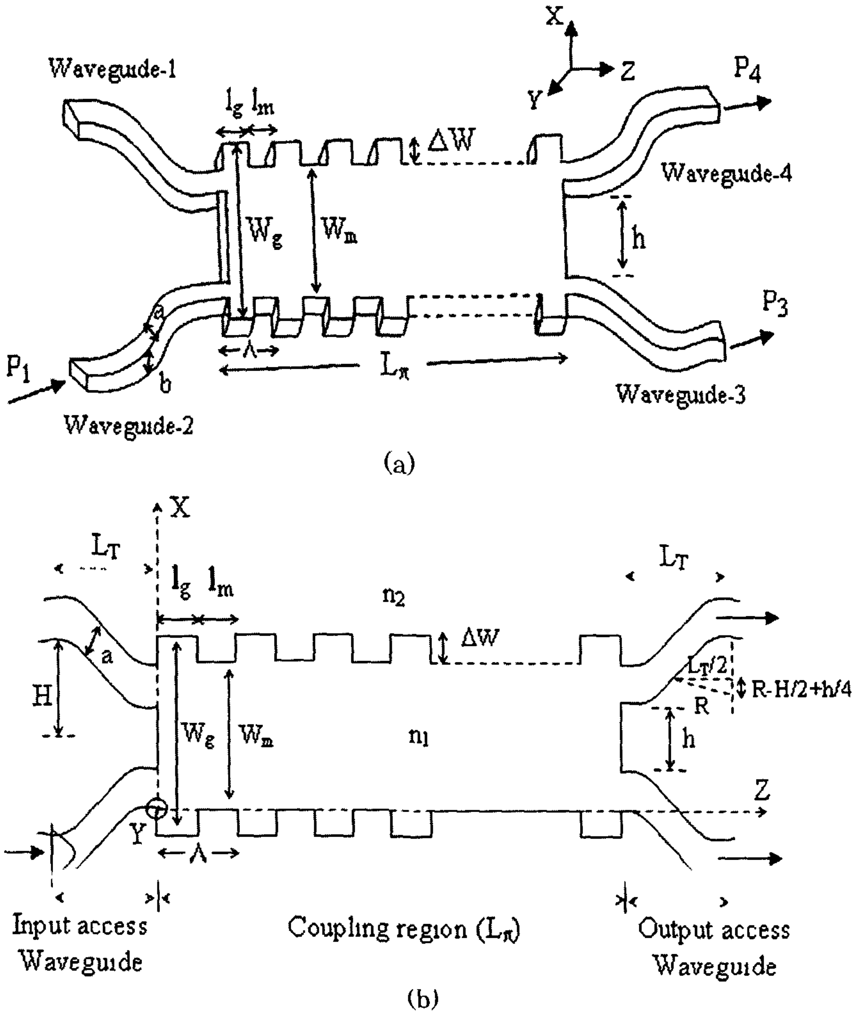

Fig-5.2: Schematic diagram of tooth shaped grating assisted multimode interference (GA-MMI) coupler (a) 3D view (b) 2D cross sectional view with x and z axis.

The input field profile H(x,0) launched into tooth shaped grating assisted multimode interference (MMI) coupler (z=0) is composed of mode field distribution of all modes excited in GA-MMI region and in 2D approximation expressed as

$$H(x,0)=\sum_{i=0}^{r-1} b_i H_i(x) \tag{5.2}$$

where b_i is field contribution coefficient of tooth shaped grating assisted MMI coupler for i^{th} order mode and $H_i(x)$ is mode field distribution of i^{th} order mode at z =0.

The composite field profile at a distance z inside GA-MMI region can be represented in 2D approximation as a summation of all the guided modes.

$$H(x,z)=\sum_{i=0}^{r-1} H_i(x,z)=\sum_{\substack{i=0\\K=m,g}}^{r-1} b_i H_i(x)\exp\left[j\left(\beta_0^K-\beta_i^K\right)z\right] \tag{5.3}$$

where i =0, 1, 2,.....(r-1) denotes the order of guided modes, β_0^K is the propagation constant of zeroth order (fundamental mode) and β_i^K represents the propagation constant for i^{th} order mode respectively. The K=m represents the width of guided region whereas K=g is the width of grating region.

Since the width of the access waveguide (a~1.5 μm) is required to be small for single mode operation of the access waveguide by keeping the normalization frequency V~2.3, the lateral penetration of the mode field outside the waveguide is negligible for the lateral high index contrast (Δn). Thus input mode field profile $H_i(x)$ for the i^{th} mode can be approximated for tooth shaped grating assisted multimode interference (GA-MMI) region as,

$$H_i(x)=\sin\left[(i+1)\frac{\pi x}{W_g}\right] \tag{5.4}$$

At the end of tooth shaped grating assisted MMI coupling section, optical power is either transferred to the output S-bent access waveguide or lost out at the end of tooth shaped grating assisted MMI waveguide. The mode field of output access waveguides is contributed by all guided modes propagated in grating assisted MMI region. The mode fields at M-th output S-bent access waveguide can be written as

$$H_M^K(x,L) = \sum_{\substack{i=0 \\ K=m,g}}^{r-1} H_{M,i}^K(x,L) = \sum_{\substack{i=0 \\ K=m,g}}^{r-1} c_{M,i} H_i(x) \exp\left[j\left(\beta_0^K - \beta_i^K\right)L\right] \tag{5.5}$$

where L=[(N+1)l_m+Nl_g] and $c_{M,i} = \sqrt{C_{M,i}^K}$ is the i[th] order mode's contribution coefficient to the M-th output access waveguide (M=3 for the 3[rd] access waveguide and M=4 for the 4[th] access waveguide), which can be calculated by using mathematical model based on sinusoidal mode simple effective index method (SM-SEIM) as discussed in section-4.2.1 of previous chapter-4 with consideration $n_3 \rightarrow n_1$ ($h \neq 0$) , we have

$$\frac{C_{M,i}^K}{C_0} \approx \frac{\pi^2}{16b^2k^2\left(n_1^2 - n_2^2\right)} \times \exp\left\{-hk\left(n_{eff}^2 - n_2^2\right)^{1/2}\right\} \times \left[\exp\left\{bk\left(n_1^2 - n_2^2\right)^{1/2}\right\} - \exp\left\{-bk\left(n_1^2 - n_2^2\right)^{1/2}\right\}\right] \tag{5.6}$$

where for TE mode,

$$C_0 = \frac{0.4}{F_C} \times \frac{\left(n_1^2 - n_{eff(TE),K}^2\right)\sqrt{n_{eff(TE),K}^2 - n_2^2}}{n_{eff(TE),K}\left(n_1^2 - n_3^2\right)\left[W_K + \frac{2}{k_0\sqrt{n_{eff(TE),K}^2 - n_2^2}}\right]} \tag{5.7}$$

$$F_c = \frac{3(1 + 0.2h)}{\left\{13.5 + 185\left(\beta_0^K - \beta_i^K\right)\right\}h} \tag{5.8}$$

$$n_{eff(TE),K} = \beta_{TE(i)}^K \left(\frac{\lambda}{2\pi}\right) \quad ; K = m,\ g \tag{5.9}$$

Similarly, for TM mode,

$$C_0 = \frac{0.4}{F_C} \times \frac{\left(n_1^2 - n_{eff(TM),K}^2\right)\sqrt{n_{eff(TM),K}^2 - n_2^2}}{n_{eff(TM),K}\left(n_1^2 - n_3^2\right)\left[W_K + \frac{2}{k_0\sqrt{n_{eff(TM),K}^2 - n_2^2}}\right]} \tag{5.10}$$

$$F_c = \frac{3(1 + 0.2h)}{\left\{13.5 + 185\left(\beta_0^K - \beta_i^K\right)\right\}h} \tag{5.11}$$

$$n_{eff\,(TM\,),K} = \beta^{K}_{TM\,(i)}\left(\frac{\lambda}{2\pi}\right) \quad ;K = m,\ g \tag{5.12}$$

The contributed power to the M-th output S-bent access waveguide by i^{th} mode is given by [13]-[14],

$$P^{i}_{M} = \left|H^{K}_{M,i}(x,L)\right|^{2} \tag{5.13}$$

Normalized power coupled to the M^{th} output access waveguide for tooth shaped GA-MMI coupler can be approximated as,

$$\frac{P_{M,i}(x,L)}{P_{1,i}(x,o)} = \frac{\left|\sum_{i=0}^{r-1} H^{K}_{M,i}(x,L)\right|^{2}}{\left|\sum_{i=0}^{r-1} H^{K}_{1,i}(x,0)\right|^{2}}$$

$$\approx \sum_{\substack{i=0\\K=m,g}}^{r-1} C^{K}_{M,i} H^{2}_{i}(x) + \sum_{\substack{i=0\\K=m,g}}^{r-1} \sum_{\substack{j=1+i\\K=m,g}}^{r-1}\left[2\sqrt{C^{K}_{M,i}C^{K}_{M,j}}H_{i}(x)H_{j}(x)\times\cos\left\{\sum_{\substack{i=0,j=i+1\\K=m,g}}^{r-1}\left[(N+q_{K})(\beta^{K}_{i}-\beta^{K}_{j})l_{K}\right]\right\}\right] \tag{5.14}$$

where i, j = 0, 1, 2,.....(r-1) are the order of modes provided j>i, q_K=0, 1 for grating region (K=m) and guided region (K=g) respectively, N=Number of grating period and $C^{K}_{M,i}$, $C^{K}_{M,j}$ =contribution coefficients (measure of field contribution of i^{th} and j^{th} order modes to lower output access waveguides) that are obtained using equations (5.6)-(5.12), β_i, β_j=propagation constant for i^{th} and j^{th} modes which are determined from dispersive equations (as discussed in section-3.2.2 of chapter-3). The length of the guiding width (l_m) and grating width (l_g) is determined by using the following relation (5.15) [15][16],

$$l_{K} = \frac{\lambda}{4n_{eff\,(j,K)}} \quad ;K = m, g \tag{5.15}$$

Thus, the contributed power to the 3^{rd} S-bent access waveguide-3 (bar state) by i^{th} order mode is given by,

$$P^{i}_{3} = \left|H^{K}_{3,i}(x,L)\right|^{2} \tag{5.16}$$

Similarly, normalized power coupled to the 3rd S-bent access waveguide by ith order mode for tooth shaped GA-DC can be approximated as,

$$\frac{P_{3,i}(x,L)}{P_{1,i}(x,o)}=\frac{\left|\sum_{i=0}^{r-1}H_{3,i}^{K}(x,L)\right|^2}{\left|\sum_{i=0}^{r-1}H_{1,i}^{K}(x,0)\right|^2}$$

$$\approx \sum_{\substack{i=0\\K=m,g}}^{r-1}C_{3,i}^{K}H_i^2(x)+\sum_{\substack{i=0\\K=m,g}}^{r-1}\sum_{\substack{j=1+i\\K=m,g}}^{r-1}\left[2\sqrt{C_{3,i}^{K}C_{3,j}^{K}}H_i(x)H_j(x)\times\cos\left\{\sum_{\substack{i=0,j=i+1\\K=m,g}}^{r-1}\left[(N+q_K)(\beta_i^K-\beta_j^K)l_K\right]\right\}\right] \tag{5.17}$$

where $C_{3,i}^{K}=\left(c_{3,i}^{K}\right)^2$ and $c_{3,i}^{K}$ = the contribution coefficient of ith mode (which can be calculated by using a mathematical model based on SM-SEIM) for the 3rd output access Waveguide-3.

Normalized power coupled to the output access waveguide-4 (cross state) by ith order mode for tooth shaped GA-MMI can be approximated as,

$$\frac{P_{4,i}(x,L)}{P_{1,i}(x,o)}=\frac{\left|\sum_{i=0}^{r-1}H_{4,i}^{K}(x,L)\right|^2}{\left|\sum_{i=0}^{r-1}H_{1,i}^{K}(x,0)\right|^2}$$

$$\approx \sum_{\substack{i=0\\K=m,g}}^{r-1}C_{4,i}^{K}H_i^2(x)+\sum_{\substack{i=0\\K=m,g}}^{r-1}\sum_{\substack{j=1+i\\K=m,g}}^{r-1}\left[2\sqrt{C_{4,i}^{K}C_{4,j}^{K}}H_i(x)H_j(x)\times\cos\left\{\sum_{\substack{i=0,j=i+1\\K=m,g}}^{r-1}\left[(N+q_K)(\beta_i^K-\beta_j^K)l_K\right]\right\}\right] \tag{5.18}$$

where $C_{4,i}^{K}=\left(c_{4,i}^{K}\right)^2$ and $c_{4,i}^{K}$ = the contribution coefficient of ith mode (which can be calculated by using a mathematical model based on SM-SEIM) for the 4th output access Waveguide-4.

The transition length (L_T) of the S-bent access waveguide (along the z direction) from the Fig.-5.2(b) can be obtained as follows,

$$L_T = \sqrt{\left(H - \frac{h}{2}\right)\left[4R + \frac{h}{2} - H\right]} \tag{5.19}$$

where R, H and h are bending radius, height and coupling gap between two access waveguides respectively. The bending loss (T_S) in dB for S-bent access waveguides can be approximated as [17]-[18],

$$T_S = 4.343\,\alpha\,S \tag{5.20}$$

where α = loss coefficient that mainly depends on bending radius R and

$$S = 2R\cos^{-1}\left[1 - \frac{\left(H - h/2\right)}{2R}\right] \tag{5.21}$$

5.2.1 Multiple Reflection in Grating Assisted MMI Coupler

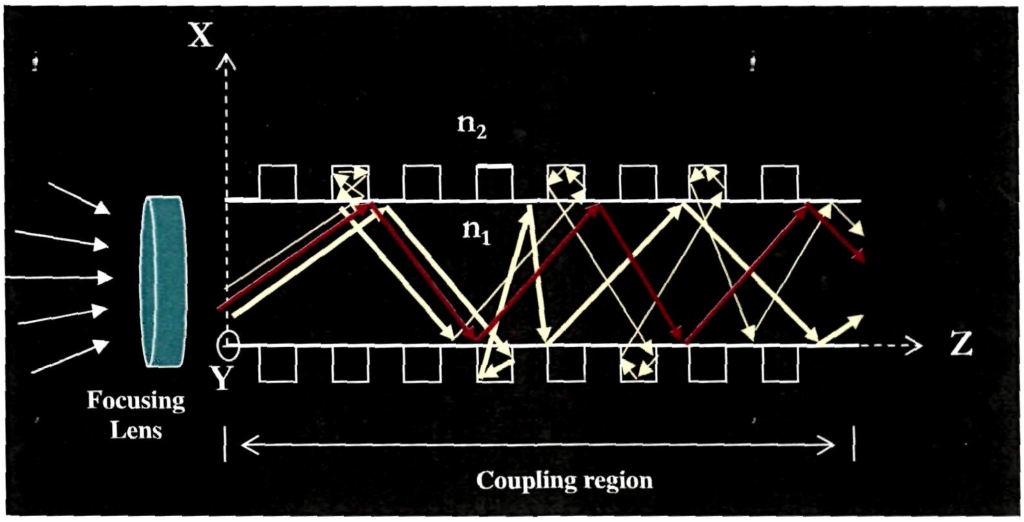

Fig-5.3: Schematic ray diagram showing the multiple reflections occur in the tooth shaped grating structures

Fig.-5.3 shows the schematic ray diagram of the multiple reflections that occurs in the tooth shaped grating geometry. The ray with red colour is reflected at the guiding width (K=m) whereas the yellow colored rays are getting multiple reflections in the grating width (K=g). It is observed that the path travelled by light in grating assisted structure is more than that of conventional structures, showing the path difference in grating assisted geometry is more that in conventional structures.

5.2.2 Coupling Characteristics of GA-MMI Coupler

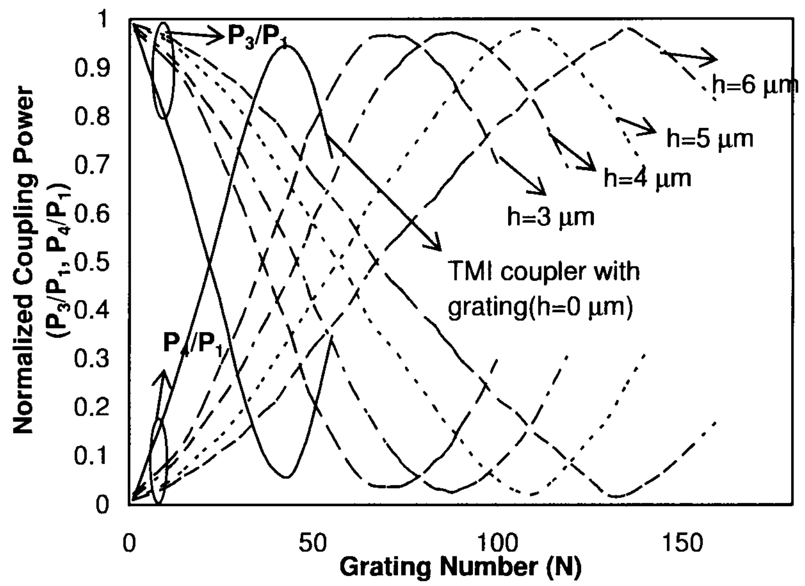

Fig-5.4: Normalized coupling power distribution of tooth shaped grating assisted geometry of two mode interference (GA-TMI) coupler with coupling gap, h=0.0 μm (solid line) and multimode interference (GA-MMI) couplers (dashed lines) for h=3.0 μm, 4.0 μm, 5.0 μm, 6.0 μm with ΔW=0.25 μm, a=1.5 μm, b=1.5 μm, cladding index~1.45, Δn=5 % and λ~1.55 μm respectively.

Fig-5.4 shows the normalized coupling power distribution versus number of grating (N) obtained by using the equations (5.6) and (5.18) for different waveguide separation gaps, h=0.0 μm, 3.0 μm, 4.0 μm, 5.0 μm and 6.0 μm for the tooth shaped grating assisted multimode interference (GA-MMI) coupler with ΔW=0.25 μm, a=1.5 μm, b=1.5 μm, l_m~0.26 μm, l_g~0.26 μm, Δn=5 %, cladding index~1.45 and wavelength (λ)~1.55 μm respectively. In the figure h=0.0 μm corresponds to grating assisted TMI coupler. It is seen from the figure that peak cross coupling power (P_4/P_1) is obtained at beat lengths where N values are 41, 70, 85, 105 and 134 for h=0.0 μm, 3.0 μm, 4.0 μm, 5.0 μm, and 6.0 μm respectively. So the beat lengths obtained using equation (5.1) are ~22.2 μm, 36.0 μm, 40.0 μm, 57.8 μm and 70.5 μm for h=0.0 μm, 3.0 μm, 4.0 μm, 5.0 μm and 6.0 μm respectively. The increase of beat length with increase of h is mainly due to excitation of higher order modes (apart from lower order modes) having less coupling efficiency as these modes are partly transferred. It is seen (not mentioned in the figure) that the number of modes excited in GA-TMI and GA-MMI coupler for h=0.0 μm, 3.0 μm, 4.0 μm, 5.0 μm, and 6.0 μm is two, four, five and six respectively. It is evident from the figure that as h decreases, the peak normalized cross coupling power decreases. This is due to increase of the radiation losses at the bending portion of the input/output access waveguides with decrease of h, which is evident from the equation (5.20) and (5.21) respectively. It is also seen (discussed latter on in this chapter) that the polarization dependence of GA-MMI coupler is almost equivalent to the GA-TMI coupler (h=0.0 μm) but is slightly more than conventional MMI/TMI couplers (as details are discussed in chapter-3, section-3.3.6 and section-3.4.6) because the number of waveguide parameters in the grating assisted geometry is more than that of conventional structures. Although L_π of GA-MMI with h=3 μm is lower than that of GA-MMI with h=4 μm, we have chosen h=4 μm because of lower bending loss which is discussed later in this chapter.

5.2.3 Beat Length of GA-MMI Coupler

Fig-5.5 shows the beat length (L_π) versus index contrast (Δn) of tooth shaped grating assisted multimode interference (GA-MMI) coupler for ΔW=0.05 μm, 0.1 μm, 0.25 μm and conventional MMI coupler (ΔW=0 μm) with a=1.5 μm, b=1.5 μm, h=4.0 μm, W_m (~2a+h)=7.0 μm, cladding index~1.45 and wavelength~1.55 μm.

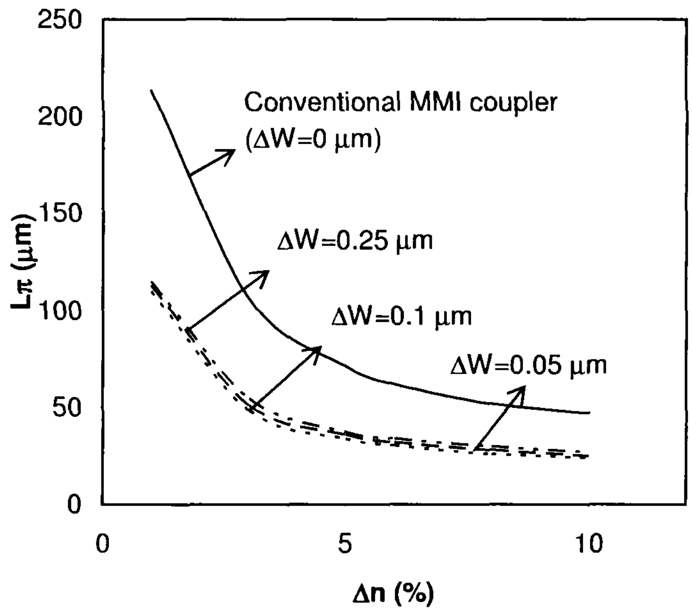

Fig-5.5: Beat length (L_π) versus index contrast (Δn) of tooth shaped grating assisted multimode interference (MMI) couplers (dashed lines) with ΔW=0.05 μm, 0.1 μm, 0.25 μm, h=4 μm and conventional MMI coupler (ΔW=0 μm, h=4 μm) (solid line).

It is observed from the plot that as the index contrast (Δn) increases, the beat length decreases and it slowly decreases for Δn>5 %. The variation of the beat length with Δn for ΔW=0.05 μm are almost close to that for ΔW=0.1 μm and 0.25 μm but the beat length for conventional MMI coupler is ~2 times higher than that for tooth shaped grating assisted MMI coupler ΔW≠0 μm). For fabrication advantage, we have chosen ΔW=0.25 μm and we have also chosen Δn=5 % for further study. For Δn=5 % and ΔW=0.25 μm, it is found that the beat length of tooth shaped grating assisted multimode interference (MMI) couplers is ~50 % lower than that of conventional

MMI couplers. The less beat length in GA-MMI coupler than that of conventional MMI coupler is due to multiple reflection occurred in the tooth shaped grating region as shown in section-5.2.1.

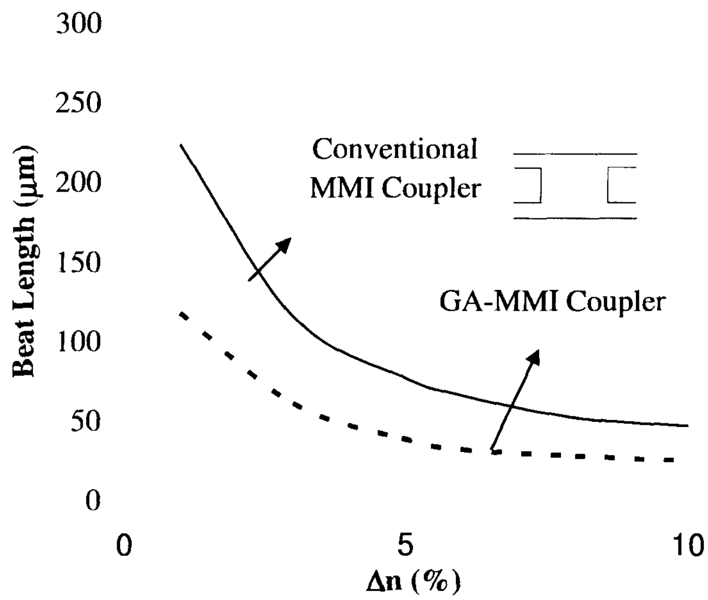

Fig-5.6: Beat length (L_π) versus index contrast (Δn) of tooth shaped grating assisted multimode interference (MMI) couplers (dashed line) for waveguide separation gaps, h~4 μm with ΔW=0.25 μm and conventional MMI coupler (ΔW=0 μm), h=4 μm (solid line) respectively.

Fig-5.6 shows the beat length (L_π) versus index contrast (Δn) of tooth shaped grating assisted structures of MMI (GA-MMI) coupler with h=4.0 μm for ΔW=0.25 μm and conventional MMI couplers (ΔW=0 μm) with a=1.5 μm, b=1.5 μm, h=4.0 μm, W_m ~2a+h, W_g ~W_m+2ΔW, cladding index~1.45 and λ~1.55 μm respectively. It is seen that beat length decreases as the index contrast (Δn) increases and for Δn>5%, L_π decreases slowly. It is also seen that the beat lengths with Δn=5 % for GA-MMI coupler (ΔW=0.25 μm) and conventional MMI coupler (ΔW=0 μm) are obtained as ~40 μm and 81 μm respectively. So the beat length of tooth shaped grating assisted multimode interference (GA-MMI) couplers is ~50% lower than that of conventional MMI coupler. The lesser beat length in GA-MMI coupler than that of conventional MMI coupler is due to multiple reflections occurred in the tooth shaped grating region as seen in section 5.2.1.

5.2.4 Beam Propagation Method (BPM) Simulation Results for GA-MMI Coupler

Since as mentioned in the previous chapters: -3 and -4, before fabrication it is required to study the beam propagation performance with the designed parameters of the structures.

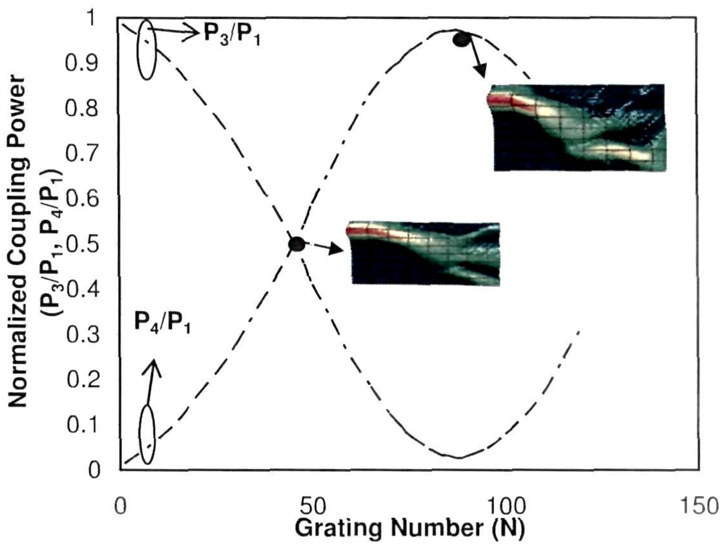

Fig-5.7: Normalized coupling power distribution of tooth shaped GA-MMI coupler for h=4.0 μm with ΔW=0.25 μm, a=b=1.5 μm, Δn=5 % and λ~1.55 μm respectively.

Fig-5.7 shows the beam propagation results with the bar coupling (P_3/P_1) state and the cross coupling (P_4/P_1) state for tooth shaped grating assisted MMI (GA-MMI) coupler with ΔW=0.25 μm, h=4 μm, W_m=7.0 μm, a=1.5 μm, b=1.5 μm, Δn=5 %, λ ~1.55 μm obtained by using optiBPM software. The figure also shows the lightwave propagation at half coupling point of 3 dB GA-MMI coupler and cross coupling point obtained by optiBPM software that is based on Finite Difference Time Domain (FDTD) method [6],[12]. It is seen that cross coupling point is obtained at coupling length of 40.1 μm which is almost close to that obtained by SEIM based on sinusoidal modes.

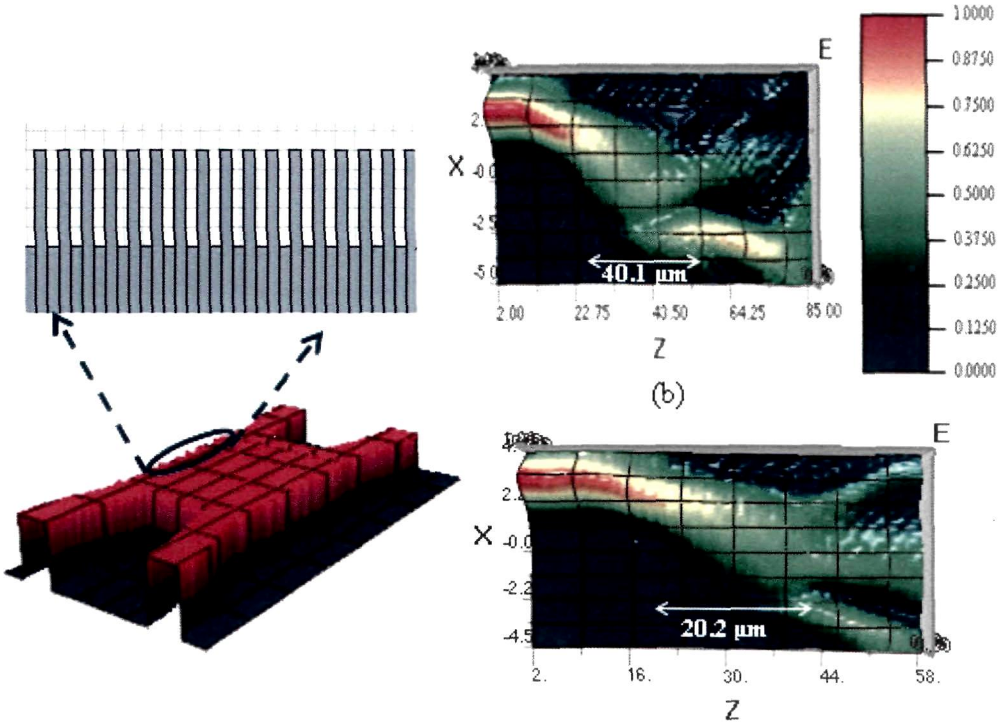

(a) (b) (c)

Fig-5.8: BPM results of grating assisted MMI (GA-MMI) coupler for (a) Layout with tooth shaped grating geometry, (b) Cross coupling state of beatlength~40.1 μm and (c) 3-dB coupler of beatlength~20.2 μm

From the BPM results as shown in Fig.-5.8, it is found that the beat lengths of GA-MMI and conventional MMI coupler are obtained as ~40.1 μm and 80.3 μm respectively which are almost close to that obtained with SM-SEIM method. It is also evident from the figures that the propagation loss in GA-MMI region is slightly more than that in conventional TMI/MMI coupler due to multiple reflections in grating region. It is found that the beat length of tooth shaped grating assisted MMI (GA-MMI) coupler at cross point~40.1 μm, 3 dB coupler~20.2 μm and bar point~80.3 μm with a=b=1.5 μm, h=4 μm, n_2=1.45 and Δn=5 % respectively, that are matching well with the theoretical results obtained by SEIM.

5.2.5 Fabrication Tolerances and Polarization Dependence of GA-MMI Coupler

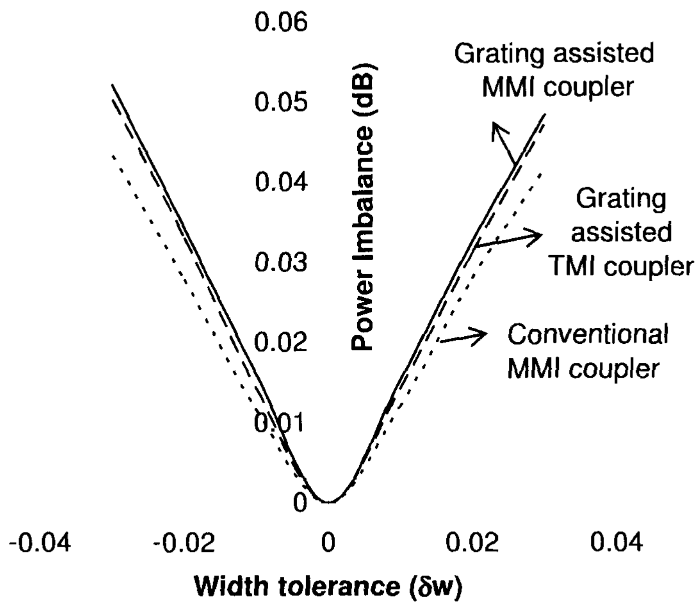

Fig-5.9: Power Imbalance characteristics versus width tolerances (δw) for tooth shaped grating assisted MMI coupler (solid line), tooth shaped grating assisted TMI coupler (dashed line) and conventional MMI coupler (dotted line) with index contrast ~5 %, cladding index~1.45, h~4.0 μm, a=b=1.5 μm and λ~1.55 μm respectively.

Since it may not be possible for accurate fabrication of device structure with exact designed parameters, it is required to study its performance degradation with a small unwanted variation of waveguide parameters. So, the effect of fabrication tolerances (δw) of MMI width on power imbalance of tooth shaped grating assisted MMI coupler and conventional MMI coupler (ΔW=0 μm) has been studied.

Fig-5.9 shows plot for power imbalance [$=10 \log_{10} (P_3/P_4)$] versus fabrication tolerances ($\pm\delta w$) of tooth shaped grating assisted MMI width with h~4.0 μm, a=1.5 μm, b=1.5 μm, index contrast~5 %, cladding index~1.45, and λ~1.55 μm. It is seen that the power imbalance increases with $\pm\delta w$ symmetrically for both the structures and the increase of power imbalance for tooth shaped grating assisted MMI coupler is slightly more than that of conventional MMI coupler due to having more number of device parameters in tooth shaped grating assisted MMI coupler. The figure also shows the variation of power imbalance with $\pm\delta w$ for GA-TMI coupler and the curve for the same is almost close to that of GA-MMI coupler. The rate of increase of power imbalance (dB) with respect to width tolerance for GA-MMI, GA-TMI and conventional MMI couplers are approximately obtained as $\frac{\partial}{\partial(\delta w)}$ [Power Imbalance (dB)] ~0.17 dB/μm, 0.16 dB/μm and 0.13 dB/μm respectively. It is also required to study the dependence of power imbalance on wavelength for conventional MMI coupler and tooth shaped grating assisted MMI coupler.

Fig-5.10 shows power imbalance versus wavelength for a~1.5 μm, b~1.5 μm, h~4.0 μm, index contrast ~5% and cladding index~1.45. In the figure, the solid line indicates the curve for 3 dB tooth shaped grating assisted MMI coupler of coupling length ~20.2 μm and the dotted line shows for 3 dB conventional MMI coupler of coupling length ~40.1 μm. It is seen from the plot that and in both cases minimum power imbalance is obtained at λ~1.55 μm and it is almost symmetrically increased in both sides of λ~1.55 μm. The increase of power imbalance for tooth shaped grating assisted MMI coupler is sharp in comparison conventional MMI coupler. The dashed line in the figure represents the variation of power imbalance versus wavelength for GA-TMI coupler and the curve for the same is almost superposed to that of GA-MMI coupler. So the dependence of power imbalance on fabrication tolerance and wavelength for GA-MMI coupler is almost same as that for GA-TMI coupler.

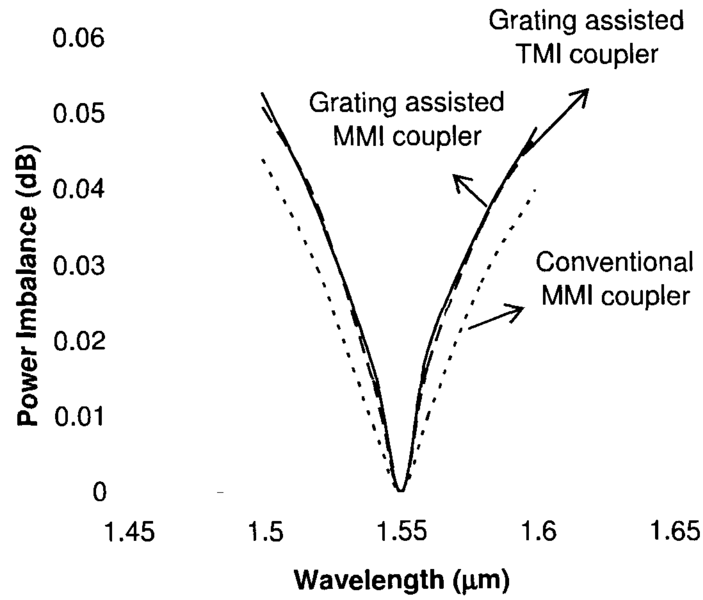

Fig-5.10: Power Imbalance characteristics versus wavelength variation for tooth shaped grating assisted MMI coupler (solid line), tooth shaped grating assisted TMI coupler (dashed line) and conventional MMI coupler (dotted line) with a=1.5 μm, b=1.5 μm, h~4.0 μm, index contrast ~5% and cladding index~1.45.

The polarization dependence characteristic of tooth shaped grating assisted MMI (GA-MMI) coupler is shown Fig-5.11. The figures shows the normalized coupling power distribution versus grating number (N) for both TE-mode and TM-mode with h=4.0 μm, ΔW=0.25 μm, a=1.5 μm, b=1.5 μm, cladding index~1.45, Δn=5% and λ~1.55 μm respectively. It is found that for TM-polarization the value of beatlength (L_π) is ~0.22 % more than that of the TE-polarization. It is also seen that the polarization dependence of GA-MMI coupler is almost equivalent to the GA-TMI coupler (h=0.0 μm) but is slightly more than conventional MMI/TMI couplers because the number of waveguide parameters in the grating assisted geometry is more than that of conventional structures.

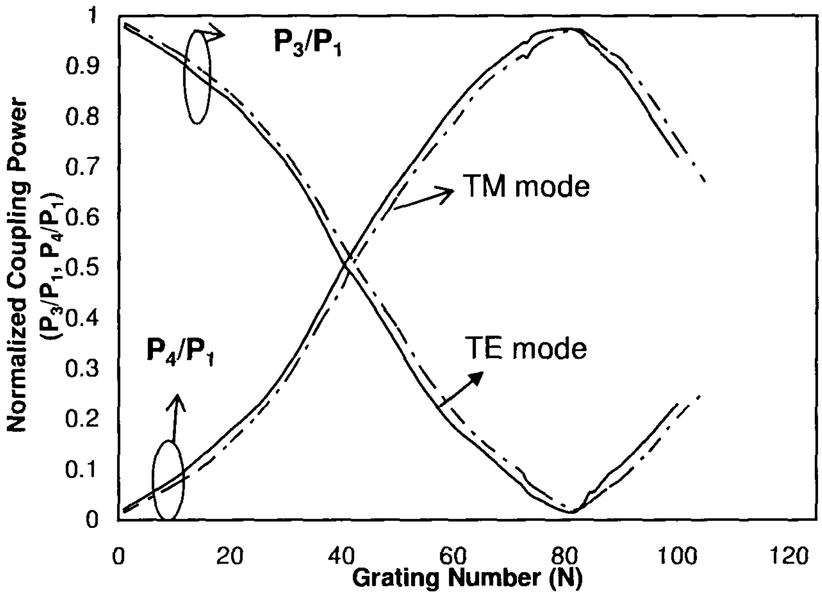

Fig-5.11: Normalized coupling power distribution of tooth shaped GA-MMI coupler for both TE-mode (solid line) and TM-mode (dashed line) with h=4.0 μm, ΔW=0.25 μm, a=1.5 μm, b=1.5 μm, cladding index~1.45, Δn=5% and λ~1.55 μm respectively.

5.3. Comparative Study of Access Waveguide Length of GA-MMI Coupler with GA-TMI Coupler

The dependence of transition length L_T and beat length L_π on h of MMI structure with tooth shaped grating is studied by considering fixed S-bending loss T_S of 0.2 dB with the equations (5.1) and (5.19)-(5.21) as shown in Fig-5.12. In the figure, h=0 μm corresponds to TMI coupler with tooth shaped grating where L_T and L_π are obtained as 132 μm and 22.2 μm respectively for same S-bending loss. The total device length L_{tot} is obtained as $2L_T + L_\pi$ = 286.2 μm. It is observed from the figure that for tooth shaped grating assisted MMI coupler, beat length increases with increase of h whereas the transition length L_T decreases with h for same T_S. The optimum value of h is obtained at crossing point of the curves (L_T versus h and L_π versus h) as ~ 4 μm at which the value of L_T and beat length L_π are ~114.5 μm and 40 μm respectively (same value of h is already chosen in section 5.2.2). The total device length L_{tot} of MMI coupler with tooth shaped grating is obtained as $2L_T + L_\pi$ = 269 μm which is 17 μm less than that of tooth shaped grating based TMI coupler. The figure also shows dependence of transition length (L_T) and beat length (L_π) on h of MMI region of the proposed structures by considering fixed S-bending loss (T_S) of 0.2 dB. It is seen that the beat length of conventional MMI coupler is two times larger than that of tooth shaped grating assisted MMI coupler.

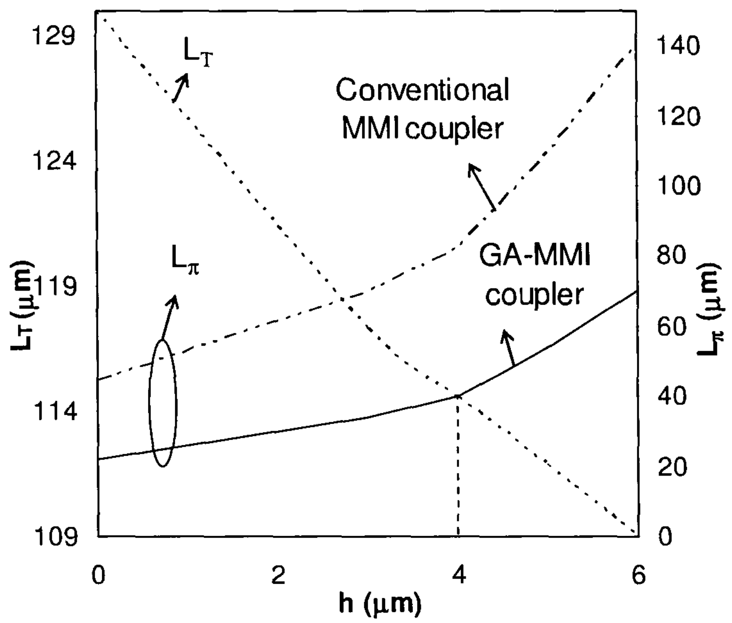

Fig-5.12: Transition length (L_T) and Beat length (L_π) versus waveguide separation gap (h) variation of tooth shaped grating assisted MMI coupler (solid line) and conventional MMI coupler (dotted line) with a=1.5 μm, b=1.5 μm, index contrast ~5% and cladding index~1.45.

In NxN photonic matrix switching applications, it is required to keep maximum access waveguide bending loss of 0.1 dB due to large scale integration [19]-[20]. So we have studied the reduction of bending loss, T_s (dotted line) with increase of h for tooth shaped grating assisted MMI coupler with a=1.5 μm, b=1.5 μm, index contrast~5 % and cladding index~1.45, as shown in Fig-5.13. The figure also shows the variation of beat length (L_π) with coupling gap (h) as a solid line. It is found that as h increases beat length increases whereas bending loss decreases with increase of h and the optimum value of h is obtained at crossing point of the curves (bending loss versus h and L_π versus h) as ~4 μm at which the value of the bending loss and beat length L_π are ~ 0.1 dB and 40 μm respectively.

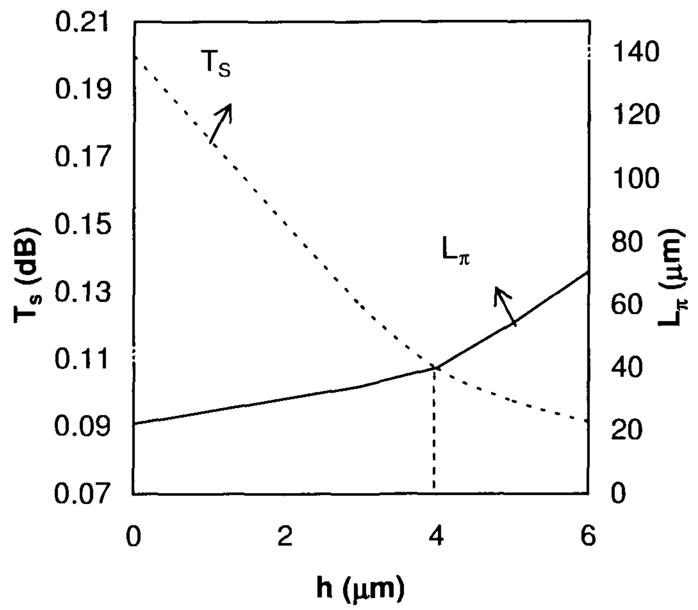

Fig-5.13: Bending loss (T_S) and Beat length (L_π) versus waveguide separation gap (h) variation for tooth shaped grating assisted MMI coupler with a=1.5 μm, b=1.5 μm, index contrast ~5 % and cladding index~1.45 respectively.

5.4. Design Device Parameters

Table-5.1: Device Design Parameters

Design Parameters	**GA-TMI Coupler**	**GA-MMI Coupler**	**Conventional TMI Coupler**	**Conventional MMI Coupler**
Core waveguide width (a), μm	1.5	1.5	1.5	1.5
Core waveguide Thickness (b), μm	1.5	1.5	1.5	1.5
Index Contrast (Δn)	5%	5%	5%	5%
Core RI (n_1), Δn=5%	1.5	1.5	1.5	1.5
Cladding RI (n_2) , Δn=5%	1.45	1.45	1.45	1.45
Coupling Gap Cladding RI (n_3)	0	1.459	0	1.459
Coupling gap (h), μm	0	4	0	4
Grating teeth width (ΔW), μm	0.25	0.25	0	0
Guiding region length (l_m), μm	0.26	0.26	0.26	0.26
Grating region length (l_g), μm	0.26	0.26	0.26	0.26
Wavelength (λ), μm	1.55	1.55	1.55	1.55
Beat length (L_π), μm	22.2	40	45	80
Access Waveguide length (L_T), μm	132	114.5	141	120
Total device length $(L_\pi+2L_T)$, μm	286.2	269	327	320

Table-5.1 shows the design parameters that is considered for the designed of tooth shaped grating assisted TMI (GA-TMI) coupler and grating assisted multimode interference (GA-MMI) coupler as discussed in the current chapter. The device lengths ($2L_T+L_\pi$) of GA-TMI coupler and GA-MMI coupler are obtained as ~286.2 μm and 269 μm respectively which shows that device length of GA-MMI coupler is ~17 μm less than GA-TMI coupler. For comparison, the device parameters of conventional TMI coupler and MMI couplers are also mentioned. It is found that the beat lengths of tooth shaped grating assisted structures are ~50% lower than that of conventional structures.

5.5. Conclusion

In this chapter, a compact 2x2 tooth shaped grating assisted multimode interference (MMI) coupler has been studied by using a mathematical model based on sinusoidal modes simple effective index method (SM-SEIM). It is found that the beat length of tooth shaped grating assisted MMI coupler (GA-MMI) with access waveguide separation h=4.0 μm is 40 μm which is ~50% less than that of conventional MMI coupler with same value of h. We have also studied dependence of access waveguide length on h with fixed value of S-bending loss for GA-MMI coupler and compared with that of tooth shaped grating assisted two-mode interference (GA-TMI) coupler. It is obtained that the device length including access waveguide length of GA-MMI coupler is less than that of GA-TMI coupler for a fixed value of access waveguide bending loss. Although the effect of fabrication tolerance on power imbalance of GA-MMI coupler is more than that of conventional MMI coupler, it is almost same as that for GA-TMI coupler. In the designed structures, each tooth shaped grating periods (Λ) consist of a guiding region (K=m) of length l_m~0.26 μm and a grating region (K=g) of length l_g~0.26 μm respectively. The fabrication of such compact photonic integrated devices with dimensions<1 μm require processes such as electron beam, focused ion beam (FIB) method etc. The process is expensive and due to our limited access/availability of these process/techniques, the fabrication of tooth shaped grating assisted structures which essentially requires electron beam technique could not be done. And as such the designs without grating (specifically conventional structures and structures with double S-bend) with dimensions≥1 μm have been fabricated with standard photolithography process which is discussed in the preceding chapter-6 and chapter-7 respectively.

References

1. Yao, C., et al. An ultracompact multimode interference wavelength splitter employing asymmetrical multi-section structures, *Opt. Exp.* **20**, 18248-18253, 2012.
2. A. Neyer, Integrated optical multichannel wavelength multiplexer for monomode systems, *Electron. Lett.* **20**, 744-746, 1984.
3. Paiam, M.R., & MacDonald, R.I. A 12-channel phased-array wavelength multiplexer with multimode interference couplers, *IEEE Photonic Tech. Lett.* **10**, 241-243, 1998.
4. Huang, J. Z., et al. A new design approach to large input/output number multimode interference couplers and its application to low-crosstalk WDM routers, *IEEE Photonic* Tech. Lett. **10**, 1292-1294, 1998.
5. Soldano, L. B., & Pennings, E.C M. Optical multi-mode interference devices based on self-imaging: Principles and Applications, *J. of Lightwave Tech.* **13**, 615-627, 1995.
6. Nishihara, H., Haruna, M., & Suhara, T. *Optical Integrated Circuits*, McGraw-Hill, New York, 1989.
7. Deka, B., et al., Transformation relationship of directional coupler with multimode interference coupler and two mode interference coupler, *J. Optics* **38**, 75-87, 2009.
8. Chiang, K.S. Effective index method for the analysis of optical waveguide couplers and arrays: an asymptotic theory, *J. of Lightwave Tech.* **9**, 62-72, 1991.
9. Wang, Q., et al., Effective index method for planar lightwave circuits containing directional couplers, *J. of Optics Communications* **259**, 133-136, 2006.
10. Chiang, K. S. Analysis of the effective-index method for the vector modes of

rectangular-core dielectric waveguides, *IEEE Transactions on Microwave Theory and Tech.*, **44**, 692-700, 1996.

11. Tsao, S. L., et al., BPM simulation and comparision of 1x2 directional waveguide couplingand Y-junction coupling silicon-on-insulator optical couplers, *Fiber and Integrated Optics*, **21**, 417-433, 2002.
12. Lifante, G. *Integrated Photonics: Fundamentals*, John Wiley, USA, 2003.
13. Sahu, P. P. A tapered structure for compact multimode interference coupler, *IEEE Photonic. Technol. Lett.* **20**, 638-640, 2008.
14. Sahu, P. P. Compact multimode interference coupler with tapered waveguide geometry, *Optics Communications.* **227**, 295-301, 2008.
15. Tsai, T. Y., et al., A novel wavelength-division-multiplexer using grating assisted two-mode interference, *IEEE Photonic Tech. Lett.* **16**, 2251-2253,2004
16. Tsai, T. Y., et al., A novel ultra compact two-mode-interference wavelength division multiplexer for 1.5 μm operation, *IEEE J. Quantum Electron.* **41**, 741-746, 2005.
17. Sahu, P. P. All-optical switch using optically controlled two mode interference coupler, *Appl. Opt.* **51**, 2601-2605, 2012.
18. Sahu, P. P. A compact optical multiplexer using silicon nano waveguides, *IEEE J. Sel. Topics Quantum Electron.* **15**, 1537-1541, 2009.
19. Kasahara, R., et al., New structure of silica-based planar lightwave circuits for low-power thermo-optic switch and its application to 8x8 optical matrix switch, *J. Lightwave Technol.* **20**, 993-1000, 2002.
20. Zhou, J., et al. Operation principle for optical switches based on two multimode interference couplers, *J. of Lightwave Tech.* **30**, 15-21, 2012.

****

CHAPTER-6

Fabrication & Characterization of Photonic Integrated Devices

Introduction

Materials for Optical Waveguides

Micro Fabrication Process Steps & Techniques for Photonic Integrated Devices

Fabrication of Directional Coupler, TMI Coupler and MMI Coupler

Characterization and Experimental Result

Conclusion

6.1. Introduction

The current chapter-6 deals with the fabrication processes steps and adopted techniques for realization of compact photonic integrated device components such as directional coupler (DC), two mode interference (TMI) coupler and multimode interference (MMI) coupler. In reference to the index of refraction, choice of material selection is a requisite necessity and this depends mainly on the function to be performed by the device. Although there are a number of candidate materials such as Ti: $LiNbO_3$ [1]-[3], GaAsInP/InP [4][5], SiON/SiO_2[6][7], GeO_2-SiO_2/SiO_2[8][9], SOI [10][11], polymer [12]-[14] etc. for development of compact photonic components; Silicon shows the property of opaque in the visible spectrum whereas transparent at the infrared wavelengths incorporates its application in optical transmission to guide light [7][15]. As discussed in chapter-2 and designed in previous chapters, for the fabrication of designed device components Silicon Oxynitride (SiO_xN_y) has been chosen as the core material surrounded by Silica (SiO_2) cladding layer for the following advantages [7][15]-[16]:

- SiO_xN_y is intrinsically compatible with the silicon processing technology.
- It shows a combination of chemical inertness, the low chemical permeability of silicon nitride and the excellent dielectric interface properties of silicon dioxide.
- The most important feature of this material is the variation of refractive index with changes in composition, or more precisely with the ratio of oxygen and nitrogen atoms. This feature enables one to tailor the refractive index and thereby customize the design of waveguides.
- Further, the luminescent properties of SiO_xN_y might lead to the future integration of electro optic devices with passive waveguides.

6.2. Fabrication Process and Techniques for Integrated Devices

Fig-6.1(a)-(c) shows the flow chart of adopted fabrication process steps and techniques which are discussed in detail along with process parameters in the subsequent sections.

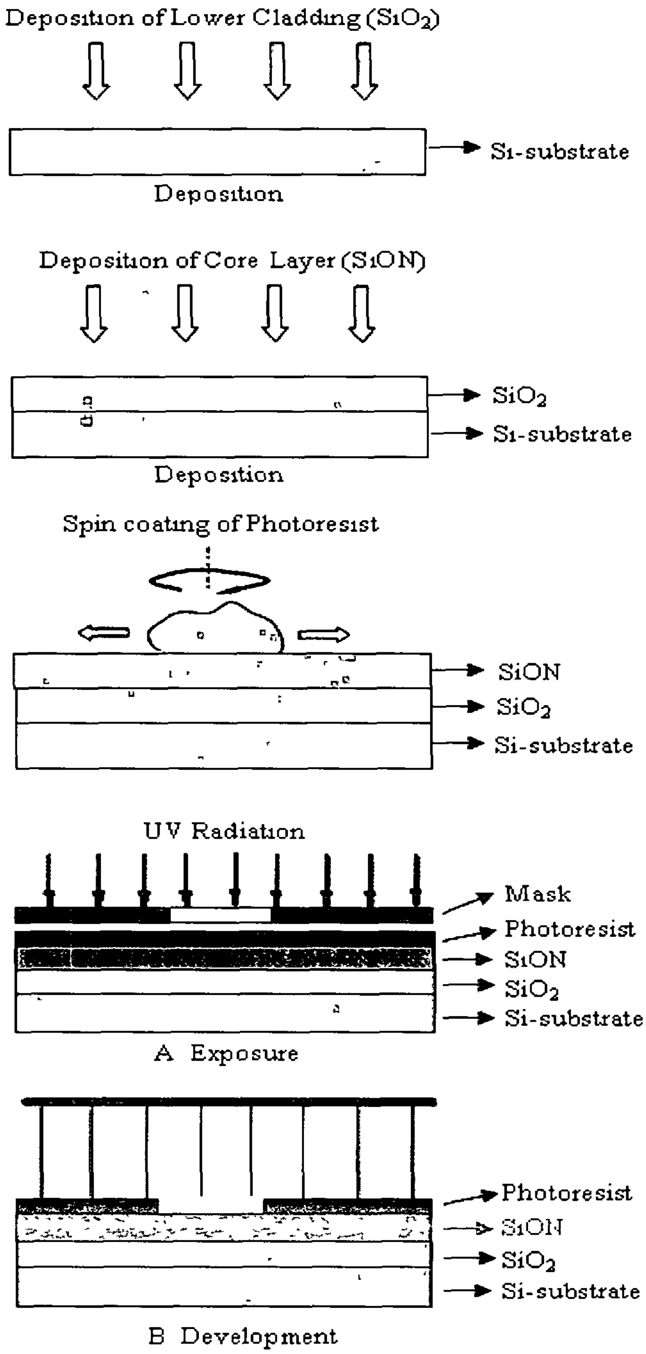

Fig-6.1(a): Detail scheme for fabrication of channel waveguide structure

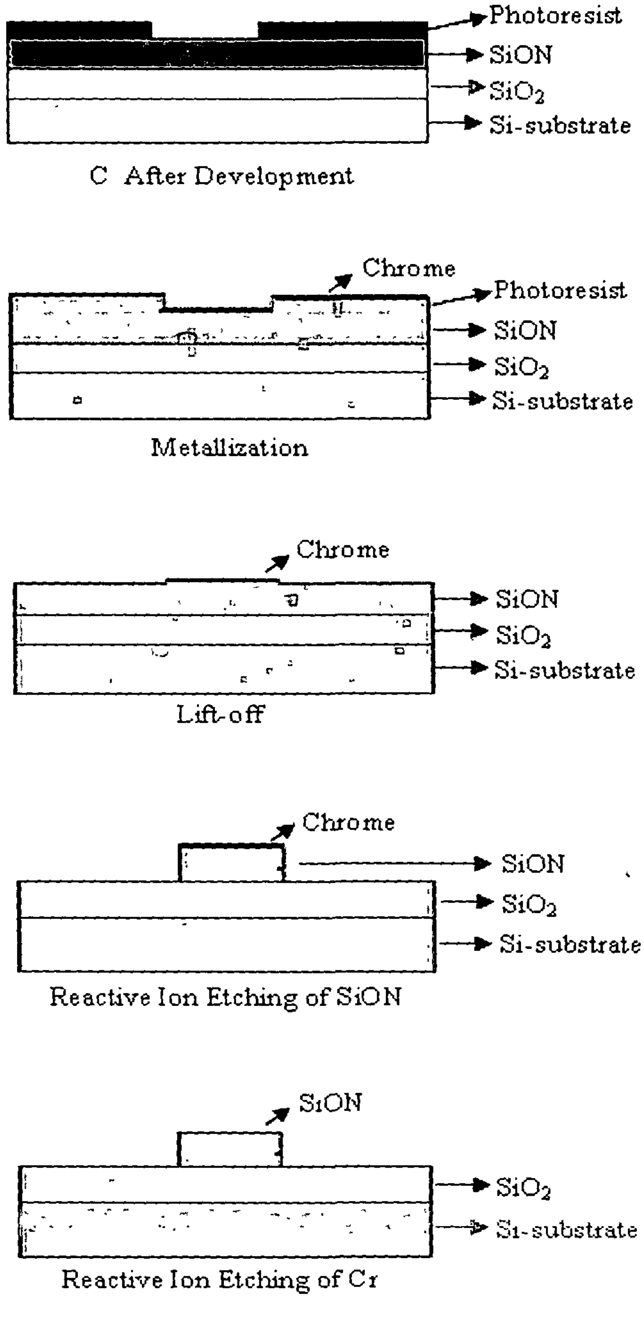

Fig-6.1(b): Detail scheme for fabrication of channel waveguide structure

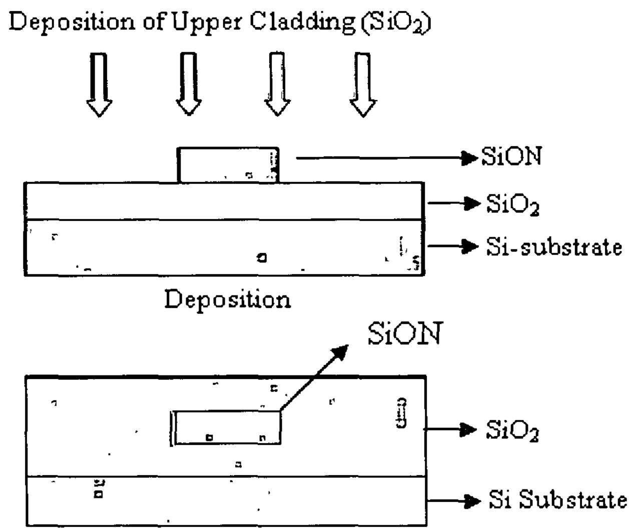

Fig-6.1(c): Detail scheme for fabrication of channel waveguide structure

In this research effort the process of fabrication begins with the deposition of lower (cladding) layer of SiO_2, grown by high-pressure thermal oxidization- Dry-Wet-Dry Oxidization, and Plasma Enhanced Chemical Vapor Deposition (PECVD). The detail deposition process is discussed later in this chapter. The silicon oxynitride (SiON) film as a core layer is deposited using silane (SiH_4) and nitrous oxide (N_2O) precursor gases in the PECVD reactor which is also discussed in details later on. Previous works [17]-[21] have optimized low loss SiO_xN_y films with index contrast (Δn) <5%-7% and above which the loss increases rapidly. Although the high index contrast materials based waveguide devices reduces device dimension, these material shows poor transmission properties in the high index range. Because of the high refractive index difference (n=2 for Si_3N_4, vs n =1.45 for SiO_2), the core layer need to be relatively thin to ensure single-mode operation. Thermal oxidation is performed using a quartz-tube electric furnace to heat Si wafers in a flowing oxygen atmosphere [20]-[22]. To grow a thick SiO_2 layer, the oxidation rate can be enhanced by using steam or steam-added oxygen atmospheres (Wet oxidation). The refractive index of the SiO_2 layer exhibits slight dependence on the atmosphere. The thickness of the underlying oxide buffer layer must be large enough to ensure that the optical mode remains well confined in the core (Silicon Oxynitride) layers and does not leak into the high-index silicon substrate. Previous works on waveguides based geometry have been reported with propagation losses as low as 0.2 dB/cm [17]. The refractive index and the thickness of the films were measured using Ellipsometer and Profilometer. To understand the material behavior of deposited films, composition analysis are also carried out using high resolution FTIR spectroscopy. Table-3.2 shows the design parameters of DC, TMI coupler and MMI coupler as details are discussed in chapter-3. The designed DC, TMI coupler and MMI coupler with these waveguide parameters are then fabricated and experimentally tested using SiON as the waveguide core material with SiO_2 cladding layer. The detail each fabrication process steps and experimental results are discussed in the proceeding sections.

Table-6.1: Design parameters of DC, TMI coupler and MMI coupler

Design Parameters	**Directional Coupler**	**MMI Coupler**	**TMI Coupler**
Core waveguide width (a), μm	1.5	1.5	1.5
Core waveguide Thickness (b), μm	1.5	1.5	1.5
Index Contrast (Δn)	5%	5%	5%
Core RI (n_1) , Δn=5%	1.5	1.5	1.5
Cladding RI (n_2)	1.45	1.45	1.45
Coupling Gap Cladding RI (n_3)	1.45	1.4945	----
Coupling gap (h), μm	0.5	4	0
Wavelength (λ), μm	1.55	1.55	1.55
Beat Length (L_π), μm	91	80	45

6.2.1 Preparation of Wafer for Fabrication

Wafer specifications : Si wafer

Type	: P-type
Orientation	: <100>
Thickness	: 525 ± 0.25 μm
Diameter	: 100 mm
Resistivity	: 1-15 ohms-cm
Surface	: one side polished

Wafer Cleaning Process: The RCA clean is a standard set of wafer cleaning steps which need to be performed before high temp processing steps (such as oxidation, diffusion, CVD etc.) of silicon wafers in fabrication process. Werner Kern developed the basic procedure in 1965 while working for RCA, the Radio Corporation of America. It involves the following:

1. Removal of the organic contaminants (Organic Clean)
2. Removal of thin oxide layer (Oxide Strip)
3. Removal of ionic contamination (Ionic Clean)

The wafers are prepared by soaking them in DI water. The first step RCA-1 (also called SC-1, where SC stands for Standard Clean) is performed with a 1:1:5 solution of NH_4OH (ammonium hydroxide) + H_2O_2 (hydrogen peroxide) + H_2O (water) at 75 or 80 °C typically for 10 minutes. This treatment results in the formation of a thin silicon dioxide layer (about 10 Angstrom) on the silicon surface, along with a certain degree of metallic contamination (notably Iron) that shall be removed in subsequent steps. This is followed by transferring the wafers into a DI water bath.

The second step is a short immersion in a 1:50 solution of HF + H_2O at 25 °C, in order to remove the thin oxide layer and some fraction of ionic contaminants.

The third and last step RCA-2 (also called SC-2) is performed with a 1:1:6 solutions of HCl + H_2O_2 + H_2O at 75 or 80 °C. This treatment effectively removes the remaining traces of metallic (ionic) contaminants. The details cleaning process steps approached are as follows:

The cleaning processes are carried out in the Chemical Wet bench as shown in Fig.-6.2.

RCA (WET BENCH)

Fig-6.2. Chemical Wet Bench

The RCA (Radio Corporation of America) is having 2 process steps as discussed above: **RCA-1 and RCA-2**.

<u>RCA-1</u>: (DI water: H_2O_2: NH_4OH=5:1:1)

DI water =200 ml

H_2O_2 = 40 ml

NH_4OH =40 ml

In case, if we don't have Ammonium Hydroxide, we can also use ammonium solution.

- Temperature of the solution = 75-80° C
- RCA-1 function : Remove Organic residues

- Quartz beaker is mandatory.
- Magnetic stirrer: rotate uniformly and mix the solution and also maintain the temperature 75-80° C.
- Wafer holder: used to hold the wafer.
- Exhaust to be on, while performing RCA Cleaning.

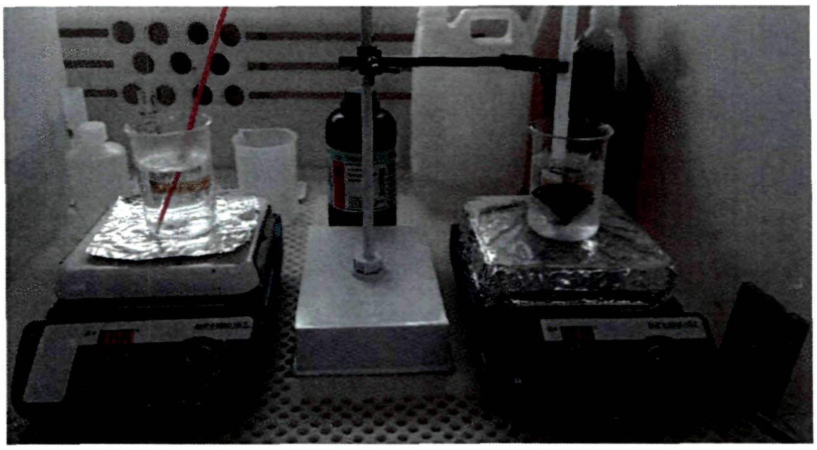

Fig-6.3: RCA-1 Cleaning Process

RCA-1 Cleaning Procedure:

RCA-1 cleaning removes the surface contaminants like dust, grease etc. The process steps are:

Step-1: Take 200 ml DI water into quartz beaker then add 40 ml H_2O_2 and 40 ml NH_4OH to DI water. Once the solution is prepared, keep it on a hot plate and set temperature to 250° C. The temperature of the solution is maintained at 75- 80° C.

Step-2: A magnetic Stirrer put in the solution so that it uniformly rotates and mix the solution.

Step-3: Once solution gets heated up to 80° C, load silicon wafer into wafer holder and immerse into heated RAC-1 solution for 10 minutes. After 10 minutes of cleaning take out wafers from the solution and rinse with DI water thoroughly for 1 minute, so that it can be cool down.

Step-4: After doing RCA-1, all beakers should be washed with DI water. Acid waste and DI water to be disposed in drain.

RCA-2: (DI water: H_2O_2: HCL=6:1:1)

DI =240 ml

H_2O_2 = 40 ml

HCL =40 ml

- Temperature of the solution = 75-80° C
- RCA-2 function : Remove metallic residues
- Quartz beaker is mandatory.
- Magnetic stirrer: rotate uniformly and mix the solution and also maintain the temperature 75-80° C.
- Wafer holder: used to hold the wafers.
- Exhaust to be on, while performing RCA Cleaning.

Fig-6.4: RCA-2 Cleaning Process

RCA-2 Cleaning Procedure:

The RCA-2 cleaning removes the metallic contaminants from the wafer. The cleaning process steps are:

Step-1: Take 240 ml DI water into quartz beaker .Add 40 ml H_2O_2 and 40 ml HCl to DI water. Once the solution is prepared, keep it on a hot plate and set temperature to 250° C. The solution will be needed to be heated 75- 80° C.

Step-2: Magnetic Stirrer put in the solution so that it uniformly rotates and mix the solution.

Step-3: Once solution gets heated up to 80° C, load silicon wafer into wafer holder and immerse into heated RAC-2 solution for 10 minutes. After 10 minutes of cleaning take out wafers from the solution and rinse with DI water thoroughly for 1minute, so that it can be cool down.

Step-4: After doing RCA-2, all beakers should be washed with DI water. Acid waste and DI water to be disposed in drain.

After RCA-1 and RCA-2 cleaning process, next process step is:

<u>HF (hydrofluoric acid solution) DIP</u>: (DI water: HF=10:1)

DI water = 100 ml

HF= 1 ml

- This process takes about 5 to 7 minutes to complete.
- Never use a glass beaker with HF since HF'attacks glass, always use plastic beaker.

Procedure:

Take 100 ml of DI water using measuring cylinder and pour into polypropylene beaker and then 1 ml of HF in a polypropylene measuring cylinder and add to DI water and mix thoroughly using Teflon rod. Then dip RCA-2 cleaned silicon wafer into dilute HF solution for 15 seconds and finally rinse with DI water for 1 min. Next, wafers should be blow dry with Nitrogen and store in a wafer box.

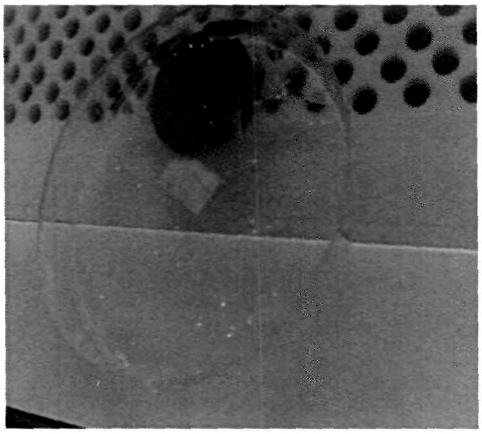

Fig-6.5: (a) HF solution dipped Wafer

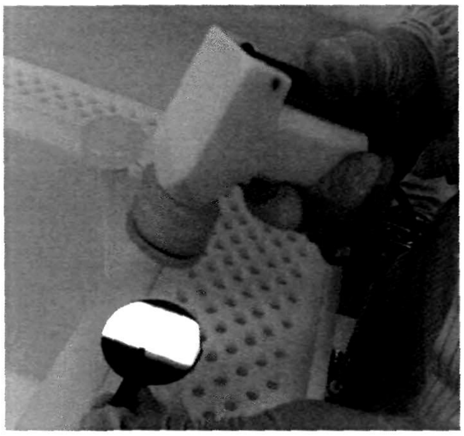

Fig-6.5(b): Blow dry with Nitrogen

Now the wafers are ready for thermal wet oxidation process.

6.2.2 Deposition of Silica (SiO_2) Layer as Lower Cladding

In thermal oxidation, silicon wafers are oxidized in furnaces at about 1000^0 C. The furnaces consist of a quartz tube in which the wafers are placed on a carrier made of quartz glass. For heating there are several heating zones and for chemical supply multiple pipes. Quartz glass has a very high melting point (above 1500^0 C) and thus is applicable for high temperature processes. To avoid cracks or warping, the quartz tube is heated slowly (e.g. $+10^0$ C per minute). The tempering of the tube can be done very accurate via individual heating zones. Depending on the gases different oxidations occur (a thermal oxidation has to take place on a bare silicon surface). Fig-6.7 shows the schematic diagram of Wet Oxidation Furnance/Tempress Furnance used for dry-wet-dry oxidation.

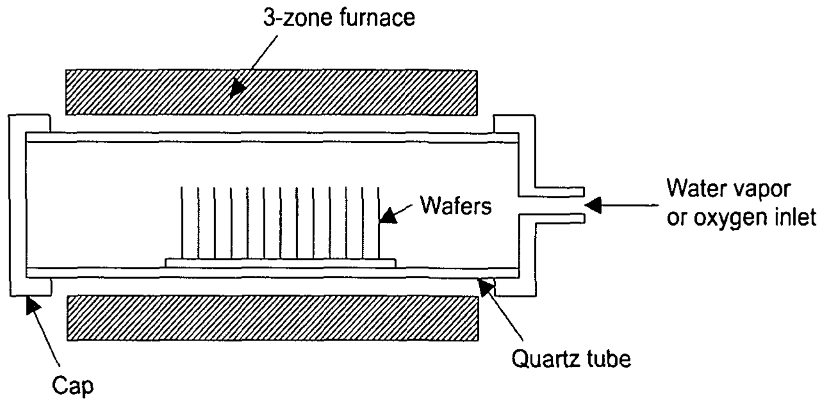

Fig.-6.7: Schematic diagram of an oxidation furnace

The thermal oxidation can be divided into the dry and wet oxidation:

The dry oxidation takes place under pure oxygen atmosphere. The silicon and oxide reacts to form silicon dioxide (SiO_2):

$$Si + O_2 \rightarrow SiO_2$$

In wet thermal oxidation, the oxygen is led through a bubbler vessel filled with heated water (about ~95^0 C), so that in addition to oxygen water is present in the quartz tube as steam. The oxidation is given by:

$$Si + 2H_2O \rightarrow SiO_2 + 2H_2$$

This process is done by 90^0 C to 1000^0 C. The characteristics of wet thermal oxidation are:

i. Fast growth rate even on low temperatures
ii. Less quality than dry oxides

This dry process is done at 1000 to 1200^0 C actually. To create a very thin and stable oxide the process can be done at even lower temperatures of about 800^0 C. Characteristic of the dry oxidation:

i. Slow growth of oxide
ii. High density
iii. High breakdown voltage

In the beginning, the oxygen and silicon react to form silicon dioxide. Now the oxide layer at the surface has to be surpassed by other oxygen atoms which have to diffuse through the dioxide layer to react with the silicon crystal beneath. For this reason the growth rate primarily depends on the reaction time of oxygen and silicon, while at a certain thickness the oxidation rate is mainly determined by the velocity of diffusion of the oxygen through the silicon dioxide. With increasing thickness of the dioxide the growth rate decreases. Since the layer is amorphous, not all bonds in the silicon dioxide are intact. Partial there are dangling bonds (free electrons and holes) at the interface of silicon and SiO_2, and therefore there is a slightly positively charged zone at the interface. Since these charges affect the integrated circuit in a negative manner, therefore in general these charges are reduced with a higher temperature during oxidation or by using the wet oxidation which causes only a light charge.

Details Oxidation Procedure:

A. Growth of SiO_2 of 1 μm thickness: Dry-Wet-Dry

Material: SiO_2
Thickness: 2-3 μm (for >1 μm PECVD is preferred)

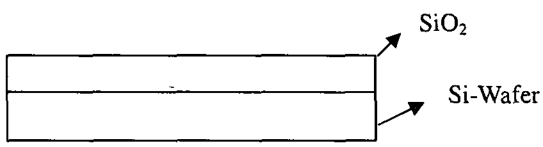

At the first, switch-on the mains of thermal wet oxidation furnace to grow 1 μm oxide layer on the top of the cleaned silicon wafer. Through Digital temperature controller the furnace is ramp up and executes the temperature.

1 Display mode

2 Program mode

3 Execute mode

Fig-6.8: Digital temperature controller

Thermal oxidation is carried out for growing SiO_2 layer on the cleaned Si surfaces. SiO_2 layer of thickness~1 μm is grown in the first step of oxidation using dry-wet- dry oxidation sequence.

The steps for thermal oxidation are as follows.

Step-A: Set the oxidation furnace temperature to 1100^0 C and purge the furnace with pure N_2 gas.

N_2 Flow rate -1 liter/min for 15 min.

Step-B: Load wafers in oxidation furnace in a N_2 ambient (N_2 is used only during loading and unloading of wafers in oxidation furnace).

Step-C: Carry out dry oxidation for 10 min.

Drive the O_2 into the furnace. Dry oxidation is to get the uniform layer of thickness and good interface between Si and Oxide.

O_2 Flow rate -1 liter/min.

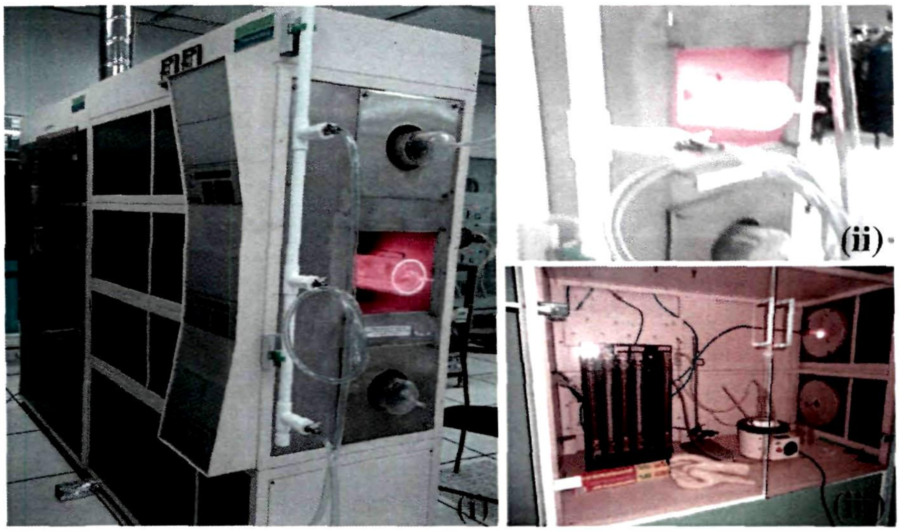

Fig-6.9: (i) Oxidation Furnace, (ii) Front view of the furnace chamber (iii) Back view along with bubbler and gas (Installed at CeNSE, IISc.)

Step-D: Carry out Wet oxidation for 3 hours.

Heat the water up to 97° C and connect to the furnace. Pass the O_2 through bubbler. The oxygen carries water vapours along with it to the wafer surface enabling wet oxidation to take place.

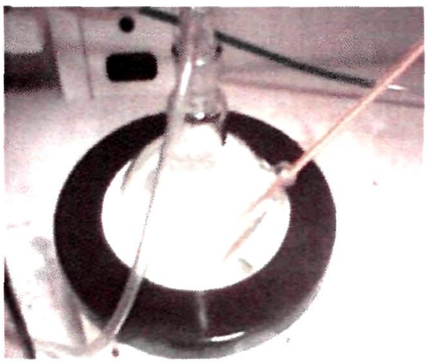

Fig.-6.10: Bubbler

Step-E: Carry out dry oxidation for 10 min.

Hence a 1 μm of SiO_2 is grown by the above process. At the end of this duration, the ambient gas is again switched to N_2 and wafers are unloaded.

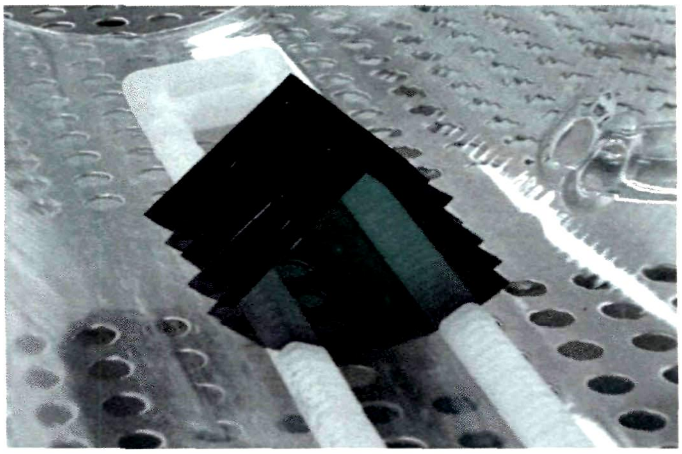

Fig.-6.11: Unloaded Si-wafer after oxidation

Colour of 1 μm oxide - green violet.

The dry-wet-dry sequence used in the process helps achieve a good quality Si-SiO_2 interface (enabled by dry oxidation) and at the same time a faster oxidation rate is achieved (due to wet oxidation).

Note: Initially 25-35 min will take to set the furnace temperature 1100^0 C and water heater to 97^0 C.

Timings:

Loading of wafers: 1: 10 p.m

Dry oxidation: 1:20 p.m to 1:30 p.m

Wet Oxidation: 1:30 p.m to 5:10 p.m

Dry Oxidation: 5:10 p.m to 5:20 p.m

Unloading of wafers: 5:40 p.m

Thickness Measurement of Deposited SiO_2 Layer:

The thickness of the growth SiO_2 layer on the top of a Si-wafer by using thermal oxidation technique is measured with the help of Ellipsometer Thickness Measurement System (Model: XLS100 from J.A. Woollam Co. Inc). Fig-6.12(a) shows the photograph of the system whereas Fig.-6.12(b) shows the schematic diagram. The measured result indicating the thickness of deposited SiO_2 lower cladding layer of ~1 μm (10455.19 A^0) is shown in Fig-6.13.

Further on the top of thermally grown SiO_2 layer of thickness ~1 μm, another layer of SiO_2 of thickness ~2 μm is deposited using Plasma Enhanced Chemical Vapor Deposition (PECVD) technique.

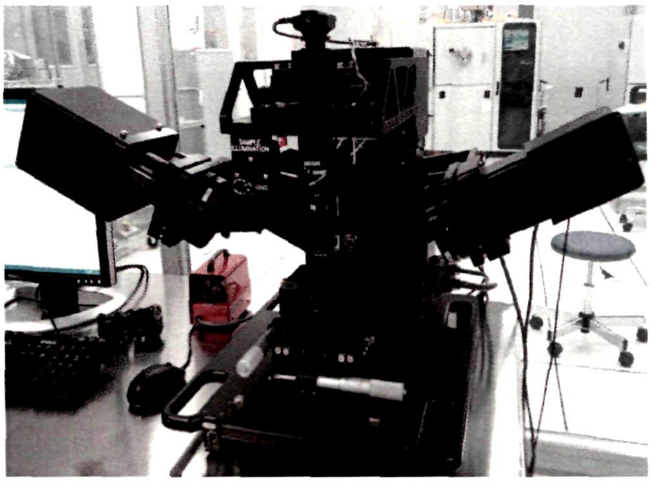

Fig.-6.12(a): Ellipsometer Measurement System (Model: XLS100)
(Installed at CeNSE, IISc., Bangalore)

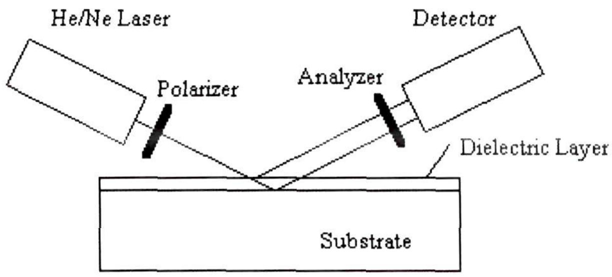

Fig.-6.12(b): Schematic of Ellipsometer

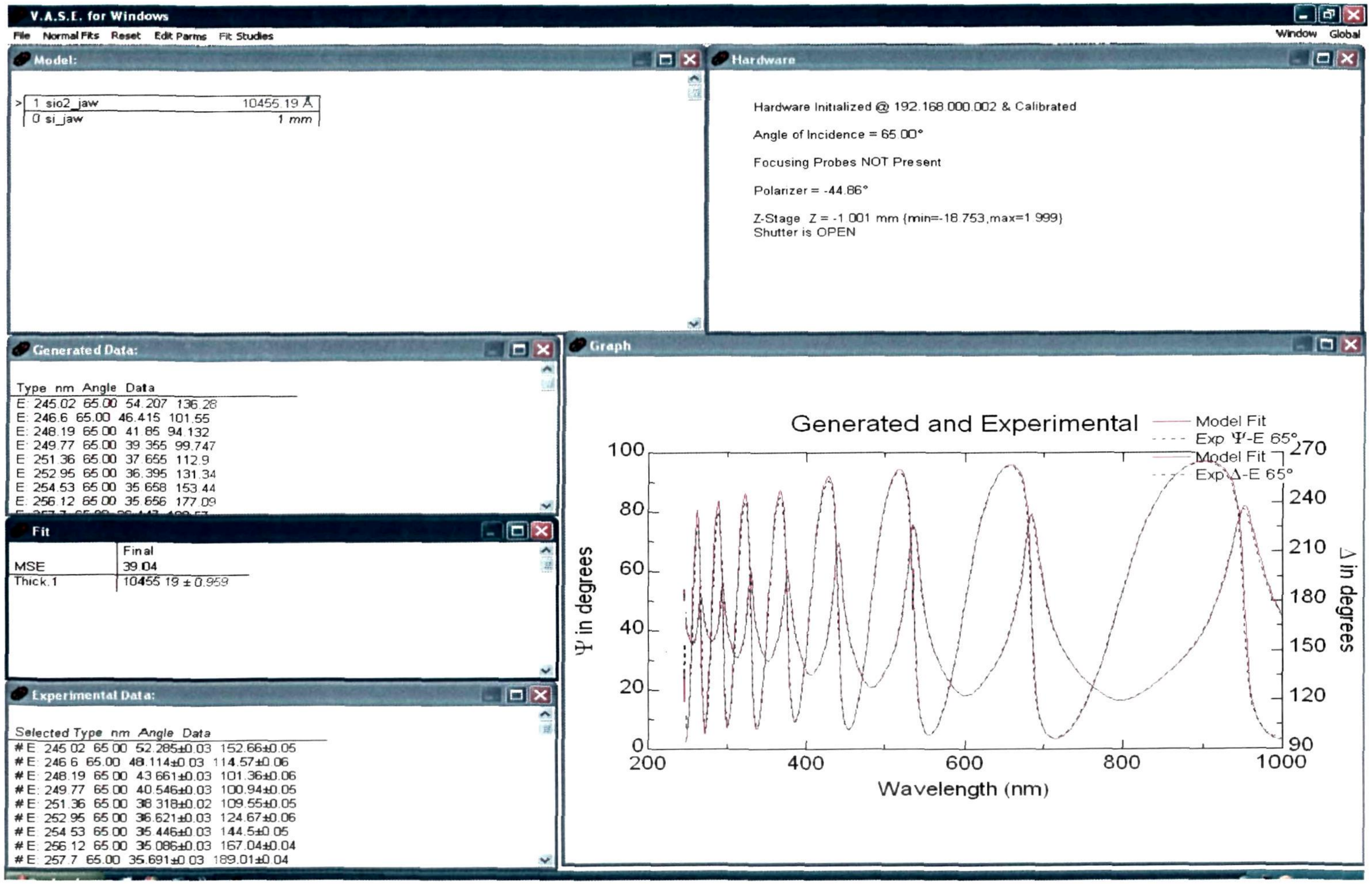

Fig.-6.13: Measured thickness of SiO_2 layer ~1 μm deposited using thermal oxidation

B. Deposition of Silica (SiO_2) Layer using PECVD Method

The basic reaction for the formation of the silica (SiO_2) using SiH_4 and N_2O precursor gases in PECVD is as follows:

$$SiH_4\ (gas) + 4\ N_2O = SiO_2\ (solid) + 2\ H_20\ (gas) + 4\ N_2\ (gas)$$

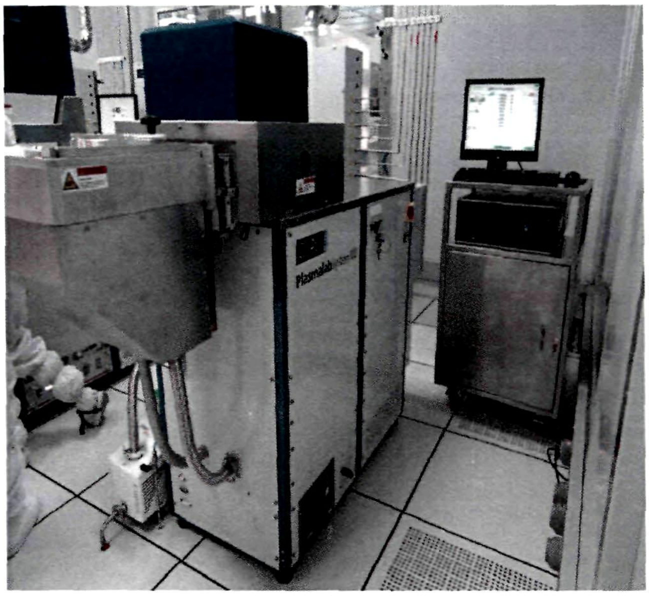

Fig-6.14: PECVD system (Oxford PlasmaLabSystem100)
(Installed at CeNSE, IISc.)

Fig-6.14 shows the schematic view of the PECVD system (PlasmaLabSystem100) from Oxford Instrument System which is used for deposition of SiO_2 lower cladding layer of thickness ~2 μm with the following process parameters.

Process parameters used:

RF power @ 13.56 MHz	: 20 W
Pump pressure	: 1000 mTorr
Silane (SiH_4) flow rate	: 8.5 sccm
N_2O flow rate	: 710 sccm

N_2 flow rate	: 161 sccm
Substrate temperature	: 350^0 C
Deposition rate	: 1 µm/25 min

The details of PECVD system is discussed in the proceeding section-6.2.3. The thickness and refractive index of the deposited SiO_2 layer is measured using ellipsometer. Fig.-6.15 shows the process parameters of SiO_2 deposition using PECVD system whereas the measured thickness of SiO_2 layer (~3 µm) is shown in Fig.-6.16.

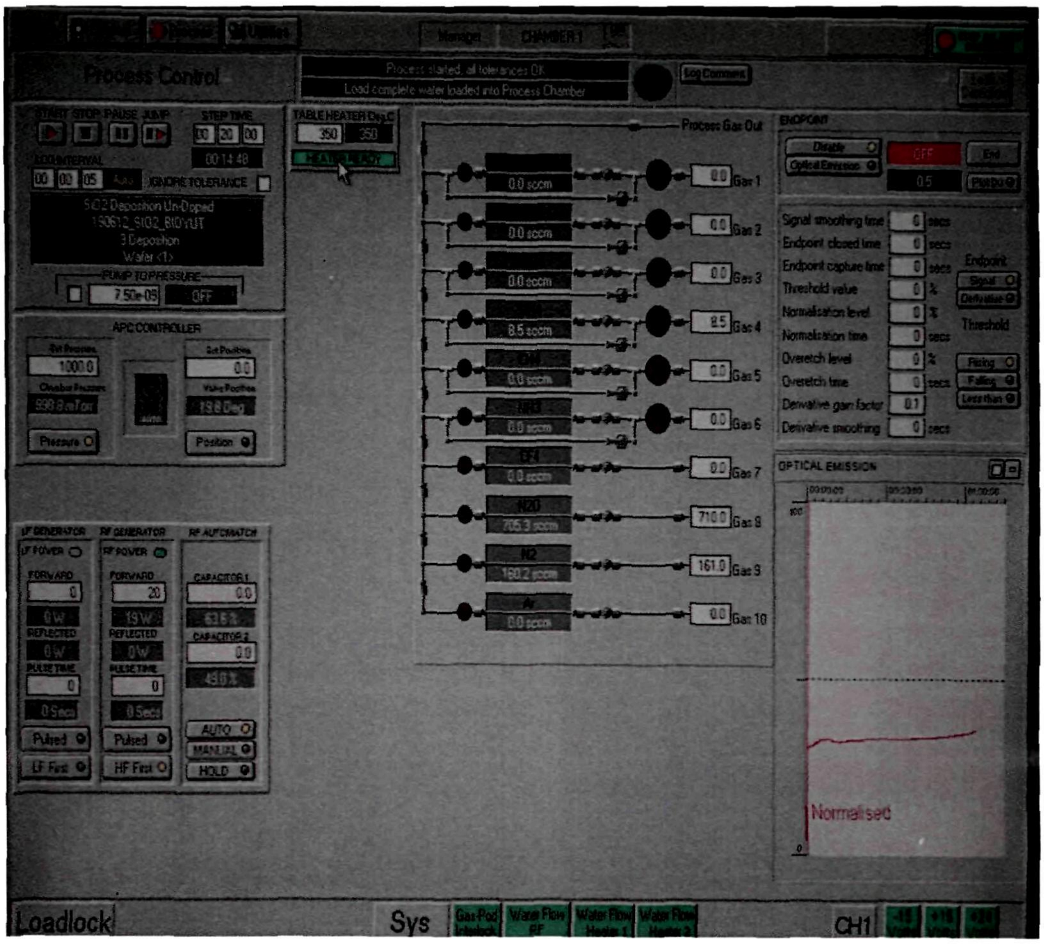

Fig-6.15: Process parameters for deposition of SiO_2 layer using PECVD

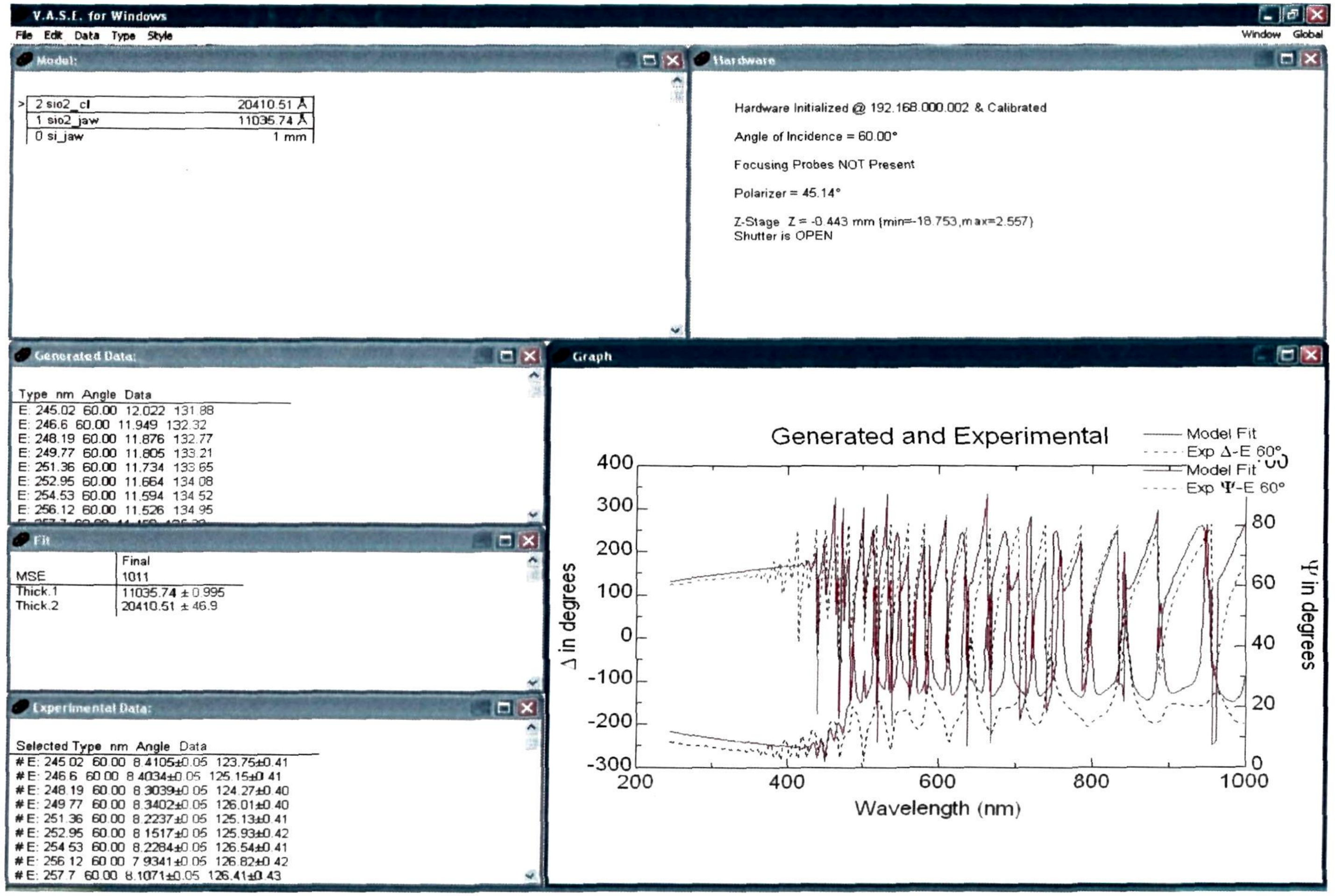

Fig.-6.16: Measured thickness of SiO_2 layer ~2 μm deposited using PECVD

6.2.3 Deposition of Silicon Oxynitride (SiON) as Guiding Layer

Material : SiON

Thickness : 1.5 μm

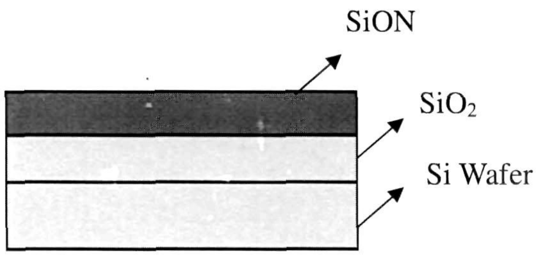

Among the variety of techniques available for silicon oxynitride production, plasma enhanced chemical vapour deposition (PECVD) technique is one of the most widely utilized due to the relative high deposition rates and low deposition temperatures [6][7]. On the other hand, for optical applications, besides the tunability of the refractive index of the materials involved, thick films (3–5 μm) with lower internal stress are essential. Plasma Enhanced Chemical Vapor Deposition (PECVD) for silicon oxynitride (SiON) layers results in a flexible material for optical waveguides. Deposition of silicon oxide and oxynitride by PECVD is identified as quite attractive technology for development of compact optical devices as films fabricated by this process easily matches the refractive index profile by changing the process parameters. In the PECVD process, the precursors used and the deposition parameters strongly influence the optical properties and quality of the deposited films. For the most part of PECVD processes for waveguide fabrication, nitrous oxide (N_2O) and silane (SiH_4) are used as main precursors for fabrication of pure silica.The basic reaction for the formation of SiON is given below,

$$SiH_4 + N_2O + NH_3 \rightarrow SiO_xN_yH_z \text{ (solid)} + H_2O \text{ (gas)} + N_2 \text{ (gas)}$$

$$\rightarrow SiO_xN_y \text{ (solid)} + H_2O \text{ (gas)} + HCl \text{ (gas) (after annealing)}$$

Process Parameters used:

Si-Substrate temperature	: 350^0 C
RF power @ 13.56MHz	: 20 W
Pressure	: 1000 mTorr
SiH_4 flow rate	: 10 sccm
NH_3 flow rate	: 10 sccm
N_2O flow rate	: 200 sccm
N_2 flow rate	: 500 sccm
Deposition rate	: 1 μm/20 min

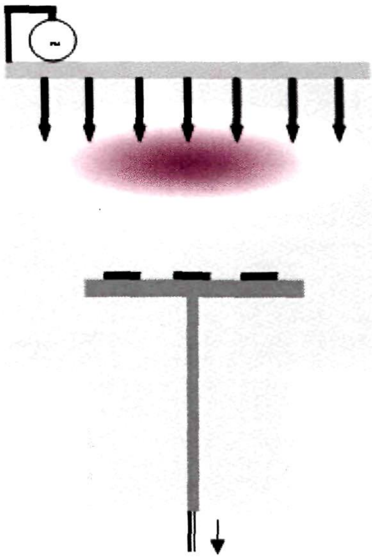

Fig.-6.17: PECVD technology (courtesy: Oxford Instrument System)

The silicon oxynitride films are deposited by using plasma enhanced chemical vapor deposition (PECVD) system (PlasmaLabSystem100) of Oxford Instruments System as shown in Fig-6.14 and Fig-6.17. The precursor gases are fed through a shower head which evenly distributes the gas mixture over the substrate holder; exhaust gases are pumped out from the bottom of the reactor. The plasma is created between the shower head and the substrate holder and hence the substrate is in direct contact with the plasma. This system can be operated at two different frequencies: 13.56 MHz and 100 kHz. The system can be programmed to switch back and forth between the two frequencies automatically during a deposition run. Fig.-6.18 shows the process parameters with precursor gases used for SiON deposition by PECVD whereas the measured thickness of SiON layer obtained by using Ellipsometer is shown in Fig.-6.19. The refractive index and thickness of the deposited films were measured using a Model 2010 prism coupler from Metricon Corporation and Ellipsometer respectively. It uses a 632.8 nm He-Ne laser with a rutile prism to couple the beam into the film. All the measurements were done at TE polarization mode using a single film on substrate algorithm.

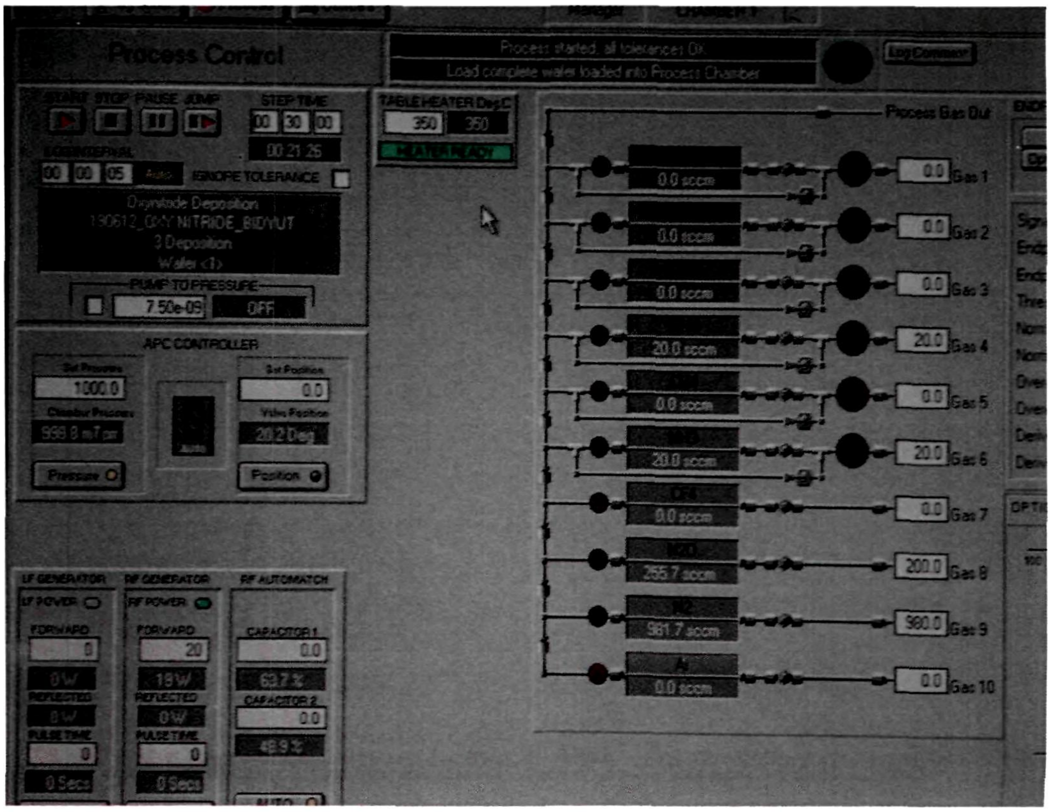

Fig-6.18: Process parameters for deposition of SiON layer using PECVD

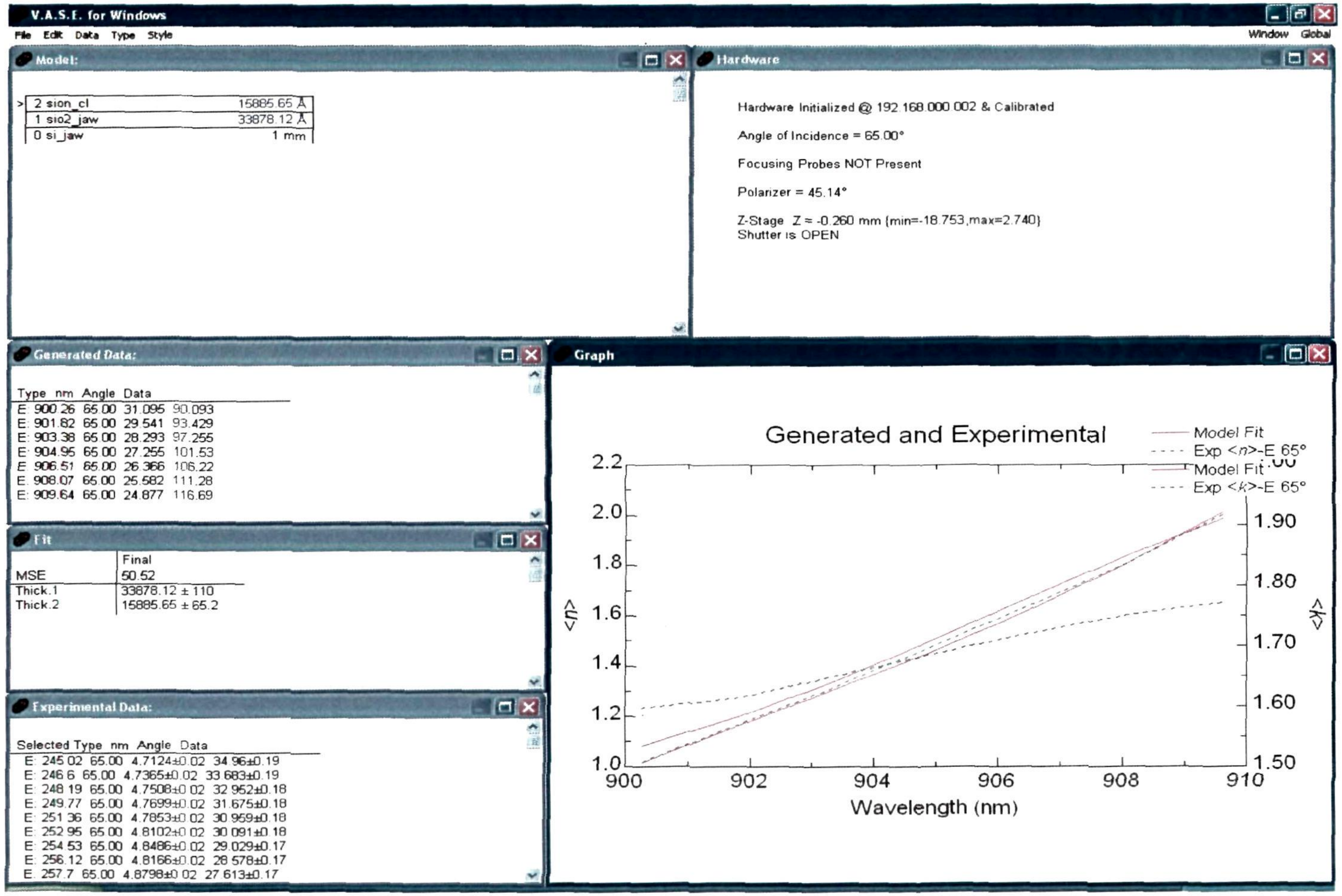

Fig.-6.19: Measured thickness of SiON layer ~1.5 μm deposited using PECVD

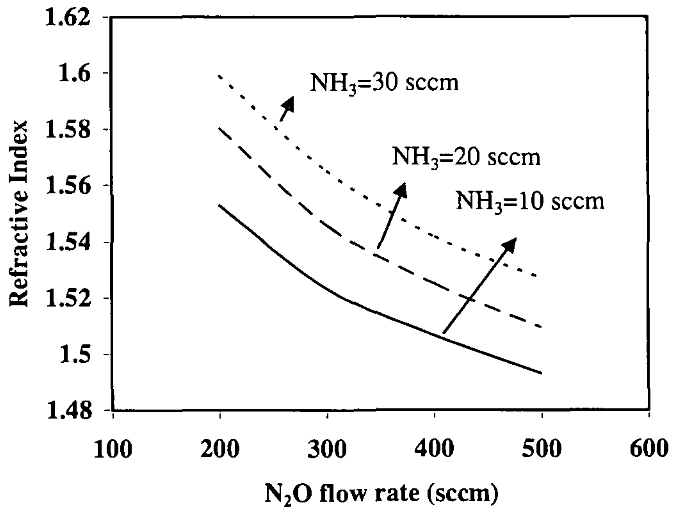

Fig.-6.20: Refractive index variation of SiON films as a function of N_2O and NH_3

It is seen that different factors such as flow rates of gases, pressure, power, temperature etc. affect both the deposition rates and refractive index of the deposited SiON films. Fig.-6.20 shows the refractive index relation with the N_2O gas flow rates for 3 different NH_3 gas flow levels. The refractive index of deposited SiON films can be modified successively between 1.55 and 1.495, which is the range of interest for waveguide application. Higher refractive indices up to 1.912 are probable by exploiting a lower N_2O/SiH_4 ratio or using a greater NH_3 flow rate. But high refractive index is not suitable to waveguide application. A common tendency discovered is that the refractive index decreases when flow rate of N_2O increases owing to nitrogen's weaker chemical reactivity compared to oxygen [19]-[20]. This occurs because oxygen atoms are more reactive than nitrogen atoms and large amount of oxygen with small amount of nitrogen will be incorporated into the silicon oxynitride film, resulting in refractive index closer to that of stoichiometric SiO_2. At lower N_2O flow rate and in the absence of ammonia, a large index film was produced because of the higher silicon abundance (silicon rich films). Besides, as the flow rate of ammonia gas was increased, the refractive index was enhanced due to the increase in nitrogen as well as hydrogen contents.

6.2.4 Preparation of Mask

The LaserWriter System is a useful tool for transfer of designed patterns on a Cr mask plate or directly on the substrate. The system transforms a laser beam into a controlled writing tool for photolithographic mask fabrication or for direct in-situ processing on planar substrates.

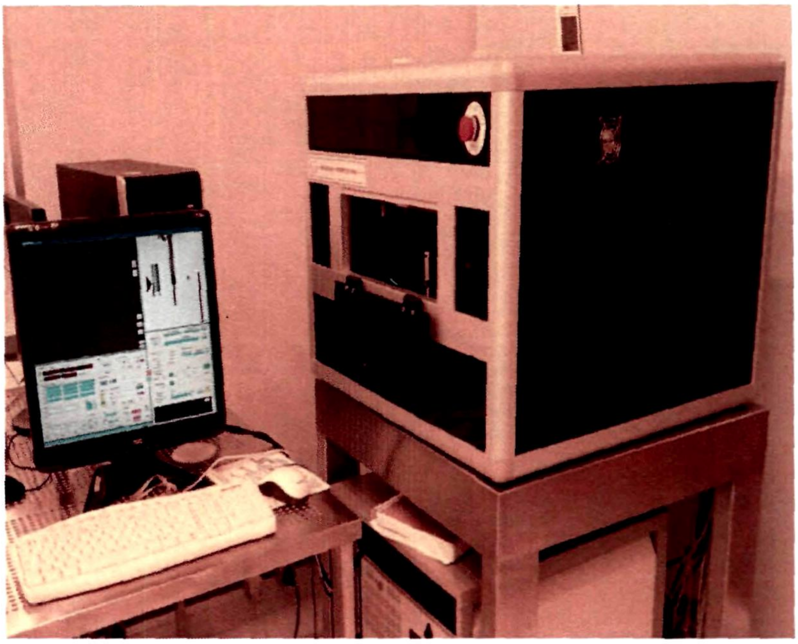

Fig.-6.21: Microtech LW 405A Laser Writer used for Mask Preparation (Installed at CeNSE, IISc.)

The Laser Writer [Model: Microtech LW 405A] is used for preparation of 4 inch Cr-Mask plate. The mask layout of the design patterns is prepared using L-Edit software and optiBPM software before writing to the mask plate. The LaserWriter is driven by a MICROTECH proprietary data format - LDF, LaserDraw Format -obtained by automatic translation from a number of industry standard languages accepted by the LaserWriter, such as CIF, DXF, and GDSII. Fig-6.22 shows the photograph of prepared mask.

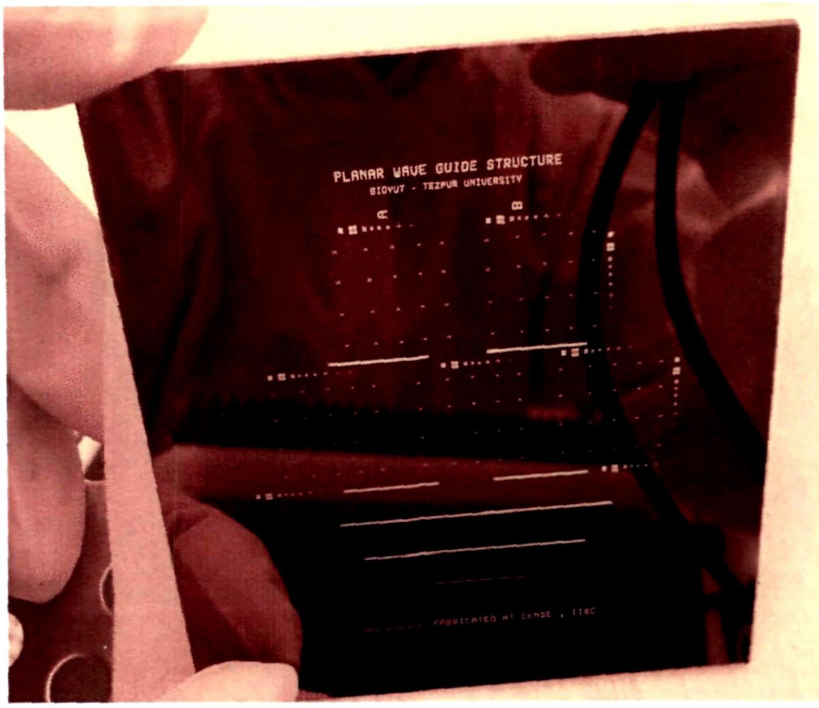

Fig.-6.22: Patterned Mask for Photolithography

6.2.5 Annealing

The PECVD deposited SiON layer contains certain amount of O-H bonds, N-H bonds, and Si-H bonds that are known to be main cause of optical absorption at 1.38 μm, 1.48 μm and 1.51 μm respectively. In order to eliminate these bonds, the deposited SiON layer has been annealed at 800^0-1000^0 C for 3 hrs with N_2 ambient using the First Nano drive-in furnace. For higher annealing temperatures (>1000^0 C), a large number of cracks occurred in the deposited SiON film. Fig-6.23 shows the First Nano's EasyTube® 6000 Horizontal Furnace System installed at CeNSE, IISc., Bangalore. The FTIR spectroscopy of SiON deposited film after annealing and before annealing is carried out which is shown in Fig.-6.24. This FTIR spectroscopy is carried out at SAIF, Tezpur University.

Fig.-6.23: First Nano Drive-in Furnace (Installed at CeNSE, IISc.)

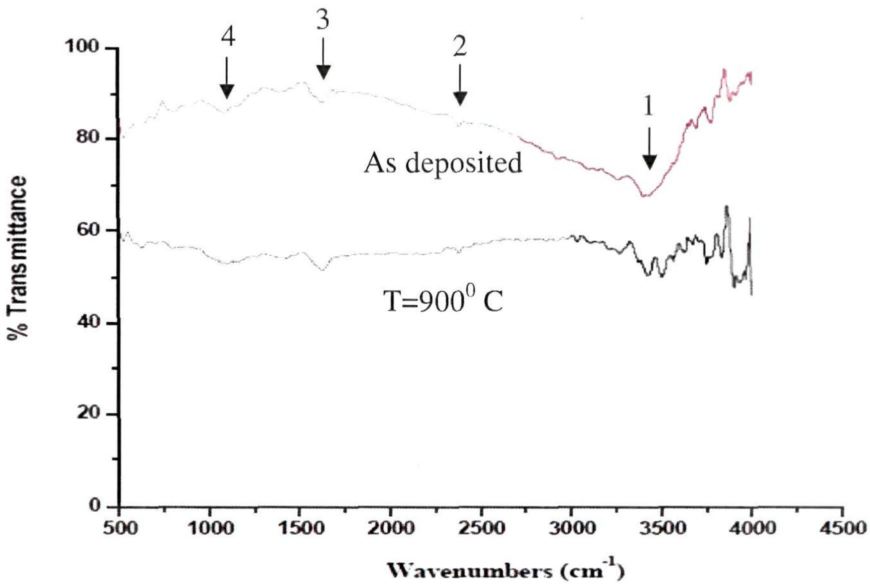

Fig.-6.24: FTIR analysis of SiON layer (**1**: Si-O-H, **2**: -Si-H, **3**: -N-H_2 and **4**: Si-O-H, -Si-H bonds)

6.2.6 Transfer of Pattern on Guiding Layer

After cleaning the mask plate (prepared using Laser Writer as discussed in section-6.2.4) using acetone and IPA, the standard photolithography is performed for the transfer of designed patterns on the top of SiON core layer using EVG 620 double sided mask aligner set-up. The details process steps are discussed as follows:

6.2.6.1 Spin Coating of Photoresist

Process Parameters:

Positive photoresist (PR)	: AZ315B
Developer	: MF26A
Thickness of photo resist	: 1-1.2 μm (4000 RPM)
Exposure	: 85 mJ/cm2
Standard NUV	: 350-450 nm
Lamp power	: 350 W-500 W

The positive photoresist (AZ315B) is coated on sample with spinner coater at 4000 rpm for 40 second. An exposure with UV light is given for 1.5 sec, after pre-baking of sample at 125^0 C for 1 min. The photoresist (PR) is developed in developer for 60 sec and then the sample is kept in oven for post baking at 125^0 C for 1 min in order to make further hardening of the exposed portion of photoresist.

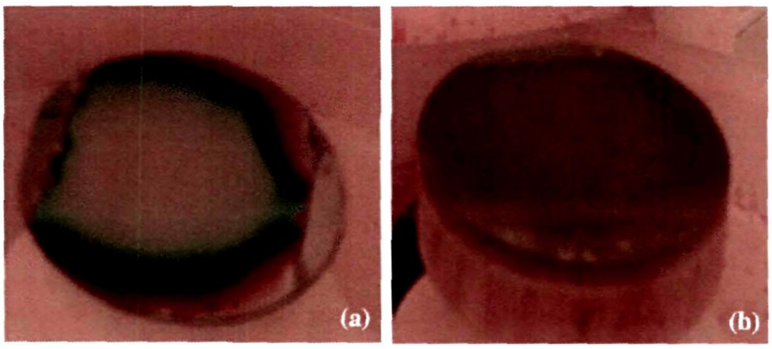

Fig-6.25: Photoresist on the sample (a) before spinning (b) after spinning

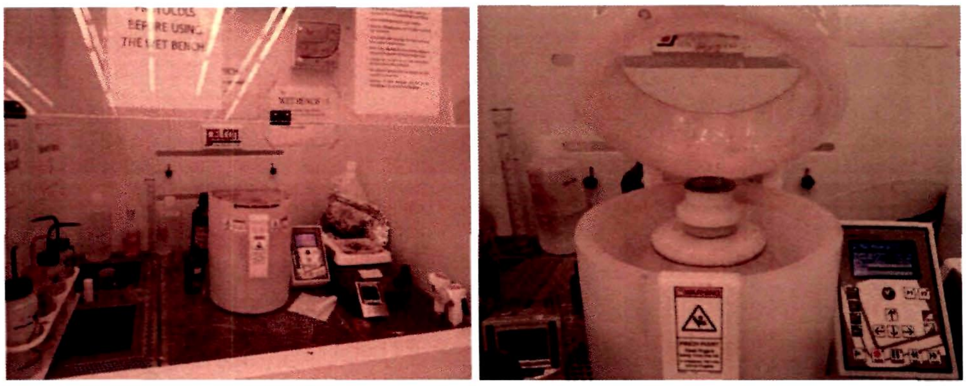

Fig-6.26: Wet Bench and Spin coater (Installed at CeNSE, IISc.)

6.2.6.2 Photolithography

Photolithography is the standard process to transfer a pattern that has been designed with computer-aided-engineering (CAE) software packages, on to a certain material (mask plate). The process steps involved in photolithography are resist coating, exposure, development, lift-off and etching etc. In the photolithographic process, a photoresist layer is spin-coated on to the material to be patterned. Next, the photoresist layer is exposed to ultraviolet (UV) light through the mask. This step is done in a mask aligner, in which mask and wafer are aligned with each other before the subsequent exposure step is performed. A mask with the desired pattern is created which is a glass plate with a patterned opaque layer (typically chromium) on the surface. Resist is coated on the waveguide substrate by a spinner. It is essential that the resist film coating is thin and as uniform and as free of pinholes as possible. The baking of the resist films has been done in an oven after coating to vaporize the solvent completely and to enhance adhesion to the substrate. Depending on the mask aligner generation, mask and substrate are brought in contact or close proximity (contact and proximity printing) or the image of the mask is projected (projection printing) on to the photoresist-coated substrate. Fig-6.27 shows the photograph of EVG Mask Alligner Photolithography Set-up installed at CeNSE, IISc., which is used for transfer of patterns to sample.

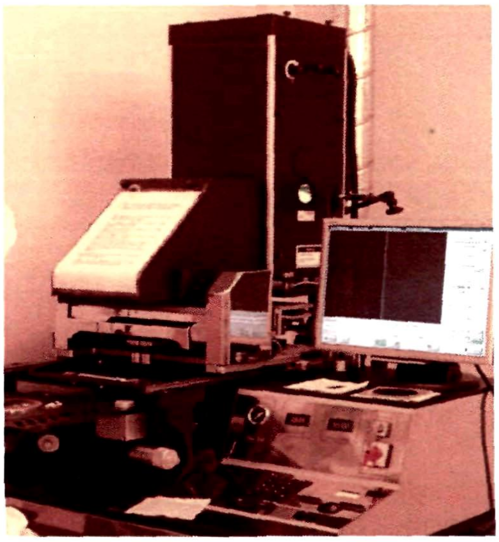

Fig-6.27: EVG 620 Mask Aligner Photolithography Set-up (CeNSE, IISc.)

Fig.-6.28 shows the basic steps of photolithography (positive) whereas the basic differences of positive and negative photolithography are shown in Fig.-6.29.

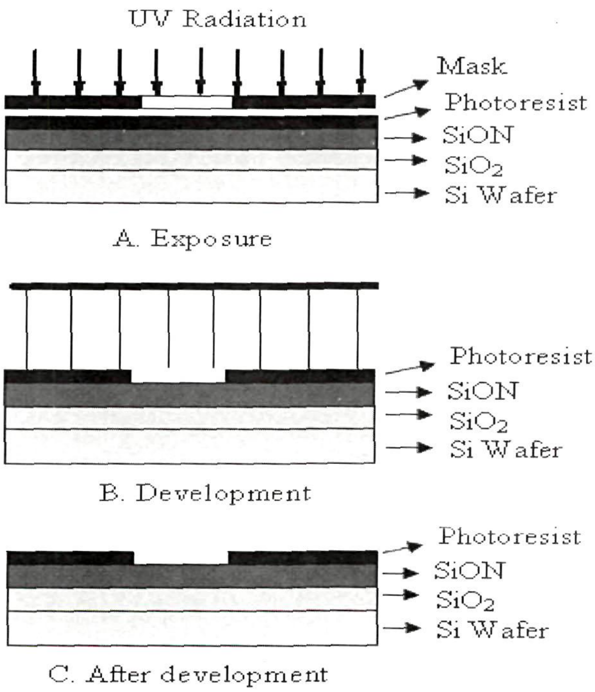

Fig.-6.28: Photolithography steps

Depending on whether positive or negative photoresist was used, the exposed or the unexposed photoresist areas, respectively, are removed during the resist development process. The remaining photoresist acts as a protective mask during the subsequent etching process, which transfers the pattern onto the underlying material. Alternatively, the patterned photoresist can be used as a mask for a subsequent ion implantation. After the etching or ion implantation step, the remaining photoresist is removed, and the next layer can be deposited and patterned.

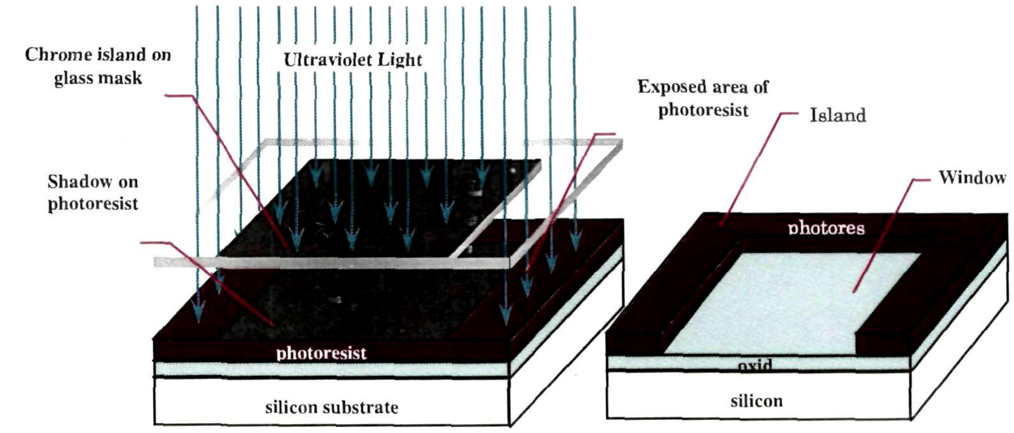

Fig.-6.29(a): Positive Photolithography

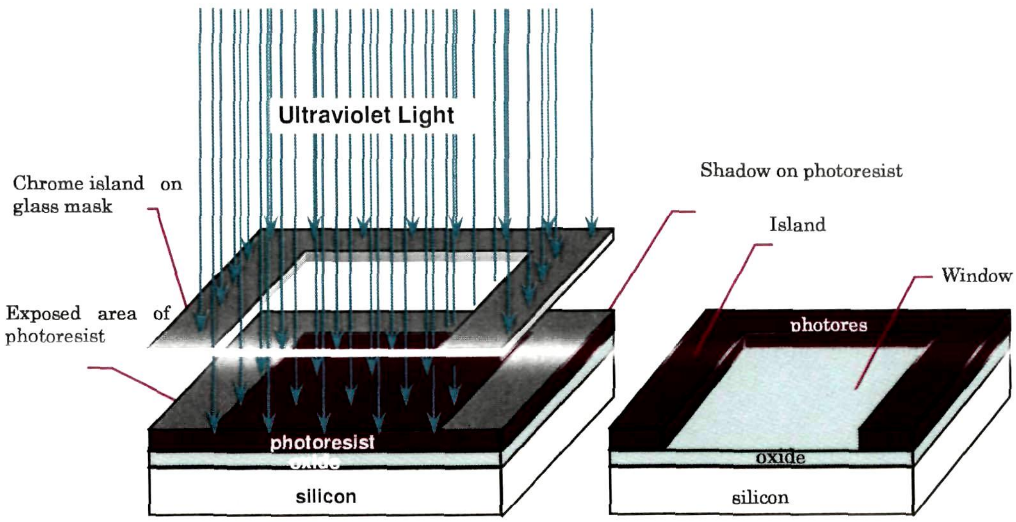

Fig.-6.29(b): Positive Photolithography (www.me.ccny.cuny.edu)

6.2.6.2.1 Mask Cleaning

The mask pattern made on the chromium (Cr) plate is cleaned using piranha solution (a mixer of H_2O_2 + H_2SO_4) before used in mask aligner system.

6.2.6.2.2 Alignment and Exposure

Before giving the exposure to the sample, proper alignment should be taken care off for the well matching of the alignment marks at the mask plate. The mask pattern was aligned upon wafer before transfer of the same using EVG-620 alignment set up as shown in Fig- 6.27. After soft baking (at 125^0 C for 30 sec), the mask pattern is transferred on wafer via exposure of UV light where they were aligned on the mask. The exposure time is optimized, during the experiment (~1.5 seconds) after the several iterations were made. Proper UV exposure time is essential to deliver light with the proper intensity, directionality, spectral characteristics and uniformity across the wafer.

6.2.6.2.3 Development and Post Baking

The photoresist (AZ315B) is developed in developer solution (MF26A) for 60 sec and then the sample is kept in oven for post baking at 125^0 C for 1 min in order to make further hardening of the exposed portion of photoresist.

6.2.6.3 Metallization

Material : Chrome (Cr) metal

Thickness: 150 nm-200 nm

Method : RF Sputtering/Thermal evaporation vacuum coating unit

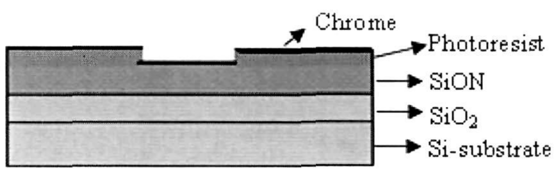

Metallization

Process Parameters:

RF power: 100 W

Ar flow rate: 200 sccm

O_2 flow rate: 20 sccm

The so-called *lift-off technique* is used to structure a thin-film material, which would be difficult to etch. Here, the thin-film material is deposited on top of the patterned photoresist layer. In order to avoid a continuous film, the thickness of the deposited film must be less than the resist thickness. In this regards, a chromium (Cr) metal layer of 150 nm thicknesses is deposited over the patterned wafer with the guiding layer using RF Sputtering unit. The total time taken for the deposition of chrome layer (thickness 150 nm) is ~ 2-3 hrs, whereas deposition rate is 1.25 nm/sec. The photograph of RF sputtering unit is shown in Fig-6.30 whereas Fig.-6.31 shows the window of process parameters respectively.

Fig.-6.30: RF sputtering unit (Installed at CeNSE, IISc.)

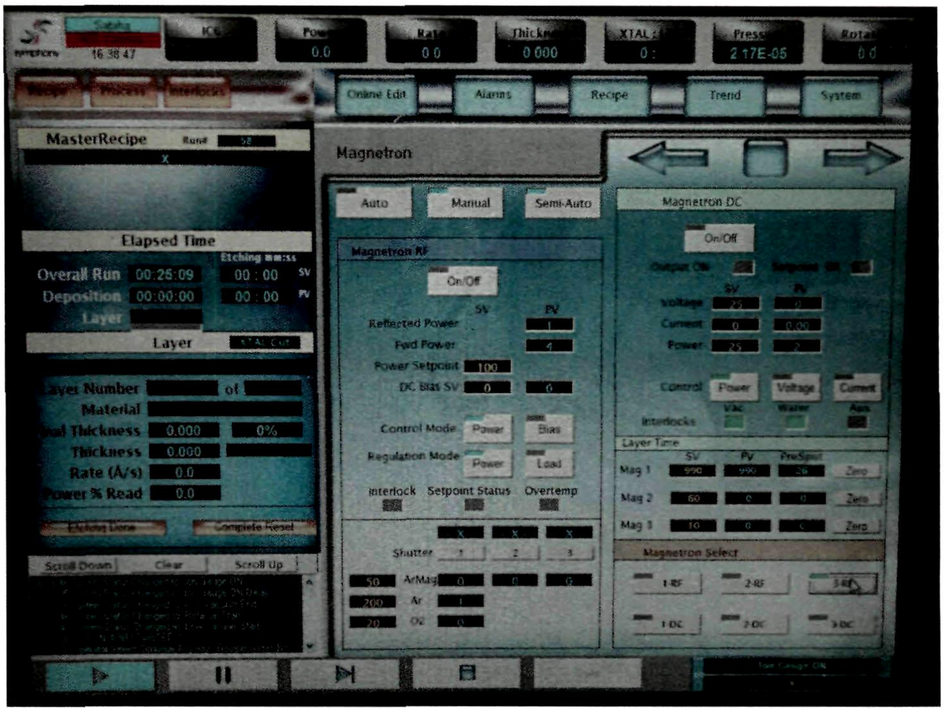

Fig-6.31: Process parameters used for Cr metallization

6.2.6.4 Lift-off Technique

The lift off technique is widely used for the patterning of relatively thin waveguide cores. After metal deposition on photoresist content surface of the wafer, it was kept in boiled acetone for 3 minutes. The metal was lift from the places where the photo resist was present because photo resist is soluble in acetone. By removing the underneath photoresist, the thin-film material on top is also removed by 'lifting it off', leaving a structured thin film on the substrate.

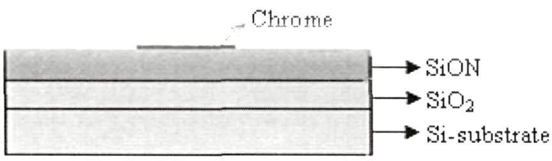

Lift-off

After the lift-off, the structures are verified with the help of optical microscope (shown in Fig.-6.32) before approaching to the further fabrication process. Fig-6.33 (a)-(c) shows the microphotograph of successful example structures whereas a few break/damage example structures are shown in Fig-6.34(a)-(c) respectively.

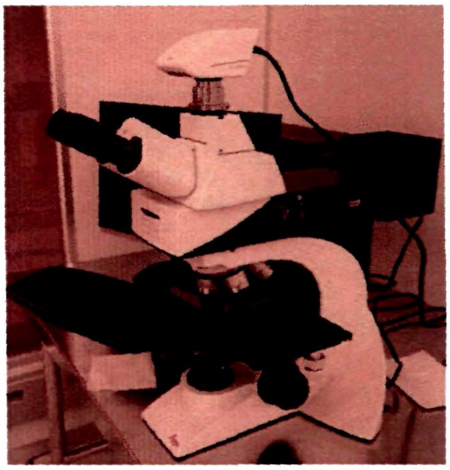

Fig-6.32: Optical Microscope (Model: Leika DFC290 at CeNSE, IISc.)

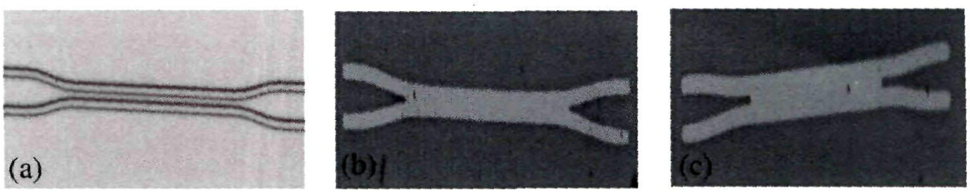

Fig-6.33: Microphotograph of successful lift-off structures (a) DC, (b) TMI coupler and (c) MMI coupler

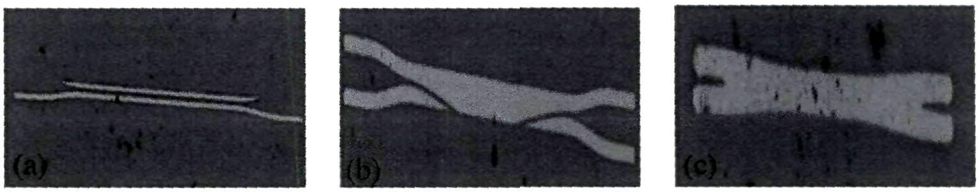

Fig-6.34: Microphotograph of failed lift-off structures (a) DC, (b) TMI coupler and (c) MMI coupler

6.2.6.5 Reactive Ion Etching

Reactive Ion Etching (RIE) is a dry etching technique which is used to selectively etch thin films in various device structures. The etching characteristic - selectivity, etch profile, etch rate, uniformity, reproducibility- can be controlled very precisely in the reactive ion etching. It involves a combination of both Physical Etching as well as Chemical Etching. Selection of an appropriate recipe (combination) of gases is an important issue. Typically the etch rates are slow and can be controlled by regulating parameters like the Electrode Bias, applied RF Power, Chamber pressure and flow rate of gases chosen in the recipe. RIE is capable of providing highly anisotropic profiles with reasonable selectivity. It is also possible to add custom recipes to etch new materials which are extremely useful for research purposes.

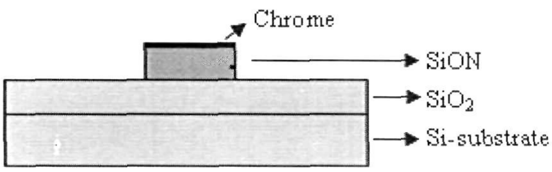

Reactive Ion Etching of SiON

Material to be etch	:	SiON
Thickness	:	1-2 μm
Method	:	F –based

Process Parameters:

RF power	: 50 W (Lower electrode)
ICP power	: 2500 W (Top)
Chamber Pressure	: 5 mTorr
SF_6 flow rate	: 9 sccm
CHF_3 flow rate	: 40 sccm
Etch rate	: 366 nm/min
Etch duration	: 6 minutes (for depth 2.2 μm)

For the RIE process, the etch rates of the SiO_xN_y films were determined first. The films were first etched separately and the etch rate of each film was determined. Following this, the patterned wafers were etched with an assigned time for the correct depth. Several issues were important for the etching processes: the side-wall anisotropy, side-wall roughness and grass formation. For the side-wall anisotropy, a mixture of tri-fluoromethane (CHF_3) and argon (Ar) were used as the process gas. With the above parameter specifications, the anisotropy and roughness were found to be within the limits of tolerance. In an RIE system, reactive ions are generated in plasma and are accelerated towards the surface to be etched, thus providing directional etching characteristics.

The basic reaction for the RIE of SiON can be written:

$$4CHF_3 + 2O_2 + 3SiON \rightarrow SiF_4 + CO_2 + 2H_2O + N_2$$

Fig.-6.35 shows the photograph of RIE system whereas the etch depth measurement result is shown in Fig.-6.37 obtained by using Dektak Set-up which is shown in Fig.-6.36 respectively.

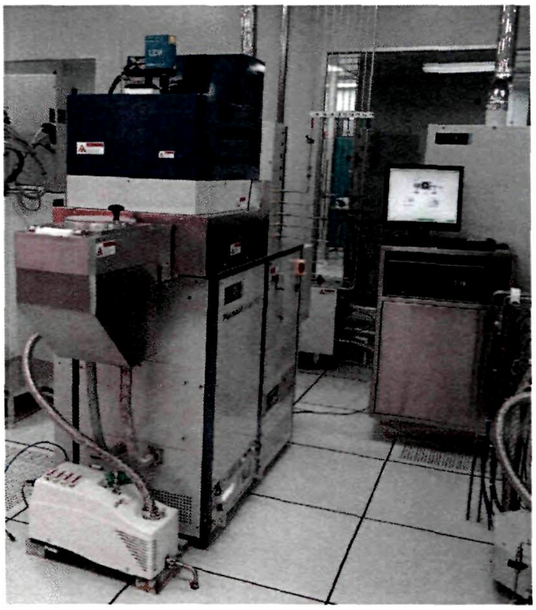

Fig-6.35: RIE Set-up, F based (PlasmaLabSys-Oxford Instrument System), CeNSE

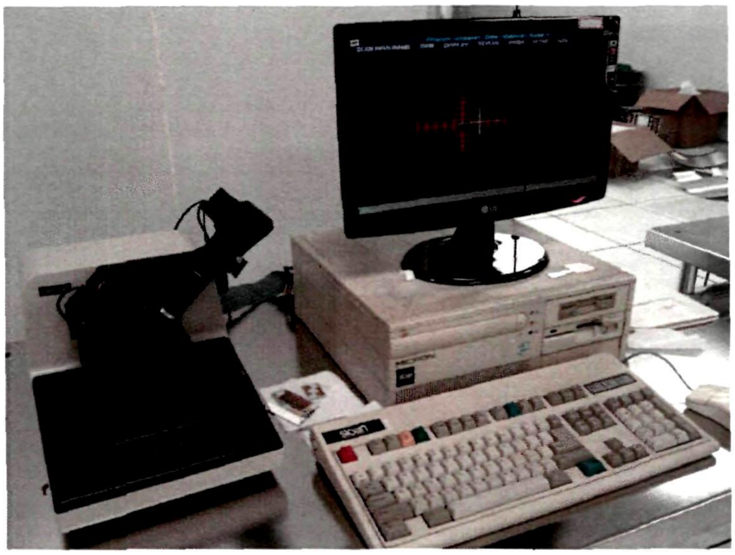

Fig.-6.36: Dektak Set-up for step height measurement (CeNSE, IISc.)

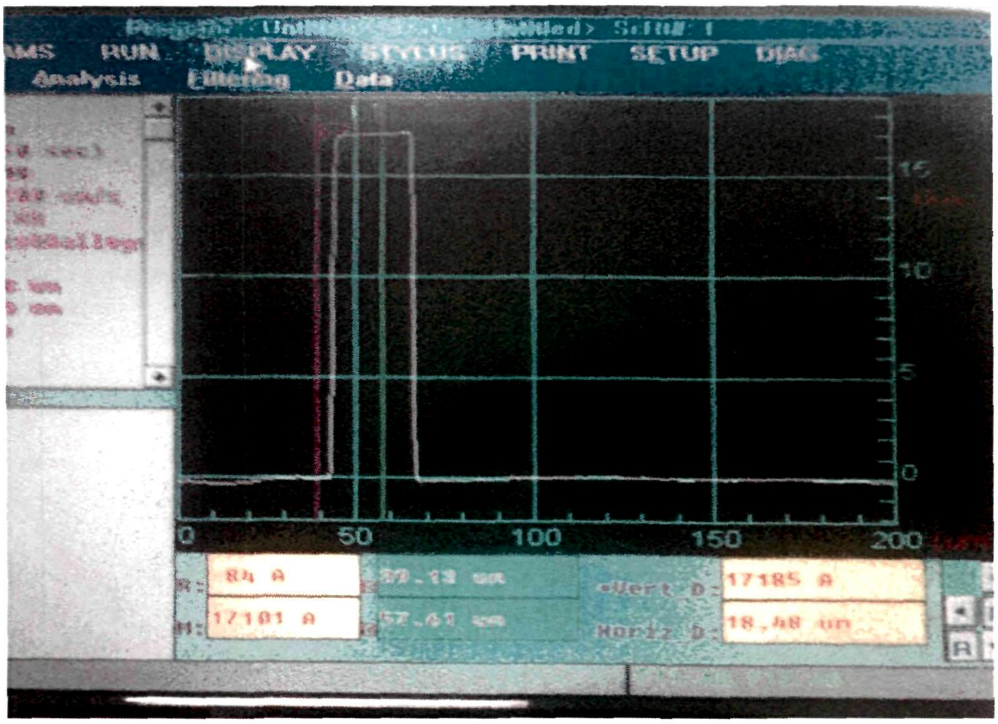

Fig-6.37: Step height measurement after RIE of SiON layer using Dektak system (depth~1.71 μm)

6.2.6.6 Wet Etching/RIE of Metallization (Cr) layer

Material to be etched : Cr

Thickness : 150 nm

Etchant used : $H_2O:H_2O_2$

Table-6.2: List of available etchants for wet etching

Concentrations	Etchants	Rate
2:3:12	$KMnO_4$: $NaOH:H_2O$	
3:1	$H_2O:H_2O_2$	
Concentrated and dilute	HCl	
3:1	$HCl:H_2O_2$	
2:1	FeCl: HCl	
	Cyantek CR-7s (Perchloric based)	7 min/μm
1:1	HCl: glycerine	12 min/μm after depassivation
1:3	[50g NaOH+100 ml H_2O]: [30g $K_3Fe(CN)_6$+100 ml H_2O]	

6.2.7 Deposition of Top Cladding

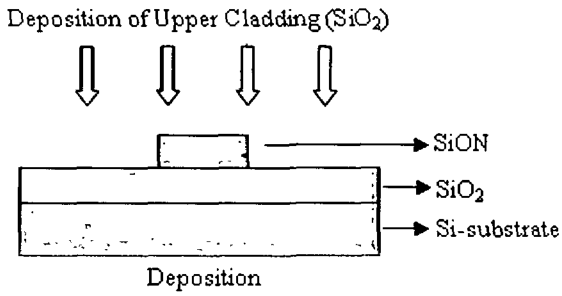

Material to be deposit : SiO_2

Thickness : 2-3 μm

Method : PECVD

The basic reaction for the formation of the silica (SiO_2) can be written as follows:

$$SiH_4\,(gas) + 4N_2O = SiO_2\,(solid) + 2H_2O\,(gas) + 4N_2\,(gas)$$

The top cladding layer of SiO_2 is deposited using PECVD set-up (as shown in Fig.-6.14) with the following process parameters and a layer of thickness~3 μm is achieved which takes around ~2 hrs for deposition process.

Process parameters used:

RF power @ 13.56 MHz	: 20 W
Pump pressure	: 1000 mTorr
Silane (SiH_4) flow rate	: 8.5 sccm
N_2O flow rate	: 710 sccm
N_2 flow rate	: 161 sccm
Substrate temperature	: 350^0 C
Deposition rate	: 1 μm/25 min

6.3. Fabrication of DC,TMI Coupler and MMI Coupler

As discussed in the chapter-3, the designed PID components– conventional directional coupler, two-mode interference coupler and multimode interference coupler are realized using the above mentioned fabrication techniques and process steps. Fabrication is carried out with the design parameter (for Δn=5%, n_1=1.5, n_2=1.45 and for Δn=3%, n_1=1.8, n_2=1.45, a=b=1.5 μm) as discussed in chapter-3 with SiON waveguide core surrounded by SiO_2 cladding layer. The flow chart of fabrication process steps is shown in the Fig.-6.39 whereas Fig.-6.38(a)-(c) shows the SEM images of fabricated device components, (a) Directional Coupler (DC), (b) Two Mode Interference (TMI) coupler and (c) Multimode Interference (MMI) coupler respectively. The measured experimental results are discussed in the proceeding sections.

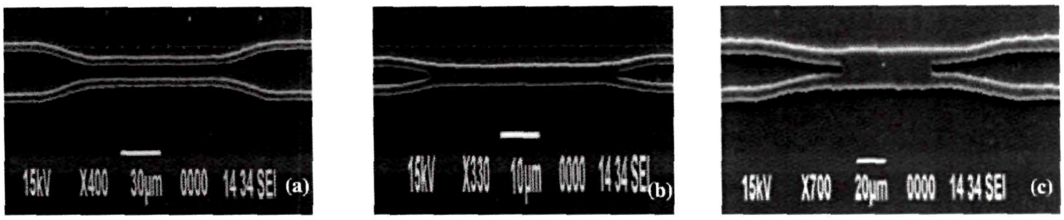

Fig-6.38: SEM images of fabricated (a) Directional Coupler (DC), (b) Two Mode Interference (TMI) coupler and (c) Multimode Interference (MMI) coupler

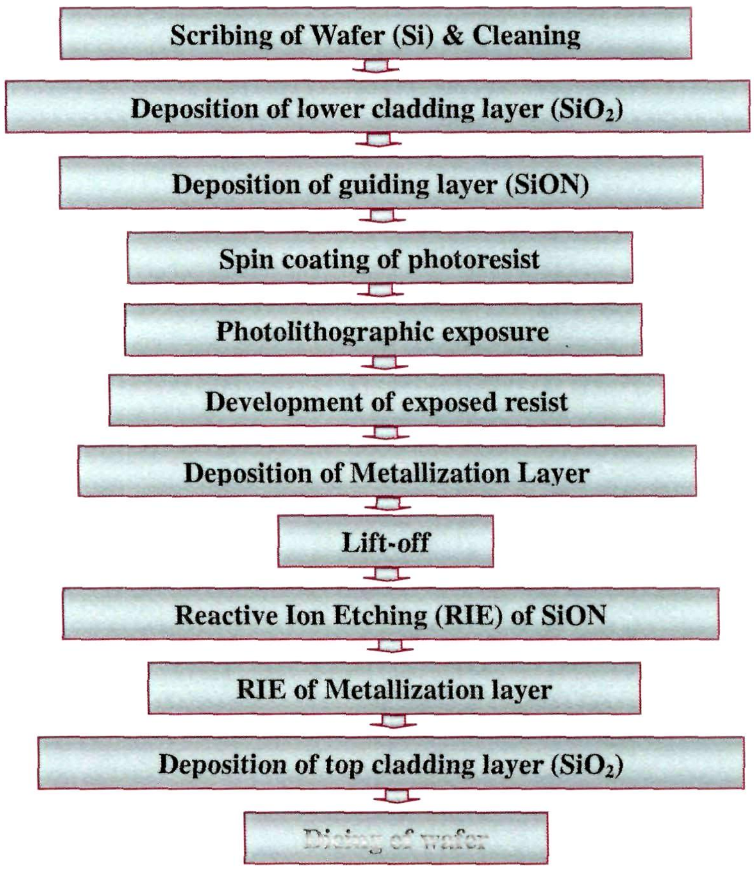

Fig-6.39: Flow chart of fabrication process steps

6.4. Experimental Set-up and Measurements

After the fabrication of the designed structures (as discussed in previous sections of the current chapter) of conventional directional coupler, two-mode interference coupler and multimode interference coupler with silicon oxynitride as the core material surrounded by silica cladding layer, the optical power loss measurement is execute for performance evaluation of the developed device components. After the dicing and polishing of waveguide end faces, optical loss characterization is done by end fire coupling method.

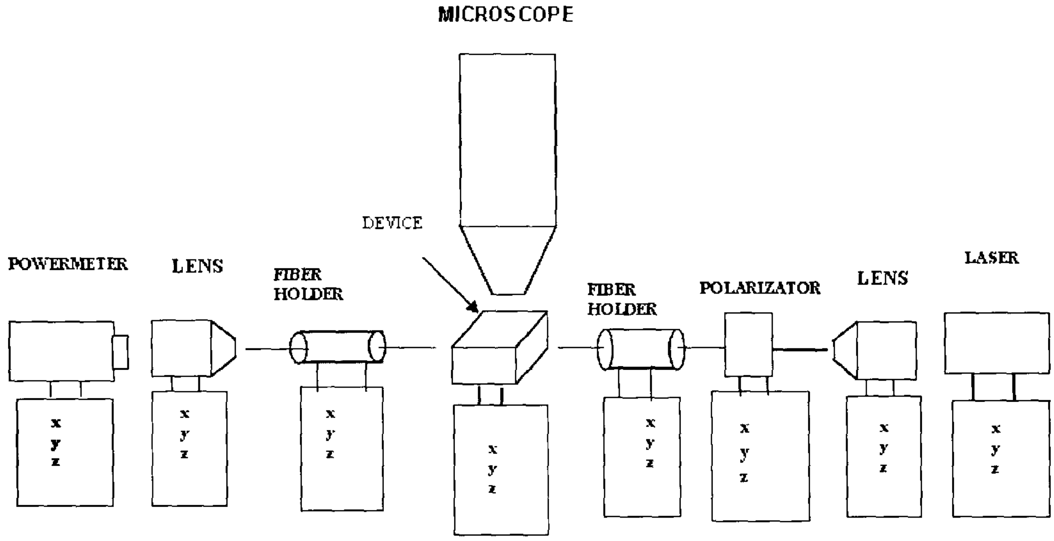

Fig-6.40: Schematic block diagram of a Power loss measurement set-up

Fig.-6.40 shows the schematic block representation of the experimental set-up that is used for measurement of power loss whereas the photograph of the developed measurement set-up in the laboratory is shown in Fig.-6.41. Helium Neon laser (He-Ne) is used as a source of light which is focused by using a focusing lens (10X and 20X) into an optical fiber with a polarizer that enable us to choose TE or TM polarized light. The transmitted light through the testing devices to the other end is measured using power sensor (Ge doped/Model: FieldMax II-VIS from Cohernt Inc.) attached to the Powermeter (Model: FieldMax II-TOP from Cohernt Inc.). The complete set-up is kept on the top of vibration free optical bread board of size (1 m x

1 m x 1 m). The measured experimental results are discussed later in this current chapter. For measurement of beam spot at the end waveguides, the powermeter with power sensor is replaced in the above set-up with a CCD camera. The measured field spots are also discussed later on.

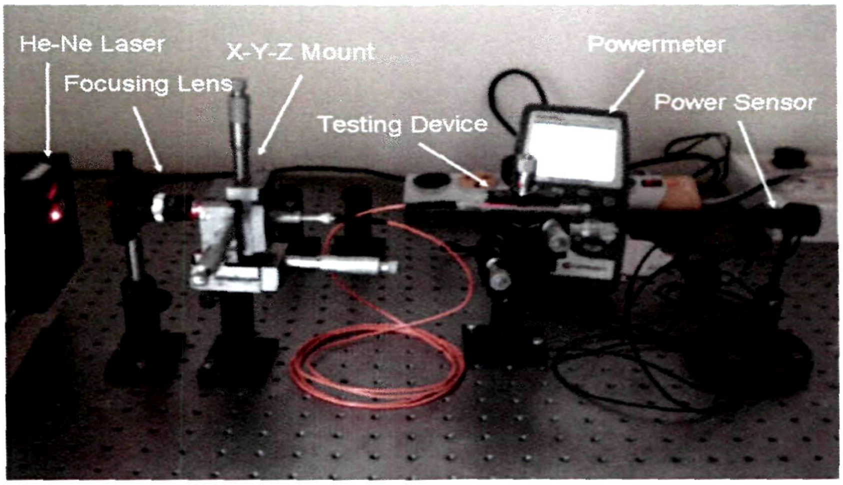

Fig-6.41: Power loss measurement set-up

6.5. Experimental Results and Characterization

The fabricated device components are studied for power loss characteristics with the help of developed power loss measurements set-up and also determined the power imbalance with respect to the width tolerances. The measured experimental results are compared with the results obtained (as in the chapter-3) by simple effective index method which is discussed in details as follows.

6.5.1 Coupling Characteristics of Directional Coupler with Δn=5 %

Fig-6.42 shows the normalized coupled power versus beat length with experimental measured results for DC of coupling gap h~0.5 μm, n_2=1.45, Δn=5 % and λ=1.55 μm. The black squares of the plot indicate the measured experimental results. From the plot, it is seen that the experimental measured results for the output powers at the output access waveguides (cross and bar states) are matching well with the results obtained by using SEIM. The inset images in the figure shows the SEM photograph of the fabricated conventional directional coupler of beat length~91.2 μm and the 3 dB coupler of beat length~45.4 μm respectively. The beam spot is taken at the cross output access waveguide at beat length~91.2 μm whereas the second image shows the beam spot at the bar state.

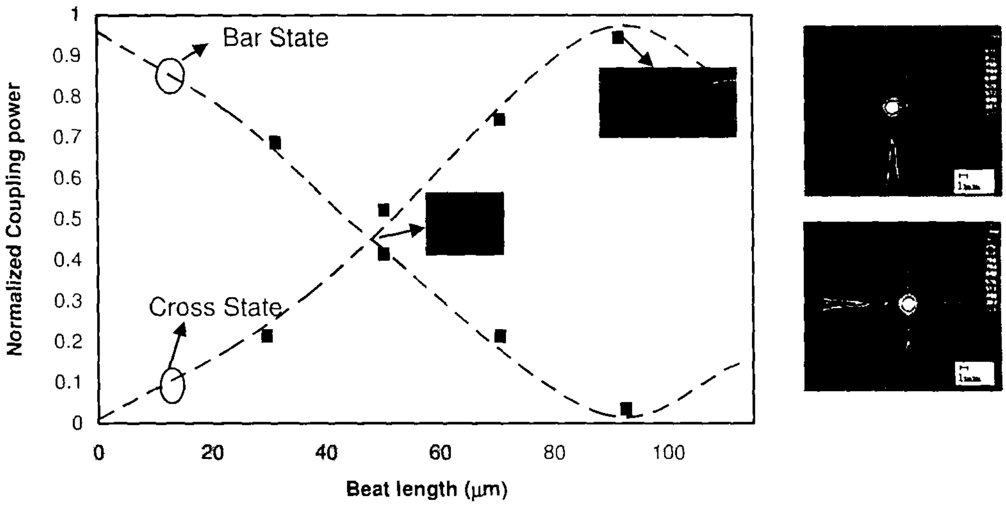

Fig-6.42: Normalized coupled power versus beat length with experimental measured results for DC of coupling gap h~0.5 μm, n_2=1.45, Δn =5% and λ=1.55 μm.

6.5.2 Coupling Characteristics of TMI Coupler with Δn=5%

Fig-6.43 shows the normalized coupled power versus beat length with experimental measured results for conventional TMI coupler. It is found that the beat length of the fabricated TMI coupler with Δn=5 % with h=0 μm, n_2=1.45, Δn=5 % are obtained as cross state~45.1 μm whereas 3 dB coupler of beatlength~22.6 μm respectively which are close to the results obtained by simple effective index method (SEIM) and beam propagation method (BPM). The black squares indicate the measured experimental results.

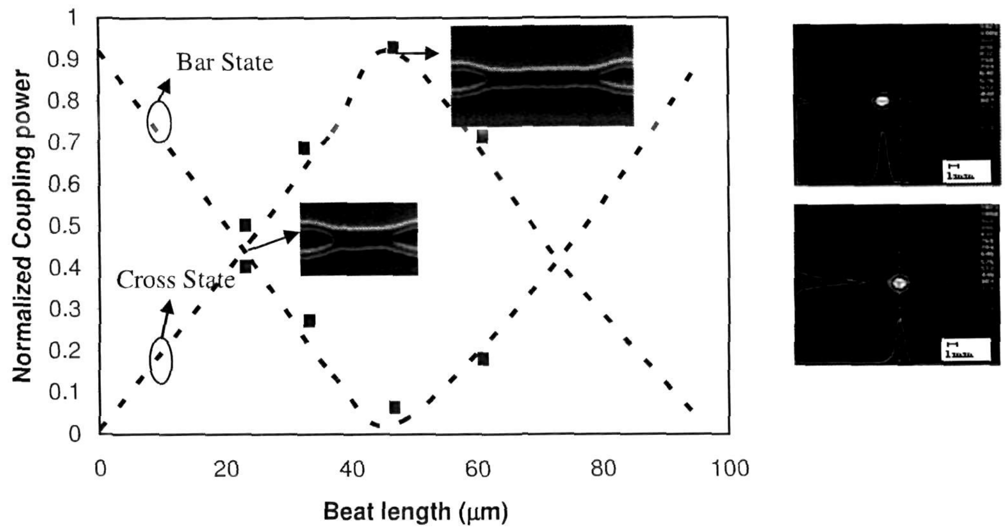

Fig-6.43: Normalized coupled power versus beat length with Δn=5 % for two mode interference (TMI) coupler with coupling gap h~0 μm, 2a=3 μm.

6.5.3 Coupling Characteristics of MMI Coupler with Δn=5%

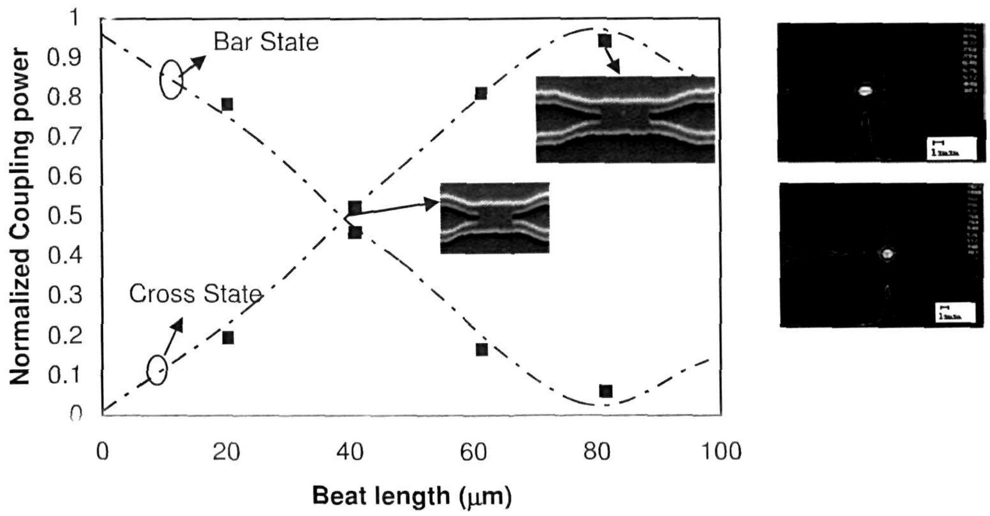

Fig-6.44: Normalized coupled power versus beat length with Δn=5% for multimode interference (MMI) coupler with coupling gap h~4 μm

Fig-6.44 shows the normalized coupled power versus beat length with experimental measured results for conventional MMI coupler. It is found that the beat length of the fabricated MMI coupler with Δn=5% with h=4 μm, n_2=1.45, Δn=5% are obtained as cross state ~79.9 μm whereas 3 dB coupler of beatlength ~ 40.1 μm respectively which are close to the results obtained by simple effective index method (SEIM) and beam propagation method (BPM) as details are discussed in chapter-3. The black squares of the plot indicate the measured experimental results.

6.5.4 Power Imbalance Characteristics DC, TMI Coupler and MMI Coupler

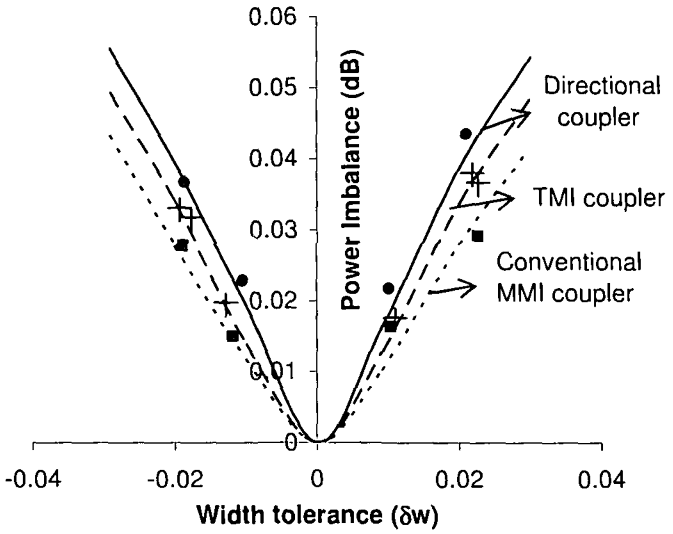

Fig-6.45: Power Imbalance characteristics versus width tolerances (δw) for conventional directional coupler (h~0.5 μm), conventional TMI coupler (h~0 μm) and conventional MMI coupler (h~4.0 μm), with index contrast ~5 %, cladding index~1.45, a=1.5 μm, b=1.5 μm and λ~1.55 μm respectively.

Fig-6.45 shows plot for power imbalance [=10 $\log_{10}$ (P_3/P_4)] versus fabrication tolerances (±δw) of conventional directional coupler (h~0.5 μm), conventional TMI coupler (h~0 μm) and conventional MMI coupler (h~4.0 μm) with index contrast ~5%, cladding index~1.45, a=1.5 μm, b=1.5 μm and λ~1.55 μm respectively. It is seen that the power imbalance increases with ±δw=0 μm symmetrically for both the structures and the increase of power imbalance for directional coupler is slightly more than that of conventional MMI coupler and TMI coupler. The cross, dot and square signs shows the respective experimental values which are closed to that of the theoretical results obtained by simple effective index method (SEIM) based on sinusoidal modes. The rate of increase of power imbalance (dB) with respect to width tolerance for conventional DC, TMI and MMI couplers are approximately obtained as $\frac{\partial}{\partial(\delta w)}$[Power Imbalance (dB)]~0.15 dB/μm, 0.18 dB/μm and 0.13 dB/μm respectively. It is also required to study the dependence of power imbalance on wavelength for conventional MMI coupler and tooth shaped grating assisted MMI coupler. Finally, an overall comparison of experimental results with the results obtained by simple effective index method (SEIM) is summarized in the Table-6.3.

Table-6.3: Comparison of SEIM results with fabricated results

Device Type	**Coupling Length (L_π), μm**			
	SEIM Result		**Experimental results**	
	Cross	**3 dB**	**Cross**	**3 dB**
Directional Coupler	91 μm	45.1 μm	91.2 μm	45.4 μm
TMI Coupler	45 μm	22.3 μm	45.1 μm	22.6 μm
MMI Coupler	80 μm	39.9 μm	79.9 μm	40.1 μm

It is found that the tolerances between experimental results with SEIM based theoretical results are within ~10%.

6.6. Conclusion

In this chapter the design device components such as directional coupler, two mode interference coupler and multimode interference coupler are studied experimentally and compare the measured results with the results obtained by using simple effective index method (SEIM) based on sinusoidal modes. The adopted fabrication process steps and techniques along with process parameters are also discussed in details. The fabrication process and most of the characterizations are carried out under INUP at the Center of Excellence in Nano Science and Engineering (CeNSE), Indian Institute of Science (IISc.), Bangalore. The experimental measurement (power loss) and FTIR analysis are carried out at Tezpur University. From these studies, it is found that the beat length of DC, TMI coupler and MMI coupler are ~ 91.2 μm, 45.1 μm and 79.9 μm respectively which are almost closed to that obtained theoretically as discussed in chapter-3. The deviations of experimental results are within 10% tolerance.

References

1. Runde, D, et al. Mode-selective coupler for wavelength multiplexing using $LiNbO_3$:Ti optical waveguides, *Cent. Eur. J. Phys.* **6**, 588-592, 2008
2. Rottmann, F., et al. Integrated-optic wavelength multiplerxers on lithium niobate based on two-mode interference, *J. of Lightwave Tech.* **6**, 946-952, 1988.
3. Lin, J.P., et al. Four-channel wavelength division multiplexer on Ti: $LiNbO_3$ *Electronics Lett.* **25**, 1608-1609, 1989.
4. Chin, M. K., et al., High-index-contrast waveguides and devices, *Appl. Opt.* **44**, 3077-3086, 2005.
5. Chan, H.P., et al. A wide angle X-junction polymeric thermo optic digital switch with low crosstalk, *IEEE Photonic Tech. Lett.* **15**, 1210-1212, 2003.
6. Worhoff, K., et al., Design, tolerance analysis and fabrication of silicon oxynitride based planar optical waveguides for communication devices, *J. of Lightwave Tech.* **17**, 1401-1407, 1999.

7. Bona, G. L., et al. SiON high refractive-index waveguide and planar lightwave circuit, *IBM J. Res. & Dev.* **47**, 239-249, 2003.
8. Miya, T. Silica-based planar lightwave circuits: passive and thermally active devices, *IEEE J. Sel. Topics Quantum Electron.* **6**, 38-45, 2000.
9. Levy, D. S., et al. Fabrication of ultracompact 3 dB 2x2 MMI power splitters, *IEEE Photonic Tech. Lett.* **11**, 1009-1011, 1999.
10. Yamada, H., et al. Si photonic wire waveguide devices, *J. of IEICE Trans. Electron.* **E90-C**, 59-64. 2007.
11. Kashahara, R, et al., New structures of silica-based planar light wave circuits for low power thermooptic switch and its application to 8x8 optical matrix switch, *J. Lightwave Tech.* **20**, 993-1000, 2002.
12. Mule, A.V., et al. Photopolymer-based diffractive and MMI waveguide couplers, *IEEE Photonic Tech. Lett.* **16**, 2490-2492, 2004.
13. Ibrahim, M. H., et al. A novel 1x2 multimode interference optical wavelength filter based on photodefinable benzocyclobuene polymer, *J. of Microwave and Optical Tech. Lett.* **49**, 1024-1028, 2007.
14. Chan, H.P., et al. A wide angle X-junction polymeric thermo optic digital switch with low crosstalk, *IEEE Photonic Tech. Lett.* **15**, 1210-1212, 2003.
15. Chen, K., et al., Silicon oxynitride optical waveguide ring resonator utilizing a two-mode interference structure, *Int. J. Photoenergy* **Dec**, 1-5, 2012.
16. Sahu, P. P. Silicon oxinitride: a material for compact waveguide device, *Indian J. Phys.*, **82**, 265-272, 2008.
17. Henry, C. H. et al., Low Loss Si_3N_4-SiO_2 Optical Waveguides on Si, *Appl. Opt.*, **26**, 2621–2624, 1987.
18. Das, A. K. and Sahu, P. P. Compact integrated optical devices using high index contrast waveguides in, *Proc. of IEEE International conference on Wireless and Optical Communication Network Conference,* Digital No-01666673, 1-5, 2006.
19. M.G. Hussein, M.G. et al. Stability of low refractive index PECVD silicon oxynitride layers, *Proceedings Symposium IEEE/LEOS Benelux Chapter*, 77-80,

2003.

20. Naskar, S *Deposition and Characterisation of Silicon Oxynitride material for the Fabrication of Optical Waveguides*, Ph. D. thesis, Case Western Reserve University, 2006.
21. Nishihara, H., Haruna, M., & Suhara, T. *Optical Integrated Circuits*, McGraw-Hill, New York, 1989.
22. Gandhi, S. K. *VLSI Fabrication Principles: Silicon and Gallium Arsenide*, Willey-India, New Delhi, 2008.

****

Chapter-7:

Double S-Bend Geometry for Compact MMI Coupler

Introduction

Mathematical Model of Double S-bend structure for Multimode Interference Couplers

Results and Discussion

Conclusion

7.1. Introduction

Although grating assisted tooth shaped geometry provides lower coupling length than that of conventional structures such as TMI and MMI couplers of Photonic Integrated Devices (PID) due to having more number of multiple reflections in grating assisted tooth shaped (GATS) structures; GATS structure shows more radiation losses in the coupling region due to having large number of grating period. It is also seen in chapter-5 that overall length (L_π+2L_T) of multimode interference (MMI) coupler including coupling length (L_π) and longitudinal access waveguide length (L_T) is less than that of two mode interference (TMI) coupler as L_T of MMI coupler is lower than that of TMI coupler for a bending loss of 0.1 dB [1]. From the previous works [2]-[5], it is also found that the tapered structures of MMI coupler provides lower coupling length but there is radiation loss due to the leakage of higher order modes at tapered portion of the structure. It is seen in chapter-6 that the fabrication of grating assisted geometries require higher resolution fabrication process and techniques. So much effort should be given to reduce the coupling length by using other possible design structures such as double S-bend structure [6]-[7]. On the other hand, optical guided-wave devices often contain tapered structures [8]-[12] to achieve a highly efficient power coupling between two different optical devices.

In the current chapter, a double S-bend structure based on general interference has been proposed for MMI coupler. The proposed structure has been designed and implemented by using silica waveguides with SiON core for reduction of device length. The coupling characteristics of the proposed double S-bend MMI (DB-MMI) structure is compared with conventional MMI structure. The optimal value of the longitudinal access waveguide length and beat length for the double S-bend assisted MMI (DB-MMI) coupler is also determined and compared with the previous results for double S-bend TMI (DB-TMI) coupler [6]-[7]. The fabrication tolerance and its effect on power imbalance of the proposed tapered MMI coupler are studied and compared with other tapered MMI couplers [3]-[4].

7.2. Double S-Bend

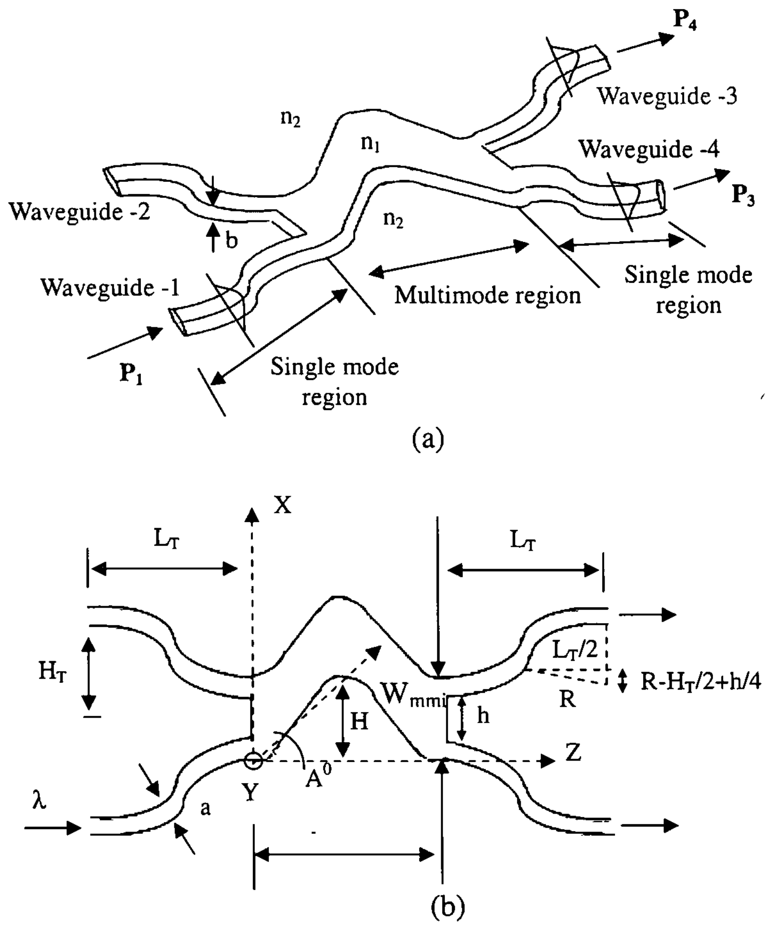

Fig.-7.1: 2x2 double S-bend MMI coupler with bending angle A^0, width W_{mmi}, access waveguide width a and thickness b (a) 3D view (b) 2D MMI structure containing x and z axis

Fig-7.1(a) shows the schematic 3D view of a double S-bend MMI (DB-MMI) coupler consists of a double S-bend coupling region of longitudinal length, L and width, W_{mmi}=2a+h (where h is the gap between two access waveguides near to MMI region and a=width of access waveguide), two single mode S-bend input access waveguides (Waveguide-1 and Waveguide-2) of core width a, thickness b and two output S-bend access waveguides (Waveguide-3 and Waveguide-4) of same core size respectively. The height (H) and longitudinal coupling length (L) of S-bend structure in double bend MMI (DB-MMI) coupling region is S sin A and S cos A respectively (where *S* is S-bend length, *A* is angle made by S-bend with *Z*-direction). The refractive index of core and surrounding cladding layer are n_1 and n_2 respectively. When the input power P_1 is launched into lower most input S-bent access waveguide, the output powers P_3 and P_4 are obtained as bar state power and cross state power respectively.

Fig-7.1(b) shows the 2D view of the double bend MMI (DB-MMI) coupler as shown in Fig-7.1(a). Since the lateral dimension (along x-axis) in DB-MMI region is ~ more than two times larger than the transverse dimension (along y-axis) as shown in Fig.-7.1(b) and transverse dimension b is chosen to be for single mode normalized frequency V≤2.3 [where, $V = (2\pi b\sqrt{n_1^2 - n_2^2})/\lambda$], the waveguide structure is to be single mode in transverse direction and has the same transverse behavior everywhere in the MMI region. So it is assume that the modal analysis can be studied by using two dimensional (2D) structures in which lateral (along x-axis) and longitudinal (along z-axis) characteristics are considered. The input field profile H(x, 0), incident on DB-MMI coupler is composed of mode field distribution of all excited modes and represented in 2D approximation as follows,

$$H(x,0) = \sum_{i=0}^{r-1} b_i H_i(x) \tag{7.1}$$

where i=0, 1, 2,....(r-1) denotes the order of guided modes and b_i = i^{th} mode field excitation coefficient of DB-MMI coupler. The mode excitation coefficients are evaluated from Fourier series coefficients of odd periodic functions. $H_i(x)$ is mode field distribution of i^{th} order mode of DB-MMI region at z=0. Based on the phase differences of excited modes at the end of the coupling region, the optical power is either transferred to the output waveguides or lost out at the end of multimode channel waveguide. Again the mode fields at the output access waveguides of width a, thickness b are assumed to be single mode where only fundamental mode is excited. The composite mode field of the output waveguides is the sum of the contribution of all the modes guided in DB-MMI section which can be express as,

$$H_M(x,z)=\sum_{i=0}^{r-1} H_{M,i}(x,L.\sec A)=\sum_{i=0}^{r-1} C_{M,i}\, H_i(x)\times \exp[j(\beta_0-\beta_i)\,L.\sec A]\; e^{-2\alpha L\sec A} \quad (7.2)$$

where α is the bending loss coefficient depends on bending angle A [7], [13] and $C_{M,i}$ is the field contribution coefficient of i[th] mode for M-th output access waveguide (M=3 for the 3[rd] access waveguide and M=4 for the 4[th] access waveguide), that determined by using simple effective index method (SEIM) based on sinusoidal modes [14]-[17] as discussed in the chapter-3. The β_0 and β_i are propagation constants of zero[th] (fundamental) mode and i[th] order mode respectively.

The normalized coupled power transferred to the 3[rd] and 4[th] output access waveguides can be define as,

$$\frac{P_3(x,L)}{P_1(x,0)}=\left|\frac{H_{1,i}(x,L.\sec A)}{H_{1,i}(x,0)}\right|^2 \quad (7.3)$$

$$\frac{P_4(x+a+h,L)}{P_1(x,0)}=\left|\frac{H_{2,i}(x+a+h,L.\sec A)}{H_{1,i}(x,0)}\right|^2 \quad (7.4)$$

where,

$$H_1(x,L.\sec A)=\sum_{i=0}^{r-1} C_{3,i}\, H_i(x)\times \exp[j(\beta_0-\beta_i)\,L.\sec A]\; e^{-2\alpha L\sec A} \quad (7.5)$$

$$H_2(x+a+h,L.\sec A)=\sum_{i=0}^{r-1} C_{4,i}\, H_i(x+a+h)\times \exp[j(\beta_0-\beta_i)\,L.\sec A]\; e^{-2\alpha L\sec A} \quad (7.6)$$

The $C_{3,i}$ and $C_{4,i}$ are the field contribution coefficients of i[th] mode for output access waveguide-3 (M=3) and waveguide-4 (M=4) respectively which are determined by using simple effective index method (SEIM) based on sinusoidal modes as discussed in chapter-3 with a consideration $n_3 \to n_1$ ($h \neq 0$), we have

$$\frac{C_{M,i}}{C_0}\approx\frac{\pi^2}{16b^2k^2(n_1^2-n_2^2)}\times\exp\left\{-hk\left(n_{eff}^2-n_2^2\right)^{1/2}\right\}\times\left[\exp\left\{bk\left(n_1^2-n_2^2\right)^{1/2}\right\}-\exp\left\{-bk\left(n_1^2-n_2^2\right)^{1/2}\right\}\right] \quad (7.7)$$

where for TE mode,

$$C_0 = \frac{0.4}{F_C} \times \frac{\left(n_1^2 - n_{eff(TE)}^2\right)\sqrt{n_{eff(TE)}^2 - n_2^2}}{n_{eff(TE)}\left(n_1^2 - n_3^2\right)\left[W_{mmi} + \dfrac{2}{k_0\sqrt{n_{eff(TE)}^2 - n_2^2}}\right]} \tag{7.8}$$

$$F_c = \frac{3(1 + 0.2h)}{\{13.5 + 185\,(\beta_0 - \beta_t)\}h} \tag{7.9}$$

$$n_{eff\,(TE)} = \beta_{TE\,(t)}\left(\frac{\lambda}{2\pi}\right) \tag{7.10}$$

Similarly, for TM mode,

$$C_0 = \frac{0.4}{F_C} \times \frac{\left(n_1^2 - n_{eff(TM)}^2\right)\sqrt{n_{eff(TM)}^2 - n_2^2}}{n_{eff(TM)}\left(n_1^2 - n_3^2\right)\left[W_{mmi} + \dfrac{2}{k_0\sqrt{n_{eff(TM)}^2 - n_2^2}}\right]} \tag{7.11}$$

$$F_c = \frac{3(1 + 0.2h)}{\{13.5 + 185\,(\beta_0 - \beta_t)\}h} \tag{7.12}$$

$$n_{eff\,(TM)} = \beta_{TM\,(t)}\left(\frac{\lambda}{2\pi}\right) \tag{7.13}$$

As shown in Fig.-7.1(b), the transition length (L_T) of the S-bend access waveguide (along z direction) can be obtained as follows,

$$L_T = \sqrt{\left(H_T - \frac{h}{2}\right)\left[4R + \frac{h}{2} - H_T\right]} \tag{7.14}$$

$$R^2 = \left(\frac{L_T}{2}\right)^2 + \left(R - \frac{H_T}{2} + \frac{h}{4}\right)^2 \tag{7.15}$$

where R, H_T and h are the bending radius, height and coupling gap between two access waveguides respectively. The double S-bend loss (T_s) in dB for the DB-MMI region can be approximated as

$$T_S = 4.343\alpha L\sec(A) \tag{7.16}$$

where α is the bending loss coefficient that depends on bending angle A and propagation constant (β).

7.2.1 Coupling Characteristics of DBMMI Coupler

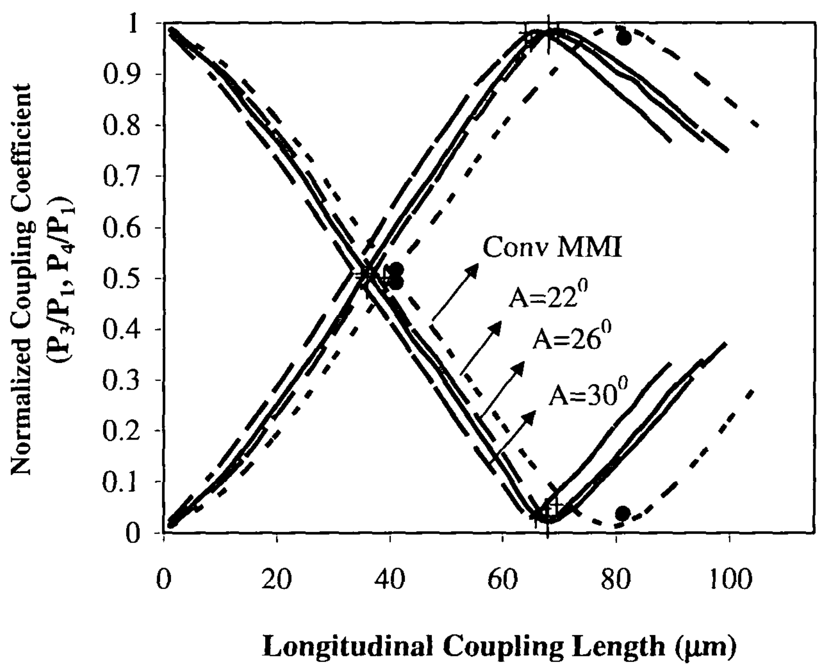

Fig.-7.2: Normalized Coupling Power characteristics vs Longitudinal Beat Length of double S-bend multimode interference coupler (dashed lines) with bending angle A=22^0, 26^0, 30^0 and conventional MMI coupler (A=0^0, dotted line) for h=4 μm, a=b=1.5 μm, wavelength~1.55 μm, cladding index~1.45 and Δn~5% respectively.

Fig-7.2 shows the normalized coupling power distribution (P_4/P_1 and P_3/P_1) versus longitudinal coupling length (L^1_π) of TE polarization determined by using (7.1) and (7.3)-(7.10) for the proposed DB-MMI coupler with different bending angles, A=22^0, 26^0 and 30^0 for h=4 μm, a=b=1.5 μm, wavelength=1.55 μm, cladding index=1.45 and Δn=5% respectively. The normalized coupled power distributions of conventional MMI coupler ($A=0^0$) is also estimated and represented by dotted line in the figure. The black dot and cross signs in the figure represents the experimental points (which is discussed later in section-7.4) for conventional MMI coupler ($A=0^0$) and DB-MMI coupler ($A=26^0$) respectively, matching well with theoretical curves. It is found that the longitudinal beat lengths (L^1_π) for conventional MMI and proposed DB-MMI structure are ~80 μm and ~67 μm respectively. It is observed (not shown in the figure) that for TM mode, the theoretical value of longitudinal beat length (L^1_π) is estimated as ~83.08 μm which is 0.24 % more than that of TE mode for the proposed structure showing the polarization independent characteristics. It is also found that the number of guided modes in DB-MMI region of width (2a+h)=7 μm is eight. In the figure, the peak normalized coupling power in case of the DB-MMI coupler decreases with bending angle (A). This is due to radiation loss at the S-bending region of the proposed structure and as bending angle increases, the bending radiation loss increases. It is seen from the figure that the peak coupling power for DB-MMI coupler with $A=26^0$ is close to that with $A=30^0$. So we have chosen $A=26^0$ for further study of DB-MMI coupler.

7.2.2 Beat Length of DBMMI Coupler

The longitudinal beat length of the proposed DB-MMI coupler with $A=26^0$ is ~67 μm which is 19% less than that of conventional MMI coupler. We have also estimated light propagation which is obtained by using optiBPM software (version 9.0) for DB-MMI coupler with $A=0^0$ (conventional), 22^0, 26^0 and 30^0 as shown in Fig-7.3. It is seen from the figure that the longitudinal beat lengths of DB-MMI coupler with $A=0^0$, 22^0, 26^0 and 30^0 are obtained as ~80 μm, 69 μm, 67 μm and 65.2 μm respectively which are almost close to those obtained theoretically from coupling characteristics obtained by SEIM based on sinusoidal modes as shown in Fig-7.2. It is also confirmed from the figure that the bending loss in conventional MMI coupler is lower than that of the proposed DB-MMI coupler but the bending loss for DB-MMI coupler with $A=22^0$ is close to that with $A=26^0$.

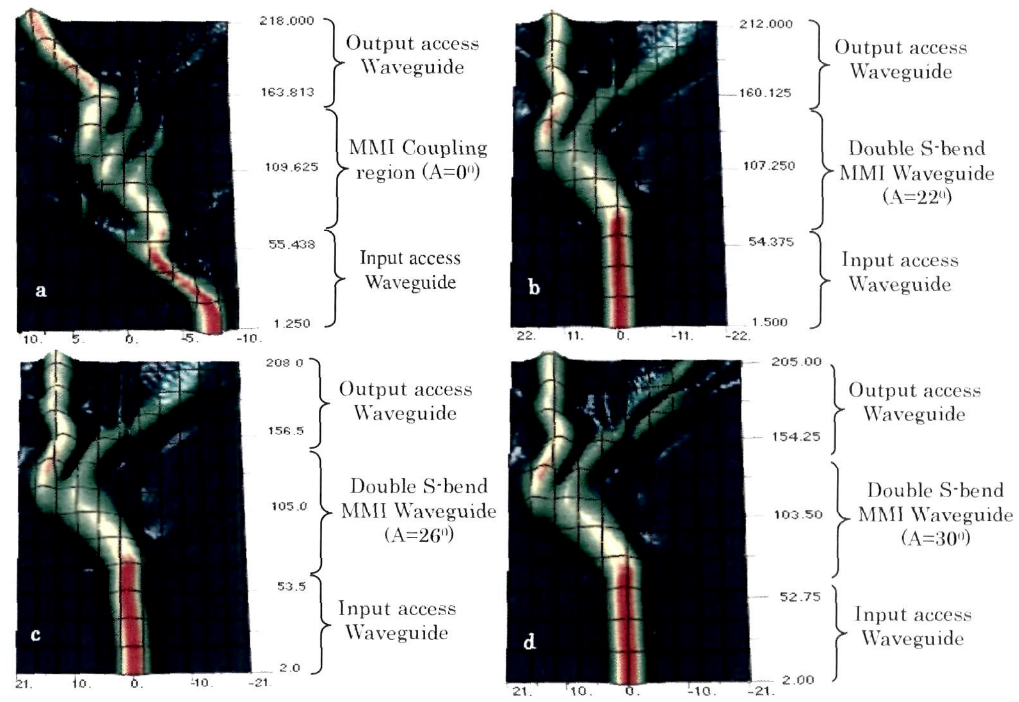

Fig-7.3: Beam propagation results of DB-MMI coupler with $W_{mmi}=7$ μm, a=b=1.5 μm, $\lambda=1.55$ μm, $n_2=1.45$ and $\Delta n=5$ % for (a) conventional ($A=0^0$), (b) $A=22^0$, (c) $A=26^0$ and (d) $A=30^0$ respectively.

7.2.3 Double S-Bend Loss

Fig.-7.4 shows the S-bend loss versus H obtained by using (7.14)-(7.16), (where H is height of S-bend in MMI region) for fundamental mode and higher order modes which are excited in MMI region of the proposed structure with $A=26^0$, h=4 μm, a~1.5 μm, wavelength~1.55 μm, cladding index~ 1.45 and Δn~5 % respectively. It is seen that S-bending loss for fundamental mode is lowest whereas that for the higher order mode is highest. This is due to more confinement of fundamental mode than higher order modes. Since the fundamental mode carry most of the power in MMI region, higher bending loss of higher order mode will not contribute much in the overall bending loss in comparison to TMI coupler. It is also seen that the double S-bend loss increases with H and almost saturates at H =11.5 μm. So we have chosen H =11.5 μm.

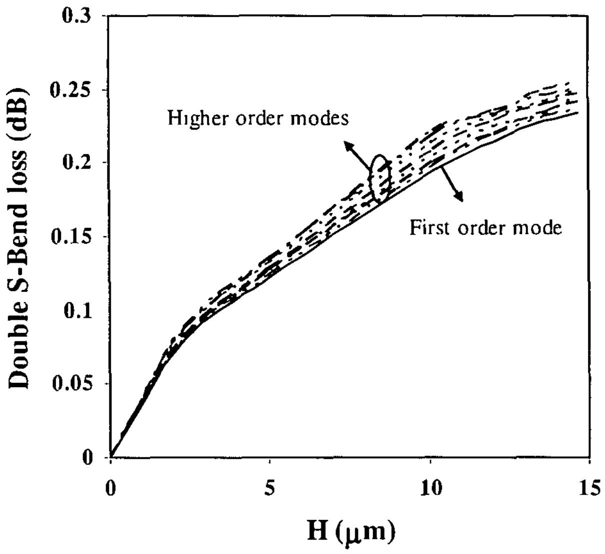

Fig.-7.4: Double S-Bend loss versus H of the proposed DB-MMI structure with bending angle A=26^0 for h=4 μm, a=b=1.5 μm, cladding index~1.45 and Δn~ 5%.

7.2.4 Fabrication Tolerances and Polarization Dependence of DBMMI Coupler

Since realization of designed device structure with the exact designed parameters is tricky, it is necessary to study its performance degradation with an unwanted deviation of waveguide parameters during fabrication process. Fig.-7.5 shows the plot of power imbalance in dB [=10 log10(P_3/P_4)] versus fabrication tolerance (± δw) of double bend MMI width obtained by using the equations (7.3) and (7.4) with a=b=1.5 μm, index contrast~5 % and cladding index~1.45 for 3dB conventional MMI coupler of L_π/2~40 μm, 3dB parabolic tapered structure [3] of

$L_\pi/2$~23 μm, 3dB tooth shaped grating assisted MMI coupler [1] with $L_\pi/2$~20 μm, 3dB proposed DB-MMI coupler of $L_\pi/2$~33.5 μm and A=26^0. In all cases, a minimum value of power imbalance is obtained at δw=0 μm.

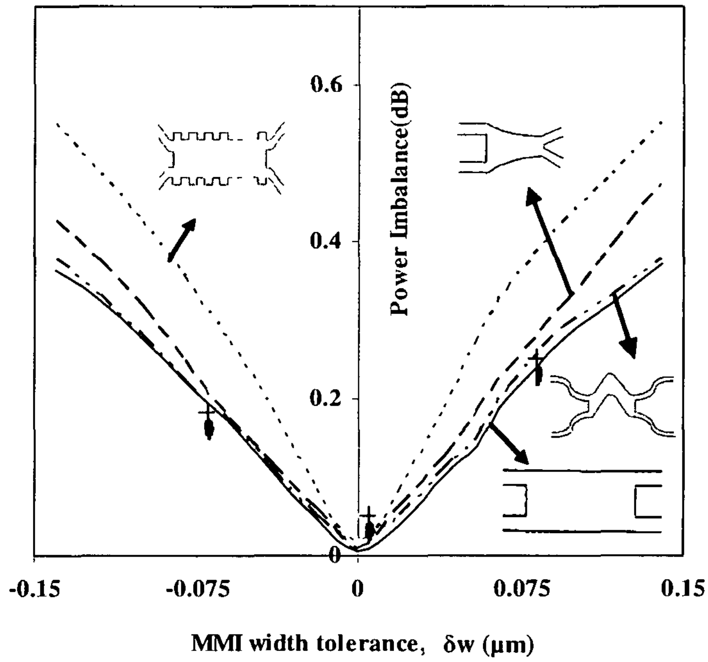

Fig.-7.5: Power imbalance characteristics versus MMI width tolerance (δw) for conventional (solid line), proposed structure and parabolic tapered (at the middle) 3dB MMI coupler with cladding index~1.45, h~4 μm, Δn~5%, a=b=1.5 μm and wavelength~1.55 μm. (•)- experimental point of 3dB conventional MMI structure, (+)- experimental point of the proposed 3dB DS-MMI coupler with A=26^0.

Although the longitudinal coupling length of tooth shaped grating assisted structures [1], [18]-[19] is lower than that of the proposed structure, the increase of power imbalance in the former case [18][19] is more than that of the proposed DB-MMI structure due to having more number of designed parameters. The rate of increase of power imbalance with respect to MMI width tolerance $\frac{\partial}{\partial(\delta w)}$ [Power

Imbalance (dB)] for GA-MMI coupler, conventional MMI coupler, DBMMI coupler are approximately obtained as 0.18 dB/μm, 0.26 dB/μm and 0.25 dB/μm respectively. The black dots and cross signs in the figure represents experimental points (which is discussed later in the section-7.4) of conventional and the proposed structure respectively, that matches well with theoretical curves.

Fig-7.6 shows power imbalance versus wavelength for a~1.5 μm, b~1.5 μm, h~4.0 μm, A=26^0, index contrast ~5 % and cladding index~1.45 respectively. In the figure, the dotted line indicates the curve for 3 dB DB-MMI coupler of coupling length ~33.5 μm and the solid line shows for 3 dB conventional MMI coupler of coupling length ~40 μm.

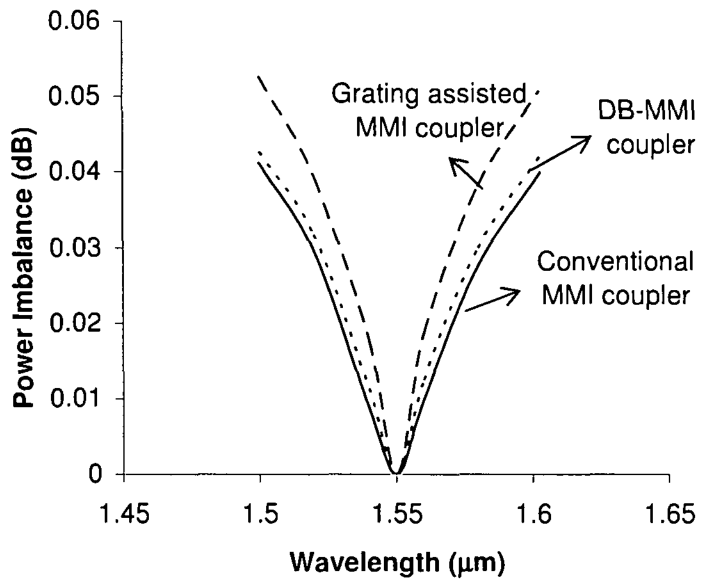

Fig-7.6: Power Imbalance characteristics versus wavelength variation for double band assisted MMI coupler (dotted line), tooth shaped grating assisted MMI coupler (dashed line) and conventional MMI coupler (solid line) with a=1.5 μm, b=1.5 μm, h~4.0 μm, A=26^0, index contrast ~5 % and cladding index~1.45.

It is observed from the plot that in both cases minimum power imbalance is obtained at λ~1.55 μm and it is symmetrically increased in both sides of λ~1.55 μm. The increase of power imbalance for double band MMI coupler is sharp in comparison conventional MMI coupler. The dashed line in the figure represents the variation of power imbalance versus wavelength for GA-MMI coupler. The dependence of power imbalance on fabrication tolerance and wavelength for DB-MMI coupler is almost close to that for conventional MMI coupler.

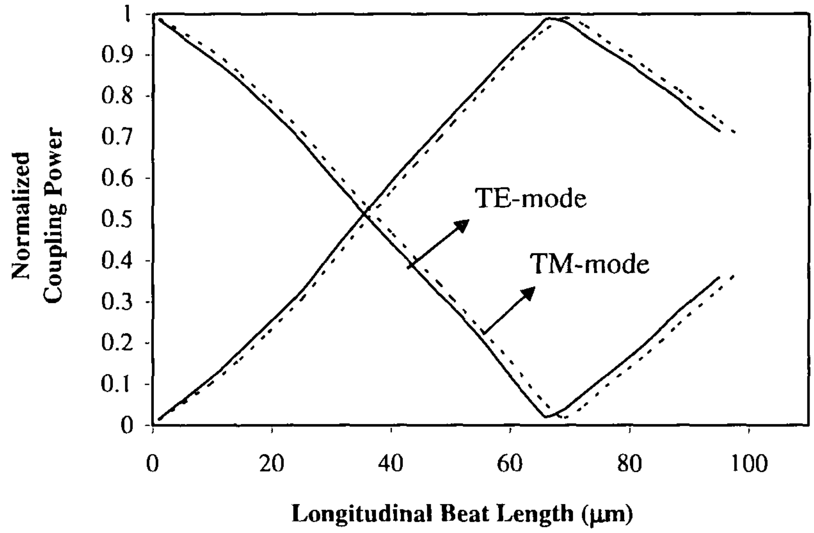

Fig-7.7: Normalized coupling power distribution of DB-MMI coupler for both TE-mode (solid line) and TM-mode (dashed line) with h=4.0 μm, A=26^0, a=b=1.5 μm, cladding index~1.45, Δn=5% and λ~1.55 μm respectively.

Fig-7.7 shows the normalized coupling power distribution versus longitudinal coupling length of DB-MMI coupler for both TE-mode (solid line) and TM-mode (dashed line) with h=4.0 μm, A=26^0, a=1.5 μm, b=1.5 μm, cladding index~1.45, Δn=5 % and λ~1.55 μm respectively. It is found that for TM-polarization the value of longitudinal beat length (L^l_π) is ~0.24 % more than TE-polarization. The polarization dependence of DB-MMI coupler is slightly more than conventional MMI/TMI couplers because the number of waveguide parameters in the double band geometry is more than that of conventional structures.

7.3. Dependence of h on L_T and Longitudinal Beat Length of DBMMI Coupler

In N x N photonic matrix switching applications [20][21], it is required to keep maximum access waveguide bending loss of 0.1 dB due to large scale integration. Keeping same access waveguide bending loss, the reduction of longitudinal access waveguide length (L_T) is studied with increase of coupling gap (h) by using (7.14)-(7.16) for the proposed DB-MMI coupler with A=26^0, a=b=1.5 μm, index contrast~5%, cladding index~1.45, H_T=7 μm and R=200 μm as shown in Fig-7.8. The cross signs in the figure represents the experimental values of L_T and longitudinal beat length (L^1_π) for fabricated DB-MMI coupler.

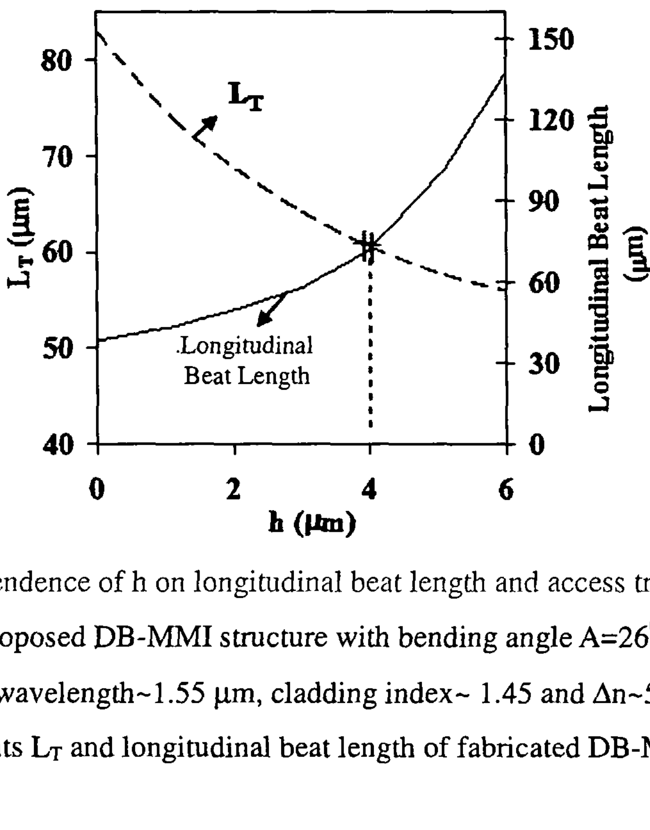

Fig.-7.8: Dependence of h on longitudinal beat length and access transition length (L_T) of the proposed DB-MMI structure with bending angle A=26^0 for h=4 μm, a=b=1.5 μm, wavelength~1.55 μm, cladding index~ 1.45 and Δn~5 %. The cross sign represents L_T and longitudinal beat length of fabricated DB-MMI coupler.

The Fig-7.8 also shows the variation of longitudinal beat length with h. It is seen that as h increases longitudinal beat length of DB-MMI region increases whereas L_T decreases with increase of h and the optimum value for h is obtained at the crossing point of the curves (h~4 μm), at which the value of the L_T and L_π are ~63 μm and 67 μm respectively. The device length of the proposed DB-MMI coupler is obtained as $(2L_T+L_\pi)$~193 μm. In the figure, the h=0 μm corresponds to the double S-bend two mode interference (DB-TMI) coupler reported by previous authors [6]-[7]. The device length of the DB-TMI coupler is obtained as ~214.2 μm (where L_T~88 μm and L_π~38.2 μm) which is 10 % more than that of the proposed DB-MMI coupler.

7.4. Design Device Parameters

Table-7.1: Device Design Parameters

Design Parameters	DB-MMI Coupler	DB-TMI Coupler
Core waveguide width (a), μm	1.5	1.5
Core waveguide Thickness (b), μm	1.5	1.5
Index Contrast (Δn)	5%	5%
Core RI (n_1) , Δn=5%	1.5	1.5
Cladding RI (n_2)	1.45	1.45
Coupling gap (h), μm	4	0
Height of S-bend (H), , μm	11.5	11.5
Radius of bending (R)	200	200
Height of access waveguide (H_T)	7	7
Bending Loss, dB	0.1	0.1
Wavelength (λ), μm	1.55	1.55
Longitudinal coupling length (L^1_π), μm	67	38.2
Access Waveguide length (L_T), μm	63	88
Total device length (L^1_π+2 L_T), μm	193	214.2

Table-7.1 shows the design parameters that is considered for the designed of double band multimode interference (DB-MMI) coupler. For comparison device parameters of DB-TMI coupler are also mentioned in the table.

7.5. Fabrication and Experimental Results

The proposed DB-MMI couplers of width ~7 μm and coupling lengths~ 69 μm, 67 μm, 65 μm for bending angle, A=22^0, 26^0, 30^0 respectively and conventional MMI couplers of coupling lengths~80 μm with h=4 μm, a=b=1.5 μm are fabricated by using SiO_2-SiON material[22]-[32] with Δn~5 %. On the top of a silicon substrate, the embedded waveguide including the MMI section and access waveguides of core (SiON) width ~1.5 μm were formed by a combination of plasma enhanced chemical vapour deposition (PECVD), photolithography [28] and reactive ion etching (RIE) [28] process steps as details are discussed in chapter-6. The top cladding layer (SiO_2) of thickness ~3 μm is deposited using PECVD method[27]-[32].

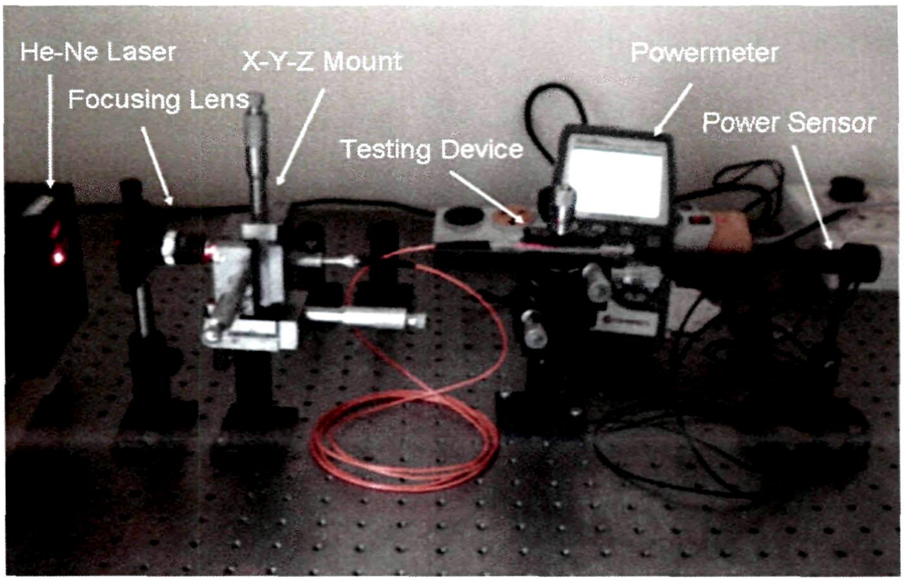

Fig-7.9: Power loss measurement set-up

Fig.-7.9 shows the experimental set-up that is used for the measurement of optical power loss of the fabricated devices and the flow chart of fabrication process steps adopted for the development of the proposed device is shown in Fig-7.10 (details are discussed in previous chapter-6).

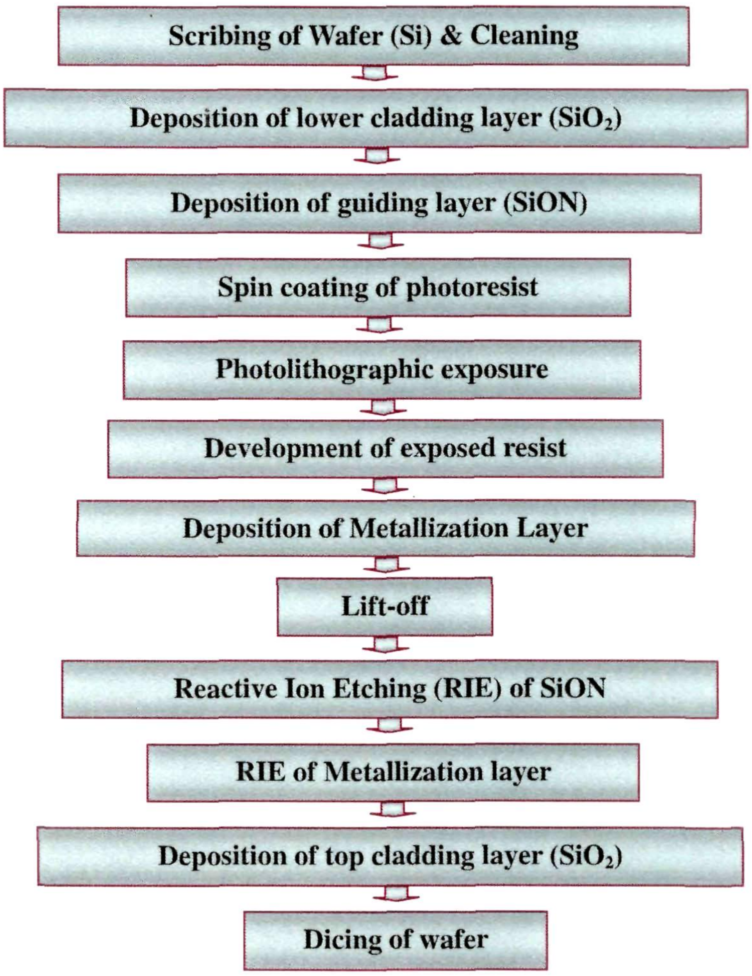

Fig.-7.10: Flow chart of fabrication process steps

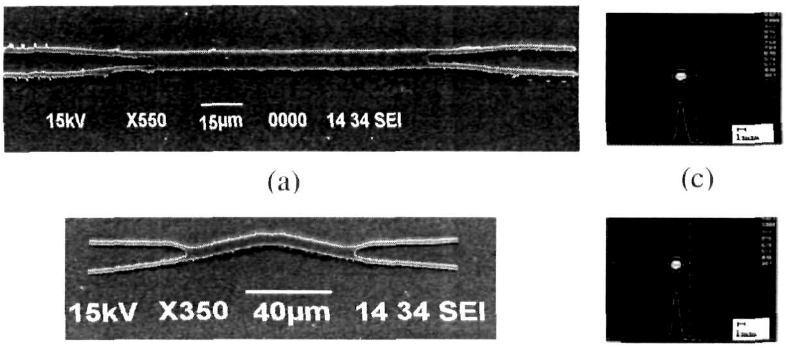

(a) (c)

(b) (d)

Fig-7.11: SEM images and corresponding beam spot measurements of (a), (c) conventional MMI coupler of longitudinal coupling length ~79.9 μm, A=0^0 and (b), (d) proposed DB-MMI coupler of longitudinal coupling length ~67.2 μm and A=26^0.

Fig-7.11(a) shows the SEM photograph of conventional MMI coupler of coupling length ~79.9 μm whereas Fig.-7.11(b) shows SEM image for DB-MMI coupler of coupling length ~ 67.2 μm respectively. The coupling into and out of the devices was made by using tapered and polarization maintaining fibers with focusing lenses, aligned to the chip and tunable stabilized laser diode by six-axis micrometer stages. The output power was detected by the movable germanium p-i-n detector attached with power meter of a minimum detectable power of 100 pW. The output field of waveguide-3 and waveguide-4 are monitored. Further, the waveguide propagation losses are obtained ~ 0.15 dB/cm which is measured for a single planar waveguide of length ~2 cm (with SiON as the core surrounded by silica cladding layer); whereas the fiber to chip loss per facet is less than 1.1 dB that are determined using the relation $-10\log[(P_{out}-P_{in})/P_{in}]$. Fig.-7.11(c) shows beam spot of output access waveguide-4 of conventional MMI coupler recorded by CCD camera at distance 10 cm whereas Fig.-7.11(d) shows the beam spot of access waveguide-4 of DB-MMI coupler recorded by CCD camera at a distance of 10 cm from access waveguide-4. The measured values of cross state and bar state coupling power for the proposed and conventional MMI structure as shown in Fig.-7.2, Fig.-7.5 and Fig.-7.8

are matching well with theoretical curves. The longitudinal beat length (L^{1}_{π}) and longitudinal access waveguide length of the proposed MMI coupler for A~26^0 obtained experimentally are also close to theoretical values as given in Fig.-7.8. The total device length of the fabricated cross coupling DB-MMI coupler is obtained as ($2L_T+L_\pi$)~193.2 μm which is less than that of conventional MMI coupler ($2L_T+L_\pi$)~213.9 μm. The power imbalance for the proposed DB-MMI coupler and conventional MMI coupler with w_{mmi}~6.9 μm, 7 μm and 7.1 μm is studied experimentally and it is seen that these results are very much close to those obtained theoretically as shown in Fig.-7.5. The accuracy of all these results is within 10%.

7.6. Conclusion

In this chapter, a double S-bend multimode interference (MMI) coupler is proposed and designed for the reduction of coupling length. The coupling characteristics of the proposed structure has been studied theoretically by using simple effective index method based sinusoidal modes and compared with those of the conventional MMI structure experimentally. Both the longitudinal access waveguide length and beat length of the double S-bend MMI (DB-MMI) coupler are optimized at access waveguide gap h~4 μm. The designed DB-MMI coupler and conventional MMI coupler are realized with silica waveguides using SiON as the core layer. It is seen both theoretically and experimentally, that the device length of the DB-MMI coupler is ~19 % and 10 % less than that of a conventional MMI coupler and existing DB-TMI coupler [6]-[7] respectively. The variation of power imbalance on fabrication tolerance of the proposed geometry is almost close to that of the conventional MMI coupler and less than that of other MMI structures.

References:

1. Deka, B., et al., Tooth-shaped grating-assisted structure for compact multimode interference coupler, *Appl. Opt.* **50**, E193-E199, 2011.

2. Yanagawa, H., et al., Index-and dimensional taper and its application to photonic devices, *J. Lightwave Technol.* **10**, 587–591, 1992.

3. Sahu, P. P. Parabolic tapered structure for an ultra compact multimode interference coupler, *Appl. Opt.* **48**, 206-211, 2009.

4. Sahu, P. P. A tapered structure for compact multimode interference coupler, *IEEE Photonic. Technol. Lett.* **20**, 638-640, 2008.

5. Yao, C., et al. An ultracompact multimode interference wavelength splitter employing asymmetrical multi-section structures, *Opt. Exp.* **20**, 18248-18253, 2012.

6. Sahu, P. P. Double S-bend structure for a compact two mode interference coupler, *Appl. Opt.*, **50**, 242-245, 2011.

7. Sahu, P. P. A double S-bend geometry with lateral offset for compact two mode interference coupler, *IEEE J. Lightwave Technol.* **29**, 2064-2068, 2011.

8. Kasaya, K., et al., A simple laterally tapered waveguide for low-loss coupling to single-mode fibers, *IEEE Photon. Technol. Lett.* **5**, 345–347, 1993.

9. Mitomi, O., et al., Design of a single-mode tapered waveguide for low-loss chip-to-fiber coupling, *IEEE J. Quantum Electron.* **30**, 1787–1793, 1994.

10. Janz, C. F., et al., Bent waveguide couplers for (de) multiplexing of arbitrary broadly separated wavelengths using two-mode interference, *IEEE Photon. Technol. Lett.* **7**, 1037-1039, 1995.

11. Wei, H., Jinzhong, Y., et al. Fabrication of 2 x 2 tapered multimode interference coupler, *Electronics Lettr.* **36**, 1618-1619, 2000.

12. Januar, I, Mickelson, A. R. Characteristics of S-Shaped Wavegude Structures by the Annealed Proton Exchange Process in LiNbO3, *IEEE J. Lightwave Technol.* **11**, 2044–2051, 1993.

13. Wang, Z., et al., Rearrangeable nonblocking thermo-optic 4x4 switching matrix in silicon-on-insulator, *IEE Proc. Optoelectron.* **152**, 160-162, 2005.

14. Nishihara, H., Haruna, M., & Suhara, T. *Optical Integrated Circuits*, McGraw-Hill, New York, 1989.

15. Deka, B., et al., Transformation relationship of directional coupler with multimode interference coupler and two mode interference coupler, *J. Optics* **38**, 75-87, 2009.
16. Chiang, K.S. Effective index method for the analysis of optical waveguide couplers and arrays: an asymptotic theory, *J. of Lightwave Tech.* **9**, 62-72, 1991.
17. Wang, Q., et al., Effective index method for planar lightwave circuits containing directional couplers, *J. of Optics Communications* **259**, 133-136, 2006.
18. Tsai, T. Y., et al., A novel ultra compact two-mode-interference wavelength division multiplexer for 1.5 μm operation, *IEEE J. Quantum Electron.* **41**, 741-746, 2005.
19. Deka, B., et al., Tooth Shaped Grating Assisted Geometry for Two Mode Interference (TMI) Coupler, *J. of Opt.*, **40**, 162-167, 2011.
20. Kasahara, R., et al., New structure of silica-based planar lightwave circuits for low-power thermo-optic switch and its application to 8x8 optical matrix switch, *J. Lightwave Technol.* **20**, 993-1000, 2002.
21. Offrein, B. J., et al., Wavelength tunable optical add-after-drop filter with flat passband for WDM networks, *IEEE Photon. Technol. Lett.* **11**, 239-241, 1999.
22. Levy, D. S., et al., Fabrication of ultracompact 3-dB 2x2 MMI power splitters, *IEEE Photonic. Technol. Lett.* **11**, 1009-1011, 1999.
23. Chin, M. K., et al., High index contrast waveguides and devices, *Appl. Opt.* **44**, 3077-3086, 2005.
24. Sahu, P. P. Silicon oxynitride a material for compact waveguide devices, *Indian J. of Physics* **82** 265-272, 2008.
25. Chen, K., et al., Silicon oxynitride optical waveguide ring resonator utilizing a two-mode interference structure, *Int. J. Photoenergy* **Dec**, 1-5, 2012.
26. Henry, C. H. et al., Low Loss Si_3N_4-SiO_2 Optical Waveguides on Si, *Appl. Opt.*, **26**, 2621–2624, 1987.

27. M.G. Hussein, M.G. et al. Stability of low refractive index PECVD silicon oxynitride layers, *Proceedings Symposium IEEE/LEOS Benelux Chapter*, 77-80, 2003.

28. Gandhi, S. K. *VLSI Fabrication Principles: Silicon and Gallium Arsenide*, Willey-India, New Delhi, 2008.

29. Bona, G. L., et al., Wavelength division multiplexed add/drop ring technology in corporate backbone networks, *Opt. Eng*. **37**, 3218-3228, 1999.

30. Hoffmann, M., et al., Low-loss fiber-matched low-temperature PECVD waveguide with small-core dimensions for optical communication systems, *IEEE Photonic. Technol. Lett*. **9**, 1238-1240, 1997.

31. Guidice, M. D., et al., Silicon oxynitride 3 dB coupler for 1540 nm single mode applications, *in Proc. ECOC'91*, 309-312, 1991.

32. Worhoff, K, et al., PECVD silicon oxynitirde optimization for application in integrated optics, *Sensors and Actuators* A **74**, 9-12, 1999.

****

Chapter-8:

Conclusion and Future Work

In this thesis, efforts have been made for the design, development and comparative study of Photonic Integrated Device (PID) components such as Directional Coupler (DC), Two Mode Interference (TMI) coupler and Multimode Interference (MMI) coupler; tooth shaped grating assisted structures and double S-band geometry. At first, these device components and their geometries as reported by previous authors have been reviewed. The available waveguide materials such as SiO_2/SiO_2-GeO_2 (Core), SiO_2/Silicon Oxynitride (SiON) core, Silicon-On-Insulator (SOI) (silicon core) etc. for the fabrication of these structures as mentioned in the second chapter are studied and compared. Out of these materials SiO_2/SiON was selected for our work owing to various advantages such as availability of wide index contrast of their waveguides, polarization sensitiveness, chemical inertness, low losses, high stability and compatibility with conventional IC processing technology.

In these studies, first of all a transformational relationship between DC, TMI and MMI coupler is established by using Simple Effective Index Method (SEIM) based on sinusoidal modes. From the transformation relationship, coupling power has been estimated in the access waveguides of both TMI coupler and MMI coupler accurately. From the coupling characteristics, it is seen that the beat lengths for conventional DC, TMI coupler and MMI couplers with index contrast $(\Delta n)=5\%$ are obtained as 91 μm, 45 μm and 80 μm respectively. In addition, the results of coupling behaviors have been compared with the beam propagation results obtained by using commercially available optiBPM software based on beam propagation method (BPM). The polarization dependence and the effect of fabrication tolerances on power imbalance have also been studied. It is seen that TMI coupler has the beat length difference between TE and TM modes (~0.25%) than the other two structures because of having few design parameters. The rate of increase of power imbalance with respect to width tolerances for TMI coupler, MMI coupler and directional coupler are approximately obtained as $\frac{\partial}{\partial(\delta w)}$ [Power Imbalance (dB)] ~ 0.18 dB/μm, 0.13 dB/μm and 0.15 dB/μm respectively which are very close to each other.

Further, as compactness is the basic requirement of PID components, our study concentrates on the inclusion of compact structure for these components. In this direction, tooth shaped grating assisted geometry for Directional Coupler (DC) and Two Mode Interference (TMI) coupler have been used and a transformation relationship have been formulated, from which the coupling power of grating assisted TMI (GA-TMI) coupler is derived using sinusoidal mode simple effective index method (SM-SEIM). The beat lengths of grating assisted directional coupler (GA-DC) and grating assisted TMI (GA-TMI) coupler are obtained as 45 μm and 22 μm respectively. It is seen that the beat length of GA-TMI coupler is ~50% less than that of the conventional TMI coupler, 51% less than that of the GA-DC and 75% less than that of the conventional directional coupler respectively. The polarization dependences of GA-TMI coupler and GA-DC are ~0.22 % and ~0.24% respectively. The rate of increase of power imbalance (dB) with respect to width tolerance for GA-TMI coupler and conventional TMI coupler are approximately obtained as $\frac{\partial}{\partial(\Delta W)}$ [Power Imbalance (dB)] ~0.16 dB/μm and 0.18 dB/μm whereas for GA-DC and conventional directional coupler are obtained as ~0.13 dB/μm and 0.15 dB/μm which are almost close to those for GA-TMI and conventional TMI coupler respectively.

We have proposed the tooth shaped grating assisted geometry for multimode interference coupler and designed for the reduction of total length. Initially, the coupling behavior of Grating Assisted MMI coupler, using Simple Effective Index Method (SEIM) based on sinusoidal modes have been analyzed theoretically and the coupling characteristics, beat length and fabrication tolerances for GA-MMI coupler with GA-DC and GA-TMI coupler are compared. It is seen that the beat length of tooth shaped GA-MMI coupler is 40 μm which is ~50% less than that of conventional MMI coupler. But the total device length having access waveguide length and the coupling length (beat length) of GA-TMI coupler and GA-MMI coupler are obtained as ~286.2 μm and 269 μm respectively which shows that device length of GA-MMI coupler is ~17 μm less than GA-TMI coupler and ~26 μm less than GA-DC respectively. The rate of increase of power imbalance (dB) with respect to width tolerance for GA-MMI, GA-TMI and conventional MMI couplers are approximately obtained as $\frac{\partial}{\partial(\delta W)}$ [Power Imbalance (dB)] ~0.17 dB/μm, 0.16 dB /μm and 0.13 dB /μm respectively. So, the rate of increase of power imbalance for GA-MMI coupler is almost same as that of the GA-TMI coupler.

The designed structures of conventional directional coupler, two mode interference coupler and multimode interference coupler were then fabricated with index contrast (Δn)~5% using Silicon Oxynitride (SiO_xN_y) as the core material surrounded by Silica (SiO_2) cladding layer with the help and support from Centre of Excellence in Nano Science and Engineering (CeNSE), Indian Institute of Science (IISc.), Bangalore under Indian Nano-electronics User Program (INUP). During the fabrication process, optimization of process parameters for deposition and etching of SiON layer using Plasma Enhanced Chemical Vapour Deposition (PECVD) and Reactive Ion Etching (RIE) were also carried out. The coupling characteristics of the fabricated devices were experimentally verified using the power loss measurement set-up available in the Integrated Optic Device and Photonics Research Laboratory at Tezpur University. It is found that the experimental values of beat length for DC, TMI coupler and MMI couplers are 91.2 μm, 45.1 μm and 79.9 μm respectively which have almost match well with the results obtained by simple effective index method based on sinusoidal modes. Although the tooth shaped grating assisted DC, TMI coupler and MMI coupler have been designed, the fabrication of tooth shaped grating assisted structures of grating width (ΔW)~0.25 μm with permissible propagation loss ~0.15 dB/cm are challenging using standard photolithography technique and fabrication process steps. Thus, instead of fabricating the grating assisted structures, it is shown theoretically that the tooth shaped grating assisted geometry certainly reduces the device length.

We have also proposed and designed double S-bend MMI (DB-MMI) coupler and studied both theoretically and experimentally using the same waveguide materials (as discussed earlier) and Simple Effective Index Method (SEIM) based on sinusoidal modes for compactness of photonic integrated devices. The coupling characteristics of DB-MMI coupler have been estimated using SEIM based on sinusoidal modes. The optimal values of longitudinal coupling length and access waveguide length are obtained as ~67 μm and 63 μm respectively at h~4 μm (gap between two access waveguides near MMI region). The designed values of DB-MMI device parameters as mentioned earlier have been fabricated by using SiO_2-SiON material with Δn~5%. It is found that the experimental values of beat length for DB-MMI coupler is ~ 67.2 μm which is 16% lower than that of the conventional MMI coupler of coupling length ~79.9 μm. The total device length of the fabricated DB-MMI coupler is obtained as ~193.2 μm which is 39% less than that of total device length of conventional MMI coupler and 9% less than that of total length of double S-band TMI (DB-TMI) coupler respectively.

As future prospects an attempt can be made to fabricate these GA-TMI coupler and GA-MMI coupler with ΔW~0.25 μm, higher index contrast (i.e. Δn>5%) and permissible propagation loss of ~0.15 dB/cm in order to use these components in large scale integrated optic devices such as wavelength division multiplexer, add/drop multiplexer and photonic matrix switches for high speed optical networks. Although the reduction of total device length of the designed devices is studied with increase of index contrast (Δn) but SiO_2/SiON material has been used with Δn maximum up to 5% only for time limitations and other constraints in fabrication of these compact device components. Moreover, insertion loss increases with increase of Δn, due to having more fiber to device coupling losses.

Further the incorporation of grating geometry with double band structures in the coupling region of DC, TMI coupler and MMI coupler will reduce the coupling length significantly and fabrication of such components is possible under high resolution pattering.

****